UNIVERSITA' DEGLI STUDI DI NAPOLI "FEDERICO II"

Doctorate School in Analysis of Environmental Systems
Ph.D. Thesis, XXVII Cycle

Assessment of landslide susceptibility in Structurally Complex Formations by integration of different A-DInSAR techniques

Advisor:
Prof. Domenico Calcaterra

PhD candidate:
Alessandro Novellino

Co-advisors:
Dr. Francesca Cigna
Dr. Massimo Ramondini
Dr. Andrew Sowter

***Coordinator of Doctorate School*:**
Prof. Maurizio Fedi

- 2015 -

Abstract

Instability events are recurring phenomena in Southern Italy due to its geological history and tectonic-geomorphological evolution leading to the occurrence of several formations identified as Structurally Complex Formations (SCFs; Esu, 1977) in a territory mainly composed of densely populated areas also in mountainous and hilly regions. SCFs are clay-dominant terrains that, usually, give origin from very-slow to extremely-slow phenomena (Cruden and Varnes, 1996) with a long evolutionary history made up of multiple reactivations that makes difficult their identification, monitoring and susceptibility evaluation.

The study has been carried out from point-wise (Bisaccia, Costa della Gaveta and Nerano cases) to wide areas (Palermo province case) where crops out SCFs as the Termini sandstones Formation (CARG, 2011), the Varicoloured Clays of Calaggio Formation (Ciaranfi *et al*., 1973), the Varicoloured Clays Unit (Mattioni *et al*., 2006) the Sicilide Unit (Vitale and Ciarcia, 2013 and references therein), the Numidian Flysch (Johansson *et al*., 1998) and the Corleone Calcarenites (Catalano R. *et al*., 2002).

The aim of this thesis is to produce updated Landslide Inventory Maps and, whenever possible, Landslide Susceptibility Maps following a new approach during the landslide mapping and landslide monitoring stages.

The Landslide Inventory Maps have taken into account the combination of geological, geomorphological, and stereoscopic surveys, as well as engineering geological investigations, namely conventional techniques. In addition innovative Advanced-Differential Interferometry Synthetic Aperture Radar (A-DInSAR) techniques have been used: the Coherent Pixels Technique – CPT (Mora *et al*., 2003; Blanco *et al*., 2008), the Intermittent Small BAseline Subset – ISBAS (Sowter *et al*., 2013) and the Ground-Based Synthetic Aperture Radar.

Finally, the Weight of Evidence method (van Westen, 1993) has been chosen to generate the Landslide Susceptibility Maps only for the point-wise studies.

In the case of Nerano (Province of Naples), the ISBAS analysis on ENVISAT images (for the period 2003-2010) has been carried out and compared with inclinometric and rainfall data. These have revealed several reactivations of a rotational slide + earth flow (Cruden and Varnes, 1996) that involves reworked clay olistostromes and limestone olistoliths inside the Termini sandstones Formation; even in recent years the landslide, despite many engineering works, has given evidence of a continuing activity. The results highlight a very slow movement in the detachment zone (<1 mm/yr), which assumes slightly higher values in the accumulation area (5 mm/yr). The Landslide Susceptibility Map confirms the high levels in the flow track and the accumulation area.

In Bisaccia (Province of Avellino), a conglomeratic slab undergoes a Deep Seated Gravitational Slope Deformation (DSGSD; Pasuto and Soldati, 2013 and references therein) due to the bedrock consolidation, made of the Varicoloured Clays of Calaggio Formation. Here the CPT processing on ENVISAT images (covering the period between 2002 and 2010), displays a vertical displacement for the town center, suffering a progressively increasing velocity from the southern (4.2 mm/yr) to the northern (15.5 mm/yr) portion of the slab that localizes four different sectors. The pattern is confirmed from the building damage map. The landslides susceptibility reaches the highest values in the adjacent valleys and at the edges of each sector.

Multiple datasets have been employed for the Costa della Gaveta case-study (Province of Potenza), these encompass: ENVISAT, TerraSAR-X and COSMO-SkyMed constellations together with Ground Based Synthetic Aperture Radar (GBSAR). The A-DInSAR data have been compared with stereoscopic analysis and the available rainfall and inclinometric data. The analysis allows for the

identification of 16 landslides (complexes and earth flows; Cruden and Varnes, 1996) developed in the Varicoloured Clays Unit that show, according to all the existing instruments, velocities between 1.5 and 30 mm/yr. The western side of Costa della Gaveta slope is the portion which suffers the highest landslides susceptibility levels.

In the Province of Palermo (northwestern Sicily) information deriving from A-DInSAR processing, specifically the ISBAS technique, have been focused on three subareas (Piana degli Albanesi, Marineo and Ventimiglia di Sicilia) for a total extension of 182 Km^2 where standard A-DInSAR algorithms showed limitations due to the widespread presence of densely vegetated areas. The radar-detected landslides have been validated through field geomorphological mapping and stereoscopic analysis proving to be highly consistent especially with slow phenomena. The outcome has allowed to confirm 152 preexisting landslides, to detect 81 new events and to change 133 previously mapped landslides, modifying their typology, boundary and/or state of activity.

The study demonstrates how a better knowledge of landslide development and their cause-effect mechanisms provided by new Earth Observation techniques is useful for Landslide Inventory and Susceptibility Maps.

The research project has been carried out at the University of Naples “Federico II”, including nine months (September 2013 – May 2014) spent in the United Kingdom, at the British Geological Survey under the supervision of Dr. Francesca Cigna and Dr. Jordan Colm and at the University of Nottingham (Department of Civil Engineering), under the supervision of Dr. Andrew Sowter where the ISBAS technique has been recently developed.

Declaration of Originality

I confirm that the work described in this thesis is my own work unless otherwise cited or acknowledged. The thesis is of my own composition and has not been submitted for any other degree at the University of Naples or any other institution.

Alessandro Novellino

March 2015

Thesis citation: Novellino A., 2015. *Assessment of landslide susceptibility in Structurally Complex Formations by integration of different A-DInSAR techniques*. PhD thesis, Federico II University of Naples, Department of Earth, Environment and Resources Sciences, Naples, Italy.

Acknowledgements

First and foremost, I would like to express my greatest and sincerely thanks to my supervisors Prof. Domenico Calcaterra, Dr. Francesca Cigna, Dr. Massimo Ramondini and Dr. Andrew Sowter because they gave me something priceless: their time.

They always provided me with a clear guidance, constructive criticism, continuous questions, constant encouragements and trust throughout my PhD study. Furthermore they taught me to think critically about my research, were always patient about my slow progress and negative results and helped me build confidence. In particular I would like to thank Prof. Domenico Calcaterra for awarding me with this PhD project three years ago even if I had no idea about arguments like remote sensing and interferometry.

I would like to thank my group with a special mention for Diego, Serena and Pierluigi for solving my endless InSAR questions and for the useful discussions and fundamental support. I gratefully acknowledge Adriana, Hannah, Lavinia and Roberto for their assistance during the writing of this thesis.

The tea break activities at the Nottingham Geospatial Institute and the British Geological Survey have always been interesting and memorable. I'm particularly thankful for the company and friendship of Ahmed, Asyran, Fifik and the BGS team in tackling technical problems with Punnet and carefully managing the use of computing resources and data storage in Nottingham.

My love and heartfelt thanks go to my classmates scattered around Europe: Alessia, Ciro, Diletta, Dino, Francesco, Gianluca, Giorgio, Giovanni, Lorenzo, Marco, Massimo and Pasquale. Thank you for your thoughts, well-wishes, phone calls, e-mails, texts, visits, editing advices, and being always on my side. You have always represented a model and a font of inspiration to me and the only ones I cannot let you

down. Of course I cannot forget my family for the love they always shows me even when I do not deserve it.

At the very end, I would like to thank H.R.M. the Queen Elizabeth II, who probably doesn't know me. However, I thank Her for being the monarch of a wonderful land, where I had the opportunity to spend nine wonderful months of the my research activity.

Table of Contents

List of Figures

List of Tables

List of Acronyms

2D: Two Dimensions

3D: Three Dimensions

A-DInSAR: Advanced-Differential SAR Interferometry

AdB: Autorità di Bacino

ADVICE: ADVanced dIsplaCement monitoring system for Early warning

AIS: Ariano Irpino Supersynthem

ALOS: Advanced Land Observing Satellite

AMC: Apenninic-Maghrebian Chain

ATI: Along-Track Interferometry

BGS: British Geological Survey

CARG: CARtografia Geologica

CARM: Conventional and A-DInSAR Results Matching

COSMO-SkyMed: COnstellation of small Satellites for Mediterranean basin Observation

CP: Corleto Perticara Formation

CPT: Coherent Pixels Technique

CSK: COSMO-SkyMed

DEM: Digital Elevation Model

DInSAR: Differential SAR Interferometry

DLR: German Aerospace Center

DSGSD: Deep-Seated Gravitational Slope Deformation

EEA: European Environmental Agency

ENVISAT: Environmental Satellite

EO: Earth Observation

ERS: European Remote Sensing

ESA: European Space Agency

ESD: Enhanced Spatial Differences

ESPRE: Extraordinary Plan for Environmental Remote Sensing

Fm: Formation

FS: Factor of Safety

GBSAR: Ground-Based SAR

GIS: Geographical Information System

GPS: Global Positioning System

HSP: Hydro-geomorphological Setting Plan

IDS: Ingegneria dei Sistemi

IFFI: Inventario dei Fenomeni Franosi in Italia

IFSAR/InSAR: Interferometric Synthetic Aperture Radar

IPTA: Interferometric Point Target Analysis

ISBAS: Intermittent Small BAseline Subset

ISPRA: Institute for Environmental Protection and Research

IUGS: International Union of Geological Sciences

JPL: Jet Propulsion Laboratory

LEWIS: Landslide Early Warning Integrated System

LiDAR: Light Detection And Ranging

LOS: Line Of Sight

Mb: Member

MORFEO: Monitoring Landslide Risk Through Earth Observation Technology

MSBAS: Multidimensional SBAS

MTI: Multi-Temporal Interferometry

NASA: National Aeronautics and Space Administration

No.: Number

PS: Permanent Scatterers

PSInSAR™: Persistent Scatterer InSAR

PSP-DIFSAR: Persistent Scatterers Pairs- DIFferential InSAR

PSTB: Pelagian Sicilian Thrust Belt

PVC: PolyVinyl Chloride

RTI: Repeat-Track Interferometry

SAR: Synthetic Aperture Radar

SBAS: Small BAseline Subset

SCF: Structurally Complex Formation

SE: Standard Error

SLAM: Service for LAndslide Monitoring

SLC: Single Look Complex

SNR: Signal Noise Ratio

SP: Strada Provinciale

SPN: Stable Point Network

SS: State Highway

STUN: Spatio-Temporal Unwrapping Network

TInSAR: Terrestrial InSAR

TLS: Terrestrial Laser Scanner

TOPSAR: Terrain Observation with Progressive Scans SAR

TSM: Target Suitability Map

TSX: TerraSAR-X

UAV: Unmanned Aerial Vehicles

USGS: United States Geological Survey

VCCF: Varicoloured Clays of Calaggio Formation

VCU: Varicoloured Clays Unit

WoE: Weight of Evidence

WP/WLI: Working Party on World Landslide Inventory

XRD: X-Ray Diffraction

XTI: cross-track interferometry

Chapter 1: Introduction

1.1 Motivation

Landslides can result in enormous casualties and huge economic losses in mountainous regions especially nowadays as development expands into unstable hillslope areas under the pressures of increasing population size and urbanization.

In this framework, Italy is particularly concerned with forecasting landslide effects (Calcaterra D. *et al*., 2003), in compliance with law no. 267/98, enforced after the disaster of the Sarno mudflows of 5 May 1998 in the Campania Region, Southern Italy (Capparelli and Versace, 2014).

Spatial and temporal landslide mapping is a crucial step to infer the potential size, or intensity (see paragraph 2.2), of this natural calamity and determine the related susceptibility, hazard, vulnerability and risk (Guzzetti *et al*., 2012).

In particular the monitoring of slopes requires continuous technological developments in order to obtain the most precise and up-to-date information on natural events and their evolution. The identification of the most efficacious monitoring system is difficult and is based on a tradeoff between technical, logistical and economic requirements available on every occasion. In recent years Remote Sensing plays a key role in the process of land use management.

This PhD thesis aims to analyze four areas, (Nerano, Bisaccia, Costa della Gaveta and Palermo province; fig.1.1) affected by very slow movements (velocity ranging between few mm/year to few cm/year) involving Structurally Complex Formations (SCFs; Esu, 1977) in Southern Italy.

The long evolutionary history of these phenomena, characterized by multiple reactivations, requires regular and continuous monitoring in order to correctly establish cause and effect correlations, and to predict possible reactivation phases that may result in severe economic damage. Indeed, even if the landslide velocities involved do not constitute a life-loss risk, they assume a key role in the every-day

life of a community because of the damage that they can provoke, directly or indirectly, to buildings, infrastructures, loss of productivity, reduction of real estate value, loss of tax revenue, and other induced economic effects.

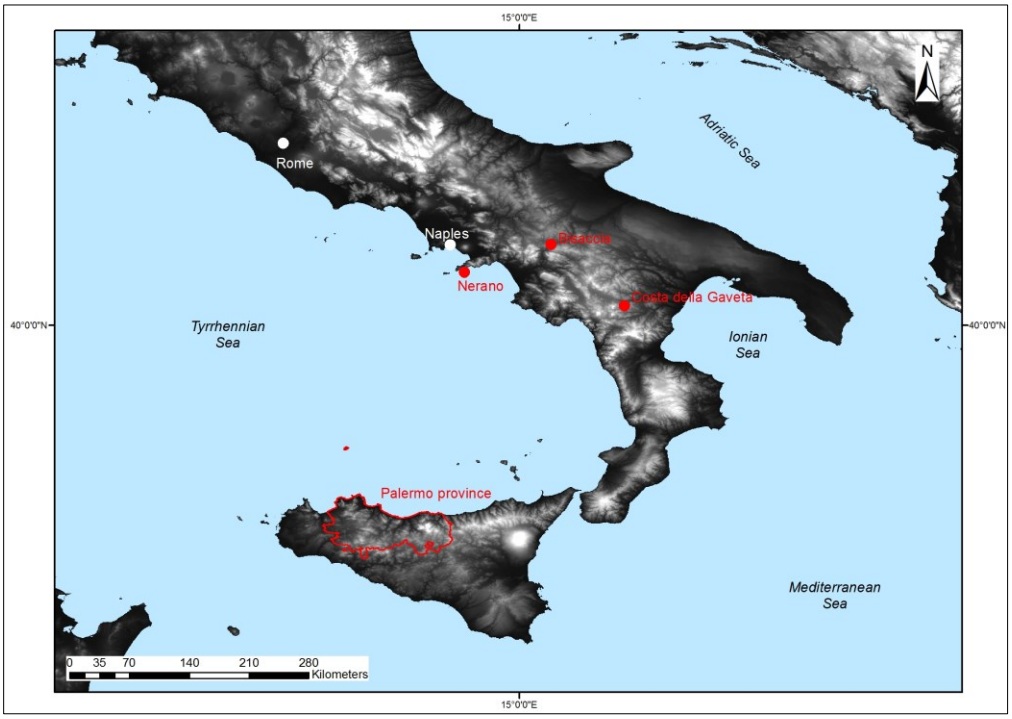

Figure 1.1 – Location of the case studies: Bisaccia (NA), Costa della Gaveta (PZ), Nerano (NA) and Palermo province.

Traditional monitoring techniques as geomorphological surveys and topographic and geotechnical measurements are usually used to detect slope deformations with a very high accuracy. Often the wide extension of the area, the absence of identifiable features, the location in inaccessible places or the restricted time and money at disposal are a hindrance to conventional slope investigations. Remote Sensing techniques, and in particular Advanced-Differential SAR Interferometry (A-DInSAR) techniques for studies of ground deformation, contributes to partially overcome all of these limitations, thereby guaranteeing a high accuracy in final results from a point-wise to a wide area investigation.

This thesis uses a multidisciplinary approach coupling innovative investigation methods with traditional technologies sustainable for the different scales of observation and geological-geomorphological settings. The comparison, integration and validation has balanced weaknesses of a

technique with strengths of the others and, therefore, has ensured a net improvement in the generation of Landslide Inventory Maps and Landslide Susceptibility Maps reducing the time and resources required for their compilation and systematic updating.

1.2 Research objectives

Recent applications of A-DInSAR techniques have demonstrated their potential for the monitoring of geohazards mainly related to their capability to provide information on wide areas (kilometer-size extension), with high spatial resolution (metres-size). Furthermore, the final results can be considered competitive with those available by using traditional ground techniques, in terms of achievable accuracy (up to a few millimeters).

The thesis intends to:

- highlight the advantages of A-DInSAR supporting in monitoring slow-moving landslides and, at the same time, to present also the main drawbacks so far encountered, in order to obtain a general framework on when and where the method can be used. Indeed the study shows how A-DInSAR techniques are not always exploitable and, when exploited, not always free-standing. This implies that they require pre-survey suitability evaluations, calibration and validation with conventional monitoring methods.
- Assimilate SAR information as routine analyses for the assessment of the spatial and temporal evolution of mass movements. In this thesis the outcomes have been combined in a bivariate statistical analysis, following the method proposed by van Westen (1992), the Weight of Evidence, to evaluate landslide susceptibility.

In particular, ground-based and satellite-based A-DInSAR analysis have been used, the latter through two different techniques: the Coherent Pixels Technique - CPT (Mora *et al*., 2003) and the Intermittent Small BAseline Subset - ISBAS (Sowter *et al*., 2013).

Microwave sensing encompassed C-band (of ENVISAT data), X-band (of Cosmo-SkyMed and TerraSAR-X data) and Ku-band (of Ground-Based SAR – GBSAR) sensors.

The imagery dataset has been used for studies of landslides at different degrees of detail: from point-wise (Bisaccia, Costa della Gaveta and Nerano cases) to wide area (Palermo province case).

The ENVISAT and Cosmo-SkyMed imagery has been obtained thanks to an agreement between the University of Naples and the Italian Ministry of Environment, Territory and Sea. TerraSAR-X data was provided through a project (ID: GEO1589) coordinated by the University of Pavia (Principal Investigator: Dr. Davide Notti). Finally the GBSAR equipment was provided by IDS (Ingegneria dei Sistemi) S.P.A. company.

1.3 Framework

The thesis has been divided into five chapters. This first chapter is an introduction to the main topics covered by the thesis together with its research objectives.

The second chapter describes the basic concepts related to landslides, definition, classification and causes, along with the derived products: susceptibility, hazard and risk zoning, with particular attention to the evaluation of susceptibility landslides. The end of the second chapter deals with the geological and geotechnical description of SFCs.

The third chapter is dedicated to materials and methods exploited in this work. It presents a brief illustration on conventional mapping and monitoring techniques in addition to a detailed description of remote sensing, DInSAR analysis, A-DInSAR techniques and their applications. The last paragraph of the third chapter explains the Weight of Evidence method.

The fourth chapter describes the application of A-DInSAR and discusses the results for the four studied sites: Nerano, Bisaccia, Costa della Gaveta and the Palermo province.

The fifth chapter discusses the conclusions of the thesis and provides a critical analysis of the obtained results highlighting strenghts and weaknesses of A-DInSAR application. Furthermore, it identifies possible future applications of the studied technology.

Finally, the appendix gives the bibliographic record of articles, proceedings and the chapter in an edited book published according to the PhD results.

Chapter 2: Landslides

A natural disaster is a major adverse event resulting from natural processes of the Earth; examples include floods, volcanic eruptions, earthquakes, tsunamis, and landslides. The latter are among the most dangerous and most frequent natural calamities.

Landslides before being a geohazard, are a natural form of erosion and are extremely important geological processes for the shaping of landscapes and landforms. They re-distribute soil and sediments in a process which can be from extremely-rapid to extremely-slow (fig. 2.6).

It is estimated that, globally, landslides cause damage for tens of billions of dollars (Table 2.1) and thousands of deaths and injuries each year, representing about 40% among all geohazard costs (Guha-Sapir *et al*., 2013).

	Climatological	**Geophysical**	**Hydrological**	**Meteorological**
Africa	0	0	0.83	0.1
Americas	22.46	0.68	0.58	79.67
Asia	0.02	2.14	19.25	6.56
Europe	4.15	15.8	4.24	0.01
Oceania	0	0	0.7	0.15

Table 2.1 – Cost of damage caused by natural disasters in 2012, by continent and type of disaster (in billion U.S. dollars). Climatological: extreme temperatures, drought, wildfire. Geophysical: earthquakes, volcanos, landslides (dry). Hydrological: floods, mudslides (wet). Meteorological: storms. From Guha-Sapir et al*., (2013).*

To prevent life-losses due to natural disasters, landslide mapping and risk zoning are fundamental, especially if one considers that landslide activity is expected to increase as a consequence of human activities, such as rapid urbanization, deforestation and climate changes, that have severely modified the natural environment, making it extremely vulnerable (Klose *et al*., 2014).

2.1 Landslides: definition, classification and causes

Mass wasting (Prothero and Schwab, 2003) is a general downslope movement of soil and/or rock under the influence of any agent like wind (grain flows), water (turbidity currents) or gravity (landslides).

The latter represents a movement of mass rock, debris, earth or man-made ground alongside a natural or artificial slope (Cruden, 1991). The absence of a movement along a slope excludes ground subsidence from this definition.

Landslides classifications follow various criteria, but the most complete and used considers: the material involved, the type of movement, the activity (state of activity, distribution of activity and style of activity) and the velocity.

In this thesis the landslide classification in terms of material and type of movement is based on the Cruden and Varnes (1996) system. Other classifications include those of Hutchinson (1988), Crozier (1989) and Dikau *et al*. (1996).

The material contained in a landslide may be geotechnically described as either rock, a solid and cemented aggregate of particles, and soil, a cohesionless aggregate of coarse-grained particles (debris) or fine-grained particles (earth). The terms applied should describe the displaced material in the landslide before it was displaced.

If the kinematics of the displaced mass is taken into account, the WP/WLI (1993a) system distinguishes five categories:

- **Fall** (fig. 2.1a), when material descends mainly through the air by falling, bouncing or rolling.
- **Topple** (fig. 2.1b) implies a forward rotation out of the slope of a mass around an axis below the centre of gravity of the displaced mass.

- **Slide** (fig. 2.1c), a downslope movement of a mass occurring dominantly on surfaces of rupture or on relatively thin zones of intense shear strain. This can be planar, generating a translational slide, or curved, generating a rotational slide.
- **Flow** (fig. 2.1d), a spatially continuous movement in which shear surfaces are closely spaced and usually not preserved. Furthermore the distribution of velocities in the displacing mass resembles that in a viscous liquid. This category does not encompass creep movement: an imperceptible slow, steady downward flow movement of slope-forming soil or rock. Movement is caused by internal shear stress sufficient to cause deformation but insufficient to cause slope failure (Highland and Bobrowsky, 2008). Also badlands are not encompassed within the flow category, and more in general in landslides. Indeed they represent a terrain where softer sedimentary rocks and clay-rich soils have been extensively eroded by wind or water. They are characterized by steep slopes, minimal vegetation and high drainage density.
- **Spread** (fig. 2.1e), defined as an extension of a cohesive terrain combined with a general subsidence of the fractured mass of cohesive material into underlying softer material prone to liquefaction or flow.

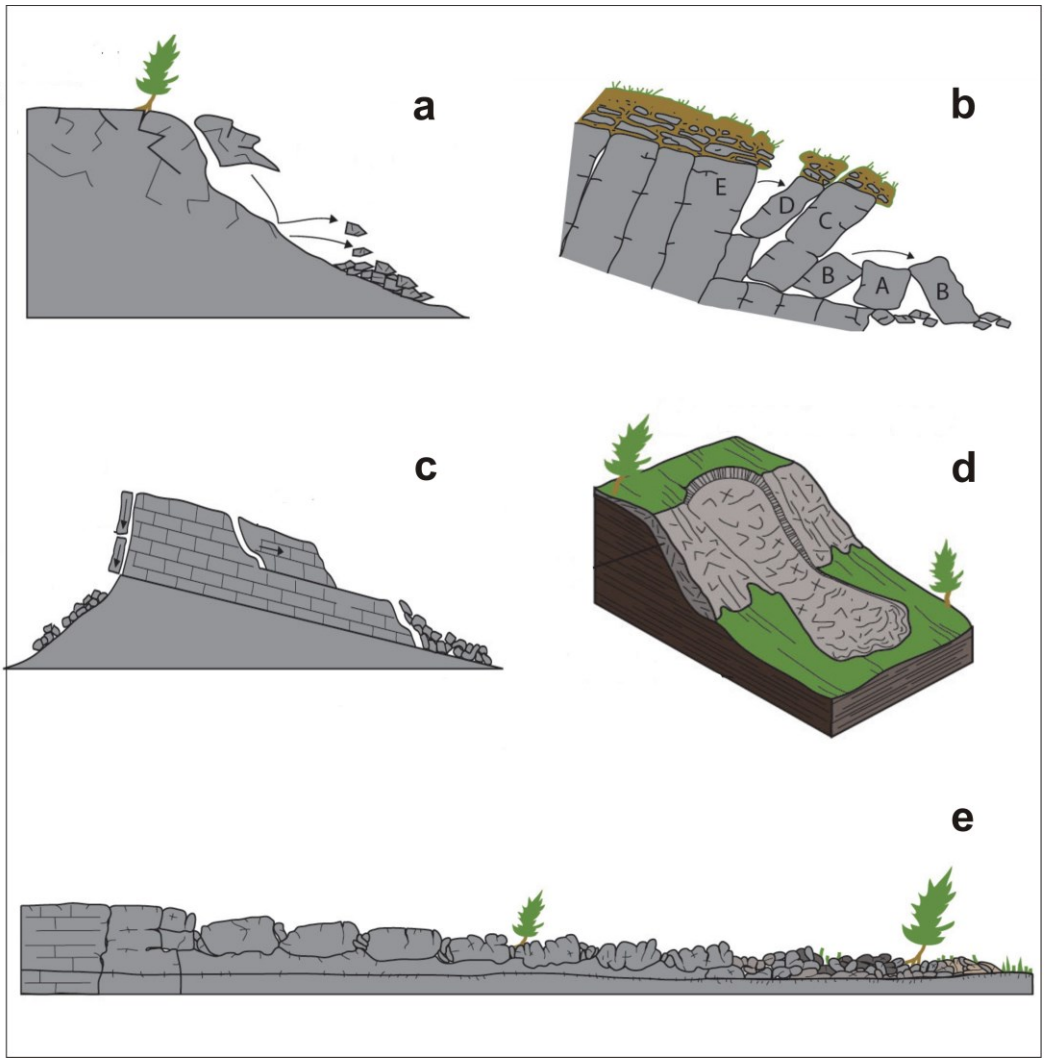

Figure 2.1 – Block diagrams illustrating the landslide classification: fall (a); topple (b); slide (c); flow (d); spread (e). After Cruden and Varnes (1996).

Finally, there are two specific types of slope deformations, known as Deep-Seated Gravitational Slope Deformation (DSGSD) and excluded from the aforementioned classification (Pasuto and Soldati, 2013): rock-spreading and soil spreading.

DSGSD refers to slope movements occurring on high relief-energy hillslopes, with size comparable to the whole slope, and displacements that are relatively small in comparison to the slope itself (Zischinsky, 1966, 1969; Nemcok, 1972; Varnes, 1978; Cruden and Varnes, 1996; Agliardi *et al*., 2001).

Rock spreading is a lateral extension of rock masses occurring along shears or tensile fractures. Two types of rock-spreading can be identified: rock spreading in homogeneous rock masses and rock spreading in brittle formations overlying ductile terrains (fig. 2.2a).

Soil-spreading is a lateral extension affecting fine-grained materials usually resulting in sudden collapses of sensitive soil layers (fig. 2.2b).

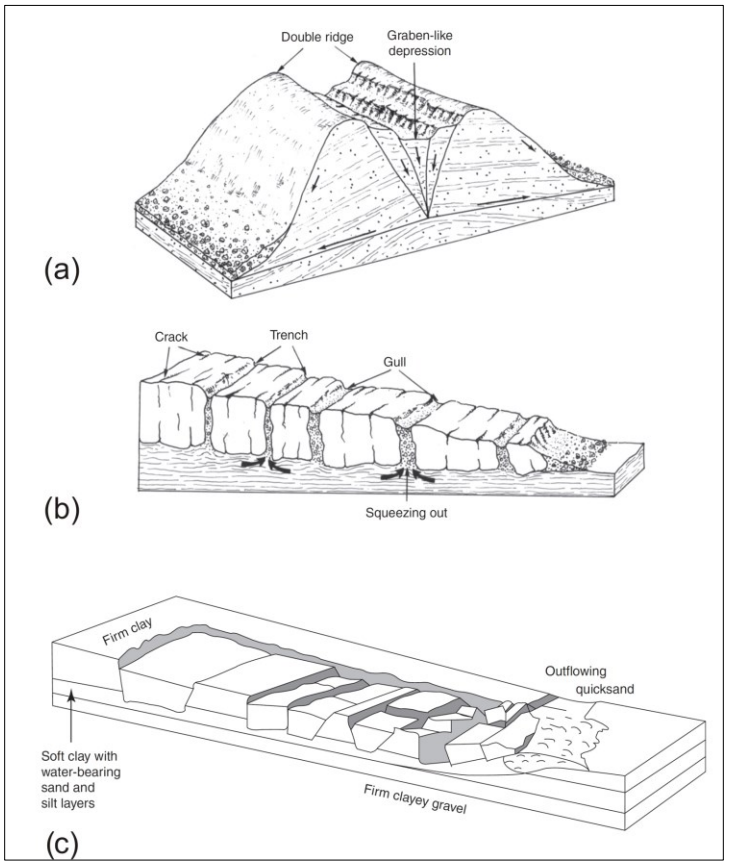

Figure 2.2 – Morphological sketches of rock spreading in homogeneous rock masses (a), rock spreading in brittle formations overlying ductile terrains (b) and soil spreading (c). After Pasuto and Soldati, 1996; Dikau et al., 1996.

Landslide activity has been grouped into three categories (fig. 2.3):

- **State of activity**, which describes what is known about the timing of movements (WP/WLI, 1993b).

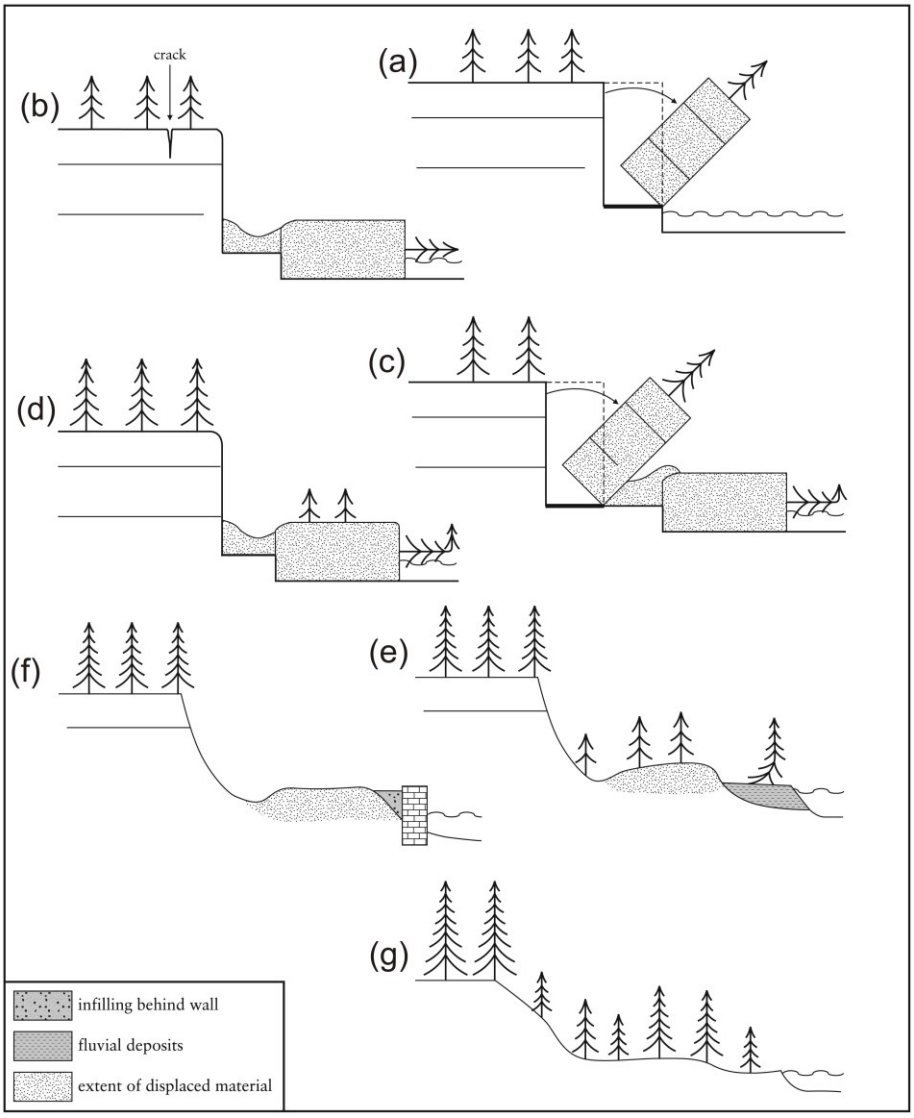

Figure 2.3 – Profile section of topples with different states of activity: active – erosion at the toe of the slope causes block to topple (a); suspended – cracking in crown () of topple (b); re-activated – another block topples (c); dormant – displaced mass begins to regain its tree cover and scarps are modified by weathering (d); abandoned - the fluvial deposition has protected the toe of the slope (e); stabilized - retaining wall protects the toe of the slope (f); and relict – uniform tree cover over slope (g). From WP/WLI, 1993b.

Active landslides (fig. 2.3a) are those that are currently moving, including first-time movements and reactivations (fig. 2.3c). Landslides that have moved within the last annual cycle of season but that are not moving at the present are described as **suspended** (fig. 2.3b).

Inactive landslides (figs. 2.3d-g) are those whose last movement dates back to more than one annual seasonal cycle. The inactive landslides are in turn subdivided in **dormant** (when reactivation is possible; fig. 2.3d), **abandoned** (when it is no longer influenced by its original triggers; fig. 2.3e),

stabilized (after natural or artificial protective measures; fig. 2.3f) and **relict** (when it occurrs in an extinct morpho-climatic setting; fig. 2.3g).

- **Distribution of activity**, which describes where the landslide is moving (fig. 2.4; WP/WLI, 1993b).

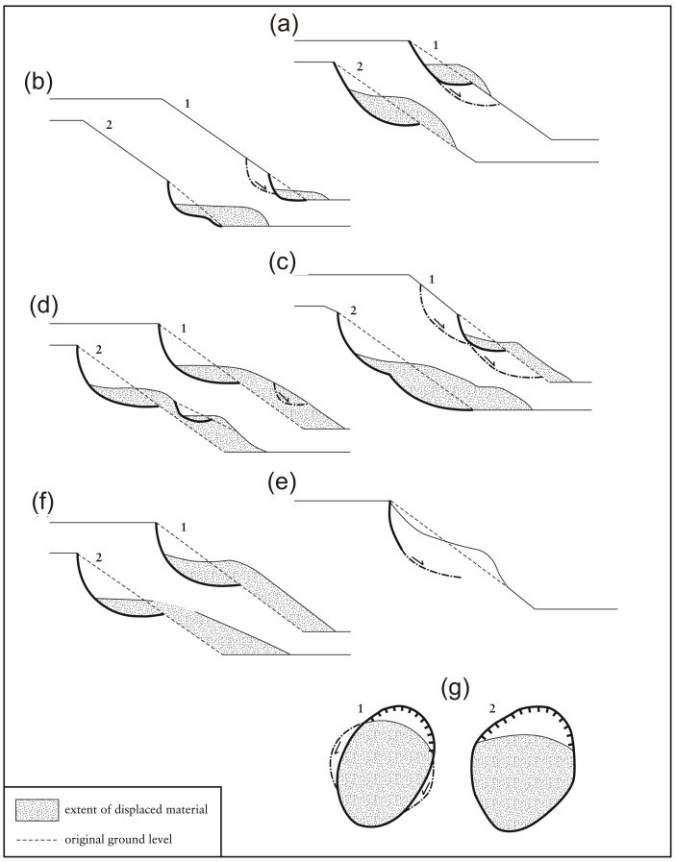

Figure 2.4 – Profile section through landslides showing different distributions of activity: advancing (a); retrogressing (b); enlarging (c); diminishing (d); confined (e); moving (f) and widening (g); from WP/WLI (1993).

An **Advancing** landslide (fig. 2.4a) has the rupture surface extending in the direction of movement. In a **retrogressive** landslide (fig. 2.4b) the rupture surface is extending in the direction opposite to the movement of the displaced material. If the rupture surface of the landslide is extending in two or more directions the landslide is **enlarging** (fig. 2.4c). In a **diminishing** landslide (fig. 2.4d) the volume of displaced material is decreasing. The presence of a scarp, with no visible rupture surface of the displaced mass, is defined as a **confined** landslide (fig. 2.4e). In a **moving** landslide (fig. 2.4f) the displaced material continues to move without any visible change in the rupture surface and the volume

of the displaced material. Finally a **widening** landslide (fig. 2.4g) has the rupture surface extending into one or both flanks of the landslide.

- **Style of Activity**, which indicates the manner in which different movements contribute to the landslide (fig. 2.5; WP/WLI, 1993b).

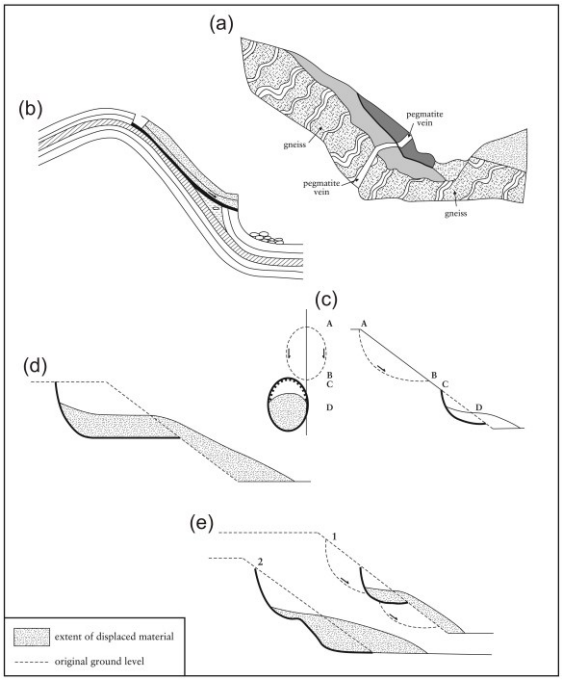

Figure 2.5 – Sections through landslides showing different styles of activity (WP/WLI, 1993b): complex (a); composite (b); successive (c); single (d) and multiple (e).

A **complex** landslide (fig. 2.5a) exhibits at least two types of movement (falling, toppling, sliding, spreading and flowing) in temporal sequence. At least two types of movement simultaneously in different parts of the displacing mass characterize a **composite** landslide (fig. 2.5b). A **successive** landslide (fig. 2.5c) is the same as a nearby, earlier landslide, but does not share displaced material or rupture surface with it. In a **single** landslide (fig. 2.5d) there is only a single movement of displaced material, whereas a **multiple** landslide (fig. 2.5e) shows repeated development of the same type of movement.

Landslide velocity (fig. 2.6) refers to the highest speed attained after the slope failure, according to the classification of Cruden and Varnes (1996).

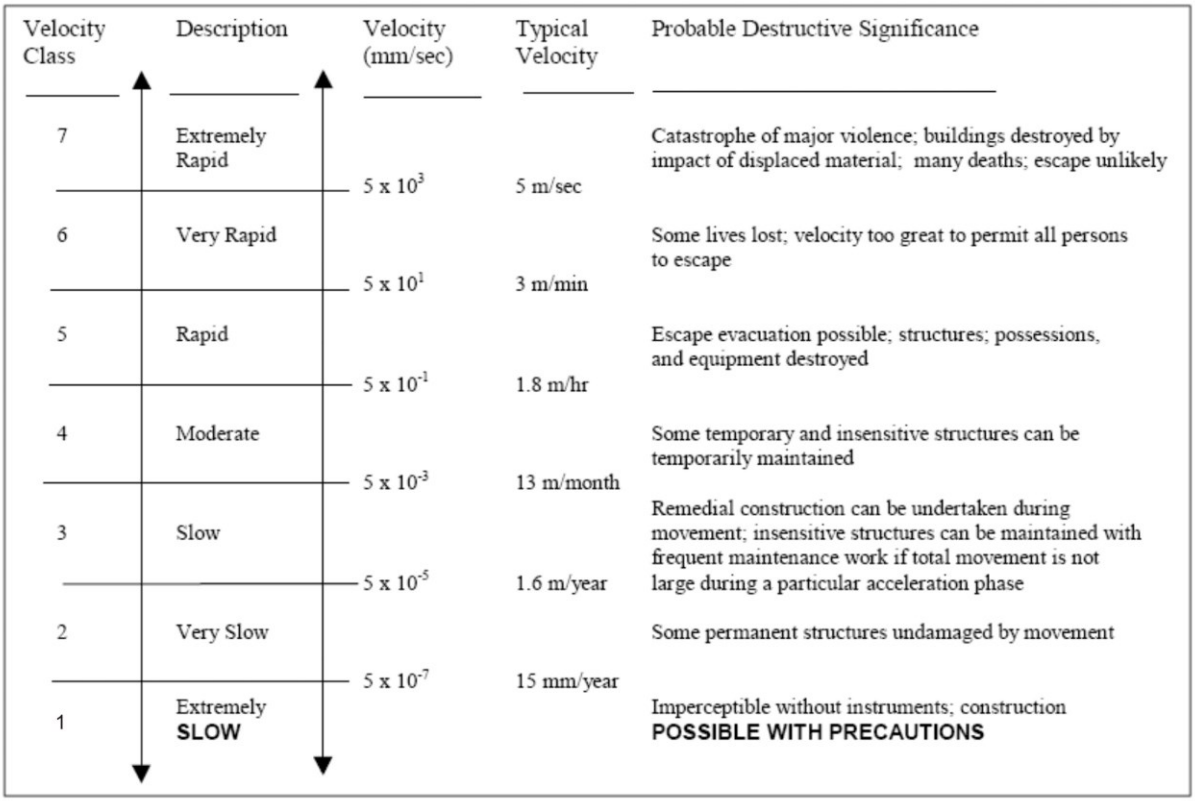

Figure 2.6 - The landslide velocity classification and the corresponding potential damage (Cruden and Varnes, 1996).

The velocity of mass movement is one of the most important aspects in landslide studies and evaluation of landslide risk (see paragraph 2.2). In figure 2.6, seven classes of velocity with the corresponding damage have been identified. They range from extremely rapid events the rate of which can exceed the speed of a running person (5 m/sec) to extremely slow events (below 16 mm/year) which can be imperceptible without appropriate instruments.

Due to the main intrinsic characteristics of A-DInSAR-derived estimates (see paragraph 3.2.2), these are currently only applicable (Cigna *et al*., 2011) to extremely-slow and very-slow movements (velocity <16 mm/year and 16 mm/year≤ velocity <1.6 m/year, respectively) that generally persist over long time periods (several years). This feature limits the use of A-DInSAR in terms of landslide typology to phenomena such as DSGSD, creep, and to slides, flows, and complex landslides, as long as their velocities do not exceed the above-mentioned rates.

Landslides can have several, and sometimes combined, predisposing causes (Alexander, 1992). They are static or dynamic factors which influence the edge of stability over time and act as catalysts to allow other dynamic destabilizing factors to operate more effectively.

They are mainly summarized as follows:

- Geological factors (e.g., weak materials, weathered materials, sheared materials and jointed or fissured materials).
- Morphological factors (e.g., tectonic uplift, volcanic uplift, fluvial erosion, wave erosion, glacial erosion, slope angle, vegetation change and surface runoff).
- Physical factors (e.g., slope loading, intense rainfall, thawing, rapid drawdown, rapid snow melt, earthquake, volcanic eruption, ground water changes, soil pore water pressure and seismic activity).
- Human factors (e.g., loading of slope or its crest, excavation of slope or its toe, deforestation, irrigation, artificial vibration and mining activities).

Despite all these destabilizing factors, only one is the triggering factor which actually initiates the landslide event (Varnes, 1978; Keefer, 1984; Wieczorek, 1996). Common landslide triggering mechanisms including intense rainfall, rapid snowmelt, water-level changes, volcanic eruptions and natural or artificial shaking events (e.g., earthquakes or explosions).

Information about location, classification, volume, activity and, when possible, date of occurrence of individual landslides in an area are summarized in the Landslide Inventory Map (IUGS, 1997).

Independently from the methods adopted, the Landslide Inventory Map represents the first, and mandatory data to obtain information on landslide susceptibility, hazard and risk zoning (see paragraph 2.2). Usually a Landslide Inventory Map, in addition to landslide information, also documents creeps and badlands occurrence. Despite these features are not directly related to any landslide processes

however they are connected to the evolution of the slopes and therefore they represent useful information for the assessment of landslide distribution.

2.2 Landslide susceptibility, hazard and risk zoning

The information reported within Inventory maps represents crucial and preparatory data for every landslide hazard or risk study, since they facilitate the assessment of the spatial and temporal frequencies of landslides along with their intensity, susceptibility and vulnerability (Fell *et al*., 2008).

In landslide zoning the definitions of susceptibility, hazard and risk terms mainly follow the IUGS (1997) parameters.

Following those definitions, a landslide susceptibility map represents an intermediate step between the so called landslide inventory map and a landslide hazard map that is calculated with reference to a given time frame for which the expected frequency or probability of occurrence of an event is evaluated (Corominas *et al*., 2014).

In Italy, according to the national law no. 183/1989, the issue of landslide susceptibility, landslide hazard and landslide risk is generally dealt with by specific governmental agencies, the River Basin Authorities (RBAs), whose jurisdiction is either national, inter-regional or regional (Di Martire *et al*., 2012) and is expressed in the Hydro-geomorphological Setting Plan (HSP).

In reference to the Landslide Susceptibility Maps, in the past three decades, a large number of models have been proposed and tested.

Since landslide susceptibility assessment is a spatial evaluation, differences arise in the way of selection of an appropriate terrain subdivision, namely of a "mapping unit" (Varnes and IAEG, 1984; Soeters and Van Westen, 1996; Guzzetti *et al*., 1999, 2005; Van Den Eeckhaut *et al*., 2006). Globally, there are two main criteria: **direct**, based on geomorphological criteria, and **indirect**. In direct mapping

the geomorphologist, based on his experience and knowledge of the terrain conditions, determines the degree of susceptibility directly (Amadesi *et al*., 1977). The indirect approach is divided in three groups: **heuristic**, **statistical** and **deterministic**. The heuristic approach is based on the opinion of an expert geomorphologist who defines the weighed value for each environmental factor considered to be the input for the landslide susceptibility zonation.

The statistical approach (e.g., SINMAP, Calcaterra D. *et al*., 2004) is based on the assumption that future landslides are more likely to occur under the same geological and geomorphological conditions that led to past slope instability. The combination of these conditions are statistically determined and, based on similar existing conditions, quantitative estimation of landslide occurrences are generated for areas free of landslides (Soeters and van Westen, 1996).

The methods described thus far give no information on the stability of a slope, for such information deterministic methods are necessary. The latter use slope physically-based stability models (e.g., SHALSTAB, Montgomery and Dietrich, 1994) that quantitatively produce a stability index by calculating the Factor of Safety (FS), namely the ratio of resisting forces to driving forces. If the resisting force of slope materials, whether consolidated bedrock or unconsolidated sediments, is consider as the shear strength of the materials and the driving forces are considered as the predisposing causes (see paragraph 2.1), the slope stability can be mathematically expressed as the Factor of Safety (FS), namely the ratio of resisting forces to driving forces.

If the factor of safety is less than or equal to 1 (i.e., $FS \leq 1$), the slope will fail because driving forces will equal or exceed the resisting forces. If FS is significantly greater than 1, the slope will be quite stable. However if FS is only slightly greater than 1, small disturbances may cause the slope to fail.

The statistical approach is of two types: bivariate or multivariate. In bivariate statistical analysis, each causal factor map (i.e., the driving forces of paragraph 2.1) is combined with the landslide distribution map and weighed values based on landslide densities are calculated for each causal factor class (e.g., the Frequecy Ratio, Yilmaz, 2009; Yalcin *et al*., 2011; Pourghasemi *et al*., 2012; Shahabi *et al*., 2014). On the other hand, in multivariate statistical analysis, the weights of causal factors controlling landslide occurrence indicate the relative contribution of each of these factors to the degree of hazard within a defined land unit (e.g., the Logistic Regression, Dai and Lee, 2002; Yilmaz, 2009; Pradhan, 2010; Yalcin *et al*., 2011; Shahabi *et al*., 2014). One of the main advantages of the statistical bivariate approach is the unbiased influence of each factor, the easy updating of the landslide susceptibility assessment procedure and the relatively easy application for land-use planning (Magliulo *et al*., 2009) and, as a general principle, the choice among the different landslide susceptibility options is principally based on these aspects.

Therefore this thesis uses one of the best known bivariate methods, the Weight of Evidence, that will be discussed in paragraph 3.3.

2.3 Landslides in Structurally Complex Formations of Southern Italy

The landslides under investigation cropping out in the SCFs of the Apenninic-Maghrebian Chain (AMC; Barreca *et al*., 2010) and the Pelagian Sicilian Thrust Belt (PSTB; Barreca *et al*., 2010).

The fold-and-thrust belts of AMC and PSTB, represent a segment of the Alpine orogeny system in the central sector of the western Mediterranean Sea. They resulted from the convergence between the Afro-Adria and European plates started in Neogene (Vitale and Ciarcia, 2013). The collision consumed a branch of the Neo-Tethyan oceanic plate, the Ligurian Ocean, by subduction.

The AMC displays an E-vergence while the PSTB has a S-vergence (figs. 2.7-2.8). Despite the different vergences, the orogens show a similar architecture, characterized by the tectonic superposition

of several basins to platform successions with unconformable wedge-top basin deposits at the top, sealing contacts between the different tectonic units (e.g., Casero *et al*., 1988; Butler *et al*., 1992; Butler *et al*., 1993; Mazzoli and Helman, 1994; Storti and McClay, 1995; Doglioni *et al*., 1996; Cello and Mazzoli, 1999; Menardi Noguera and Rea, 2000; Faccenna *et al*., 2001a, 2001b; Cosentino *et al*., 2003; Catalano S. *et al*., 2004; Shiner *et al*., 2004; Guerrera et al., 2005; Patacca and Scandone, 2007; Bonardi *et al*., 2009; Cosentino *et al*., 2010; Scrocca, 2010; Frizon de Lamotte *et al*., 2011; Roure *et al*., 2012).

The main cropping out units of the AMC consist of Meso-Cenozoic rocks derived from the continental sedimentary cover of the Afro-Adria forelands. Remnants of oceanic and thinned continental crust basin realms occur on top of the thrust pile. These are named as the Ligurian Accretionary Wedge and include: the Liguride Unit, North Calabrian Unit, Sicilide Unit and Parasicilide Unit (Ciarcia *et al*., 2012).

The Mesozoic cover was formed, in this Mediterranean sector, by shallow marine carbonates of the Apenninic and Apulian platforms and deepwater, mixed clastic cherty carbonates of the Lagonegro-Molise basin. The preorogenic sequence was then covered by Miocene flyschoid units deposited within the following thrust belt evolution (Mostardini and Merlini, 1986; Bonardi *et al*., 2009).

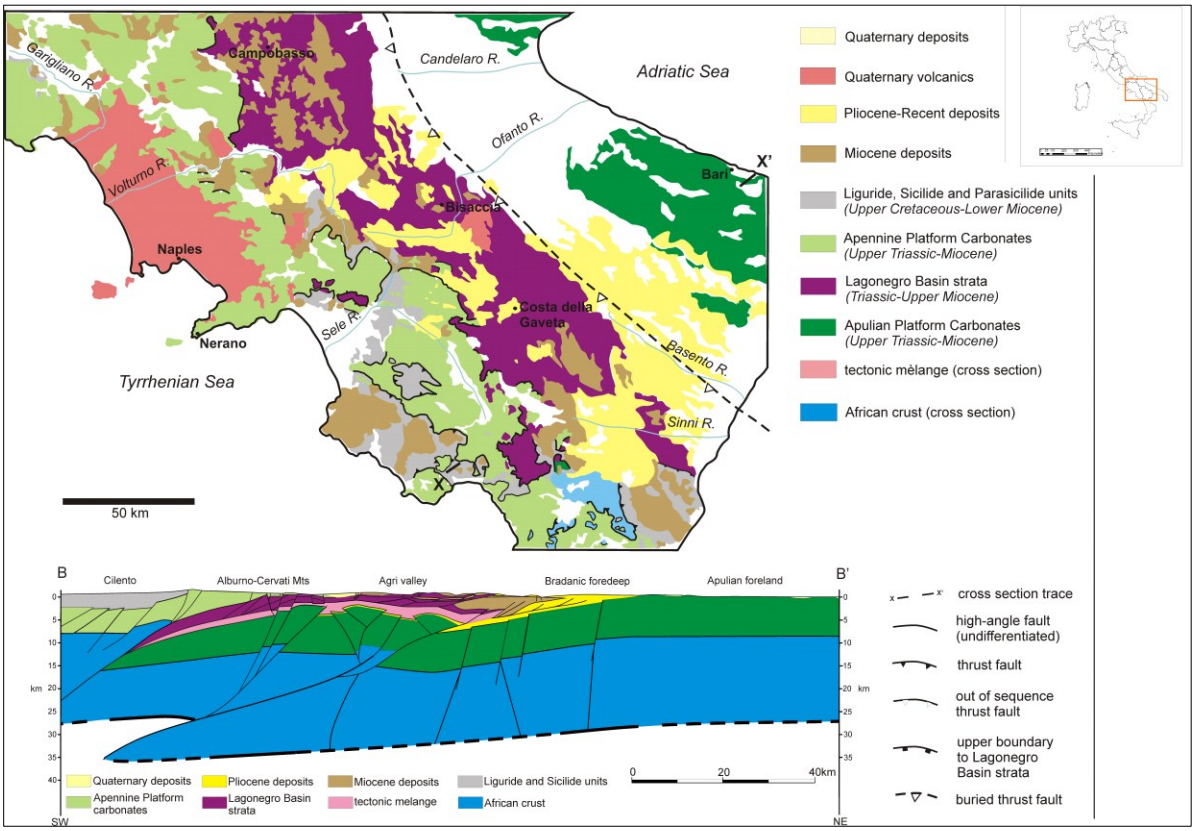

Figure 2.7 - Geological map of the AMC with location of the crustal cross-section (after Bonardi et al.*, 1988).*

In the PSTB (fig. 2.8), the tectonic nappes derive from the Miocene-Pliocene deformation of Meso-Cenozoic domains successions located in the northern portion of the Africa-Adria plate (Bernoulli and Jenkins, 1974; Catalano R. and D'Argenio, 1978; Stampfly and Borel, 2002). The paleogeographic domains are represented by basinal sedimentary successions (Imerese-Sicanian Domain), geometrically interposed between carbonate platforms: the innermost Panormide Unit and the more external Hyblean-Pelagian Domain (Nigro and Renda, 1999).

The roof of the PSTB tectonic edifice is characterized by the Sicilide Units and the Numidyan Flysch (Johansson *et al*., 1998) detached from their substrate (Accaino *et al*., 2010; Basilone, 2011). These are overlain by wedge-top basins filled by Miocene-Lower Pleistocene clastic deposits, evaporites and carbonates (e.g. Corleone Calcarenites, Catalano R. *et al*., 2002; San Cipirello Marls, Basilone, 2011; Terravecchia Formation, Catalano R. *et al*., 2010).

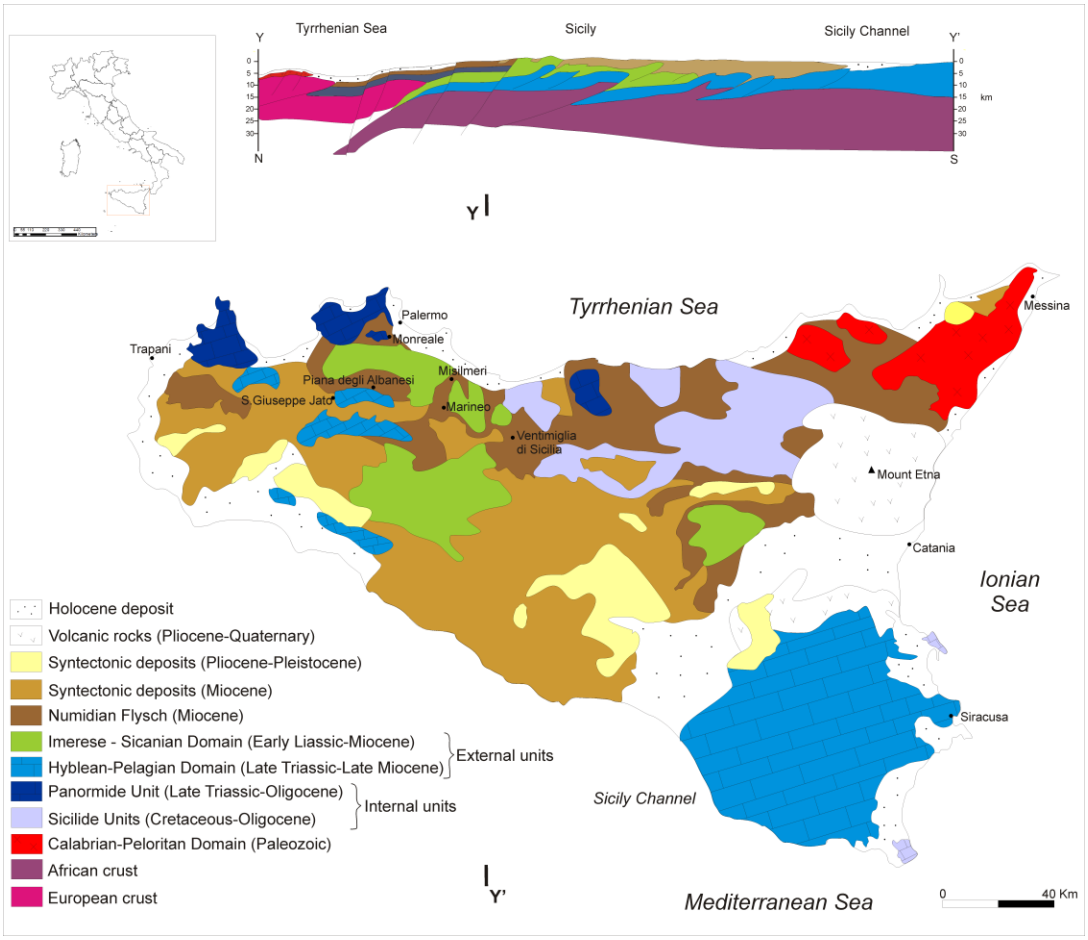

Figure 2.8 - Geological map of the PSTB with location of the crustal cross-sections (after Catalano S. et al.*, 2004; Finetti* et al.*, 2005).*

In the AMC and PSTB, the main basin-slope deposits are found, amongst others, within the Sicilide, Parasicilide and Imerese-Sicanian units. These were formed by turbidites in the deep marine facies of the Ligurian Ocean (Vitale and Ciarcia, 2013) which then suffered compressive tectonic deformations during the Alpine orogeny. This was followed by an extensional phase during the Plio-Pleistocene epochs (Mazzoli and Helman, 1994).

These terrains, together with most of the thrust-top terrains of the AMC and PSTB, are stratigraphically and genetically identified in the Italian geological literature as 'Argille Varicolori' or 'Argille scagliose' (e.g., Bianconi, 1940; Ogniben, 1969 and references therein; Mostardini and Merlini 1986; Casero *et al.*, 1988; Pescatore *et al.*, 1988; Carbone *et al.*, 1991; Monaco and Tortorici, 1995; Gallicchio *et al.*, 1996; Monaco *et al.*, 1998; Pescatore *et al.*, 1999; Lentini *et al.*, 2002). These terms

highlight the wide range of colour and their predisposition to split into progressively smaller flakes with polished surfaces (Vannucchi *et al*., 2003).

If their geotechnical properties are taken into account, these terrains are classified as Structurally Complex Formations - SCFs (Esu, 1977).

The SCF term describes materials characterized by large and scale-dependent heterogeneity in the lithological and structural features, because of the genesis and the tectonic history experienced (Esu, 1977).

The heterogeneity led to the development of a scaly-fabric with the alternation of 'hard' (rock-like material) and 'weak' horizons (soil-like material) characterizing geotechnical parameters more than index and state properties (Picarelli *et al*., 2005).

Esu (1977) divided the SCFs into 3 groups (A, B and C) based on lithological composition. The first two groups are, in turn, subdivided on the basis of the progressive chaotic structure (fig., 2.9):

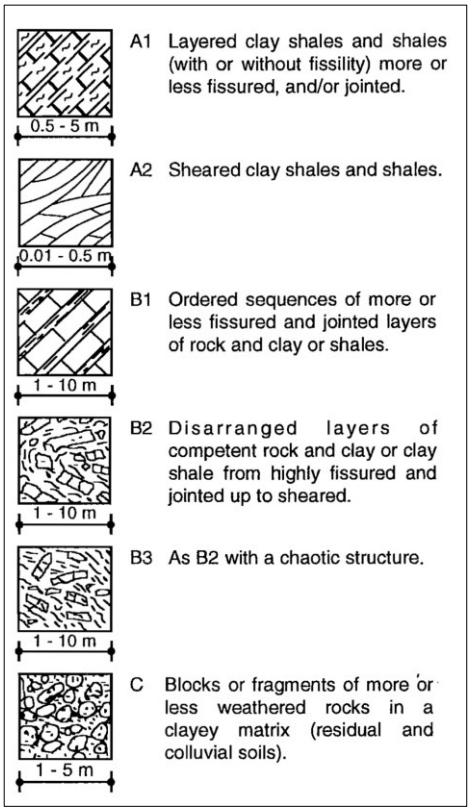

Figure 2.9 – Classification of the Structurally Complex Formations with relative explanation for each category (after Esu, 1977).

The **A Group** is constituted by fine-grained and lithologically homogeneous materials, with the presence of structural discontinuities.

In turn, this group is divided into two subgroups:

- A1: poorly fissured and/or fractured clays where the most significant discontinuities are represented by stratification and joints.
- A2: intensely fissured and/or fractured, particularly by tectonic stresses, scaly clays.

The **B Group** is constituted by two kinds of soils with different mechanical characteristics like rock or less weathered rocks in a clayey matrix, as typical of most flysch terrains; it includes three subgroups:

• B1: regular alternation of rock and fissured and/or fractured clays.

• B2: chaotic setting of rock strata and highly fissured/fractured or scaly clays.

• B3: scaly clays produced as the effect of tectonics, which include rocks.

The **C Group** is constituted by heterogeneous materials like rock or less weathered rocks in a clayey matrix with a completely disarranged fabric. They are typical of alteration blankets or landslide products.

All the studied areas are included in the SCFs. Such materials are commonly affected by extensive mass movements because of their poor mechanical properties that can be degraded by the weathering of the shallow layers.

The resulting instabilities are characterized by a long evolutionary history with an intermittent state of activity (Del Prete *et al*., 1992), where the large and rapid dislocations associated with the primary detachment are followed by multiple and slower reactivations of the already deformed masses, correlated to the recurrences of rainfall events, seismic events or human activities.

Many of the Italian landsliding areas occur in the SCFs, giving origin to movements with very-slow to extremely-slow velocities that represent the perfect targets for A-DInSAR analysis.

Among the most famous landslides in SCFs studied during the last twenty years, are (fig. 2.10): Senerchia (Cotecchia *et al*., 2001), Agnone (Calcaterra D. *et al*., 2008), Santo Stefano d'Aveto (Tofani *et al*., 2013), San Fratello (Ciampalini *et al*., 2013), Montaguto (Giordan *et al*., 2013) and Cirò (Confuorto *et al*., 2014).

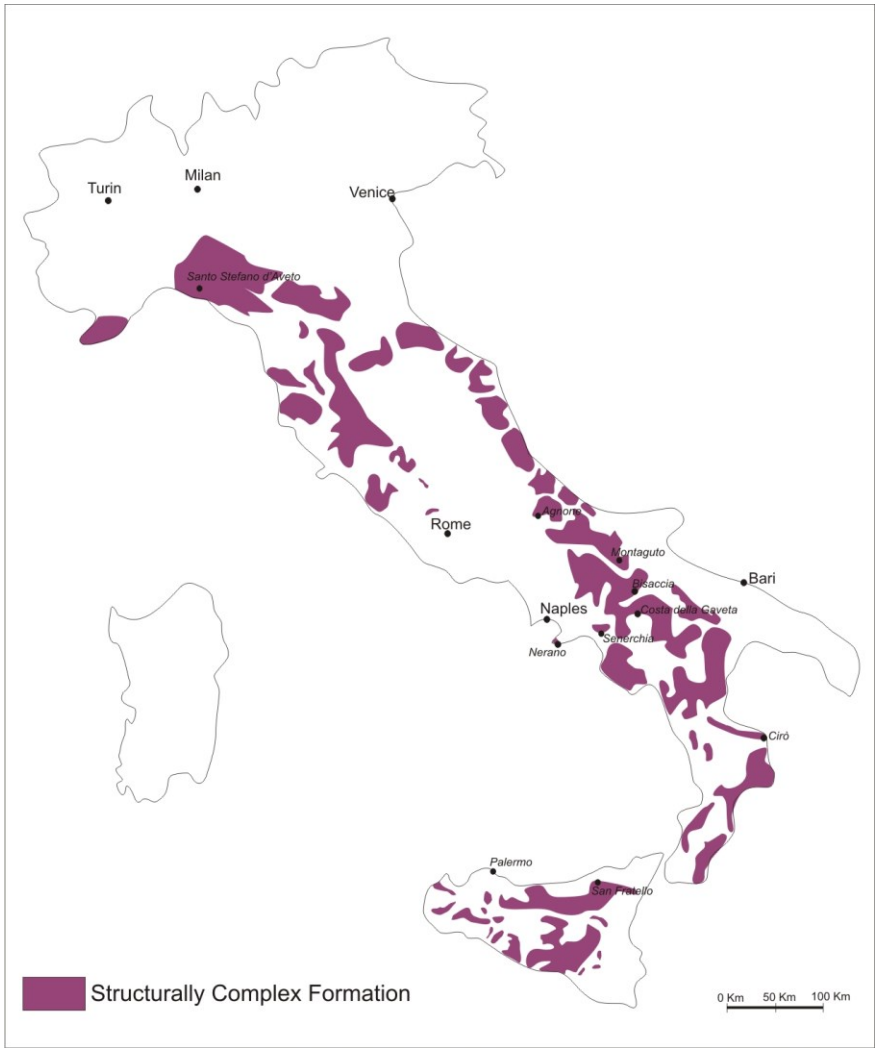

Figure 2.10 – The Italian outcrops of SCFs with the location of famous landslide case studies in the geotechnical literature and the four case studies of this thesis (after D'Elia, 1991).

Chapter 3: Materials and methods

3.1 Landslide mapping

Landslides leave discernible signs, most of which can be recognized, classified and mapped through two types of investigations. one is ground-based: geomorphological field surveys, geotechnical and geophysical studies (i.e., subsurface exploration; Franklin, 1984; Petley, 1984). The second is remote-based: cartographic and bibliographic review, stereoscopic analysis (Rib and Liang, 1978; Turner and Schuster, 1996) and remote sensing *s.s.* (Singhroy, 2005 and reference therein). Among these, only remote sensing is considered innovative because it has recently become extensively used in analyzing Earth's surface deformations (Tofani *et al*., 2013).

The most exploited, and often preliminary, recognition of landslide is represented by geomorphological field evidence: such as changes in the form, position or appearance of the topographic surface. Other signs of slope failure may reflect lithological, geological, land use, infrastructures or other types of surface and sub-surface changes (Brunsden, 1985; 1993).

Geotechnical analyses are necessary to precisely determine the type of materials involved in the slide, the depth of the slip surface, and thus the thickness and geometry of the landslide mass, the water-table level, and the degree of disruption of the landslide materials (Dunnicliff, 1988 and reference therein).

In landslide studies also geophysical methods have been successfully applied over the last forty year making use of resistivity (e.g., Donnelly *et al*. 2005), self-potential (e.g., Lapenna *et al*. 2005), low frequency electromagnetics (e.g., Schmutz *et al*. 2000), ground-penetrating radar (e.g., Roch *et al*. 2005), seismic methods (e.g., Glade *et al*. 2005). and gravity (e.g., Del Gaudio *et al*. 2000). These methods have been used to determine slope subsurface characteristics such as the depth to bedrock, stratigraphic layers, zones of saturation, the ground-water table and also to determine the texture,

porosity and degree of consolidation of subsurface materials along with the geometry of the units involved.

Remote-based methods include cartographic reviews of all the landslides appearing on earlier maps: some of which could be spatially adjusted in the updated maps to more accurately fit the current map base. some could be substantially reinterpreted, while others could be fully confirmed.

The bibliographic review of archives, chronicles, and newspapers is also used to identify past landslide events, to compile landslide catalogues and to prepare landslide maps (e.g., Reichenbach *et al*., 1998; Salvati *et al*., 2003).

The recognition of landslides through the visual analysis of stereoscopic aerial photographs (or photogrammetry) is an empirical technique that requires experience and training (Speight, 1977; Rib and Liang, 1978; Van Zuidam, 1985; Antonini *et al*., 2002). this approach allows landslides to be easily recognized and classified reducing time of fieldwork. if the quality of the images is high enough, geomorphological features associated with mass movements such as scarps, counterscarps, trenches, debris flows, rockfalls and debris fans can also be mapped (Strozzi *et al*., 2013). more details will be given in paragraph 3.2.1.

Finally, landslides can be identified through innovative remote sensing technologies, such as a-dinsar radar image processing (Czuchlewski *et al*., 2003; Hilley *et al*., 2004; Catani *et al*., 2005), the interpretation of high resolution multispectral images (Cheng *et al*., 2004), or the analysis of high quality digital elevation models obtained from optical space or airborne sensors (e.g., LiDAR; Mckean and Roering, 2004; Catani *et al*., 2005; Debella-Gilo and Kääb, 2012).

Remote sensing techniques overcomes the limitations of conventional landslide mapping, especially in the definition of landslide extension and state of activity, giving information about superficial terrain

displacements (see paragraph 3.2). however their outputs always require validation through integration with one or more of the conventional mapping techniques.

3.2 Landslide monitoring

Instability analysis starts with landslide mapping but a whole landslide investigation is obtained only through the regular observation and recording of the spatial and temporal evolution of a process: this step is called monitoring.

Landslide monitoring is based on the systematic temporal measurement of physical parameters whose variation is the result of stresses induced by driving forces (see paragraph 2.1). They include:

- Shallow displacement (measured by means of photogrammetry, benchmarks, theodolites, total stations, GPS, extensometers, LiDAR and A-DInSAR).
- Deep displacement (measured by means of inclinometers).
- Pore pressure (measured by means of piezometers and tensiometers).
- Soil-water content (measured by means of time domain reflectometry).
- Seismic acceleration (measured by means of seismographs).
- Metereological data (measured by means of rain gauges).

The choice of instruments and methods of a monitoring system depends upon the characteristics of the deformation, budget and time at disposal.

In this chapter only the technologies applied in the thesis will be discussed. Others technologies are described in Wieczorek and Snyder (2009) and references therein. In particular, in paragraph 3.3 a broad description of remote sensing focused on the A-DInSAR method will be given as part of an innovative technology during the monitoring phase.

3.2.1 Photogrammetry

Photogrammetry is the science of making measurements from photographs. Stereoscopy is a branch of photogrammetry used to create the illusion of depth in an image by means of a stereoscope for binocular vision. Any stereoscopic image is called a stereogram.

Most stereoscopic methods present a pair of offset two-dimensional images separately to the left and right eye of the viewer. These two-dimensional images are then combined to give the perception of 3D depth of a wide portion of territory (hundreds of meters extension).

The interpretation of aerial photographs has proven to be an effective technique for the recognition and delineation of landslides (Soeters and Van Westen 1996). It is an effective technique for recognizing and delineating the three-dimensional overview of the terrain considering shape, size, photographic colour, tone, mottling, texture, pattern of objects, site topography, and setting (Guzzetti *et al*., 2012).

The interpreter can detect and classify landslide morphological forms based on experience, and on the analysis of a set of characteristics (a "signature") that can be identified on the images: scarps, counterscarps, trenches, debris flows, rockfalls and debris fans but also the interrelations of drainage, surface cover, geology materials, and human activities on the landscape can be viewed and evaluated.

Aerial photographs also allow the delineation of surface and near-surface drainage channels and the tracing of important relations in drainage, topography and other natural and man-made elements that seldom are correlated properly on the ground but become obvious in photographs. The advantage of wide area 3D observing is particularly evident for the mapping of large landslides that are hardly recognizable through site surveys. On the other hand, the latter are essential to identify failures of small dimensions hardly recognizable from aerial photographs (Strozzi *et al*., 2013).

During the monitoring stages, recent photographs can be compared with old ones to examine the progressive development of the slope.

Figure 3.1 – A stereoscope used to analyze pairs of aerial photographs

3.2.2 Inclinometers

Geotechnical monitoring makes use of sensors permanently working on or in the structure or region under consideration. They can operate on a 24-hour basis and measure the change of geometrical and/or physical characteristics of the deforming item (relative deformation). They can also use a telemetric system for real-time transmission of measurement data to a control center. Inclinometers represent one of the main geotechnical sensors used for monitoring the subsurface horizontal displacement inside boreholes located within the landslide (Borgatti *et al*., 2006; Mihalinec and Ortolan 2008, Yin *et al*., 2008; Jongmans *et al*., 2009). Inclinometers allow for the evaluation of the depth of the sliding surfaces by measuring the 2D direction of displacement (azimuth) along two vertical axes of initially casing boreholes. In order to obtain the maximum displacements, the two axes are oriented in parallel and perpendicular with respect to the slope dip direction.

The inclinometer probe is periodically lowered in the borehole to survey the casing. The first survey establishes the initial profile of the casing (so called ‘zero reading’) while subsequent readings reveal changes in the profile if ground movement occurs.

Two classes of inclinometers exist, namely probe and in-place inclinometers, both commonly based on accelerometer sensors, which use a closed-loop servo-accelerometer circuit: each sensor measures the inclination in one plane and two sensors are usually installed in the so called biaxial sensors (Mikkelsen, 1996). The main disadvantage of this type of instrument is that curvature is only observed in one axis.

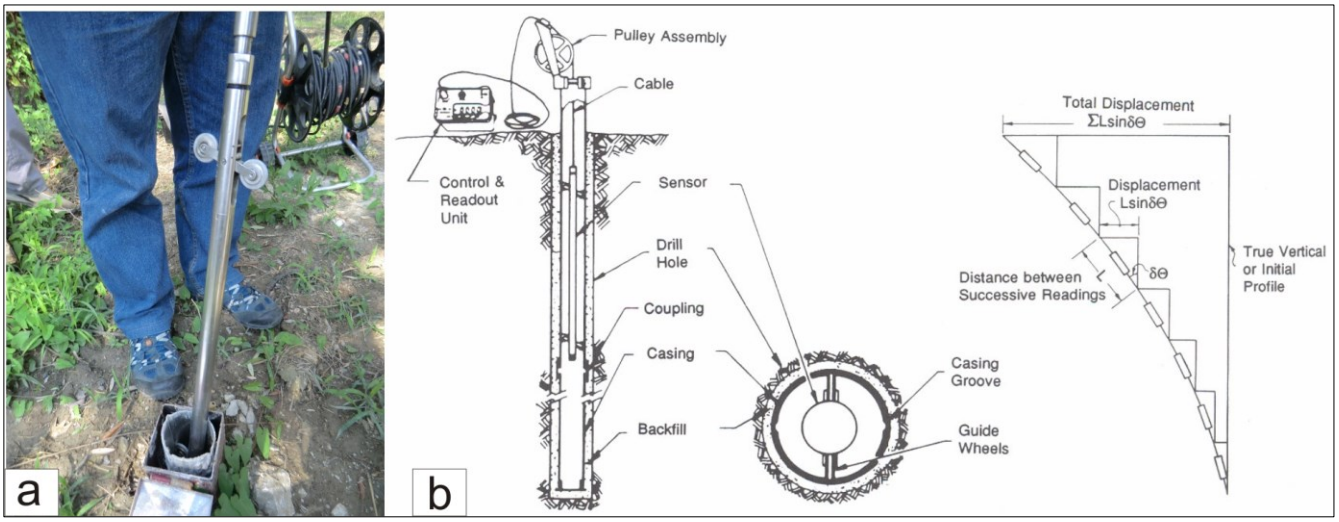

Figure 3.2 – Probe inclinometer lowered in a stainless inclinometer casing (a) and scheme of its installation and reading inside a borehole (b).

3.2.3 Piezometers

Especially shallow landslides are triggered by slope saturation following heavy rainfall (see paragraph 2.1). Measurement of groundwater levels form an important part of slope stability analysis (Wieczorek and Snyder, 2009 and references therein).

Piezometers measure the pore pressure of groundwater within a geological structure, thus giving an indication of the build-up of stresses and strains within the rock mass.

Common types of borehole piezometers are the vibrating wire, pneumatic, hydraulic cell piezometer and open standpipe piezometer as the one used in this thesis (see paragraph 4.1.2).

An open standpipe piezometer will typically have a PVC casing down to the depth of interest, and a slotted or screened casing within the zone where water pressure needs to be measured. The casing is sealed into the borehole with clay, bentonite or concrete to prevent surface water from contaminating the groundwater supply.

As in the case of inclinometers, a piezometric probe is periodically lowered in the borehole. This is a pressure gauge (or transducer) who converts pressure into an electrical signal and can be a vibrating-wire, pneumatic, or strain-gauge in operation. When the probe buzzer sounds, or the probe light lights, the length of cable required to reach this water level is measured from the top of the standpipe.

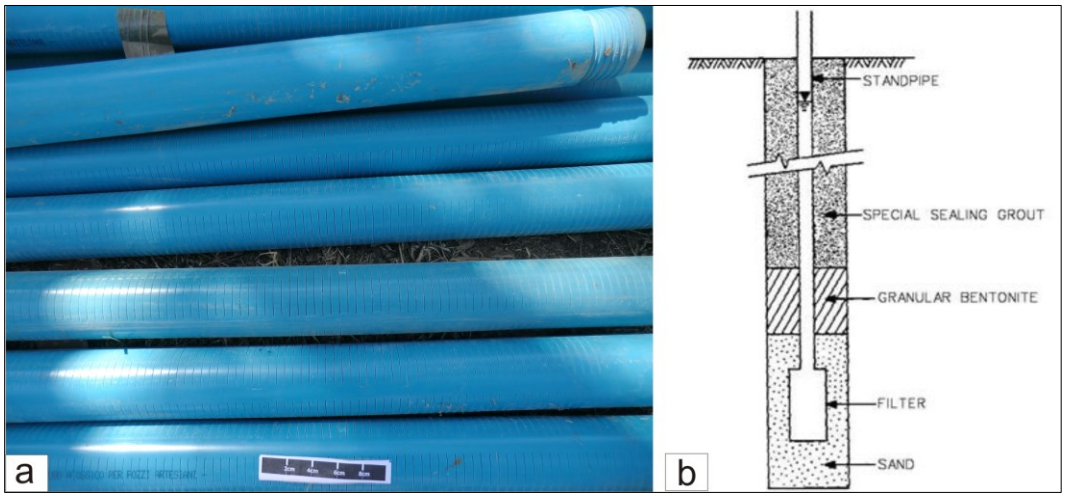

Figure 3.3 – Open standpipe piezometer (a) and scheme of its installation in a borehole (b).

3.2.4 Rain gauges

As stated in paragraph 2.1, rainfall represents a major landslide triggering factor and threshold levels of precipitation can be defined to provide early warning of conditions that may lead to catastrophic slope failure (Guzzetti *et al*., 2007).

High-resolution temporal rainfall data can be obtained by using appropriate instruments, such as automatic tipping bucket rain gauges, weighing rain gauge, acoustic rain gauge, optical rain gauge weather radar and other types of remote sensors and overall known as pluviometers (De Luca, 2014). These are used to gather and measure the amount of liquid precipitation over a set period of time.

A standard tipping bucket rain gauge is composed of three parts arranged on a mounting bracket: a funnel, a measuring tube and an overflow tube. The funnel directs the precipitation into the measuring tube. The measuring tube, when full, pours the excess water in the overflow tube. The process then repeats itself allowing for precise measurement of rainfall intensity and amount (Ahrens, 2007).

Despite the huge amount of different rain gauges precipitation measurements are always expressed as a vertical depth of water or the water equivalent of solid precipitation that reaches horizontal ground or the horizontal ground projection plane of the earth's surface.

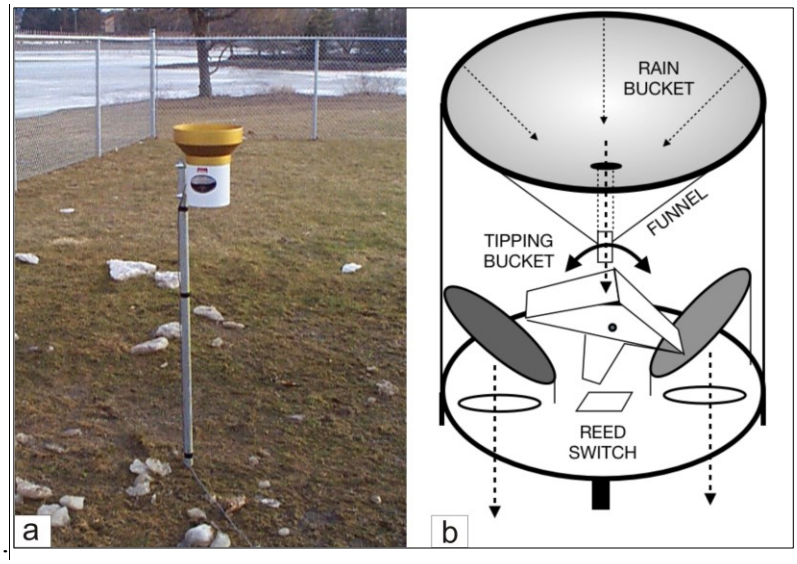

Figure 3.4 – A pluviometer mounting bracket (a) and scheme of a tipping bucket type (b).

The aggregation over different temporal resolutions of the rainfall time series assumes a crucial role in the comparison with displacement time series especially for shallow and intermittent landslides. While pluviometers guarantee at least a daily reading, displacement readings are generally temporally less frequent. The higher is the displacement measurement time span, the more difficult is the detection of seasonal variations.

Indeed ERS and ENVISAT datasets are usually not used for landslide research because of the temporal sampling of these satellites, which is 35 days between each SAR image in the best of cases (see table 3.1). On the other hand, the COSMO-SkyMed and TerraSAR-X satellites present a shorter temporal revisit time (8 and 11 days for each SAR image in the best of cases, respectively) that allows for an accurate study of time series displacements (Herrera *et al*., 2011).

3.3 Remote sensing and Synthetic Aperture Radar

Today, Earth Observation (EO) techniques are making rapid advances, allowing for more effective landslide detection, mapping, monitoring and hazard analysis (Tofani *et al*., 2013). Remote Sensing or EO is the science of acquiring, processing and interpreting data obtained from an object without being in contact with it. This is possible by exploiting electromagnetic waves, the interaction of which with targets (through transmission, absorption, emission, scattering or reflection) allows for the determination of the physical properties of the matter or its position (Sabins, 1996). According to this definition LiDAR, GPS and photogrammetry, quoted in the previous paragraph, are also part of the Earth Observation instruments.

Synthetic Aperture Radar (SAR) is a microwave imaging system, with a cloud-penetrating capability because of the existence of an atmospheric window region for these wavelengths (fig. 3.5). SAR sensors consist of an antenna with a day and night operational capability because it is an active system providing its own energy source for illumination.

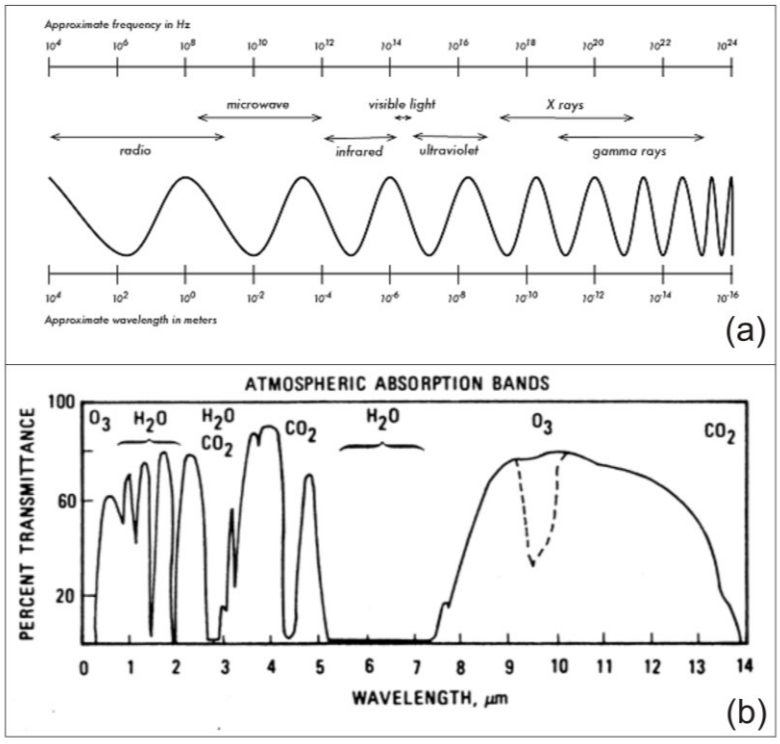

Figure 3.5 – Electromagnetic spectrum (a) and expanded diagram of the microwave region for transmission through the atmosphere (b). After Sabins, 1978.

The SAR antenna, mounted on a mobile ground, airborne or satellite device, transmits a radiation, whose λ ranging from 140 cm to 0.8 cm, that is reflected from a target and acquired again. The direction between the antenna and the object is called the Line of Sight (LOS). The forward motion of the antenna during acquisition is used to 'synthesize' a very long antenna allowing to reach a good pixel resolution with antenna structures of reasonable size.

There are four different ways to obtain a SAR image (Rosen *et al*., 2000):

- Using two different angular apertures on a single platform of the same antenna, often called **cross-track interferometry** (XTI). Other terms are "single-track" and "single-pass interferometry".
- With the **Repeat-Track Interferometry** (RTI) or **Multi-Temporal Interferometry** (MTI) the orbits of different space-borne SAR satellites are controlled in such a way that they nearly retrace themselves after several days. Aircrafts can also be controlled to repeat flight paths accurately. For space-borne systems, RTI is usually termed "repeat-pass interferometry".
- **Along-Track Interferometry** (ATI) considers the arrangement of two antennas along the flight track on a single platform. The small antennas separation and short time interval, makes the ATI able to detect objects with very small LOS motion components and has been used to measure tidal motions (Romeiser and Thompson, 2000; Romeiser *et al*., 2005).
- It is also possible to acquire SAR images through a portable and ground based SAR antenna, the **GBSAR** (Ground Based SAR or Terrestrial InSAR/TInSAR; Luzi, 2010). In this case the motion for synthesizing the SAR image is obtained through a linear rail where the microwave transceiver moves regularly.

Satellites are able to achieved a complete Earth's surface coverage by combination of the orbital satellite motion along the meridians (almost polar orbits) and the Earth's rotation in the equatorial

plane. This possibility comes from the fact that during orbits that go from South to North (ascending passes) and from North to South (descending passes), the SAR antenna pointing is usually fixed to the same side of the orbital plane with respect to the velocity vector (fig. 3.6).

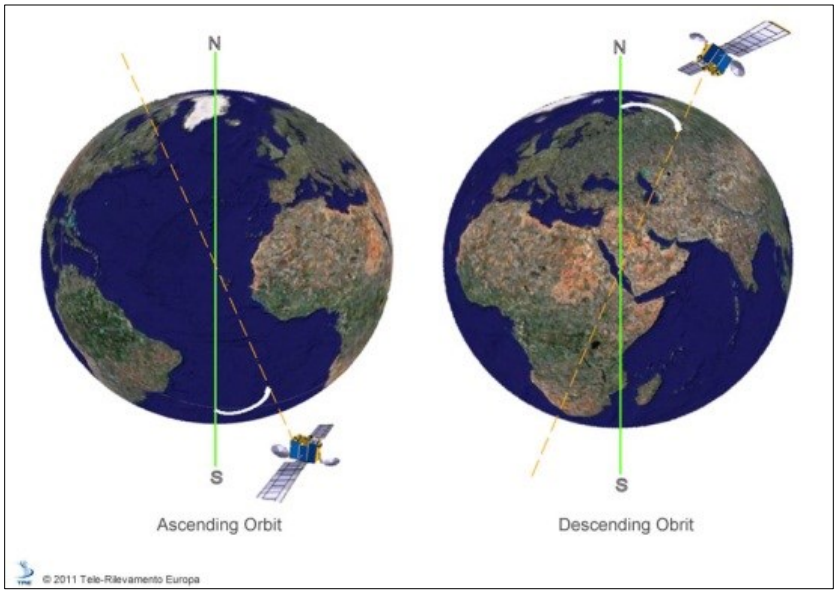

Figure 3.6 – Ascending (left) and descending paths (right). From TRE (2013).

The satellite Seasat launched in 1978 was the first satellite with an imaging SAR system used as a scientific sensor (Table 3.1) while GBSAR has a more recent application, couple of years, in particular for monitoring landslides and slopes (Luzi, 2010).

The earlier SAR satellites in the 90's and 2000's (ERS-1, ERS-2, Radarsat-1 and Envisat; Table 3.1) were all right-looking satellites, meaning that microwave beams were transmitting and receiving only on the right side of the satellite, relative to its orbital path, and that the system could not rotate. Newer satellites, from 2007 onward, (Radarsat-2, TerraSAR-X and COSMO-SkyMed; Table 3.1) have both right-looking and left-looking capabilities; thus they can 'look' to the right or the left of the craft, but not in both directions simultaneously.

sensor	agency	lifetime	revisiting time	ground resolution	wavelength (λ)	incident angle
ERS1+ERS2	European Space Agency	1992-2000	35 days	25m	5.6 cm (C-band)	23.3°
ENVISAT	European Space Agency	2002-2010	35 days	15m/100m	5.6 cm (C-band)	23.3°
RADARSAT -1	RADARSAT Inetrnational	1995-2013	24 days	10m/100m	5.6 cm (C-band)	10° - 60°
ALOS	Japanese Aerospace Exploration Agency	2006-2011	46 days	7m/100m	24.1cm (L-band)	8° - 60°
RADARSAT -2	Canadian Space Agency	2007-ongoing	24 days	3m/100m	5.6 cm (C-band)	10° - 60°
TerraSAR-X	Deutsches Zentrum für Luft- und Raumfahrt	2007-ongoing	11days	1m/16m	3.1 cm (X-band)	20° - 55°
COSMO-SkyMed	Italian Space Agency	2007-ongoing	1/8days	1m/100m	3.1 cm (X-band)	20° - 60°
Sentinel-1 (A+B)	European Space Agency	2013-ongoing	6 days	5m/100m	5.6 cm (C-band)	18° - 47°

Table 3.1- Main SAR missions and related features.

Depending upon the system of configuration, satellite SAR sensors can acquire data in different modes that correspond to different beam footprint extensions (figure 3.7):

- **Stripmap**: antenna pointing is fixed relative to the flight line, usually normal to the flight line. The result is a moving antenna footprint that sweeps along a strip of terrain parallel to the path motion. The stripmap mode is normally used for the mapping of large areas with low-resolution data.
- **ScanSAR**: the sensor steers the antenna beam to illuminate a strip of terrain at any angle to path of platform motion. The principle of the ScanSAR is to share the radar operation time between two or more separate sub-swaths in such a way as to obtain full image coverage of each with a medium-resolution data.
- **Spotlight**: The sensor steers its antenna beam to continuously illuminate a specific (and predetermined) spot or terrain patch being imaged while the platform flies by in a straight line. The spotlight mode is a practical choice when the mission objective is to collect high-resolution data from one or more localized areas.

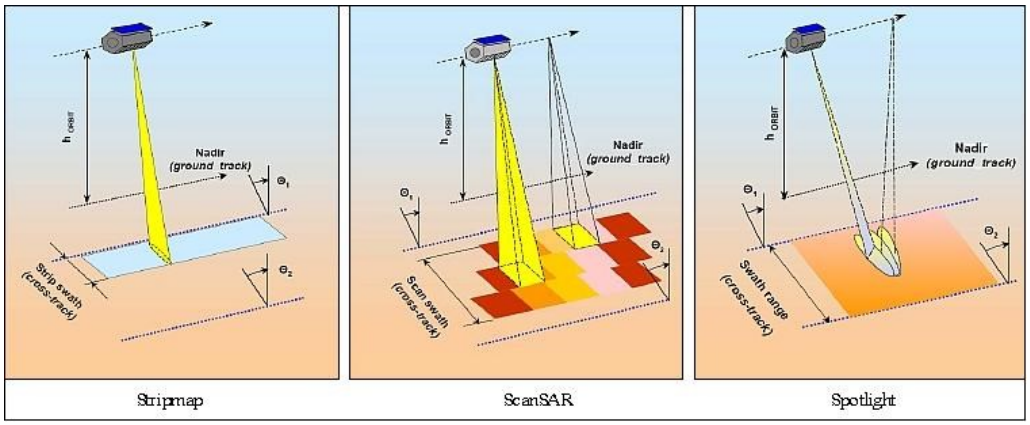

Figure 3.7 – Different acquisition modes for SAR sensors (after ESA, 2007).

The angle between the radar beam and a line perpendicular to the surface is referred to as the off-nadir, or look angle (θ). It changes from near-range, the value at the shortest path of radar beam, to far-range, the value at the longest path of radar beam (figs. 3.7 - 3.8).

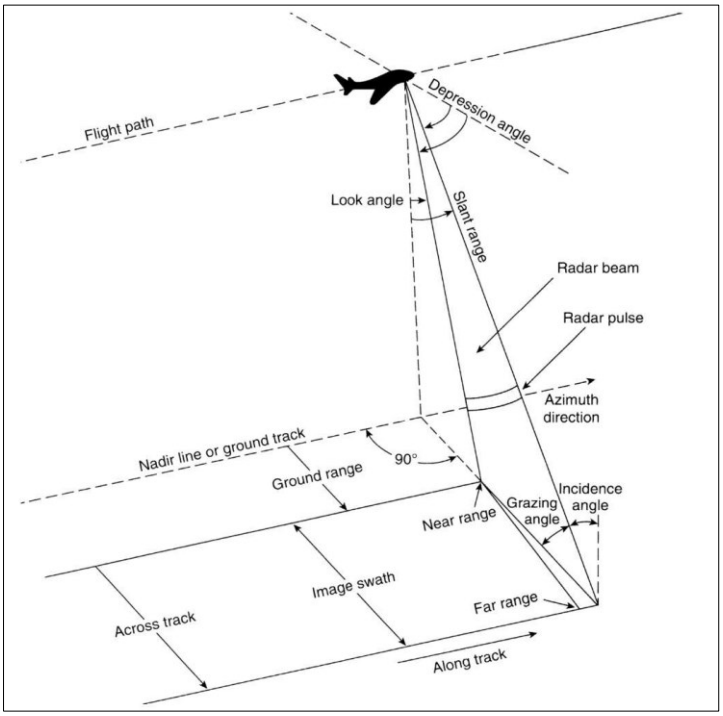

Figure 3.8 - Typical imaging scenario for a SAR system. The platform carrying the SAR instrument follows a track known as the 'along-track' or 'azimuth' direction. The radar antenna points to the right side, imaging the terrain below. The distance from the aperture to a target on the surface in the look direction is known as the 'cross-track' or 'range direction' and is terrain dependent. The radar sends a pulse that sweeps through the antenna beam, effectively returning the integrated backscatter over the pulse and azimuth beam extent at any given instant. The azimuth extent can be many kilometers. Matched-filtering creates fine resolution in range. Synthetic aperture processing creates fine resolution in azimuth (from Simons and Rosen, 2007).

The average off-nadir angle of the ERS and ENVISAT satellites has been fixed at about 23°, but all subsequent satellites were fitted with the means to vary the viewing angle of the sensors, ranging from values of 20^{o} to 50^{o}. The side-scanning acquires images as slant-range scale, corresponding to the radar

coordinate system. The image is geometrically distorted as a function of the incident angle with respect to the surface morphology, namely the ground-range coordinate system.

The result is the compression of features in the near-range relative to features in the far range (a compression between the size of a pixel in ground range and a pixel in slant range view), creating effects referred to as: layover, foreshortening and shadowing (fig. 3.9). They depend on the value between θ angle and slope inclination (α) and are expressed in the R-index map (Notti *et al*., 2010, 2014).

- **Foreshortening** occurs when the radar beam reaches the base of a tall feature tilted towards the radar (e.g. a mountain) before it reaches the top (fig. 3.9a). Again, because the radar measures distance in slant-range, the slope (from point a to point b) will appear compressed and the length of the slope will be represented incorrectly (a' to b').
- **Layover** occurs when the radar beam reaches the top of a tall feature (b) before it reaches the base (a) (fig. 3.9b). The return signal from the top of the feature will be received before the signal from the bottom. As a result, the top of the feature is displaced towards the radar from its true position on the ground, and "lays over" the base of the feature (b' to a').
- **Shadowing** occurs when the radar beam is not able to illuminate the ground surface. It is typical of the far range areas, behind vertical features or slopes with steep sides (fig. 3.9c). Since the radar beam does not illuminate the surface, shadowed regions will appear dark on an image as no energy is available to be backscattered. The geometrical reason is because $\alpha > 90^{o}-\theta$.

The combined ascending and descending acquisition allows to avoid issues as foreshortening, layover and shadow effects giving a complete vision of the study area.

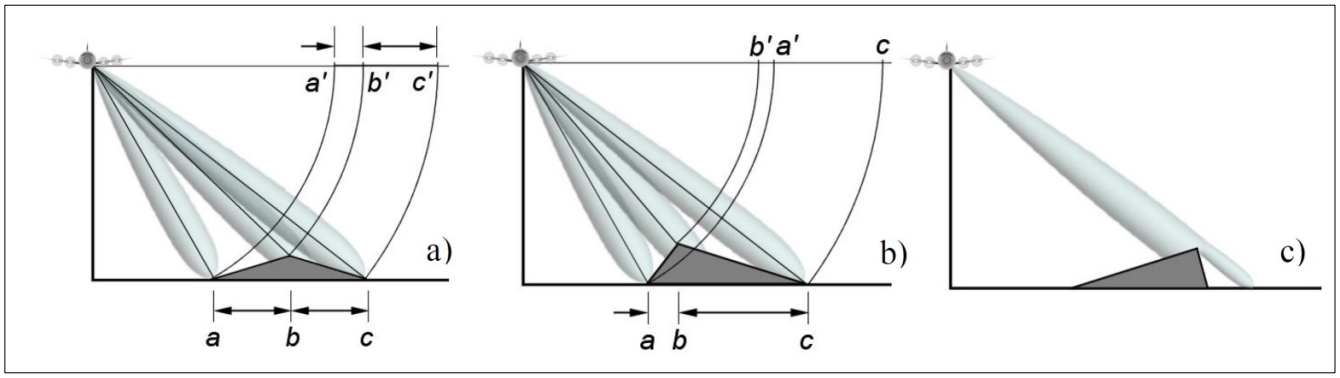

Figure 3.9 - Schematic illustration showing how features on the landscape are projected on to the line of sight of the satellite radar beam. After ESA, 2007.

Therefore the R-index map gives a probabilistic value to obtain radar targets over certain areas. The values can be generated with a Geographical Information System (GIS) software.

The final result is an index that changes from -1 values to +1. The negative values indicate the areas affected by layover effects; small and positive values (<0.4) indicate a strong pixel compression that limits the presence of targets and correspond to foreshortening effects. Values close to 1 could represent shadowing areas while the value of 1 indicates a slope that is parallel to the LOS. In general when the value of R-Index is greater than 0.4, the slope is well oriented and the main factor that influences the target distribution is the land use.

The area visibility also has a crucial importance for the applicability of radar analysis (Cascini *et al*., 2009). Area visibility refers to the measurable percentage of movement along a slope that can be determined when using SAR (Plank *et al*., 2012). Indeed, the satellite is only able to detect movements occurring along the LOS direction so the measurable percentage of movement is almost 100% of the real movement on ground, if the motion direction of the landslide is parallel to the satellite line of sight (perpendicular to the satellite orbit), or 0%, when the motion direction of the landslide is parallel to the flight pass of the satellite (azimuth). All the other directions have an intermediate value. A GIS-procedure can be easily formulated to calculate the horizontal and the vertical components of the measurable percentage of movement considering only four parameters: β (angle between the satellite

LOS and the slope's dip direction α), α (the slope's dip direction), ε (the angle between the E–W axis and LOS) and ω (the dip of slope).

After the SAR image has been acquired, the focusing process takes place. This process involves the storage of raw data, where the signal energy coming from a point target is spread in range and azimuth, into a single pixel of the output image. Now radar images, called Single Look Complex (SLC), can be displayed as real and imaginary components of a sinusoidal wave. In the SLC format the real part stands for the phase value (θ) and the imaginary for the amplitude value (A) (fig. 3.10; Hanssen, 2001).

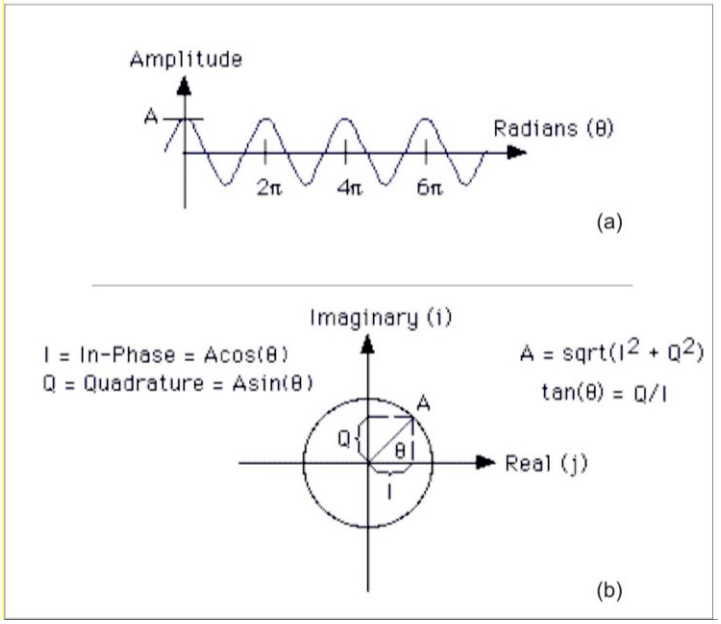

Figure 3.10 – (a) Polar representation of a sinusoidal wavelength in terms of its Amplitude (A) and Phase components (θ). (b) Representation of Amplitude sinusoidal signal in terms of Imaginary/Quadrature (Q) and Real/In-Phase (I) component in a complex plane, as occurs in SAR images. Modified from Sarmap, 2009.

In the SLC, amplitude is the energy of the backscattered signal expressed as a distance. When a signal leaves the transmitting sensor, it is broadcast at a specific energy level. On reaching an object on the ground surface, that energy level is changed depending on a number of circumstances that relate primarily to the reflective quality of the object. Metal and hard objects (buildings, roads and outcrops) have a high reflective quality and, therefore, the amplitude of the reflected signal will be much higher than the background noise of the system. Softer materials, such as wood, crops, asphalt, have a lower

capacity to reflect incident radar energy and so the amplitude of the reflected signal is strongly diminished.

Because each resolution cell of a SAR image comprises many scattering elements, the incoming signals will have different signal strengths, creating a spotty appearance and the resulting amplitude image will appear speckled. Constant levels of reflectivity, often bright spots, are indicators of stable reflections of radar signals. When the speckle is varied, from image to image, the pixels are temporally decorrelated across the data set and the speckling should be minimized by means of the multilooking process. The multilooking process averages the amplitude of adjacent pixels in the SLC by merging of adjacent n-pixels thus reducing the noise but, at the same time, the resolution (Goldstein, 1995).

SLC also records phase values, the key element in any interferometric analysis, since it is related to the sensor-to-target distance. This subject will be discussed in the following paragraph.

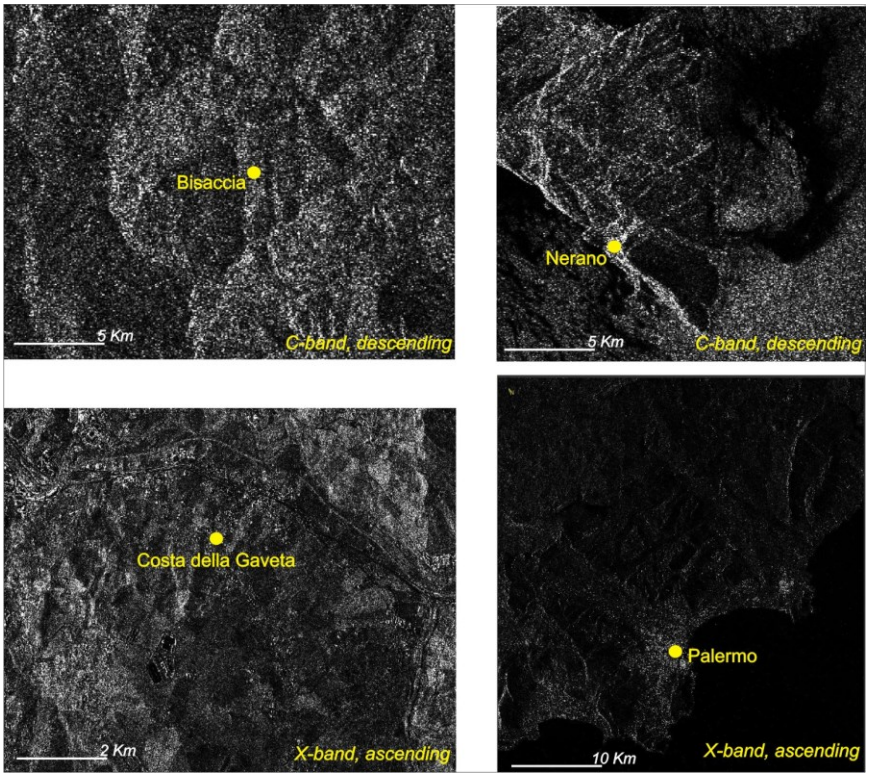

Figure 3.11 - SLC amplitude images for the studied areas. The cross-range is represented by the vertical axis and range by the horizontal axis.

3.3.1 InSAR, DInSAR and A-DInSAR techniques

Interferometric Synthetic Aperture Radar (InSAR or IFSAR), is the measurement of signal phase change, or interference, detected by comparing the phase values of two co-registered (aligned) SAR images acquired at different time for the same area (Massonett and Rabaute, 1993).

Indeed scatterers at different distances from the radar introduce different delays between transmission and reception of the radiation. The sensitivity of phase data to the sensor-target distance is affected by the wavelength capacity. The phase difference between two SLCs is represented by an interferogram. When the two images are acquired in a short temporal interval InSAR is used to convert the phase difference into an altitude for each image point, allowing the reconstruction of its three-dimensional location and therefore the generation of a Digital Elevation Model (DEM) (Rosen *et al*., 2000).

Mathematically, the SAR interferogram is generated by cross-multiplying, pixel by pixel, the first SAR image with the complex conjugate of the second (Massonnet and Feigl, 1998). Thus, the interferogram amplitude is the amplitude of the first image multiplied by that of the second one, whereas its phase (the interferometric phase) is the phase difference between the images ($\Delta\varphi$).

The phase noise can be estimated from an interferometric SAR pair by means of the coherence value (γ) (Prati *et al*., 2010) deriving from the equation [1]:

$$\gamma = \frac{\sum_{n,m} y_{(n,m)1} * y_{(n,m)2}}{\sqrt{\sum_{n,m} |y^2_{(n,m)1}| * |y^2_{(n,m)2}|}} \qquad [1]$$

where y_1 and y_2 are the first and second complex images respectively, while n and m refer to the column and row of each pixel (fig. 3.11).

The coherence expresses the cross-correlation coefficient of the SAR pair estimated for each pixel (fig. 3.12a); it varies in the range [0, 1]. The two extremes refer to the limit situations of noisy data totally uncorrelated and high-quality phase data fully correlated, respectively.

Due to the sinusoidal nature of the transmitted signal, $\Delta\phi$ is proportional to the two-way travel distance 2R of the radiation divided by the transmitted wavelength λ and can be expressed in the form of the following equation [2]:

$$\Delta\phi = \frac{4\pi}{\lambda}\Delta R + \alpha + noise \qquad [2]$$

Where λ is the sensor's wavelength (Table 3.1), ΔR is the object displacement and α is a phase shift due to different atmospheric conditions at the time of the two radar acquisitions.

The phase in the interferograms can only be measured in 2π (namely can only have values between $-\pi$ to $+\pi$) and each cycle in phase from $-\pi$ to $+\pi$ is called a 'fringe' (fig. 3.12b). The conversion of phase value is obtained by adding the correct integer multiple value of 2π. In this way, the "sawtooth" fringes will be turned into smooth continuous curves so that the total distance to the satellite is known. This process is termed unwrapping.

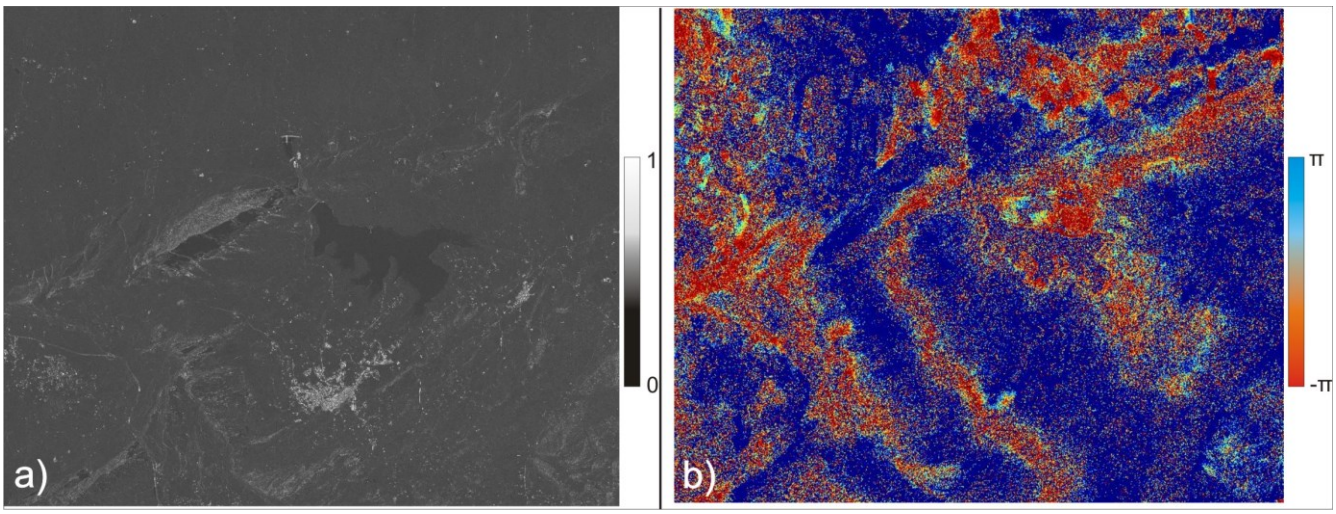

Figure 3.12 – Average coherence map obtained from 38 ascending COSMO-SkyMed images in Piana degli Albanesi area (a). Differential Interferogram with COSMO-SkyMed ascending images obtained on 1/7/2009 and 17/7/2009 (b).

Multitemporal differential interferometry is used to obtain information about moving objects on the ground acquired from two SLCs.

The word "differential" refers to the subtraction of the topographic phase contribution based on a digital elevation model and represented by the so called simulated interferogram, from the real

interferogram produced with a standard InSAR processing. After this step, the phase contribution due to object deformation need to be isolated from other disturbances in phase related to: changes in the reflectivity of the ground due to **temporal decorrelation**, changes in the viewing perspective due to **spatial decorrelation** and changes in the **atmospheric conditions**.

Temporal decorrelation involves a loss of meaningful phase relation between corresponding pixels in an image pair and usually results from variation in the moisture content or in the vegetation. Thus, decorrelation times can be as long as months to years for arid terrains and as short as several hours to several days for rainy and/or forested areas. Sparsely vegetated terrains can have decorrelation times between several days to several months. Snow-covered and frozen terrains are generally coherent over the short-term, but are sensitive to melting and snowfall.

The interferograms usually have a rather noisy phase value, at least in the case of repeat-pass acquisitions that are strongly affected by temporal decorrelation generated from the speckle effect, the problem is solved through the multilooking process quoted in paragraph 3.2.

Spatial decorrelation determines the variation in the phase signal because of the different satellite viewing geometries that modify the relative locations of the scattering cells. The different viewing geometries are denoted by the satellite baseline: the difference in orbit position from one satellite pass to the next. The variation of phase with viewing geometry leads to a maximum separation between two observation locations that can be optimal for DInSAR analysis. This maximum separation is called critical baseline, and is inversely proportional to the radar wavelength, the range resolution and directily proportional to the incidence angle and the sensor-target distance (Hetland *et al*., 2012).

Altough the atmosphere becomes more trasparent to microwaves, when interferometric SAR images are not simultaneous, the radiation travel path for each can be affected differently by the atmosphere. In particular, different atmospheric humidity, temperature and pressure between the two images will have a visible consequence on the interferometric phase (ESA, 2007).

Only when spatial, temporal and atmospheric decorrelation effects are limited, it is possible to obtain coerent interferograms where the shift in signal phase only linked to ground movement (fig. 3.13)

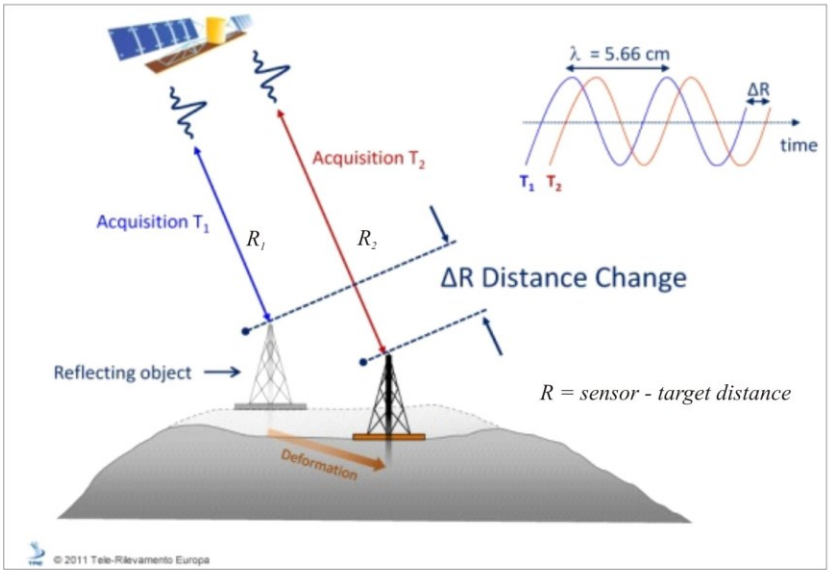

Figure 3.13 - A schematic representation showing the relationship between ground displacement and signal phase shift. The numerical value of the wavelength is that of a C-band sensor (modified from TRE, 2013). Because the phase distance at each acquisition is $4\pi r/\lambda$, the $\Delta\phi$ corresponds to $(4\pi*R_2)/\lambda - (4\pi*R_1)/\lambda$.

But one of the primary limitations of DInSAR analysys is the difficulty in separating the different contributions affecting the interferometric phase signal. The only way to compensate for these limitations is to process data using the A-DInSAR techniques, which exploit a stack of long time series (from days to months) of SAR images (at least 20 images) for the same area.

From this perspective, if the DInSAR is able to provide a "snapshot" of a given deformation process in the time interval between the acquisition of two scenes, the A-DInSAR approaches are able to provide displacement information over time, such as long-term time series of displacements (Rocca *et al*., 2014).

For the A-DInSAR analysis typical limitations are:

- **points density**, because of the absence of measurements in areas where no targets can be identified, such as heavily vegetated areas. This can be solved by installing artificial reflectors (corner reflectors), carefully designed to create a radar measurement points.

- **Geometrical distorsion** that reduces (in foreshortening and layovering areas) or completely deletes (for shadowing areas) the presence of targets, independently from their electromagnetic properties. This mainly occurs in areas of rough morphology and in mountainous and hilly regions (fig. 3.9).
- **Visibility**, since satellite orbits are roughly N-S oriented, displacements along W-E oriented slopes are no detected or underestimated.
- **Velocity limit**, because a quarter of the wavelength (λ) represents the maximum displacement that can be recorded between two successive acquisitions. This effect is called aliasing and limits the analysis to very-slow and extremely slow movements (fig. 2.6) (Hanssen, 2005; Crosetto *et al*., 2010). This velocity limit is expressed by formula 3:

$$D_{lim} = \frac{4/\lambda}{\mathrm{RT}} \qquad [3]$$

  Where D_{lim} is the maximum achievable displacement and RT is the revisiting time of the sensor (expressed in years). For X-band the limit is set to 40 cm/yr, while for C-band is 15 cm/yr.
- **3D displacement retrieval**, because an interferogram delivers only the component of the deformation along the LOS direction or at most, if both the acquisition geometries are available, along the vertical and horizontal component. In 2006 Bechor and Zebker developed a new method, named Multiple Aperture InSAR (MAI), based on the split-beam processing of InSAR data to create forward- and backward-looking interferograms. The phase difference between the two modified interferograms also provides the along-track displacement component allowing to obtain target 3D movements.
- **Relative displacements**, the movements are actually determined relatively with regard to the reference point within the observed area. As a rule, this correspond to a well measured geodetic point which is estimated not to be subject to major movements. Therefore in the case of

GBSAR acquisition, the steadiness of the installation site should also be taken into account, otherwise the GBSAR movements will also affect the measurements acquired by this instrument.

These constraints should be taken into account in the selection of the study area, since they will affect the suitability of the radar images for A-DInSAR applications (Colesanti and Wasowski, 2006; Cascini *et al*., 2009). However new insights to the geodetic science are pointing to their overcoming; this topic will be reclaimed and deepened in chapter 6.

Despite this, there are huge advantages deriving from the A-DInSAR analysis:

- The observation of remote or difficult to access locations, regardless of the weather and light conditions.
- The millimeter accuracy of deformations.
- The possibility of examining large portions of the Earth's surface in a short time if the sensors are mounted on aircrafts or satellites, and the possibility of obtaining continuous measurements of a more restricted area with greater detail if the sensors are ground-based.
- The possibility of converting into GIS software information deriving from other sources related to geology, geomorphology, hydrogeology and geotechnical engineering.
- The availability of a decanal archive (for some areas since 1992) with which to implement and compare the new information acquired for the same area.

Several A-DInSAR procedures have been developed in the last decade. The main ones are chronologically ordered: the Persistent Scatterers InSAR technique (PSInSAR™; Ferretti *et al*., 2001), the Small BAseline Subset technique (SBAS; Berardino *et al*., 2002), the Coherent Pixels Technique (CPT; Mora *et al*., 2003), the Interferometric Point Target Analysis (IPTA; Wegmüller *et al*., 2005),

the Spatio-Temporal Unwrapping Network (STUN; Kampes and Adam, 2005), the Enhanced Spatial Differences (ESD; Fornaro *et al*., 2007), the Stable Point Network (SPN, Crosetto *et al*., 2008), the Persistent Scatterers Pairs- DIFferential InSAR method (PSP-DIFSAR; Costantini *et al*., 2000; Costantini *et al*., 2008), the SqueeSAR™ method (Ferretti *et al.*, 2011), the Multidimensional SBAS (MSBAS; Samsonov and d'Oreye, 2012) and the Intermittent SBAS (ISBAS; Sowter *et al*., 2013).

The adopted pair selection strategy allows for the identification of two advanced A-DInSAR algorithm "families" (Hooper, 2008): one based on permanent (or persistent) scatterers (PSInSAR™, IPTA, STUN, SPN, PSP and SqueeSAR™) and one based on small baseline exploitation (SBAS, CPT, ESD, MSBAS and ISBAS). The permanent scatterers approach studies the phase information over objects characterized by a high coherence stability over time. A set of candidates are then identified with a threshold over the pixel amplitude dispersion, defined as the ratio of the standard deviation of the amplitude over its mean (Ferretti *et al*., 2001).

The results are implemented by computing, at full resolution, differential interferograms of all the acquisitions (so-called slave images) with respect to the same reference image (so-called master image).

On the other hand, the small baseline approach refers to the method of interferogram formation rather than to the criteria of pixel selection. Indeed only pairs of images with small values of spatial and temporal baseline (below the critical baseline, see paragraph 3.2.1) are considered in order to reduce both spatial decorrelation and topography errors. Consequently pixels with a high phase stability in space, expressed by their coherence value (γ), are taken into consideration (Reeves *et al*., 2014).

The ISBAS approach represents an innovation of the standard SBAS methodology, since it increases the number of targets via the choice of two thresholds: the first concerns the coherence value (γ) to discriminate good from low coherence pixels; the second allows the inclusion of pixels that are

intermittently coherent (Bateson *et al*., 2015) also in part of the interferogram stacking (p). Additional information about ISBAS will be given in paragraph 4.4.

3.3.2 Applications

Recently interferometric studies with geological and engineering geology application have been carried out concerning the following geohazards:

- **Coastal erosion**, InSAR data detected coastal geomorphological patterns by analyzing the balance between the deposited and the evacuated sediments. This information was used to model ocean waves, wind and river energy in relation to shoreline changes (Marghany *et al*., 2011).
- **Earthquakes** and **active faults**, DInSAR studies described the displacement field, namely the vertical and the horizontal shifts of the region of an earthquake. It was also possible to know the details of displacement gradients in the vicinity of the fault rupture and new faults were recognized (Atzori, 2013; Novellino *et al*., 2014a).
- **Glaciology,** A-DInSAR monitoring of ice sheet and glacier flow rates allowed the calculation of acceleration or deceleration in motion of ice masses (Strozzi *et al*., 2008).
- **Infrastructure stability** (bridges, buildings, dam, railway and roads) can be monitored in order to identify unexpected dangerous events that can occur during the construction and operation phases (Di Martire *et al*., 2014).
- **Landslides** can be analyzed to define their extension, velocity and state of activity (Confuorto *et al*., 2014), according to the WP/WLI 1993a and WP/WLI 1993b guidelines.
- **Subsidence** phenomena can be analyzed in relation to oil and gas extraction (Teatini *et al*., 2011), mining activity (Racoules *et al*., 2006), consolidation of young sedimentary deposits

(Aldiss *et al*., 2014) or widespread pumping of ground water (Chassaurd *et al*., 2014; Syafiudin *et al*., 2014).

- **Volcanology,** A-DInSAR provides information on volcanic-induced earthquakes and on the changes in the shape of a volcano caused by magma chamber expansion or contraction (Lagios *et al*., 2013; Walter *et al*., 2014).
- **Heritage sites,** can be better preserved against the damaging effects of geohazards (e.g., earthquakes, coastal erosion, landslides) (Tapete *et al*., 2012).

An example of how InSAR reads a subsidence, is given in Figure 3.14.

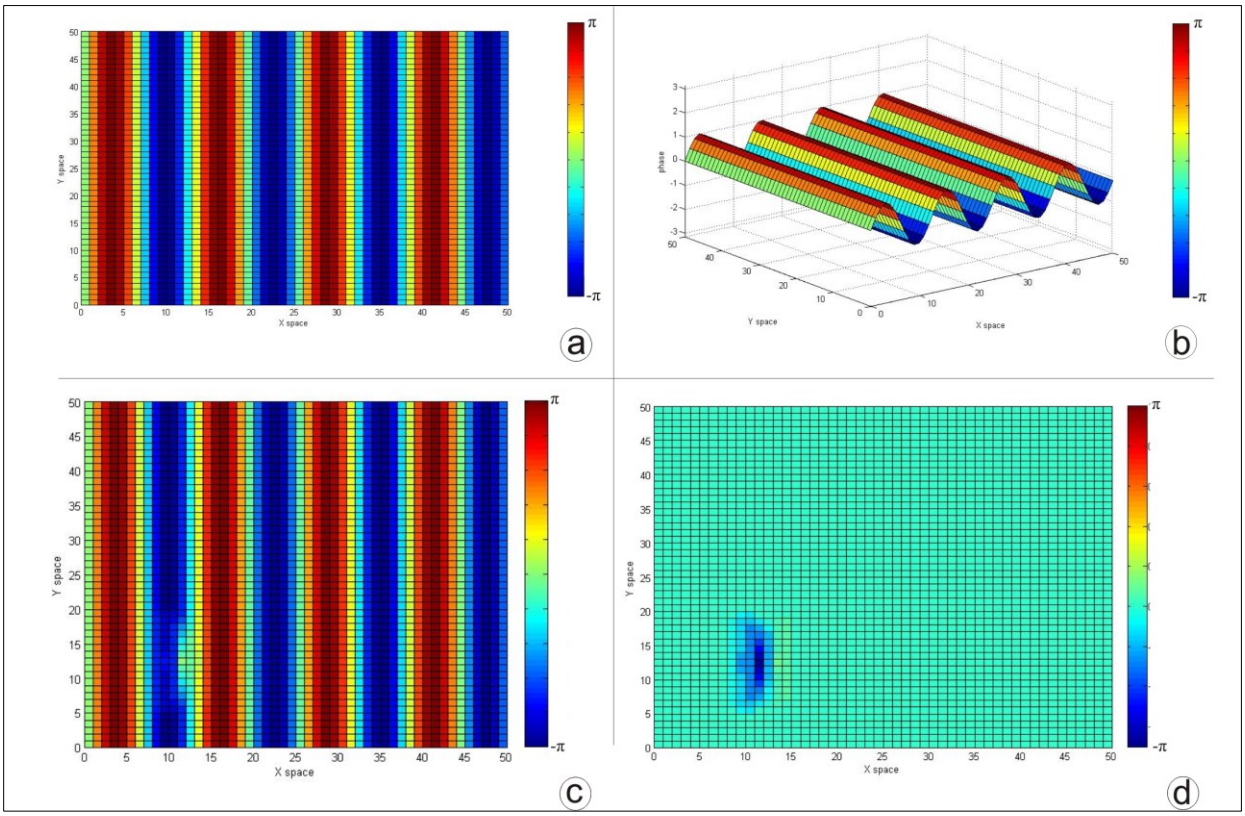

Figure 3.14 – An example of how a deformation is represented in interferometry for a ground displacement when λ=31 mm. Map view of the phase values of a flat surface at T_1 (a). 3D view of a (b). Map view of the phase values of the same flat surface at T_2, following a deformation event of 15 mm (c). Map view of the interferometric matrix obtained from the phase difference between a and c (d).

3.4 Weight of Evidence

The Weight of Evidence (WoE) method uses the Bayesian probability model and was originally developed for mineral potential assessment (Bonham-Carter *et al*. 1989).

In the point-wise studied areas a GIS-supported implementation of the WoE, tailored for landslide susceptibility mapping has been used; it was developed by van Westen (1993) at the University of Delft.

Geological and geomorphological data (among the lithology, slope angle, slope aspect, land use, flow accumulation, road proximity, fault/fold proximity) have been used as input parameters for the WoE, but now also involving the A-DInSAR displacement information as input layers/multi-class map.

The A-DInSAR information have been considered in terms of different classes within the following layers: target velocity, targets density and targets distance.

In the WoE method all landslide conditioning factors that can be mapped are entered into a GIS environment and converted from vector to raster maps.

After this step, an overlay is made of each factor map with the landslide inventory map (therefore it is a bivariate statistical analysis) and the frequency statistics are calculated for their combinations. The overlay led to maps containing four classes, representing the presence or absence of the landslides and of the potential landslide conditioning factor. The frequency, expressed as number of pixels, can be calculated with a GIS program (Table 3.2).

		B_i: potential landslide conditioning factor	
		present	*absent*
S: landslides	*present*	*Npix1*	*Npix2*
	absent	*Npix3*	*Npix4*

Table 3.2 - Possible combinations of a potential landslide conditioning factor and a landslide inventory map. Npix = number of pixels. From van Westen et al.*, 2003.*

More precisely, the importance of each factor for the occurrence of landslides is judged by comparing the landsliding pixels within the area occupied by the factor, with the landsliding pixels in the whole

area. Positive (W_i^+) and negative weights (W_i^-) are therefore assigned to each of the different classes (i) into which a factor map is classified.

For each factor, W_i^+ is used for those pixels of a factor (represented as a class in a multi-class map) to indicate the importance of the presence of the factor for the occurrence of landslides. If W_i^+ is positive the presence of that factor is favourable for the occurrence of landslides, and if W_i^+ is negative it is not favourable. W_i^- is used to evaluate the importance of the absence of that factor for the occurrence of landslides. When W_i^- is positive the absence of that factor is favourable for the occurrence of landslides. Weights with extreme values indicate that that factor has a strong influence on susceptibility mapping, while factors with a weight around zero have no relation with the occurrence of landslides.

The weights of evidence can be written in numbers of pixels as follows:

$$W_i^+ = log_e \frac{Npix1/(Npix1 + Npix2)}{Npix3/(Npix3 + Npix4)} \quad [4] \qquad W_i^- = log_e \frac{Npix2/(Npix1 + Npix2)}{Npix4/(Npix3 + Npix4)} \quad [5]$$

Since all of the maps are multi-class maps, containing several factors (classes), the presence of one factor (e.g. one specific lithological unit) implies the absence of other factors of the same map (e.g. all the other lithological units). Therefore in order to obtain the total weight of each factor (Wmap), the positive weight of the factor (W_i^+) itself should be added to the sum of every W_i^- of its multiclass map (Wmintot) less the negative weight of the other factors in the same map (W_i^-):

$$\text{Wmap} = W_i^+ + \text{Wmintotal} - W_i^- \quad [6]$$

In relation to Wmap, the lower the Wmintotal, the less the multiclass map affects the instability.

Since that the Wmap can be variable, it is necessary to reclassify each number according to four categories of the landslide susceptibility map:

- **Very low**, areas for which the combination of factors is generally unlikely to adversely influence slope stability.
- **Low**, areas for which the combination of factors is less likely to adversely affect the stability conditions.
- **Moderate**, areas for which the combination of factors may adversely influence slope stability.
- **High**, areas for which existing ground conditions are likely to create serious landslide problems.

The Jenks Natural Breaks classification has been adopted as data clustering method in order to determine the best arrangement of values into different classes (Jenks, 1967). The classification seeks to reduce the variance within classes and maximize the variance between classes.

To obtain a reliable WoE susceptibility map it is essential to provide input layers with the same level of detail. Since it was not possible to provide such information for the wide-area case study, the WoE susceptibility map is not given for the Palermo subareas.

The weights are modified on varying the range of value in each class that is manually set, therefore the WoE map must be validated. The endorsement has been carried out by selecting the output with the highest coefficient of correlation with slope movements and official susceptibility maps from the RBAs through the Mapcurves method (Hargrove *et al*., 2006). Mapcurves graphically and quantitatively evaluate the degree of fit among categorical maps and quantify a goodness of fit for each polygon, as well as the entire map.

Chapter 4: Case studies

This chapter illustrates the results of the landslide study on the four test sites (fig. 1.1): Nerano (Naples province), Bisaccia (Avellino province), Costa della Gaveta (Potenza province) and Palermo province.

These sites have been chosen since they represent areas that:

- have been historically affected by slow-moving landslides, because of the presence of SCFs.

- are densely urbanized; which is notouriously advantageous for A-DInSAR analysis

4.1 Nerano (Naples province, Campania region, Italy)

In the western sector of the Sorrento peninsula, at the end of February 1963 (from 19th until 25th) a landslide detached from Capo D'Arco (340 m a.s.l.), a place near the village of Termini (fig. 4.1a). It started as a rotational slide and then developed as a flow; the landslide affected the villages of Nerano and Marina del Cantone, about 900 m downslope (Cotecchia and Melidoro, 1966), and finally reached the sea. it showed a rapid velocity (from 3 m/h to 27 m/h) and a total extension of 0.12 km^2.

The event that took place in February 1963 was triggered by a total precipitation of 289.6 mm during that month, compared to the seasonal average of 100 mm (fig. 4.2).

According to the historical records and local witnesses, similar events, but of smaller extension, had occurred also in 1936, 1939 and 1941 (cotecchia and melidoro, 1966). The landslide is still intermittently active causing local damage to roads (fig. 4.1b) and retaining walls (fig. 4.1c).

Figure 4.1 – Panoramic sketch of the 1963 landslide's crown area (a). A damaged pathway at Capo d'Arco (b) and a partial collapse of a retaining wall on the provincial road n.192 (SP192; c).

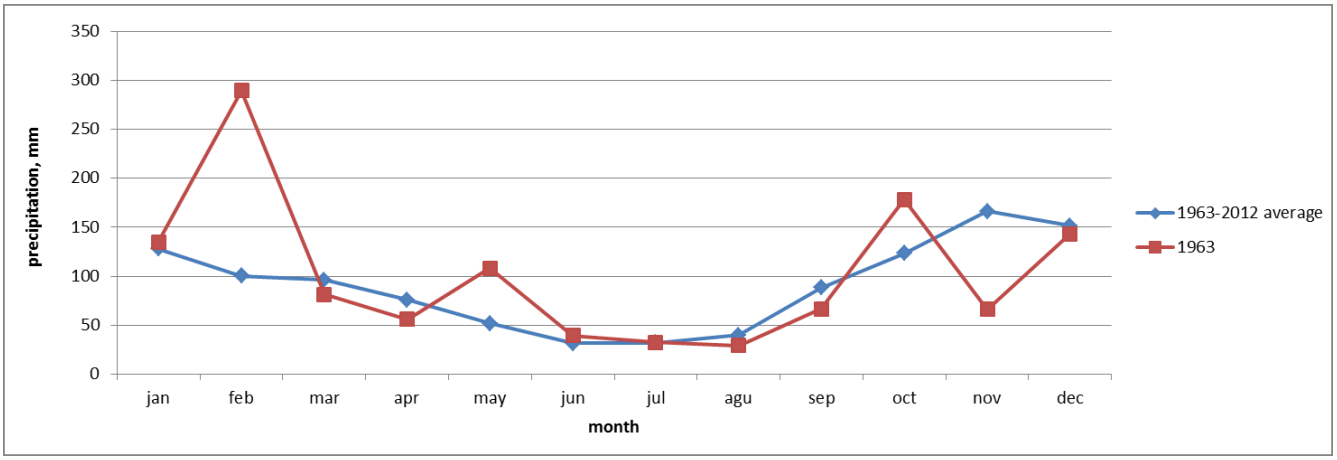

Figure 4.2 – Comparison of the average monthly precipitation from 1963 to 2012 and the 1963 rainfall data, the latter shows an evident peak at the end of February when the landslide was triggered.

4.1.1 Geological and geomorphological setting

The Sorrento peninsula belongs to the Lattari-Picentini Unit (bonardi *et al*., 2009), a portion of the shallow marine carbonates of the AMC (fig.2.7).

The outcropping rocks are composed almost exclusively of preorogenic Mesozoic carbonate sequences and, limited to the upper part, of synorogenic terrigenous deposits of Miocene age (fig. 4.3).

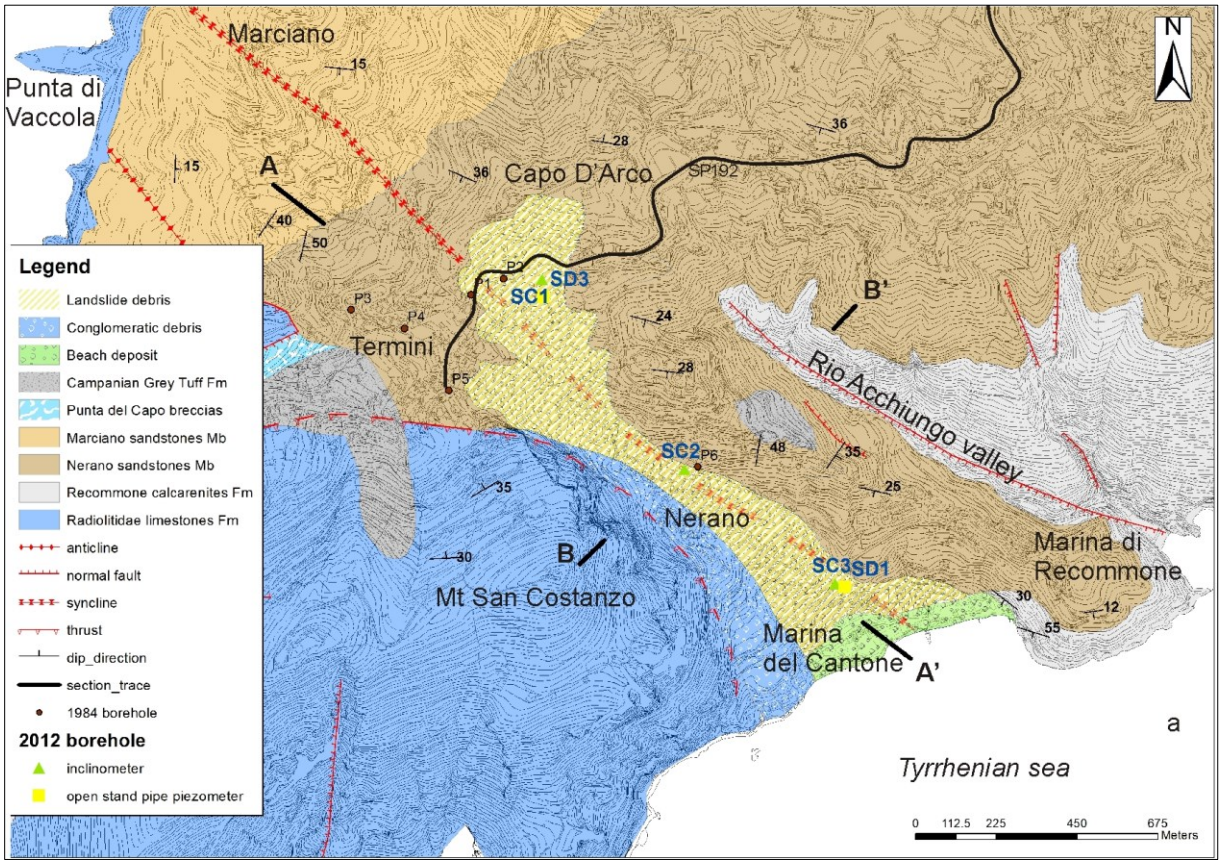

Figure 4.3 – Geological map of the Termini-Nerano area (a). A-A' and B-B' sections are in Figure 4.4 and 4.5 respectively.

More precisely, the study focused on the Punta Campanella succession (Scandone and Sgrosso, 1965; Cocco and Pescatore, 1967; De Blasio *et al*., 1981; CARG, 2010a). The Punta Campanella succession consists of, from the bottom to the top, (fig. 5.2b): the Radiolitidae limestone Formation (Turonian-Senonian), the Recommone calcarenites Formation (Lower Miocene), the Termini sandstones Formation (Serravallian), the Punta del Capo breccias (Upper Tortonian) and, finally, the Quaternary deposits consisting of slope debris, pyroclastic and beach terrains.

Radiolitidae limestone Formation (fig. 4.4a) is the bedrock of mt San Costanzo and extends along the coastline between Punta Vaccola and Capo di Sorrento. The average thickness is around 300 m and is mainly composed by bioclastic and bioconstructed calcilutites (fig. 4.4b) (Iannace *et al*., 2011).

A paraconformity boundary sets the transition to the upper Recommone calcarenites Formation (fig. 4.4c), mainly composed by glauconitic calcarenites (De Blasio *et al*., 1981).

The upper interval of the Recommone calcarenites Formation is composed of yellowish coarse-grained arenites (e.g. near Capo di Sorrento and Punta di Vaccola), interbedded with several marly-silty levels.

An unconformity marks the transition to the Termini sandstones Formation (figs. 4.4d-i), which elsewhere lies straight to the carbonate bedrock by means of a thrust. The Termini sandstones Formation (CARG, 2010a) was already known in the literature as the Arenaceous-Clayey Formation (Cotecchia and Melidoro, 1966) or the Punta Lagno Formation (Scandone and Sgrosso, 1965).

The Termini sandstone Formation (200 m thick) is constituted by two main members: the lower one is the Nerano sandstones Member where the studied landslide developed. It consists of arkosic sandstones, interbedded with siltstone and mudstone levels, cropping out south of Termini (fig. 4.4h).

A gradual vertical and lateral transition leads to the Marciano sandstone Member, a thin bedded arkosic sandstone succession interbedded with marly levels which preserve their original structures related to a turbidite origin (e.g., parallel and convolute laminations; figs. 4.4d-e).

Calcareous olistoliths (nearby Schiazzano village; fig. 4.4f) with angular unconformity relationships and clayey olistostromes (nearby Madonna della Neve, Caprile and Marciano; fig. 4.4g) with a conformity relationship have also been recognized in the Nerano sandstone Member. An angular unconformity sets the boundary with the overlying Punta del Capo breccias, a tens of meters thick unit, consisting of breccias and, secondarily of conglomerates within a sandstone matrix (fig. 4.3j).

From Miocene the sediments belong to the continental environments: slope debris (fig. 4.4l), pyroclastic (fig. 4.4k) and beach terrains.

Slope debris derive prevailingly from calcareous boulders which are mostly originated from the inverse fault on the eastern side of mt San Costanzo during the latest glacial phases (Brancaccio, 1968), while the valley lying between Termini and Nerano settlements is mainly covered with clayey-arenaceous landslide deposits, including those related to the 1963 event.

Volcanoclastic material displays a huge variability in thickness and a patchy outcrop pattern. compositionally it is a trachytic pyroclastite including amphibolite and micaceous crystals in a dark to purplish gray glassy matrix (Fedele *et al*., 2008).

Finally, the beach deposits consist of pebbles deriving from the Cretaceous carbonate bedrock and of sandstones from the flysch deposit.

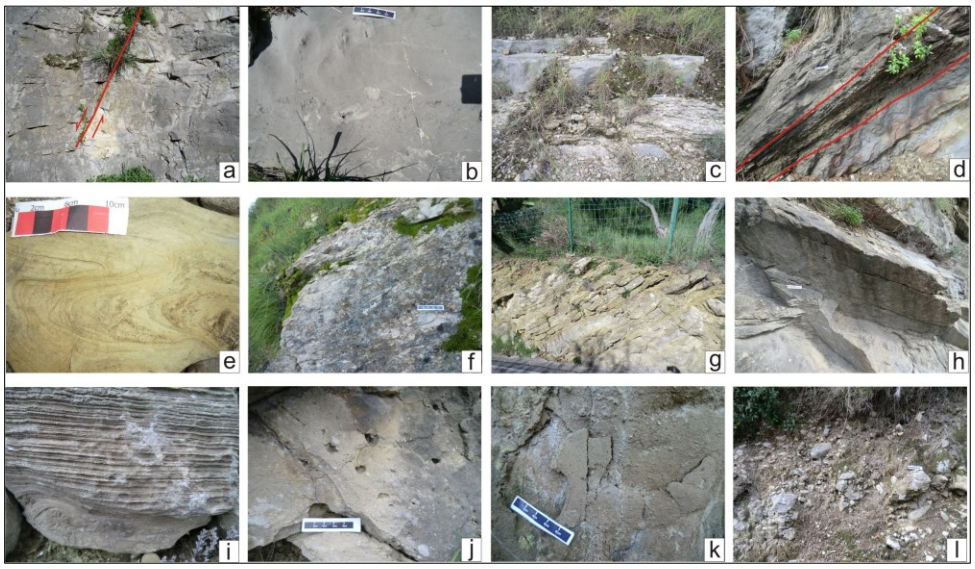

Figure 4.4 – Some examples of outcrops in the Punta Campanella area. A normal fault in the massive limestone (a). Radiolitidae shell fragments in the Radiolitidae limestone Fm (b). Gradual transition to the Recommone calcarenites Fm (c). Parallel (d) and convolute lamination (e) in the Termini sandstone Fm. Marly-calcareous olistolith (f). Clayey olistostrome in the Nerano sandstone Mb (g). Coarse sandstone (h) and fine sandstone (i) of the Termini sandstone Mb. Punta del Capo breccias (j), campanian ignimbrite (k) and slope deposit (l).

The tectonic features that most influence the geomorphology are connected to a first compressional event with a NE-vergence, followed by an extensional one (Sartori, 1990).

The compressive phase created gentle folds in the Termini sandstone Formation and the thrust east of Termini while the latest extensional phase created high-angle normal faults generating the Rio Acchiungo valley (fig. 4.2a).

The predominant clayey lithology combined with the strong tectonic deformation and the presence of "exotic" blocks (namely the olistolithes and the olistostromes), represents an important predisposing factor to slope instability in Nerano area.

Geological surveys and borehole data (see paragraph 4.1.2) allowed to define two geological cross sections for the landsliding area where older logs (P1, P3 and P4 of Figure 4.5), acquired from the Municipal Archives, are also included.

The first section (fig. 4.5), NW-SE oriented, displays how the landslide developed in the Nerano sandstone Formation where olistoliths and olistostromes were found during the in-situ campaigns.

In the A-A' section, a margin of error still remains concerning the depth of contact between the Termini sandstone Formation and the Recommone calcarenite Formation, since it was inferred from field evidences.

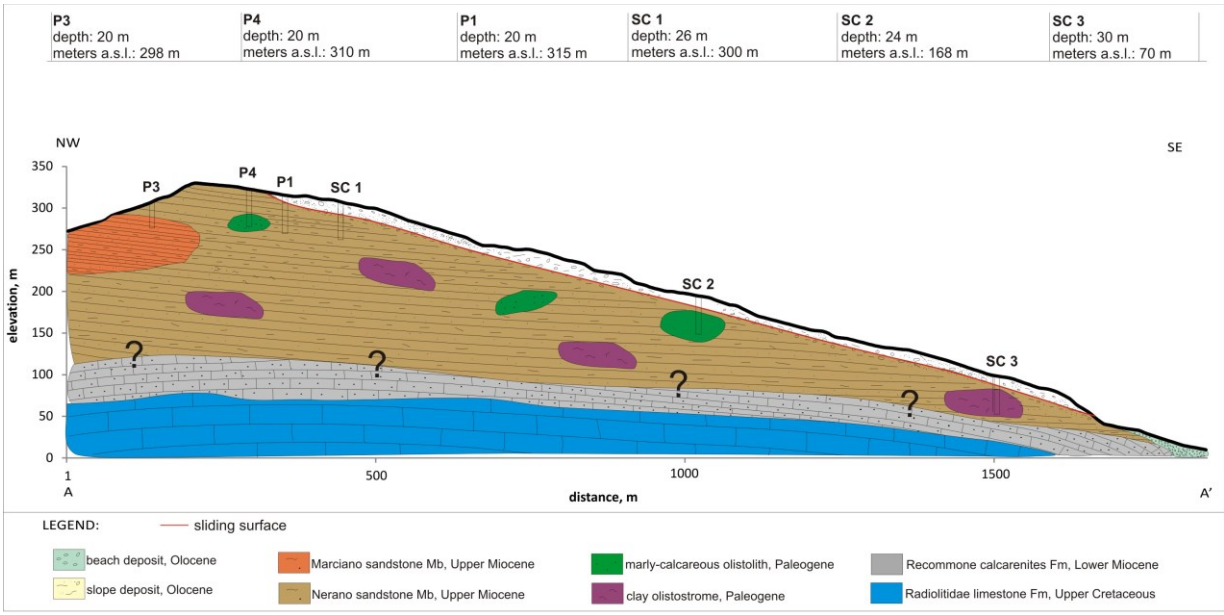

Figure 4.5 – NW-SE geological cross section. The A-A' section trace is in Figure 4.3.

The second section, SW-NE oriented, crosses the landslide track and reveals the limited extension of the 1963 landslide deposit compared to the conglomeratic debris that fill most of the Termini-Nerano valley; the valley developed above a syncline structure (NW-SE direction) and delimited to the northeast by the Rio Acchiungo valley normal fault (fig. 4.6).

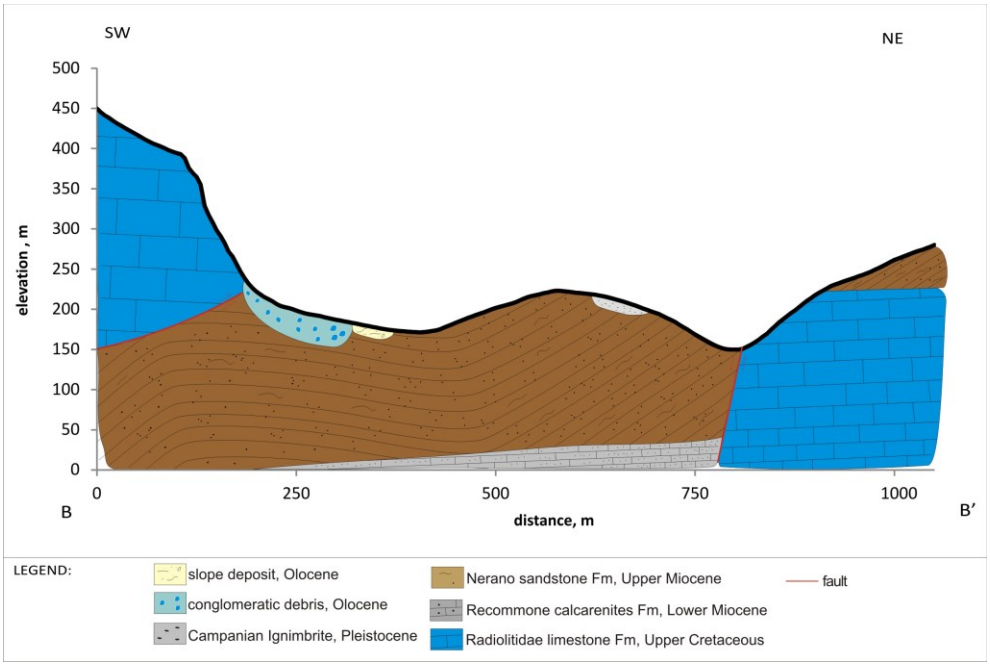

Figure 4.6 – SW-NE geological cross section. The B-B' section trace is in Figure 4.3.

Geomorphologically, Termini and Nerano settlements lie at the foothills of the eastern side of mt San Costanzo. The relief shows a steep eastern slope (dip angle higher than 60°), where continuous rock falls and cryoclastic erosion processes cause the deposition of slope debris over the Termini sandstone Formation.

On the eastern and northern sector of the investigated area the terrain morphology is generally gentler due to the wide presence of the Termini sandstone Formation. The area is characterized by hills gradually dipping towards the sea. The hills reach maximum elevations of 400-500 m a.s.l., sometimes with a flat top surface (e.g., the Sant'Agata desert). Here the most common gravitational phenomena are flows, rotational slides or complex movements (fig. 4.7).

Small basins and high-gradient streams characterize the drainage network, thereby promoting the development of short and small channels with high erosion rates and linear patterns.

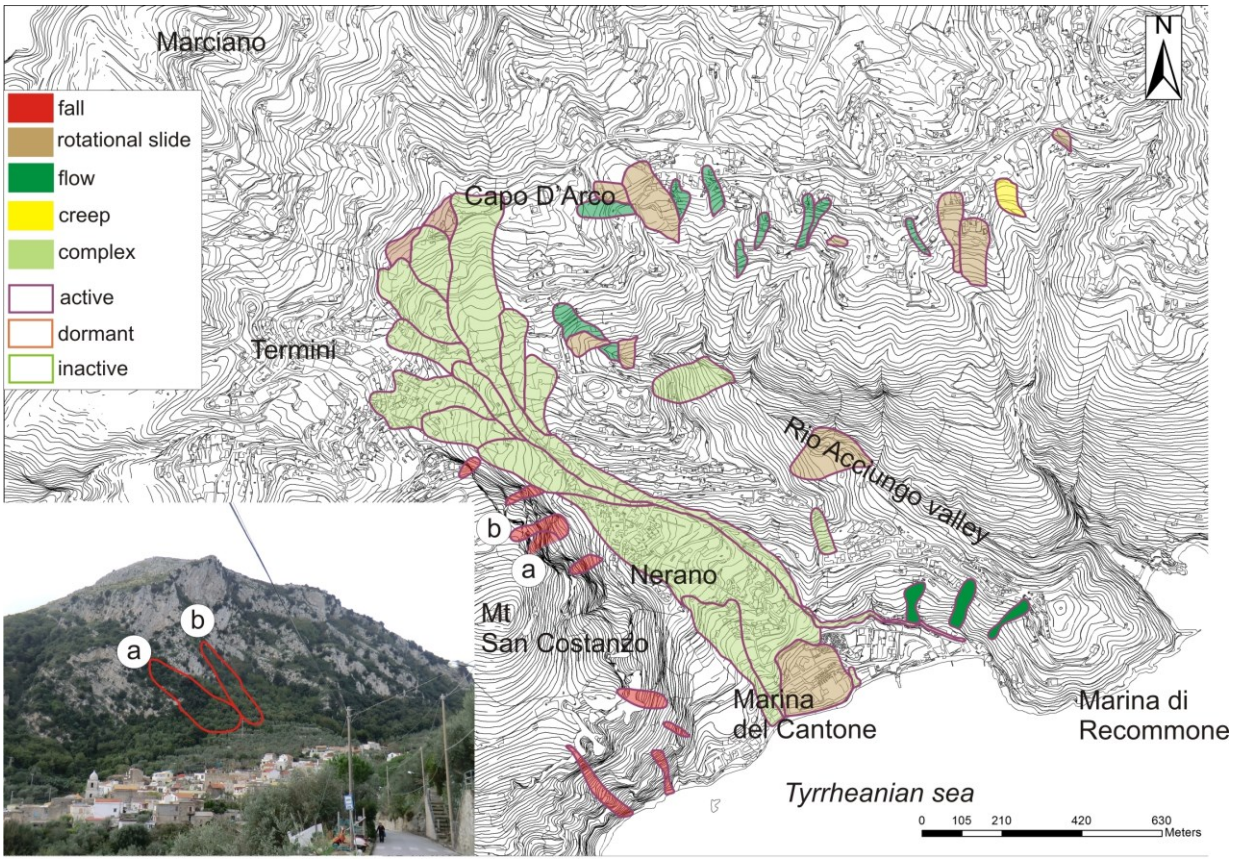

Figure 4.7 – Official landslide inventory map for the Nerano area (AdB Destra Sele, 2011). In the inset, the a and b landslides on the mt San Costanzo eastern side.

In the investigated area, the official Landslide Inventory Map of the HSP (AdB Destra Sele, 2011) reports 22 active landslides, divided as follows: 5 falls, 3 rotational slides and 14 complex landslides (rotational + flow), among which the 1963 landslide is the largest one. During the landslide mapping and monitoring stages, which are discussed in the following three paragraphs, only the rotational slides and complex landslides of the Termini-Nerano valley were taken into consideration. The inferred new landslide area will be showed in Figure 4.11.

4.1.2 Results of the landslide investigation

4.1.2.1 In-situ geological and geotechnical campaign

The geological-geomorphological analysis has been supported by in-situ investigation campaign carried out in the Summer of 2012, which focused on three key areas of the 1963 landslide: the head (nearby Capo D'Arco), the main body (nearby Nerano) and the foot area (nearby Marina del Cantone). Five boreholes were drilled, consisting of three continuous coring boreholes (from now on cited as SC1, SC2 and SC3) and two destructive drilling boreholes (from now on marked as SD1 and SD3). In SC1, SC2 and SC3 three inclinometers have been installed while in SD1 and SD3 two open stand-pipe piezometers have been installed (fig. 4.5). The boreholes have been drilled, where possible, at depths beyond the main slip surface reported from a previous geophysical campaign; the slip surface was supposed to be at depths never exceeding 25 m below ground surface (Cotecchia and Melidoro, 1966). Depending on the local stratigraphy, the screened casing of the open standpipe piezometers have been positioned from -6 to -30 m in SD1 and from -0.5 to -3.5 m in SD3 (fig. 4.8).

Furthermore, some tens of samples have been collected beyond and above the slip surface of the continuous coring boreholes, where XRD analyses (Cesarano Mar. *et al*., 2013; Cesarano Mar., 2014) and geotechnical tests (grain-size analysis, Atterberg limits and direct shear tests; Cosenza, 2013) have been performed; the latter led to the evaluation of the factor of safety (see paragraph 4.1.2.3).

The core description considers both stratigraphic and lithological-sedimentary features of the Termini sandstone Formation, being the latter the only one drilled during the in-situ campaign.

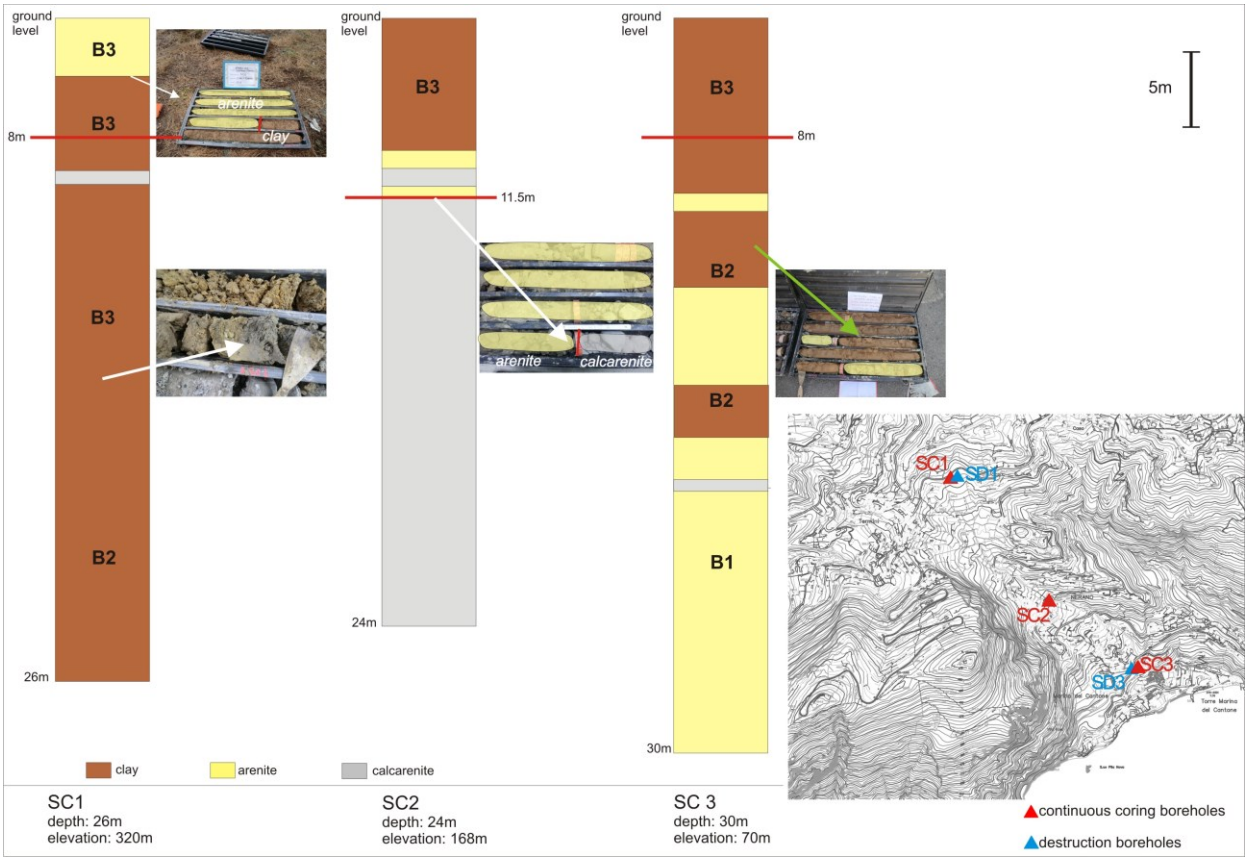

Figure 4.8 – Stratigraphic log of the continuous coring boreholes. The sliding surface is indicated with a red line. Borehole location is indicated in the bottom inset. B1, B2 and B3 refer to the esu class of SCF (see paragraph 2.3).

The SC1 borehole (fig. 4.8) is composed for the first 60 cm by soil and anthropogenic backfill material followed by about 3 m of poorly cemented ochre sandstone with a chaotic structure, ascribed to the B3 class for SCF (Esu 1977; see paragraph 2.3).

The sandstones are followed by greyish high-plasticity clays and greenish marly clays whose fracture density decreases downwards reaching the B2 category of complexity. A metric horizon of grayish calcarenite is found 2 m below the rupture surface localized at a depth of 8 m.

In SC2, after the first 20 cm of man-made material, layers of leaden-gray clay and dark green clayey marl appear. Within the first meters, the material shows a chaotic fabric which becomes more consistent with depth and displays an alternation of cemented sandstone layers with glauconitic calcarenite levels. Down to 11.5 m, the material represents the landslide deposit and can be associated to the B3 group. The calcarenitic levels are crossed by a network of discontinuities, whose spatial

density increases with depth. The latter presumably represents the stable bedrock localized at a depth of 11.5 m (fig. 4.8).

Differently from SC2, the overall configuration of SC3 shows a more homogeneous alternation of clayey and sandstone layers, all ascribed to the B1 SCF class (fig. 4.8).

The SC3 borehole reveals a succession consisting essentially of greenish and reddish silty clays and gray-blue silty sandstones; the latter are poorly cemented and glauconite-rich.

Ground truth data consist of inclinometer measurements acquired from SC1, SC2 and SC3. These reveal that the fastest moving area is the accumulation zone, with >12mm/yr from SC3, compared with the crown area, with <10mm/yr from SC1; SC2 measurements are considered unreliable and therefore will not be discussed anymore.

Regarding the landslide depth, the inclinometer data reveal the presence of a slip surface at a depth of -8 m. This suggests that the Nerano-Termini landslide represents only a reactivation of the shallow portion of the 1963 landslide deposits. The latter developed, in turn, in the Termini sandstone Formation (Nerano sandstone Member, fig. 4.4).

The piezometric readings (September 2012, December 2012 and February 2013) show a seasonal variability of the water table depths in SD1: -14 m, -7 m and -6 m, respectively. In SD3 the water table is stable at -3 to -4 m.

4.1.2.2 Aerial photographs analysis

The evolutionary history of the slope during the forty-eight year period from 1955 to 2003 has been reconstructed by interpreting stereoscopic aerial photographs (Table 4.1).

year	flying height, m	scale	frames
1955	6000	1:36000	8823-8824
1956	3900	1:27000	1795-1796
1974	2700	1:16000	993-994
1990	6200	1:36000	678-679
1996	5850	1:41000	5063-5064
1996	6000	1:41000	1104-1105
2003	4300	1:28000	3044-3045

Table 4.1 – Aerial photographs information. The data have been acquired from the Italian Military Geographic Institute (IGM).

The oldest photos available, dating back to 1955 and 1956, show two lobes of the 1941 landslide which were located east of Termini where few houses were present (fig. 4.9).

The northernmost portion of the frame is covered by a rather sparse vegetation and extensive outcrops of the Termini sandstone Formation; on the landslide eastern side several anthropogenic terraces were present. The electricity goal post was already placed in Capo d'Arco but the provincial road n.192 had a different track from the current one.

The 1974 photos follow the remedial works carried out by the Public Works Office of Naples (in 1954-1955) that led to the construction of embankments, on the eastern side of the collapsed area, and drainage trenches in the central area connected to a drainage basin downslope (fig. 4.9).

In addition to the two 1941 landslides crown areas, two new crowns are present on the western portion, where new buildings were raised. The 1941 lateral lobes were dormant while the 1941 central lobe had a retrogressive evolution (fig. 4.9).

The bioengineering interventions of the '50s developed a pine forest inside the 1963 landslide body, fully grown in the following years, as evident from the 1990 frames.

The 1990 frames reveal also: a new camping area, recent buildings in Marina del Cantone, the almost complete disappearance of human plantations and the presence of a parking lot in Nerano (where the SC2 borehole was drilled). The 1963 landslide kept its conformation of 4 lobes, of which only the largest was active (fig. 4.9).

The urban fabric was fully developed in the 1996 frames, when the perimeter of the active portion of the 1963 landslide changed. The landslide evolution is depicted from the absence of vegetation and the outcropping of the Termini sandstones Formation on the western side of the valley (fig. 4.9). The western lobes turned out to be active at that time.

The 2003 photos show a significant increase in number and volume of the landslides, with the involvement of different infrastructures, including the church of Santa Croce di Termini, still under renovation today (fig. 4.9).

In the accumulation area no evidence of active instability can be seen, because the environment has been strongly influenced by human activities and the landslide activity is very limited.

Stereoscopic analysis revealed a global increase of the depletion area from 0.04 Km^2 to 0.11 Km^2, in the 1955 – 2003 period, during which a landslide family (Guida *et al*., 1995) developed in the Termini-Nerano valley with a retrogressive evolution, characterized by a group of partially superimposed landslides of the same type, but of different age and state of activity.

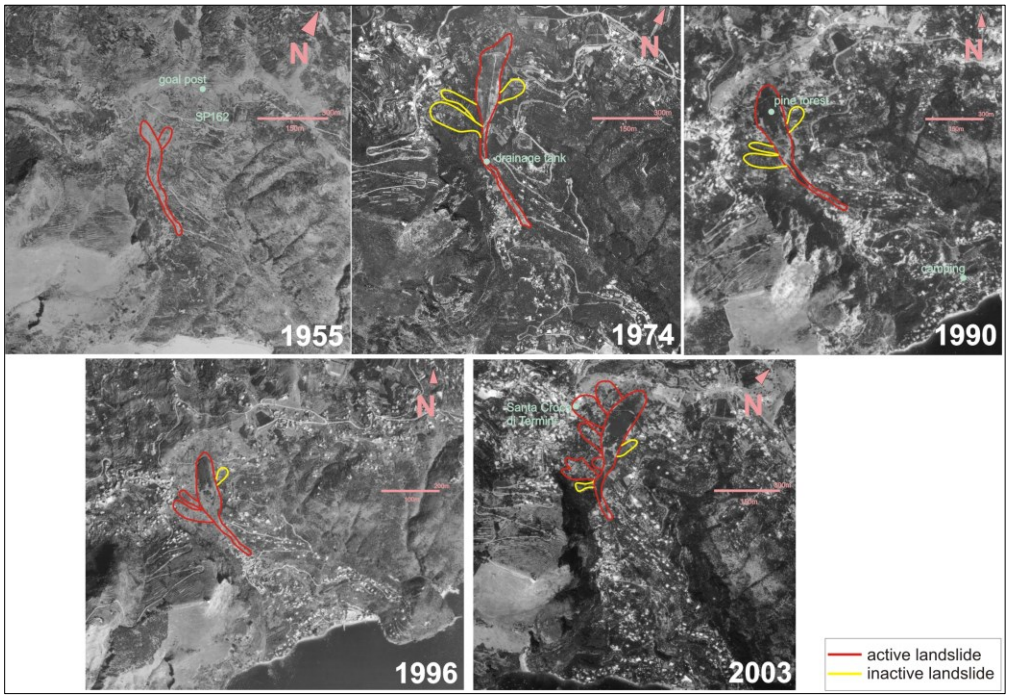

Figure 4.9 – Landslide activity maps of the Termini-Nerano valley from 1955 to 2003.

4.1.2.3 A-DInSAR analysis

Initially the A-DInSAR analysis considered the ERS and ENVISAT dataset, derived from the Persistent Scatterers Interferometry Project (PSIP) through the Italian National Geoportal (ING) of the Italian Ministry of Environment, Land and Sea (http://www.pcn.minambiente.it/viewer/). Unfortunately, these data revealed poor target densities (<30/Km^2), especially in the landslide area.

The outcome was also confirmed by the R-index map (see paragraph 3.2.1), which revealed a strong layover and foreshortening effect especially on the Termini-Nerano valley western side, where average negative R-index values were recorded (fig. 4.10a).

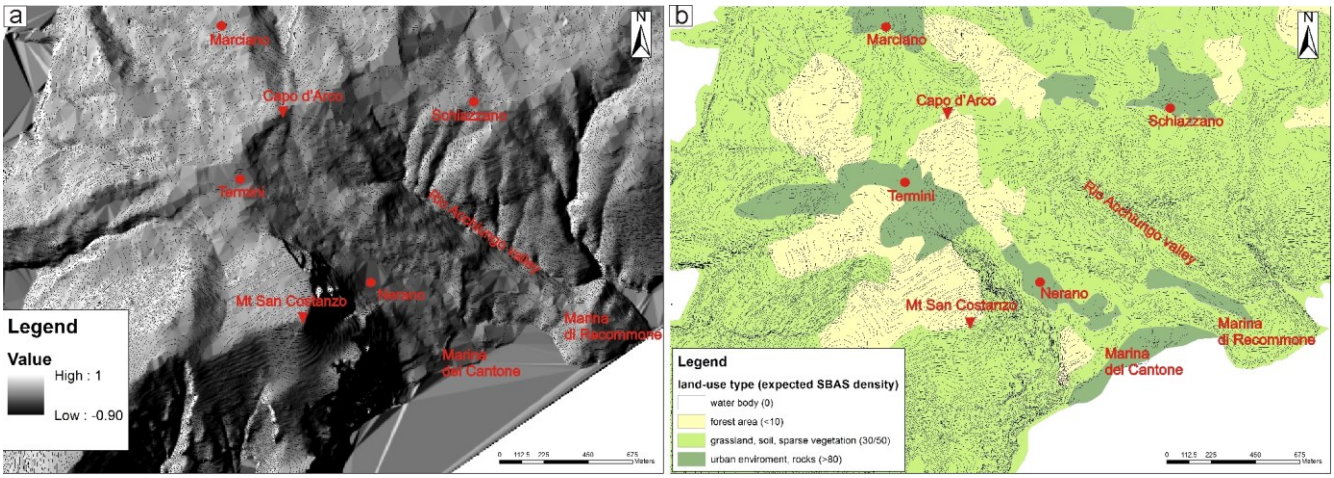

Figure 4.10 – R-Index map (a). LU-Index map (b). Land Cover information from CORINE land Cover map 2006, European Environment Agency (EEA, 2007).

In general, the slope is well oriented where the R-Index value is greater than 0.4, which occurs only in 20% of the Termini-Nerano valley. But the radar targets density depends also on land use; in this case 30% of the well-oriented slope is covered by urban fabric (4.10b). In order to obtain as many radar targets as possible, the ISBAS analysis was chosen. ISBAS processing involved 46 ENVISAT descending images (track-36, frame-2781; from 5/6/2003 to 3/6/2010); the main parameters adopted are summarized in Table 4.2.

The ISBAS technique was able to detect a total of 753 points with a density of 84 points/Km^2 inside a 9 Km^2 extended area (fig. 4.11).

Spatial baseline threshold	250 m
Temporal baseline threshold	4 years
Multilooking factor (azimuth x range)	15 x 4
Coherence threshold	0.25
Number of interferograms	252
Interferograms threshold	80
SBAS points	782
ISBAS points	1628

Table 4.2 –Main data processing parameters for the Nerano ISBAS dataset.

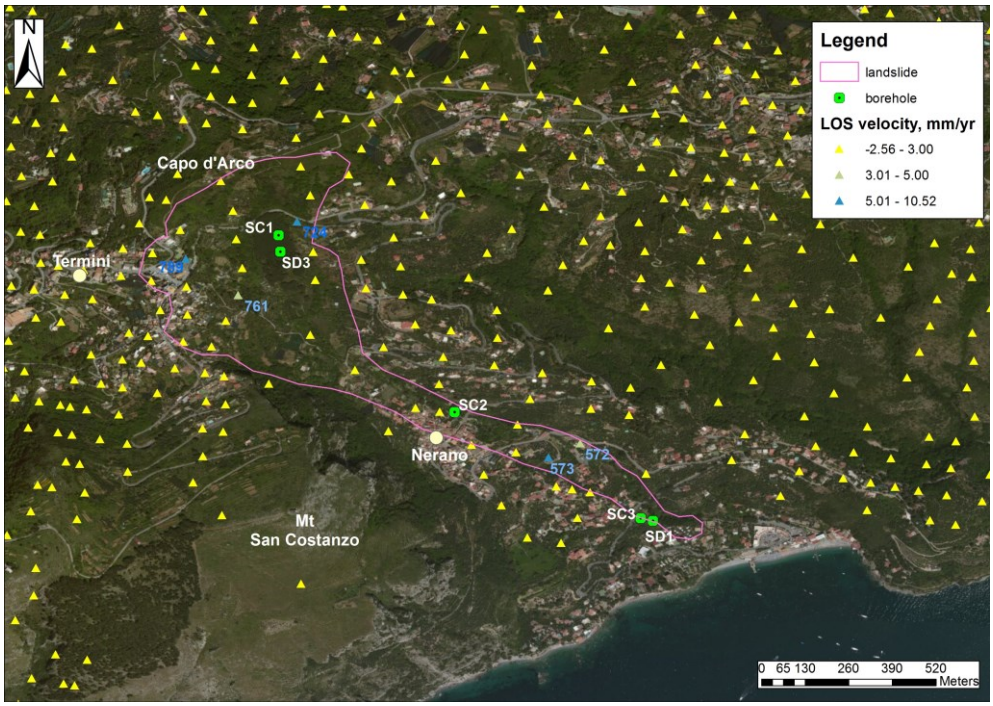

Figure 4.11 - Displacement rate measured in the Nerano landslide area. The pink line represents the landslide border. Positive values indicate displacements towards the sensor. Negative values indicate displacements away from the sensor.

Because of the average standard errors of ±0.7 mm/yr, the stable class for the ISBAS targets has been set to ±1.5mm/yr. Only six points fall outside this limit, five of which are inside the landslide border defined in this work. The sixth one is located in the northern sector of the studied area (fig. 4.11).

The radar-derived rates of movements are confirmed from the ground truth data mentioned in paragraph 4.1.2.1, although these are not overlapping in time (inclinometer data were collected from July 2012 to February 2013).

Figure 4.12 shows the match between the inclinometric displacements deduced over a year, corresponding to 12mm/yr in the crown area and to 48mm/yr in the foot area, and the displacement detected from the ISBAS targets, considering their reduced visibility of real displacements. Again, the foot area is the fastest moving portion of the landslide. The inclinometric displacement profiles show a sharp discontinuity where the unstable superficial materials, such as colluvium, shales and clays switch to the ancient landslide deposits now stabilized.

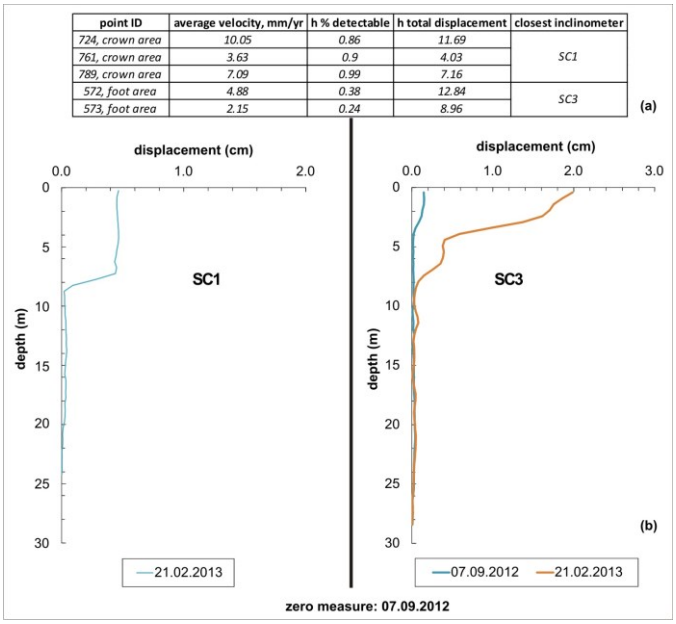

Figure 4.12 – (a) LOS average velocity values for the closest points to the inclinometric probe, the location of which is indicated in Figure 5.5.

The time series analysis of the most representative points of Figure 4.11 shows a similar intermittent trends correlated with the rainfall data available from the rain gauge station located in Pastena, 1.6 Km away from the studied area (fig. 4.13). In fact, independently from the targets location, the highest displacement rates were measured from October to January, coinciding with the greatest concentration of rainfall. On the other hand the displacement rates were decelerated from June to August, coinciding with a period when the concentration of rainfall events was significantly reduced. The piezometric levels change consistently with the dry and wet seasons from July 2012 to February 2013, but do not ever reach the ground level (Cosenza, 2013).

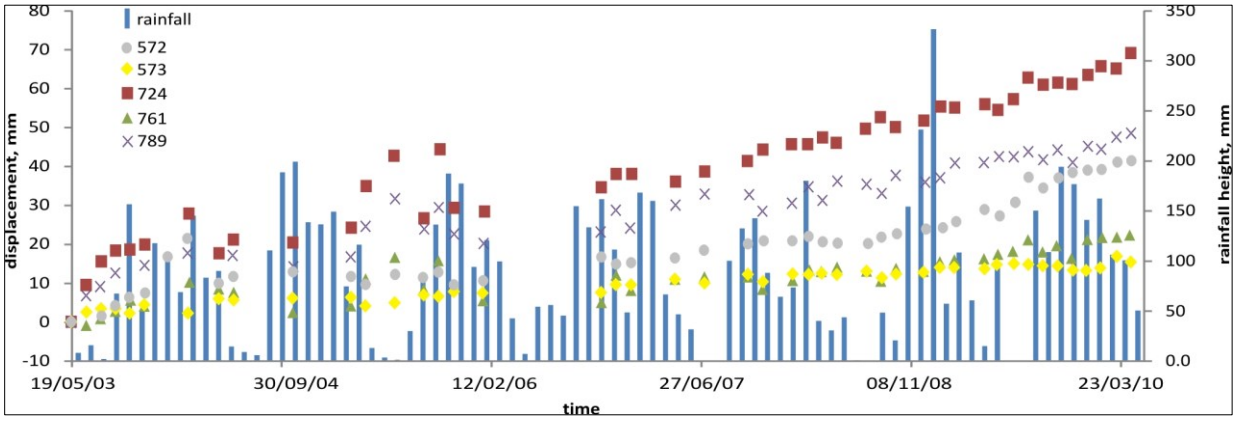

Figure 4.13 – The LOS average velocity values for the fastest points, whose location is indicated in Figure 5.9, compared with rainfall data provided by the Agro-meteorological Service of the Campania Region.

The time series analysis, historical data and low seismicity of the area, allow to demonstrate that, by 1963, the Nerano landslide is repeatedly reactivated only by heavy rainfalls. Indeed, nowadays, the factor of safety is steadily greater than 1 unless the water table reaches ground level (Cosenza, 2013).

The combination of data collected and produced for the landslide analysis permitted to define the new border reported in Figure 4.11. This has been used for the evaluation of the Landslide Susceptibility Map, discussed in the following paragraph.

4.1.3 Landslide Susceptibility Map

The Landslide Susceptibility Map has been produced considering the following parameters in the WoE calculation: lithology, slope, aspect, land use, flow accumulation, road proximity, ISBAS target velocities and fault/fold distance. The geomorphology, such as slope and aspect, was calculated from the 5 x 5 m DEM. The geomorphic type was extracted from the soil database from CORINE land Cover map (EEA, 2007).

According to the outcome, the highest Wmintot (0.79) is given by the flow accumulation which proves to be, surprisingly, the main predisposing factor to instability. The flow accumulation is related to the curvature values representing the morphology of the topography. The occurrence of a surface upwardly concave at the Termini-Nerano valley, allow to the accumulation of more water following heavy rain and to the storage for a longer period.

Instead forty percent of the area, where the Termini sandstones Formation (W_i^+=0.23 and W_i^-=-0.41) crops out, is labeled only as moderate susceptibility.

The highest susceptibility is located in Nerano and Marina del Cantone areas, due to the occurrence of a valley filled with slope deposits (W_i^+=1.96 and W_i^-=-0.17) and ISBAS moving targets. At Mt. San Costanzo and Rio Acchiungo area, despite the higher inclination (>50^o), the carbonate sequence (W_i^+=-1.16 and W_i^-=0.23) drastically reduces the landslide susceptibility (fig. 4.14).

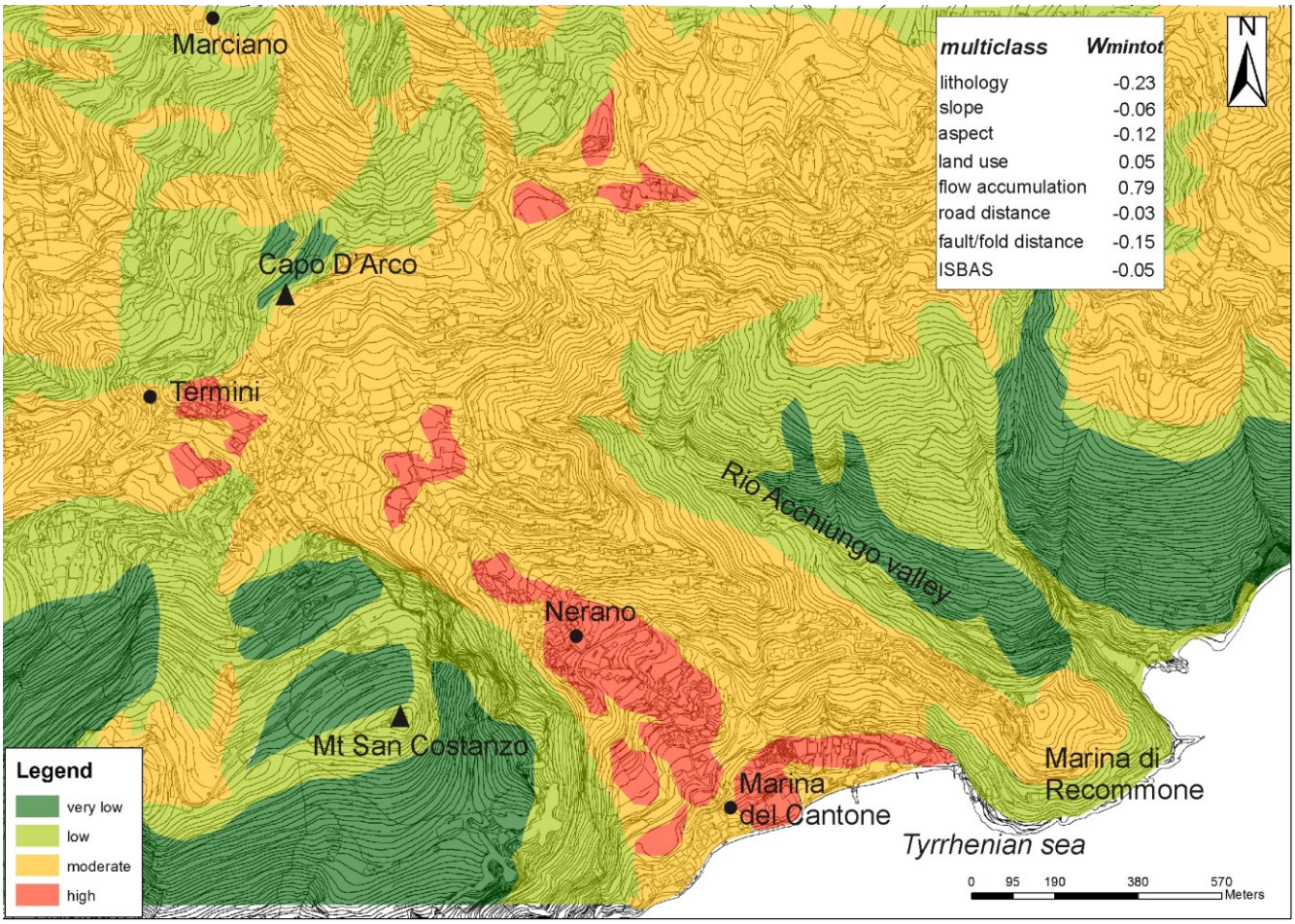

Figure 4.14 - The WoE map for Nerano area.

In conclusion, the landslide analysis in Nerano confirmed the presence of highly disturbed and fractured materials particularly prone to mass movements. The results led to the generation of an updated Landslide Inventory map pointing out to the presence of a large landslide that affect the urban areas of Nerano, Termini and Marina del Cantone (fig. 4.11).

Inside the Termini-Nerano valley the original 12 complex movements from the official Landslide Inventory Map have been combined in one active complex landslide that extends 0.32 Km^2, according to field surveys, stereoscopic and A-DInSAR analysis. The merging of the landslides has been necessary because it was not possible to access to most of the western flank portion. The main variation regards the widening of the western sector of the crown where nowadays buildings and the provincial road n.192 show signs of the negative effects of the displacements (fig. 4.1b-c).

As regards the state of activity, the landslide should be considered dormant but reactivations, involving limited portions of the whole phenomena, occur. The small extended instabilities, usually reactivated during the rainy season and involving limited parts of the 1963 landslide, have been observed and confirmed from monitoring data. The latters are globally in agreement and revealed maximum velocity <50 mm/yr in the foot area of the landslide, typical of extremely-slow and very-slow movements.

Despite the involved rates do not represent a loss of life risk, they are enough to create damage to buildings and infrastructures. The problematic scenario is also confirmed by the Landslide Susceptibility Map so suggesting, as the best cost-effective solution in order to mitigate the related susceptibility and risk, the installation of a drainage system in the Termini-Nerano valley with priority to the red areas of Figure 4.14. They act to guarantee the slope stability keeping lower the groundwater level and reducing the water content of the material after highly precipitation events.

Further work must be considered for increasing the radar targets density, a result achievable by exploiting either C- or X-bands, but above all, in the ascending geometry due to the site's morphology.

A sufficient number of A-DInSAR measurements can be eventually used in combination with the remarkable geological and geotechnical information already available to explore the slope stress-strain state and the landslide kinematic evolution by means of a Finite Element Method (FEM) modeling approach.

4.2 Bisaccia (Avellino province, Campania region, Italy)

The small town of Bisaccia is located on a conglomeratic cap, at 800 m a.s.l., whose bedrock is constituted by an over-consolidated clayey formation (fig. 4.15).

Landslides in Bisaccia area have been already studied in geomorphological and geotechnical papers (e.g. Fenelli, 1986; Fenelli and Picarelli, 1990; Di Nocera *et al*., 1995; Fiorillo *et al*., 1996; Parise and Wasowski, 1999; Picarelli *et al*., 2006). The works mainly focused on the extended slide to flow type landslides occurring in two valleys adjacent to the Bisaccia settlement, the Ferrelli valley and the Corvi valley, due to the outcrop of the clayey substratum (fig. 4.16).

The critical soil conditions had given rise to a geotechnical consolidation campaign in the 1950s consisting in eight concrete reins placed on the top of the Corvi Valley.

The geohazard framework is worsened by recurring earthquakes too as documented during historical time (1694, 1732, 1930 and 1980; Castelluccio, 2010). They have determined a low number of causalities but have always induced great damage to buildings and infrastructures. The damage pattern following the seismic events (Oddone, 1931; Fenelli *et al*., 1992) supported the hypothesis that another geohazards, a DSGSD, stroke the village and was related to the consolidation process of the clayey substratum (Picarelli, 2009), which has never been fully characterized.

In fact, soon after the 1980 Irpinia Earthquake (Amato *et al*., 1989), local authorities decided to move part of the Bisaccia inhabitants to a stable area (Piano Regolatore) one kilometer westward of Bisaccia (fig. 4.16). Other interventions included demolition of the most damaged buildings and the reinforcing of the rock slopes bordering Bisaccia.

In 1999 and 2002 the Campania region financed the installation of bioengineering control work, consisting of wood palisades, on the north-west slope of the Bisaccia hill where a landfill had previously risen.

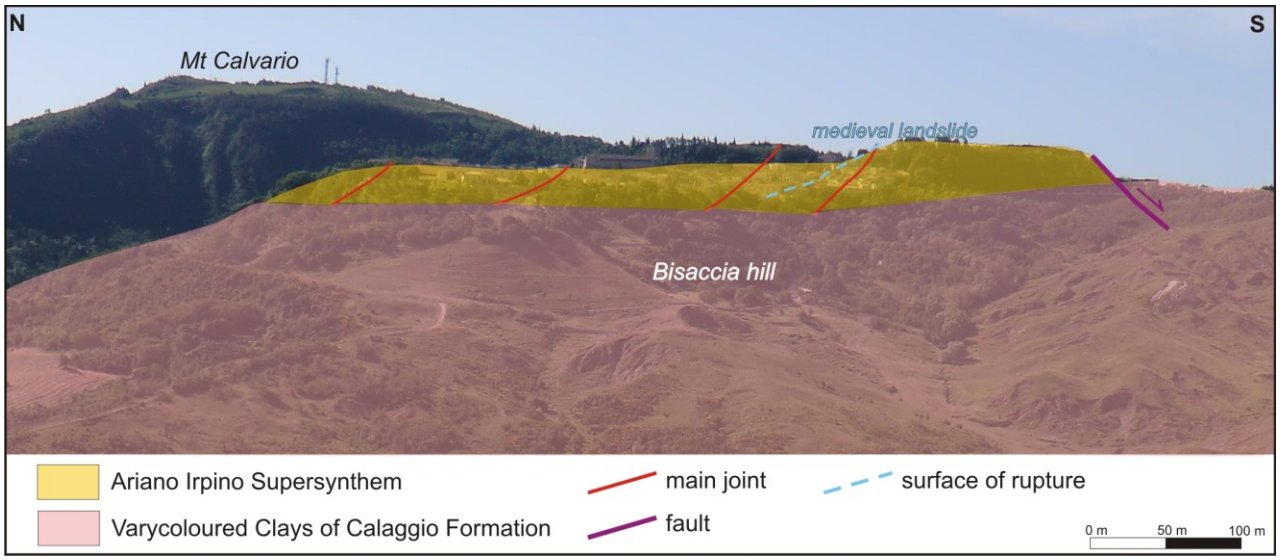

Figure 4.15 - Panoramic view of the historical town of Bisaccia, with evidence of the unconformity between the Ariano Irpino Supersynthem and the Varcioloured Clays of the Calaggio Formation (see paragraph 4.2.1 for the explanation).

4.2.1 Geological and geomorphological setting

The studied area is located on the northern side of the Ofanto river basin whose flow path developed in the Irpinia-Daunia chain sector, namely the eastern and external margin of the AMC (fig. 2.7), where the pre-orogenic sequences, belonging to the Lagonegro-Molise basin (Bonardi *et al*., 2009) are grouped in the the Vallone del Toro tectonic Unit (Pescatore *et al*., 1999).

The Vallone del Toro tectonic Unit (Middle Tortonian - Upper Messinian; Basso *et al*., 2001; 2002; Matano *et al*., 2005) is represented here by the Varicoloured Clays of Calaggio Formation (VCCF; Lower - Middle Miocene).

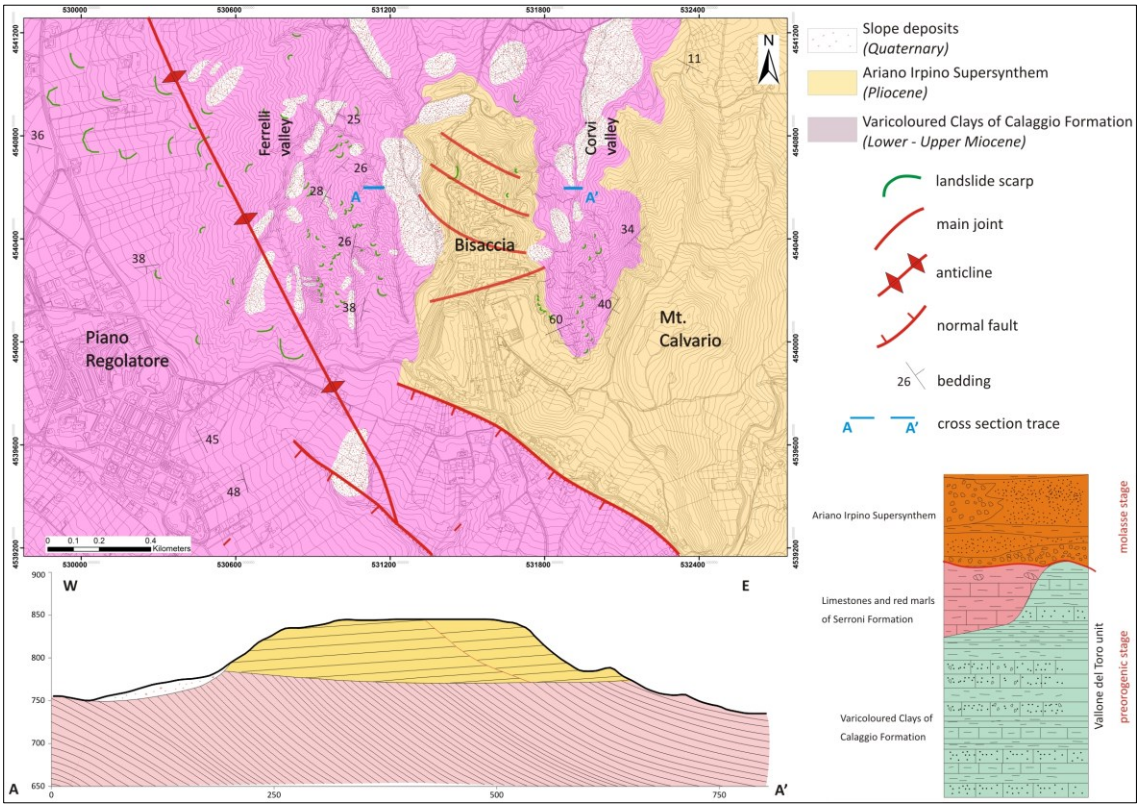

Figure 4.16 - Geological map, geological cross-section and stratigraphy of the Bisaccia area.

The VCCF (Ciaranfi *et al*., 1973) consists of a close alternation of polychromed shales and grayish turbiditic limestones in layers of decimetric thickness (fig. 4.17a). Towards the top (corresponding to the southern part of the study area) the pelitic sequence is enriched by the presence of pink marls and red calcareous marls (fig. 4.17b) and by intercalations of coarse and micaceous sandstones, for a whole thickness of about 200 m. After the VCCF deposition, the AMC orogeny generated a highly poly-deformed structure consisting of dense multi-shear surfaces especially in the clayey layers; this classifies VCCF as the B2 class of the SCF (see paragraph 2.4).

The strong influence of the mechanical properties of the VCCF resulting in the high landsliding propensity of the area, as stated by several papers that analyzed the Bisaccia slope stability after the 1980 Irpinia earthquake (e.g., Bilotta et al., 1985; Urciuoli, 1992; Maggiò and Pellegrino, 2002).

The strata dip direction is tectonically governed by two pre-Pliocenic fold sets (Casciello and Cesarano Mas., 2000): the oldest has an E-verging direction while the main and youngest one is NE-verging and

creates macro-scale reclined to recumbent folds that globally imprint a southernward dip direction (fig. 4.17).

The overlying Ariano Irpino Supersynthem (AIS) is a tectonically-controlled sedimentary terrain of the post-orogenic stage formed during Pliocene (Di Nocera *et al*., 2011), whose unconformity with the VCCF is highlighted by a gently dipping surface (<20°). The strata are made of 500 m-thick polygenic, polymictic, clast-supported and massive conglomerates (fig. 4.17c) intercalated with poorly-sorted sand, reddish-clayey and silty-clayey layers. AIS globally shows a SW dip direction and an average dip angle of 10/15° (fig. 4.16).

Quaternary deposits consist of unconsolidated and poorly-sorted detrital piles of colluvial and landslide materials concentrated into the two valleys surrounding the Bisaccia hill (fig. 4.16).

These materials derive mainly from the weathering processes of the VCCF, as demonstrated by the reddish-brownish oxidation spots and desiccation cracks (fig. 4.17d).

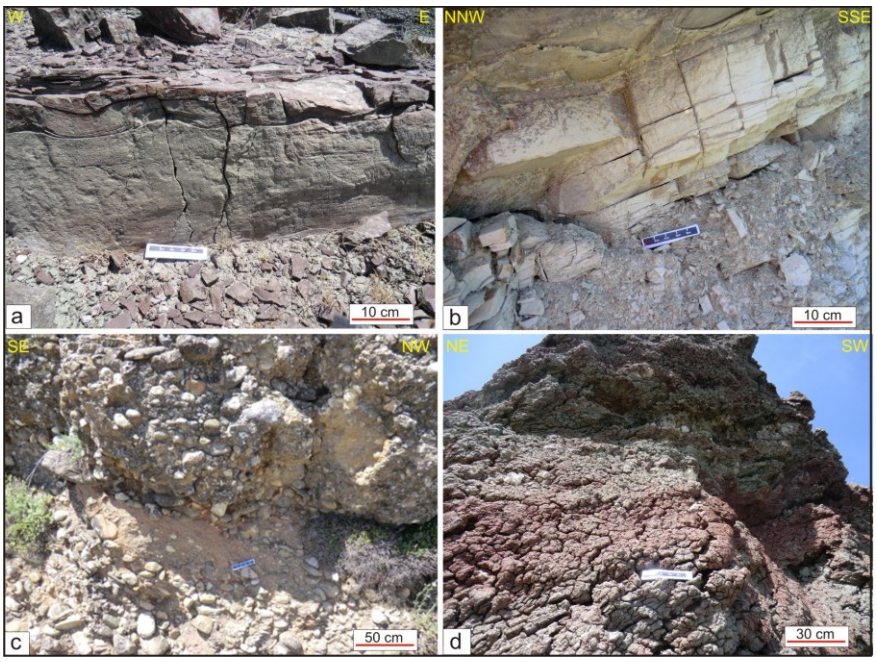

Figure 4.17 - Some examples of the main rock units cropping out in the Bisaccia area. Clay lithofacies of the VCCF (a). Marl lithofacies of the VCCF (b). Arenaceous conglomerate of the AIS (c). Effects of weathering on the VCCF in the Ferrelli valley.

The historical center of Bisaccia is located on a steep hill elongated in a N-S direction and bounded by two deep but gentle valleys, Ferrelli valley on the western side and Corvi valley on the eastern side. These valleys are truncated southwards by a set of two normal faults, NW-SE striking (fig. 4.16).

Like other planar surfaces rising in the area (e.g., Calvario, San Mauro, Santo Stefano and Formicoso), Bisaccia's hill formed during a tectonically stable period (in the Plio-Pleistocene) by fluvial erosion that slightly molded the conglomeratic sequence and concentrated in the two valleys, now located within the fine-grained rocks of the VCCF (fig. 4.16).

Despite the intense Plio-Pleistocene hydrological processes, the hydrography pattern is now absent or discontinuous; the only evidences of it are badlands and gully erosion marks of metric extension developed on the clayey outcrops.

Being controlled by the lithological, geomorphological and structural geological features, instabilities here are a common feature that directly regard the VCCF and, indirectly, the AIS.

The critical soil conditions have already been confirmed by the 'Inventario dei Fenomeni Franosi in Italia' report – IFFI (ISPRA, 2007; fig. 4.18a), which, over an area of 5.7 km^2, has classified 117 landslides, of which 38 polygonal (1 complex, 22 flows, 14 slides and 1 DSGSD). The total landsliding area is 1.3 km^2, for a Landslide Index (namely the ratio between landsliding area and the total area) of 22%, much higher if compared to the national average (8.9%; ISPRA, 2007). The remarkable propensity to instability is also underlined by an ancient rotational landslide in the heart of the Bisaccia historical center itself. This instability has given origin to a great escarpment dividing the urban settlement into two portions placed at different heights, and tilted the local thirteenth-century tower (fig. 4.15 and fig. 4.26e).

Following the geological survey carried out during the present study, the updated Landslide Inventory Map (fig. 4.18b) has documented 101 landslides (53 active, 43 dormant and only 5 inactive) and 15 badlands for a total extension of 1.18 Km^2 (1.32 km^2 if badlands are also considered). Consequently,

the Landslide Index remains essentially unchanged. Ninety-six landslides in the new inventory are represented by flows and slides. Comparing the IFFI data with our results, there is an increase in the number of polygonal landslides, because most of the original landslides have been divided in two or more phenomena and, indeed, the mean average landslide area decreases from 0.03 Km^2 to 0.01 Km^2. In other cases, what before had been considered as a flow has now been classified as badlands.

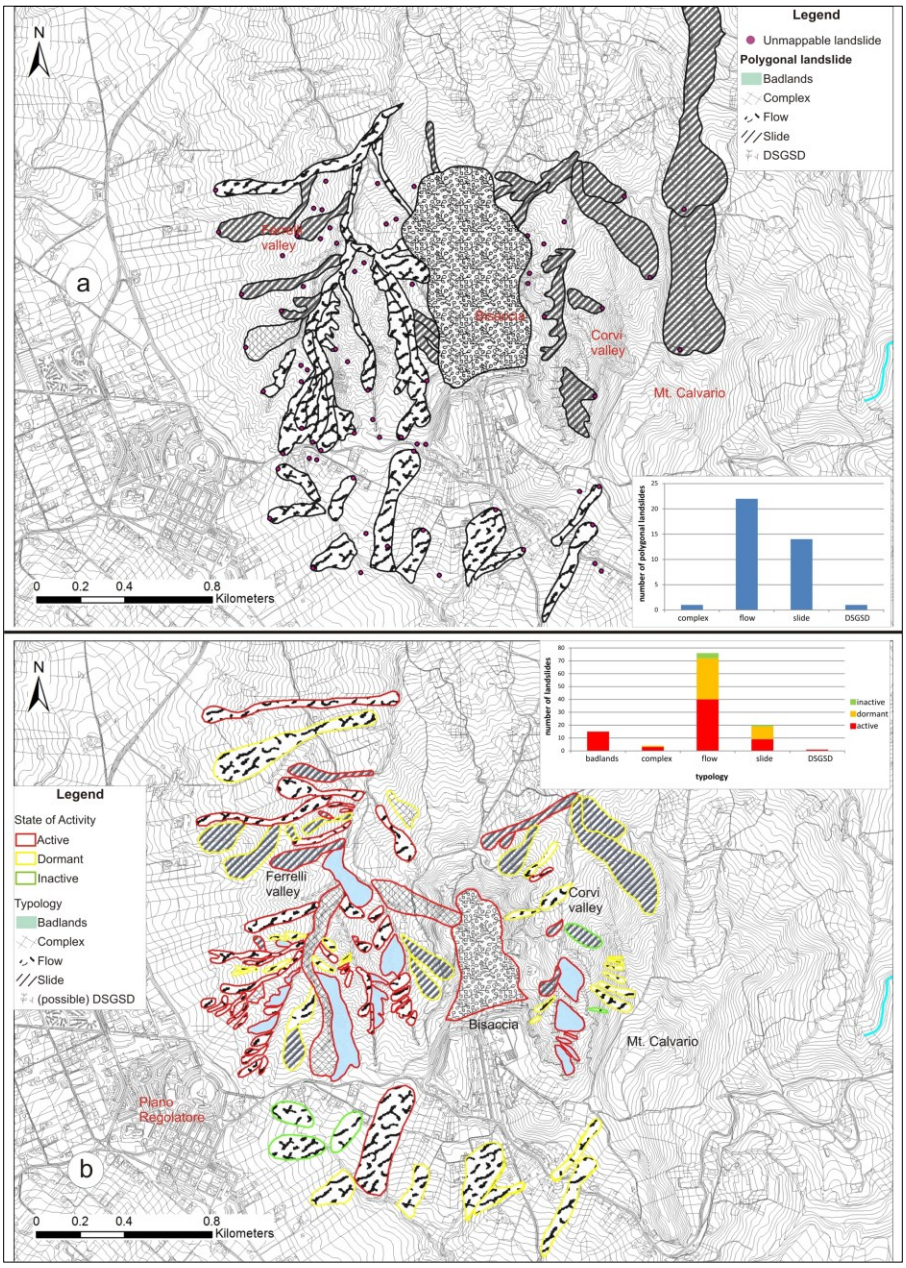

Figure 4.18 - Landslide Inventory Maps and related bar graphs for the IFFI report (a) and the present study (b).

It is worth pointing out, as shown in Figure 4.19, the higher landsliding propensity in the Ferrelli valley (74 instabilities of which 47 active) with respect to the Corvi valley (27 instabilities of which only 5 active). Thirty-eight percent of the Ferrelli valley area is unstable, while only 10% of the Corvi valley area is currently subject to landslides; a similar trend has been recognized since 1954 (fig. 4.19).

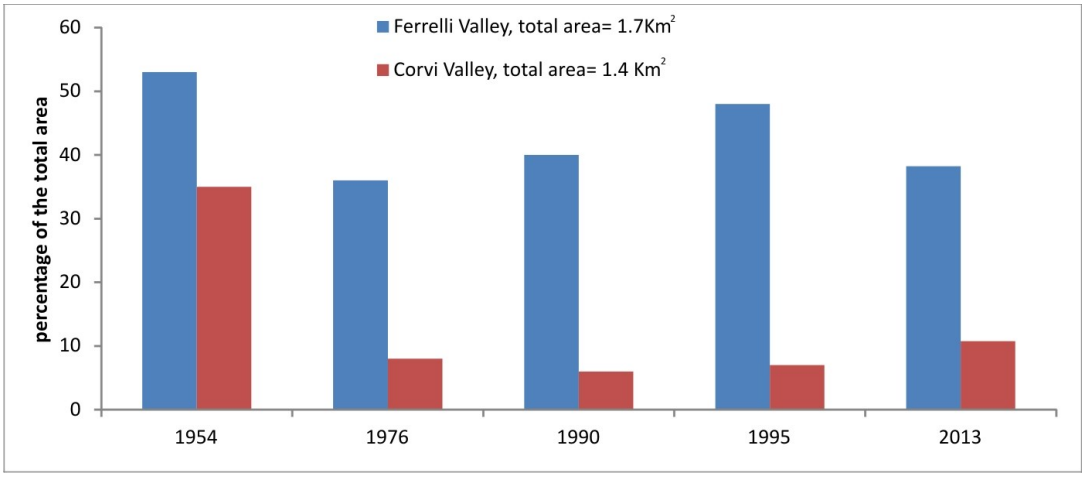

Figure 4.19 – Percentage areal extension of the active landsliding area in the Ferrelli and Corvi valleys for the period 1954-2013.Modified and updated from Parise and Wasowski (1999).

The main reason for the higher landsliding activity in the Ferrelly valley is due to the deformation observed in the VCCF of the western valley, presumably related to the proximity to the local anticline structure (fig. 4.16) and the check dams built during the mid-fifties in the Corvi valley (Parise and Wasowski, 1999). On the other hand, in the Corvi valley, the reduced landsliding area is also due to the predominance of badlands as erosional processes (fig. 4.20).

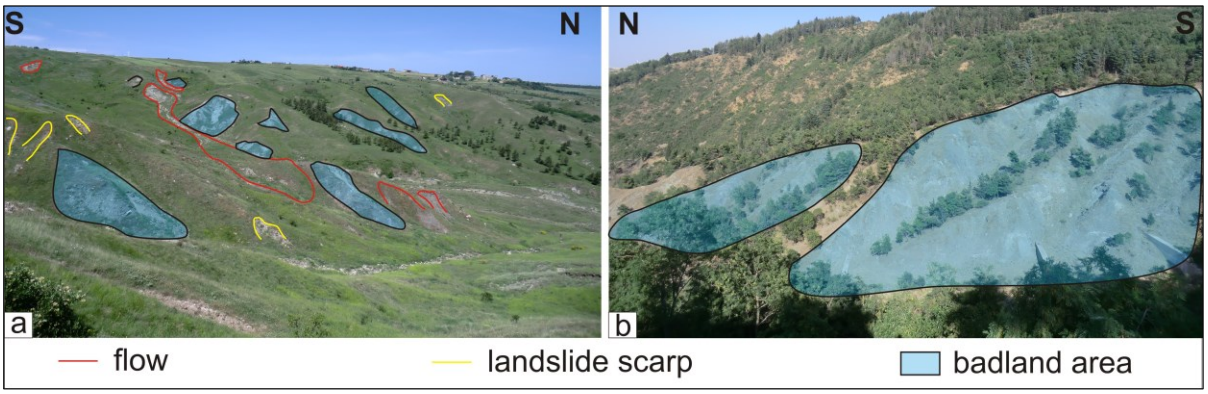

Figure 4.20 – Instabilities in the Ferrelli valley viewed from the western side of Bisaccia (a) and the Corvi valley viewed from the eastern side of Bisaccia (b).

The largest and riskiest landslide reported in the IFFI Inventory Map is the DSGSD where the Bisaccia historical center is located. The cap has an irregular rectangular shape with a sub-horizontal dip angle and rises with vertical walls on the summit of a more gentle sloping hill formed in the VCCF. It is between 80 and 115 m thick as shown by the borehole campaigns of Fenelli *et al*. (1992).

Apart from the sharply differences of the cap height in the N-S direction (fig. 4.15), no geomophological evidences (e.g. scarps, counterscarp or trenches) confirm the presence of the DSGSD because of the vegetation coverage at the bottom of the hill and the presence of buildings on the top. In order to identify and validate the DSGSD, therefore the A-DInSAR analysis of Bisaccia area has been followed by the damage map assessment of the historical center.

4.2.2 Results of the landslide investigation

4.2.2.1 A-DInSAR analysis

Due to the unavaiability of recent conventional monitoring data, the study of the Bisaccia area has taken into account only the A-DInSAR data; in particular the CPT algorithm has been chosen. Starting from the processing of the whole area, the high velocity of the events occurring within the two valleys restricted the investigation to the DSGSD phenomenon only, where the damage to buildings have been successively surveyed.

ENVISAT data have been processed for an extension of about 5 Km^2. The dataset consisted of 51 and 45 SLC images in ascending and descending frames respectively, acquired between 29/11/2002 and 30/07/2010, for the ascending dataset, and between 8/3/2003 and 19/6/2010, for the descending one. Main data processing parameters are summarized in Table 4.3.

Spatial baseline threshold	250 m
Temporal baseline threshold	211 days
Multilooking factor (azimuth x range)	15 x 4
Coherence threshold	0.4
Number of interferograms	62asc – 43desc
CPT points	513asc – 1076desc

Table 4.3– Main data processing parameters for the Bisaccia CPT dataset; asc = ascending, desc = descending.

As for Nerano, the suitability of the radar images has been verified from pre-survey suitability evaluations. Differently from the strong geometrical distorsion effects in the Termini-Nerano valley (see paragraph 4.1.2.3), the Bisaccia cap shows an inclination that never exceeds 5°, thus resulting in a good R-index map in both orbit acquisitions. Therefore layover and shadowing effects concern only the west-facing slopes in the ascending R-index map and the east-facing slopes in the descending R-index map (fig. 4.21).

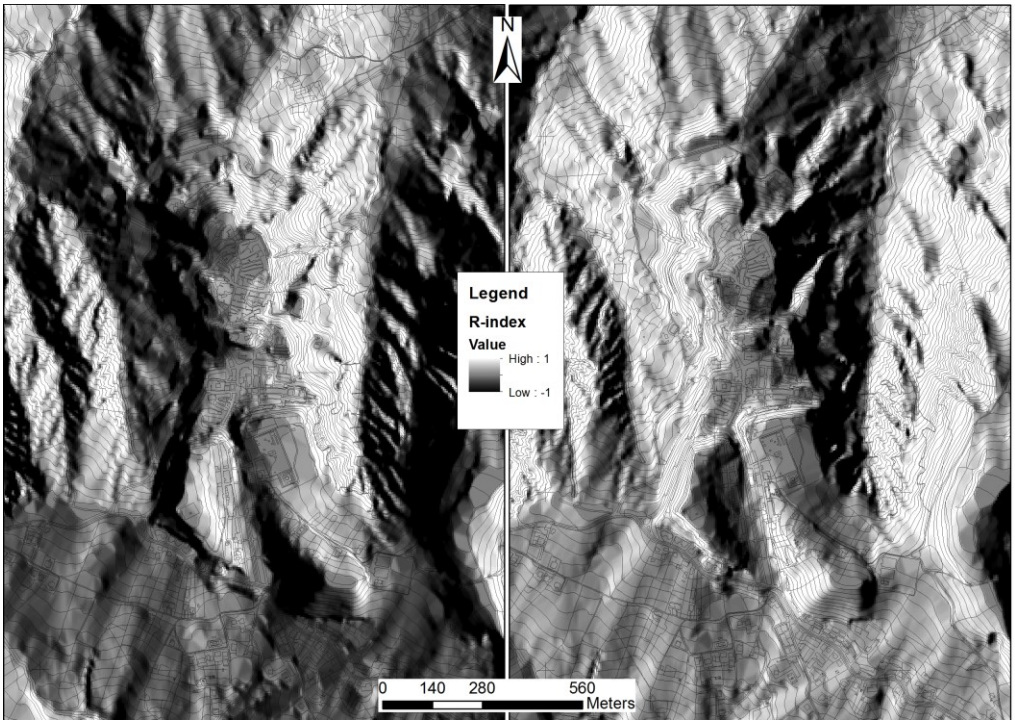

Figure 4.21 – The R-index maps for the Bisaccia cap: ascending (left) and descending (right) orbits.

Figure 4.22 shows the geocoded A-DInSAR displacement rate maps for the ascending (left side) and descending (right side) geometries. Considering both processed datasets, an average of about 70 targets/km^2 have been identified in the area under investigation.

Starting from the mean coherence values calculated by means of an estimator (ESA, 2007; Blanco, 2009), it was possible to evaluate the phase standard deviation ($\Delta\phi$) and the corresponding displacement standard deviation of ±1.5 mm/yr. With a maximum velocity of 32 mm/yr, only points with velocities higher than ±3.0 mm/yr have been considered unstable.

The Bisaccia plateau shows a motion with increasing values in displacement from the southern to the northern sector. These values are in agreement with the displacement rates reported in previous studies (Fenelli *et al*., 1992 and reference therein).

According to the velocity, five sectors, separated by four discontinuities, can be identified: A, B, C, D and E, from south to north respectively (fig. 4.22). In spite of the damage assessment (see paragraph 4.2.2.2) which recognize a fifth sector, E, the latter shows similar dispalcement rates of D and therefore they will be analyzed together.

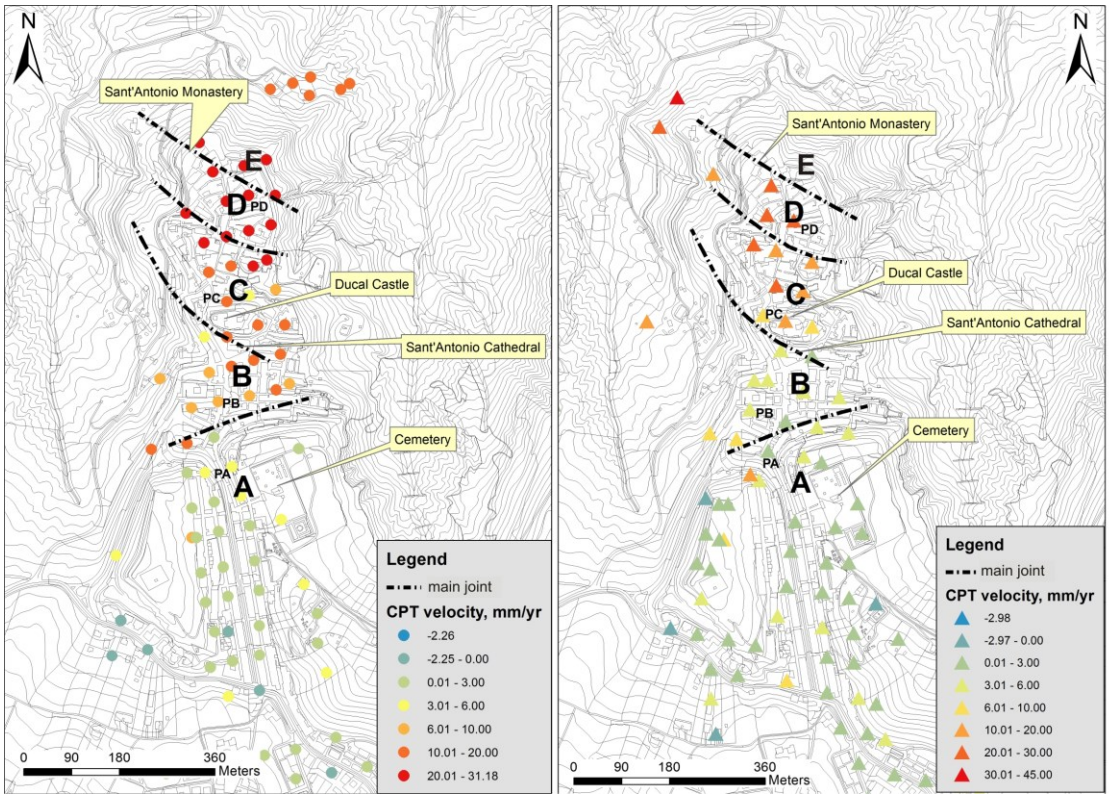

Figure 4.22- Measured displacement rates obtained from the CPT dataset: ascending (left side) and descending orbits (right side). Positive values indicate displacements away from the sensor, negative values indicate displacements towards the sensor.

The ascending and descending results show that the southernmost part (block A), centered around the cemetery area, is substantially stable, since several points show velocities lower than ±3.0 mm/yr, as confirmed by field studies.

Northwards (sector B), nearby the Sant'Antonio Cathedral, the displacement rates increase up to 9.0 mm/yr.

Sector C reaches velocities of about 15 mm/yr and near the Ducal Castle shows a subordinate rotational movement southward creating a counterslope with respect to all the other blocks.

The highest velocity values, higher than 22.0 mm/yr, are reached in sector D+E, the less extended, where in proximity of the Sant'Antonio Monastery the recorded mean velocity value, from descending orbit, is 32.0 mm/yr.

Ascending and descending equivalent targets show almost the same values because of the predominant vertical motions (Dv), whose values are calculated solving, pixel by pixel, the following formula [7] (Manzo *et al*., 2006):

$$Dv = \frac{\mathrm{Dd} * \sin\theta\mathrm{a} + \mathrm{Da} * \sin\theta\mathrm{d}}{\sin(\theta\mathrm{a} + \theta\mathrm{d})} \qquad [7]$$

Where θa and θd are the look angles for ascending and descending orbit modes respectively, while Da and Dd are the ascending and descending displacements respectively, measured along the LOS.

Globally the vertical component appears to be at least ten times greater in terms of velocity when compared to the horizontal component, with the greatest differences along the plate edges, and referred to as points PA, PB, PC, and PD of Figure 4.22. These points are characterized by the highest velocity values for each sector (Table 4.4).

	V_{asc} (mm/y)	V_{desc} (mm/y)	V_v (mm/y)	V_h (mm/y)
PA	2.6	1.7	2.3	-1.2
PB	9	2.5	6.2	-8.6
PC	12.9	15.5	15.3	3.4
PD	22.9	28.7	27.8	7.6

Table 4.4 – Results of the decomposition of ascending (Vasc) and descending (Vdesc) velocities to derive their vertical (Vv) and horizontal (Vh) components. The most representative point for each sector has been chosen, whose relative position is shown in Figure 5.24.

The block-model of Figure 4.23 illustrates the overall setting in a 3D environment. In terms of horizontal displacement, the A and B sectors show a secondary westward component, whereas the C and D sectors show a secondary eastward component.

The extension of each block of the conglomeratic cap is the following: A= 0.14 Km^2, B= 0.06 Km^2, C= 0.07 Km^2, D= 0.05 Km^2 and E= 0.06 Km^2.

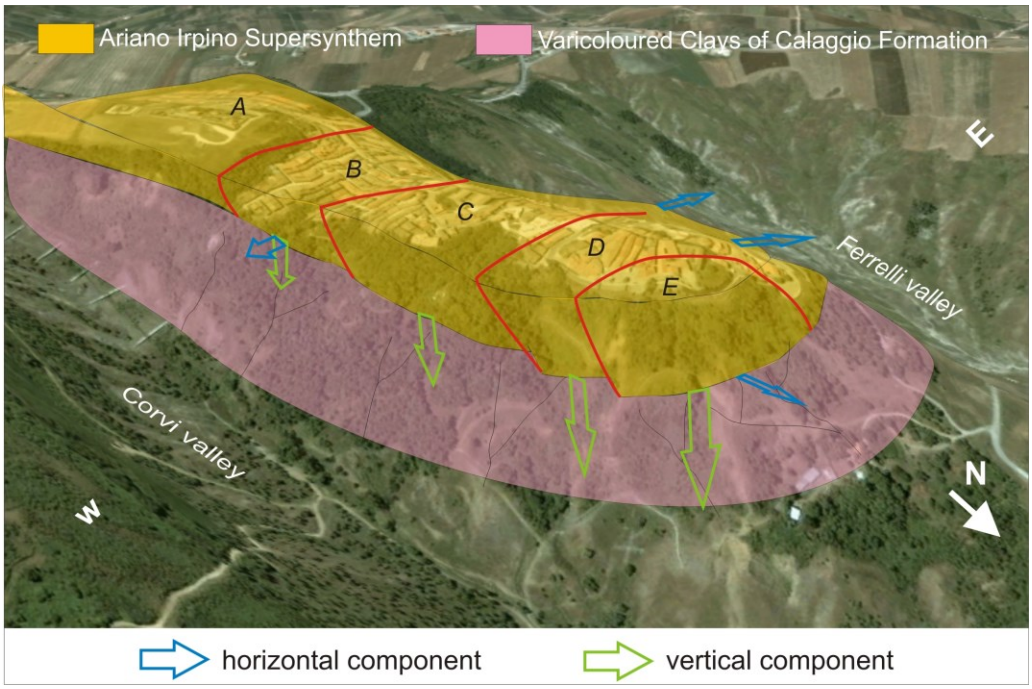

Figure 4.23 – Block-model showing the different evolution of each sector (the vertical exaggeration is 2x). Source of terrain map: Google Earth™.

Unfortunately the available ground truth data are not comparable in time; indeed they consist only of topographic measurements performed between February 1982 and October 1988 on behalf of the Universities of Ancona and Naples (Fenelli *et al*., 1992). In any case, the resulting rates match the time series deformations reported in this work and showed in Figure 4.24. In fact, they show displacement rates of the order of tens of mm/year and higher speeds towards the northern sector of the village.

The ascending and descending time-series for points displayed in Table 4.3 lack an abrupt or sudden accelerations. The trend excludes any correlation with the rainfall data, even if the latter are aggregated over different temporal resolutions (fig. 4.24).

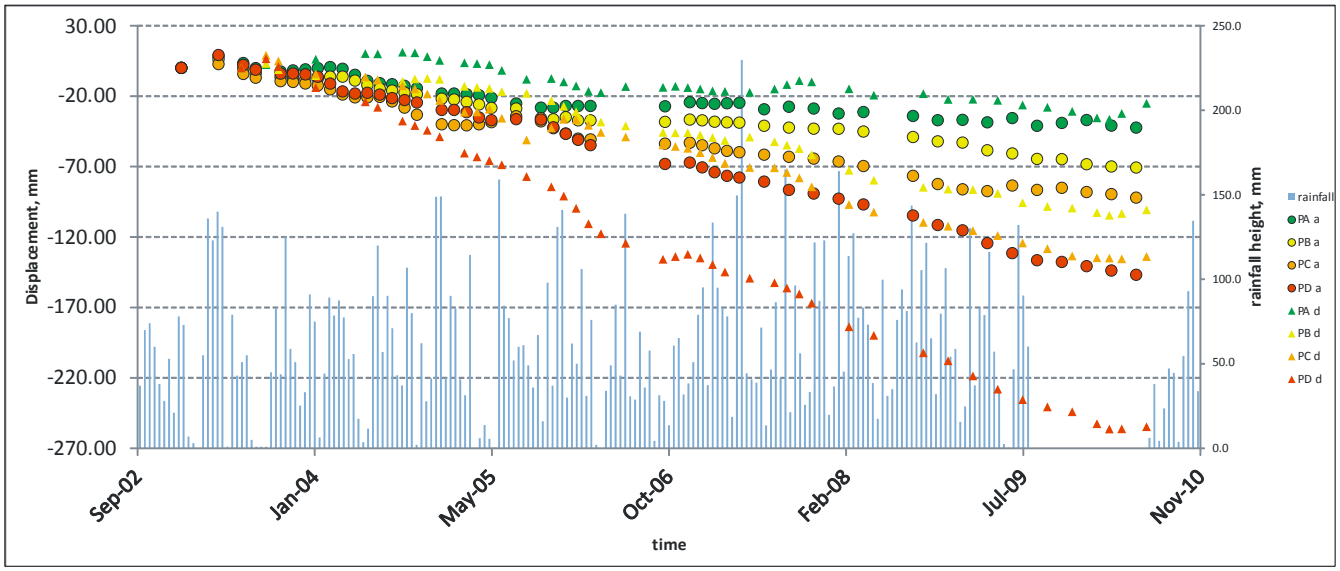

Figure 4.24 - Time series data for points belonging to the four different sectors: ascending time series are indicated as circles and descending time series as triangles. Their location is shown in Figure 4.22. Rainfall data, coming from the Bisaccia rain gauge station, have been acquired from the Regional Agency for Environmental Protection of Puglia.

These displacements are particularly evident in the sector D, which also experiences a digging-up effect more evident on the western side where a landslide undergoes a retrogressive evolution (fig. 4.18b).

4.2.2.2 Damage assessment in the urban area

Due to the already mentioned lack of conventional monitoring data, the reliability of A-DInSAR data has been verified through a specific building damage assessment procedure (Bardi *et al*., 2014), also aimed at finding indirect evidence related to the hypotesis of a DSGSD.

The building damage assessment consists in identifying any type of damage (such as fractures and/or collapses) that rocks, concrete housing and infrastructures could have suffered as a consequence of the gravity phenomenon (Cooper, 2008), as described by Chiocchio *et al*. (1997; Table 4.5). However an accurate interpretation of the urban damage is very complex and, in order to attribute it to a precise cause, very detailed information on the urban setting are required. In fact, other causes, such as bad foundation, heterogeneity of the terrain and different kind of building materials, could be

superimposed, making very difficult to find a direct correlation between the observed damage and the mass movements. In this case, the damage of buildings built or restored after the 1980 Irpinia Earthquake have been considered only (fig. 4.25a).

	stiffness	**differential settlement**
Class 0 - none damage	0	0
Class 1 - negligible damage	<2.5 ‰*H	<3 ‰*L
Class 2 - light damage	2.5 ‰*H	3 ‰*L
Class 3 - moderate damage	4 ‰*H	4/5 ‰*L
Class 4 - serious damage	8 ‰*H	7 ‰*L
Class 5 - very serious damage	>10 ‰*H	>10 ‰*L
Class 6 - partial collapse	-	-
Class 7 - total collapse	-	-

Table 4.5- Indicative values of structural deformation. H is the height of the building, L is the distance between two points or between two adjacent pillars that experienced differential settlement (from Chiocchio et al.*, 1997).*

The A-DInSAR data identified a locally stable portion (sector A), corresponding to the southernmost slab of the village where houses, streets and the cemetery were substantially undamaged, generally corresponding to class 1-negligible damage. A-DInSAR data also identified a middle area, encompassing blocks B and C, where the satellite revealed a velocity range between 9.0 mm/year up to 15 mm/year, with buildings showing ground evidence of instability, such as centimetric fractures on building walls (i.e. the Medieval castle) and also some doors or windows which are misaligned with the main structure (fig. 4.25b). The damage corresponds to class 2 (light damage) and class 3 (moderate damage) of Chiocchio *et al*.. Blocks B and C are almost impossible to discriminate nowadays from field evidence alone, because of the high urban density coverage (fig. 4.26c-e). Finally in the northern sector D and E some houses have become unusable whereas other ones require still today a partial or a complete reconstruction, reaching class 5 (very serious damage) or 6 (partial collapse) of Chiocchio *et al*.. In addition, numerous cracks have been detected on the recently paved roads (fig. 4.26f).

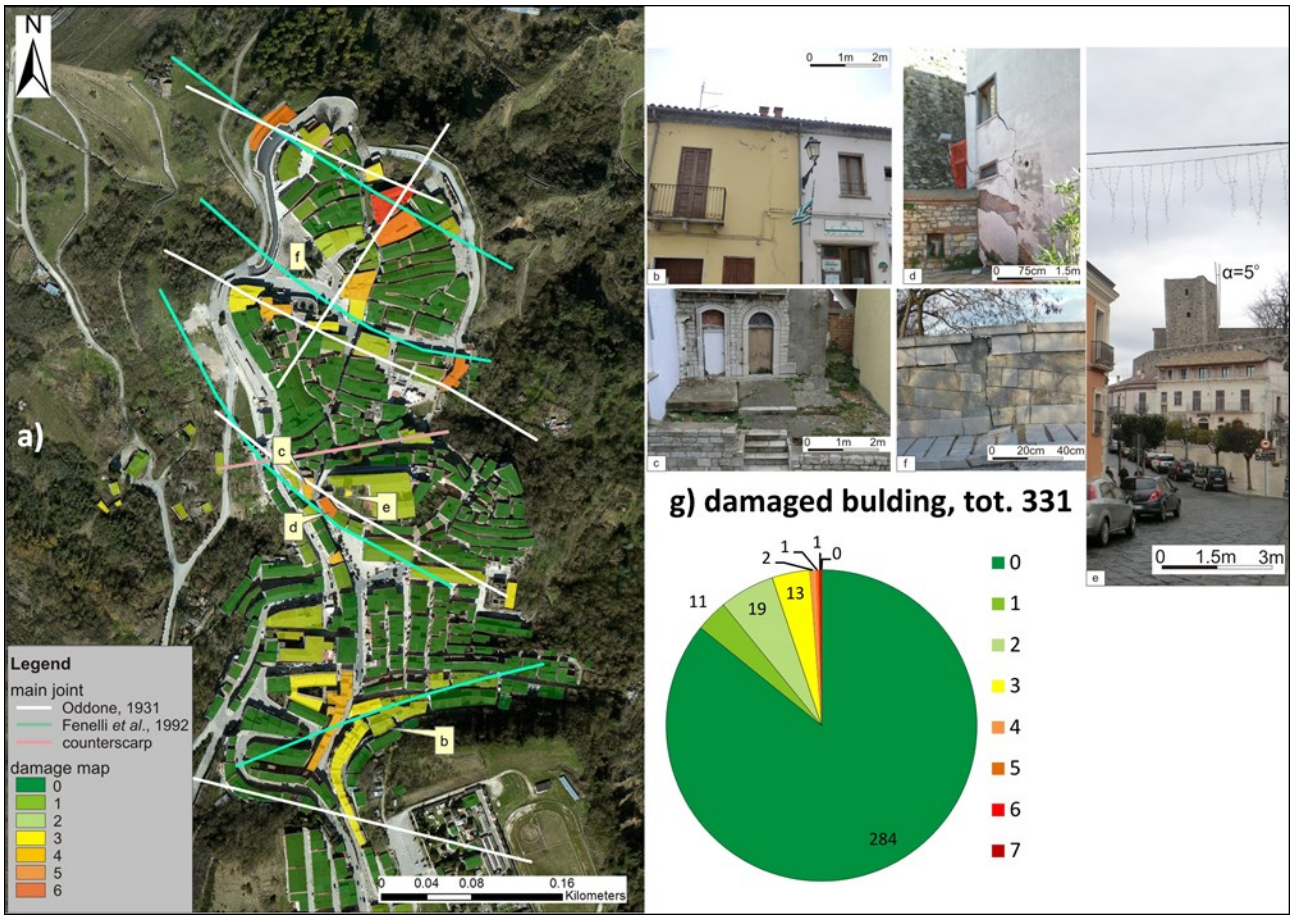

Figure 4.25 – Damage map according to Chiocchio et al.*(1997) classification and main lineaments dislocating the conglomerate slab on which Old Bisaccia rests, as reported by Oddone (1931) and Fenelli* et al*. (1992) (a). Bearing wall of class 1 (b). Street pavement of class 4 (c). Building of class 5 (d). The tilting of the 13th century tower in block C, class 3 (e). Stonewall, class 3 (f). Pie chart showing the frequency of buildings with different degrees of damage (g).*

Overall, only 47 of the 331 buildings of Bisaccia show the effect of the DSGSD (fig. 4.25f), but most of these are located close to or in correspondence to the sector edges. Furthermore it is here worth to highlight that results deriving from the damage assessment, on one hand, and from A-DInSAR analysis, on the other hand, are in agreement.

Fenelli *et al*. (1992) have already focused on the damage affecting Bisaccia and, despite the relevant temporal gap with Oddone (1931), both studies highlighted a very similar fracturing distribution in the conglomeratic slab. The pattern described in those studies globally resembles what is observed nowadays by field surveys and reported in Figure 4.25.

4.2.3 Landslide Susceptibility Map

In the Bisaccia area, the WoE has considered the following layers: lithology, slope, aspect, land use, flow accumulation and fault/fold distance. The geomorphology, such as slope and aspect, was calculated from a 5 x 5 m DEM. The geomorphic type was extracted from the soil database from CORINE land Cover map (EEA, 2007).

The CPT velocity has not been considered in the WoE calculation, because of the bias related to the absence of radar targets in the valleys.

The resulting map reveals the highest susceptibility in the Ferrelli valley, this is principally due to the lithology (VCCF, W_i^+=-0.43 and W_i^-=0.47) and land use (grazing-land, W_i^+=0.65 and W_i^-=-0.07) factors while the Corvi valley displays a slightly lower susceptibility because of the remedial works and the different land use (broad-leaved terrain, W_i^+=-0.44 and W_i^-=0.15). On the other hand, Bisaccia hill represents a very low susceptibility area with low susceptibility occurring at the transition between the sectors where the morphological jumps occur (fig. 4.26). The normal faults do not reduced the bulk-rock strength as much as the anticline along the Ferrelli valley, this explains the very low susceptibility in the southern sector of Figure 4.26.

Figure 4.26 - The WoE map for the Bisaccia area.

The investigation in Bisaccia area starts for landslide study at a watershed scale and turns out to focus on the DSGSD only. The analysis confirms an active DSGSD of rock spreading in the brittle formation (fig. 2.3b) where the conglomeratic cap, belonging to the AIS, overlies the clayey and ductile formation, belonging to the VCCF.

The DSGSD consists of in five blocks characterized by increasing velocities from south to north, likely inversely proportional to the different AIS thickness for each sector. They are separated each other by steep but small escarpments, as recognized from the geomorphological surveys. This trend is finally confirmed from the building damage map.

The relatively slow displacement rates of the DSGSD are explained with the very low consolidation coefficient of the clayish terrain which continuously inhibits pore pressure dissipation, in spite of the rapid erosion occurring on the hill slope. Such a velocity difference also explain the higher susceptibility in the valleys compared to the Bisaccia hill. Furthermore, for the VCCF, the slow dissipation of the positive pore-water pressure and consequent compression (long-term effect) is associated and accelerated with shock loading stages (short-term effect) due to the high seismicity of the area that statistically have a recurrence time ranging between thirty and fifty years (Fenelli *et al*., 1992; Picarelli *et al*., 2006 and references therein). In conclusion, a detailed geotechnical investigation of the Bisaccia historical center is required because additional boreholes should improve understanding on the spatial variability of the VCCF-AIS contact, whether the DSGSD evolution shall end in a catastrophic collapse or not.

SAR missions with shorter revisiting time (see Table 3.1) can be crucial to extend the interferometric analysis to the Bisaccia surroundings, affected by rapid movements. Otherwise the Pixel Offset (PO) tracking procedures of the SAR images are an alternative to SAR interferometry when the latter is limited by loss of coherence for the rapid motions and the large acquisition time intervals between the two SAR images (Strozzi *et al*., 2002).

4.3 Costa della Gaveta (Potenza province, Basilicata region, Italy)

The case-study is located along the valley of the Basento river, in a site called Costa della Gaveta, 3 Km east of Potenza.

The slope is historically affected by instability problems (Vassallo *et al*., 2014 and reference therein) and in order to study its evolution, the local public administration (on behalf of the Basilicata Region, the Basilicata Civil Protection, the Italian rail network and the Italian motorways network) provided financial support for geotechnical investigations from 2004 until 2012 (Di Maio *et al*., 2010; Calcaterra S. *et al*., 2012; Vassallo *et al*., 2013). Additionally, the Italian Geological Survey also installed a network of permanent and non-permanent GPS stations. The adopted controlling system makes Costa della Gaveta as one of the best monitored slopes in southern Italy, consisting of: twenty-six inclinometers, twelve piezometers, six GPS permanent stations and ten GPS non-permanent stations (fig. 4.27).

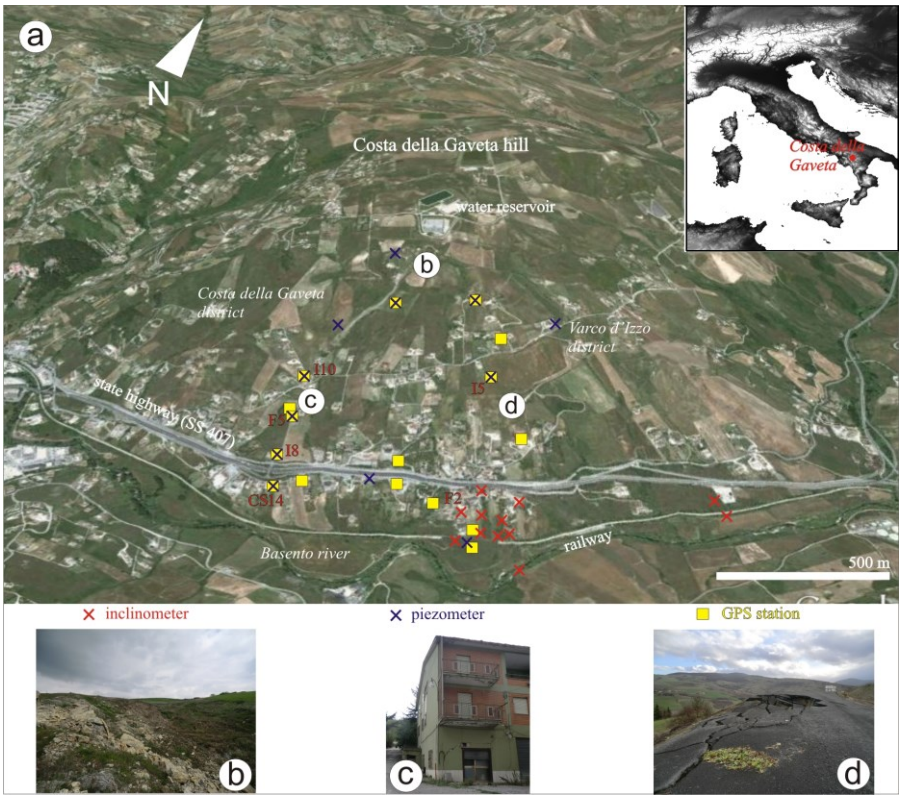

Figure 4.27 – 3D sketch of Costa della Gaveta hill, with location of inclinometers, piezometers and GPS stations (a). A landslide's crown area (b); fracture in a concrete wall(c); a damaged pavement road (d).

4.3.1 Geological and geomorphological setting

Costa della Gaveta hill is located in the Lagonegro-Molise basin sector of the AMC (fig. 2.7), here represented (Pescatore *et al*., 1988) by the pre-orogenic deposits of the Corleto Perticara Formation (CP; Upper Eocene - Lower Miocene; Mattioni *et al*., 2006) and the Varicoloured Clays Unit (VCU; Upper Cretaceous - Lower Miocene; Mattioni *et al*., 2006), together with the thrust-top deposit of the Ariano Irpino Supersynthem (AIS; Middle-Upper Pliocene; Longhitano, 2008) (fig. 4.28).

The VCU consists of ~350 m of red-green intensely tectonized shales with lenses of siliceous calcilutites, slightly argillaceous limestones, sandstones and siltstones. Towards the top of the hill, the abundance of calcilutitic and calcarenitic fractions increases (fig. 4.28a-b).

The VCU boundary with the overlying unit, the Corleto Perticara Formation, is represented by a gradual lateral and vertical transition. This 200 m thick succession, includes alternations of calcareous marls, marly limestones and calcarenites distributed in metric levels with a lower amount of brown-red clays (fig. 4.28c).

The Ariano Irpino Supersynthem is a ~1200 m-thick succession, represented by clayey and sandy conglomerate sequences (fig. 4.28d). After the VCU deposition, the area was subject to two main tectonic events: a NE-verging compressive deformation recorded by a pair of open anticline-syncline folds in the pre-orogenic sequence (fig. 4.29), followed by a NE-SW oriented extensional regime represented by normal- and strike–slip faults which are particularly evident in the VCU strata (fig. 4.30).

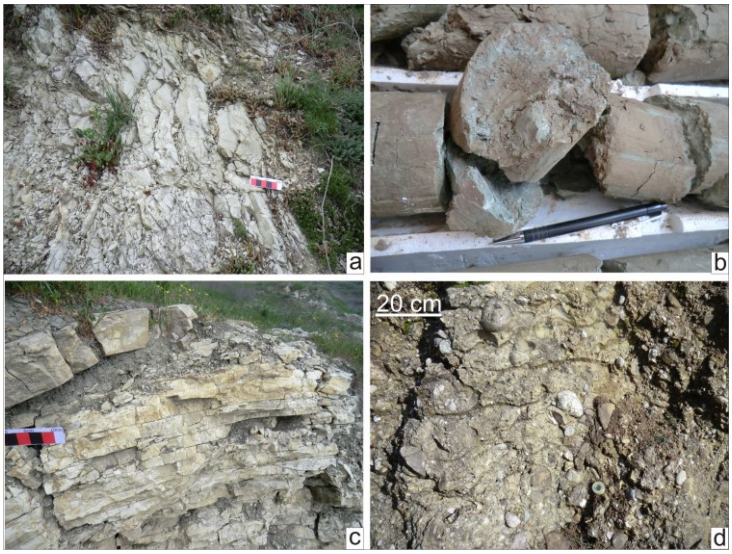

Figure 4.28 - Some examples of main rock units outcropping in the Costa della Gaveta area. Marl intervals of the AVU (a). Mesofabric of the unweathered clay portion of the AVU (b). Marly limestones of the Corleto Perticara Formation (c). Sandy conglomerate sequence of the Ariano Irpino Supersynthem (d).

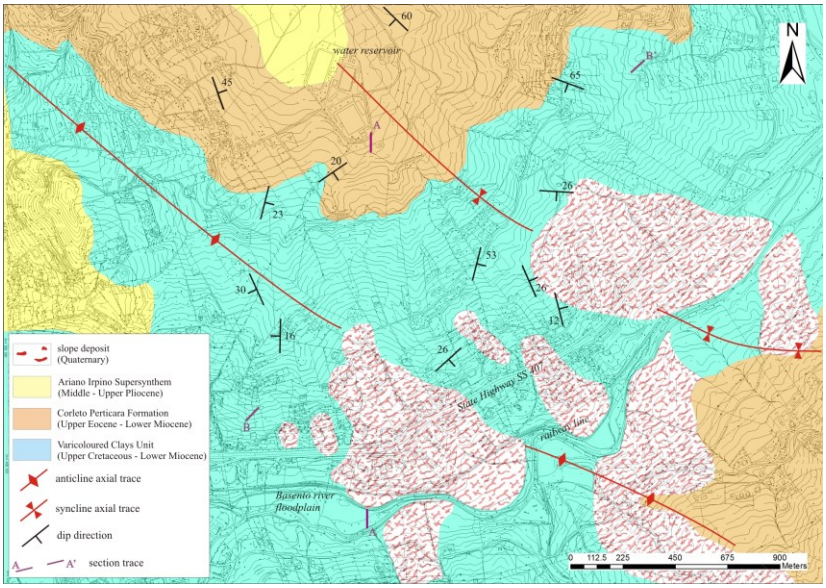

Figure 4.29 - Geological map of the Costa della Gaveta hill.

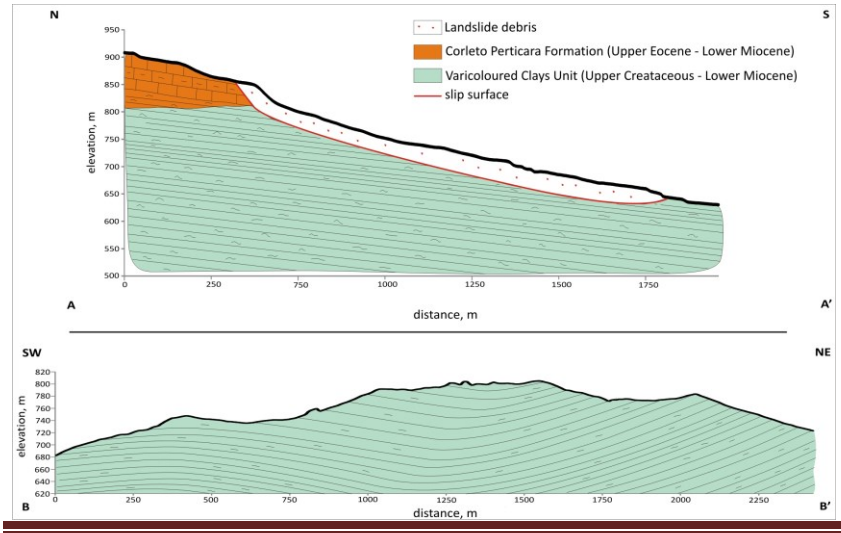

Figure 4.30 – N-S (above) and SW-NE (below) oriented geological cross-sections of the Costa della Gaveta slope.

Landslide inventory has been carried out by several authors (Perrone *et al*., 2004; Colangelo *et al*., 2006; Calcaterra S. *et al*., 2012; Di Maio *et al*., 2012), with resulting maps showing relevant differences for the corresponding study area (fig. 4.32).

The diverging versions can be explained with the geomorphological evolution of the phenomena and the acquisition of new data from monitoring campaigns. In the latest version, dating back to 2012, most of the Costa della Gaveta hill has been reported as affected by active landslides (fig. 4.31).

Figure 4.31 – The different boundaries (sky-blue line) of the active landslides in the Costa della Gaveta area, as reported by: Perrone et al*. (2004) (a); Colangelo* et al*. (2006) (b); Vassallo and Di Maio (2006) (c); Calcaterra S.* et al*. (2012) (d); Di Maio* et al*., (2012) (e).*

4.3.2 Results of the landslide investigation

4.3.2.1 Aerial photo interpretation

The geological-geomorphological landslide mapping has been supported by aerial photos interpretation of three frames acquired from the Italian Military Geographic Institute. The photos, dating back to 2003, have a flight height of 4800 m and a map scale of 1:31000.

As a result, 16 landslides have been recognized, as showed in Figure 4.33 and listed in Table 4.5. The landslides on the Costa della Gaveta slope start from an elevation between 820 m and 760 m a.s.l. along the southeast sector of the hill, whose slope angle is 8°. The length of the landslides varies between 200 m (landslide n.11) and 1500 m (landslide n.16). When they approach the Basento river valley, have caused severe damage to the local highway and railway tracks, which, in turn, have contributed to restrain a possible advancing distribution of activity towards the bottom of the valley for landslides n.10, n.14 and n.15.

Of the sixteen landslides, only the largest (n.10, n.13, n.14, n.15 and n.16; Table 4.6) can be considered active. Landslides n.3 and n.4 are dormant phenomena near the road leading to the water reservoir; these were unmentioned in the previous landslide inventory maps but have been detected from field evidences (fig. 4.32).

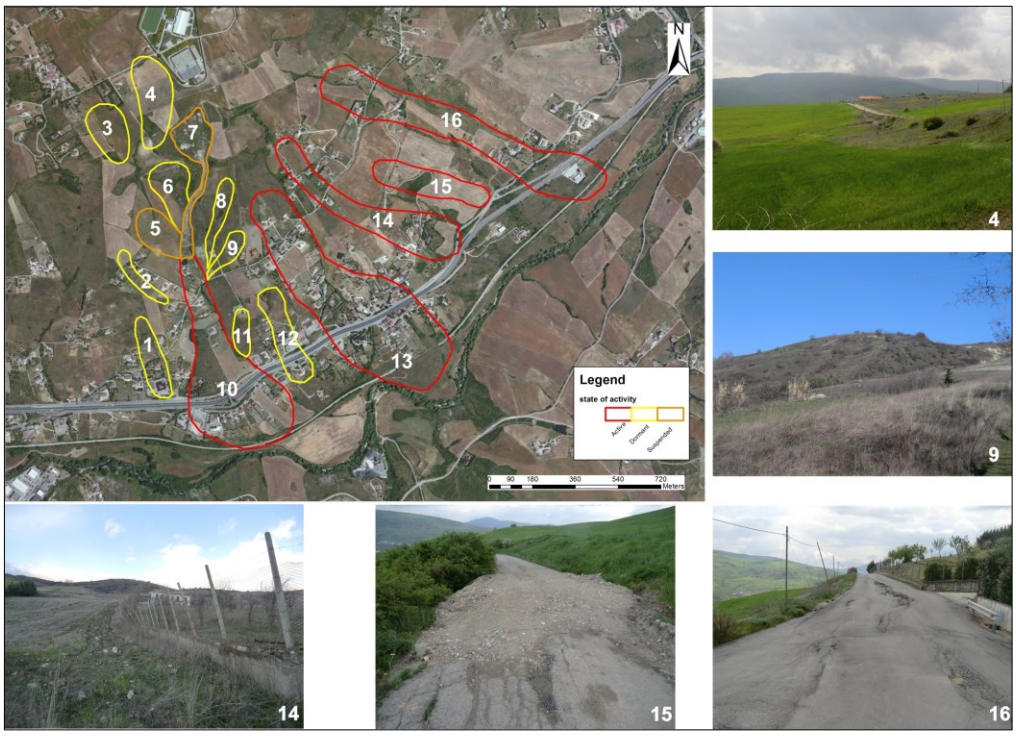

Figure 4.32 - The updated Landslide Inventory Map of the Costa della Gaveta area and the corresponding damage.

Globally, 90% of the 1.08 Km^2 landsliding area occurs in the AVU. The whole landsliding area corresponds to 45% of the investigated area.

number	typology	state of activity	distribution of activity	style of activity	area, Km^2	unit involved
1	flow	dormant	-	single	0.028	AVU
2	flow	dormant	advancing	single	0.012	AVU
3	slide	dormant	enlarging	single	0.031	CP
4	slide	dormant	retrogressive	single	0.047	CP
5	slide	suspended	moving	single	0.026	AVU
6	slide	dormant	-	single	0.03	AVU
7	slide + flow	suspended	retrogressive	complex	0.038	CP+AVU
8	flow	dormant	moving	single	0.018	AVU
9	flow	dormant	moving	single	0.012	AVU
10	flow	active	diminishing	complex	0.184	AVU
11	slide	dormant	flow	single	0.011	AVU
12	flow	dormant	-	single	0.038	AVU
13	slide + flow	active	diminishing	complex	0.278	AVU
14	slide + flow	active	retrogressive	complex	0.103	AVU
15	flow	active	retrogressive	multiple	0.048	AVU
16	slide + flow	active	retrogressive	complex	0.181	AVU

Table 4.6 – Main parameters of Costa della Gaveta landslides.

A pervasive extensional jointing affects the AVU with a NW-SE preferential pattern as shown in Figure 4.34. This structures determines the path of hydrographic network and of the largest landslides (fig. 4.33).

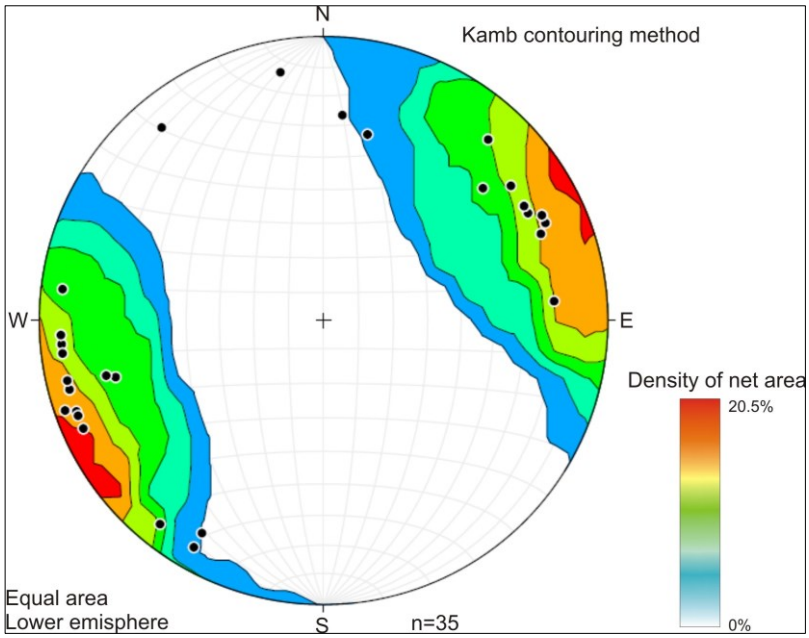

Figure 4.33 - Equal-area lower hemisphere plane to pole projection (Ramsay, 1967) of the extensional jointing in Costa della Gaveta, σ3 is NE-SW oriented.

4.3.2.2 A-DInSAR analysis

For Costa della Gaveta, displacements analysis involved the use of satellite and ground-based SAR. The satellite stack included: 24 ascending ENVISAT images (from 24/6/2003 to 27/7/2010) and 43 ascending COSMO-SkyMed images (from September 2010 to November 2011) processed with the CPT technique and 29 ascending TerraSAR-X images (from February 2010 to April 2011) processed with both the CPT and ISBAS technique. The results are indicated as follows: ENVISAT CPT, CSK CPT, TSX CPT and TSX ISBAS, respectively.

The visibility (see paragraph 3.2), namely the measurable percentage of horizontal movement along the slope, was determined following Plank *et al*. (2012); it assumed an evident role in the Costa della Gaveta because of the dip direction and dip angle of the studied slope.

From the CPT processing of ENVISAT data with a coherence threshold of 0.4, 60 interferograms and a total of 1080 points with a density of 216 points/Km^2 have been generated (Di Martire and Ramondini, 2012). Most of these are focused at the foot of the slope where the SS407 State Highway and the railway line tracks are located. The only stable area corresponds to the water reservoir in the northern sector. Landslides n.10, n.13 and n.14 are the only ones displaying a sufficient number of moving targets. The other landslides either do not have CPT points (n.3, n.4 and n.15) because of their N-S orientation, or are motionless, namely with velocities ranging between ±1.5 mm/yr (fig. 4.34).

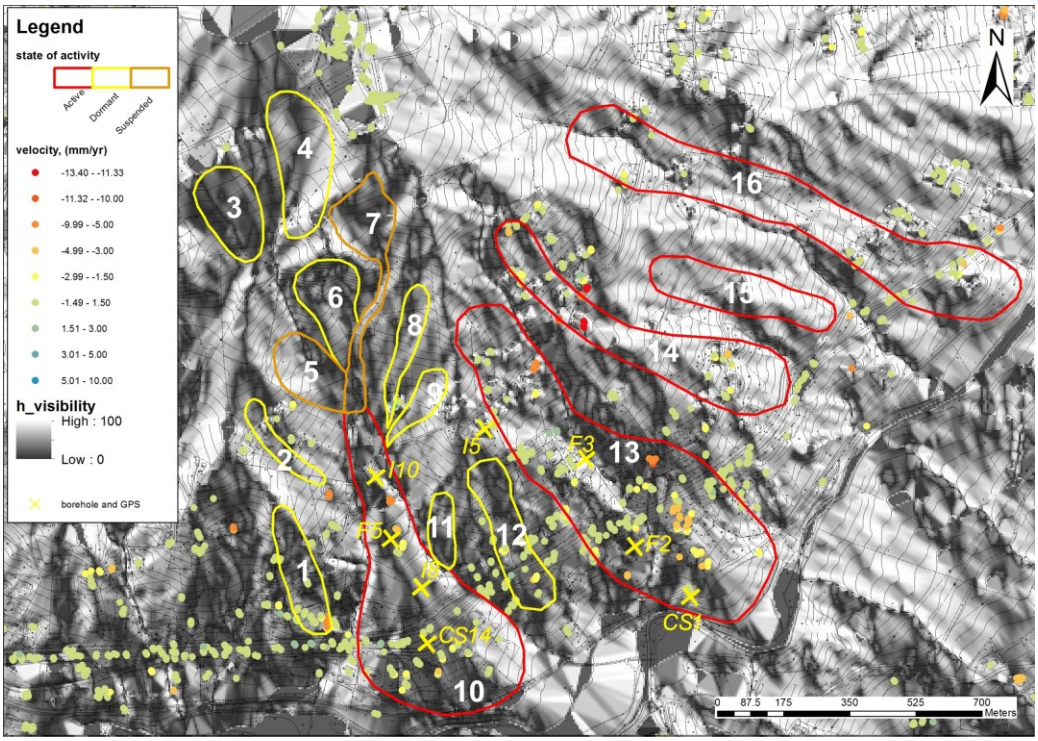

Figure 4.34 –ENVISAT CPT results: positive values indicate displacements away from the sensor, negative values indicate displacements towards the sensor. The background map represents the percentage of measurability of the horizontal movement.

The ENVISAT time series have been compared to the available ground truth data which overlap in time (Calcaterra S. *et al*., 2012). Considering the percentage of the horizontal visibility of the area, the background of Figure 4.35, the A-DInSAR results match the conventional measurements. On average, 30% of the ground displacements values have been detected by radar (Table 4.7).

ENVISAT CPT

ID	ground velocity	visibility %	A-DInSAR velocity
F2	13 mm/yr	20	3.7 mm/yr
F3	100 mm/yr	12	10 mm/yr
F5	18 mm/yr	30	4.7 mm/yr
I5	13 mm/yr	38	3.7 mm/yr
I8	9.8 mm/yr	40	12.5 mm/yr
I10	36 mm/yr	15	5.6 mm/yr
CS1	8.4 mm/yr	20	3.4 mm/yr
CS14	7.2 mm/yr	55	5.7 mm/yr

Table 4.7 – Comparison between ground truth data and CPT measurements. Location of the ground truth data is in Figure 4.33.

Adopting a coherence threshold of 0.7 on 406 interferograms produced by applying a spatial baseline of 500 m and a temporal baseline of 2 years, the CSK and the TSX datasets generated 2564 and 2586 points, respectively (Di Martire *et al*., 2013). The corresponding target density exceeds 500/Km^2 and this allowed to acquire new information for landslides n.10, n.13, n.14 and n.16 (figs. 4.35-4.36).

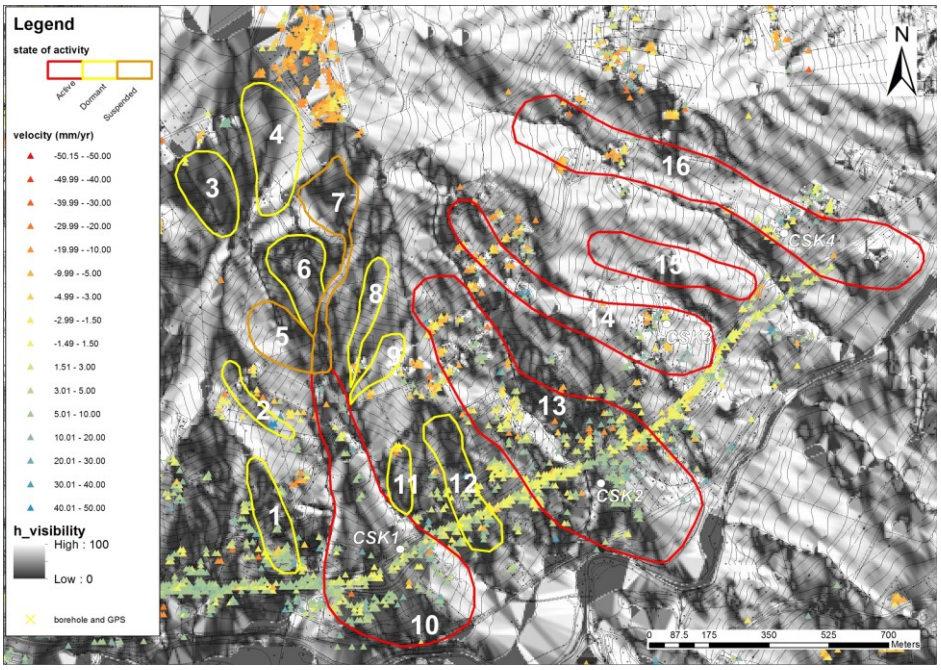

Figure 4.35 – CSK CPT results: positive values indicate displacements away from the sensor, negative values indicate displacements towards the sensor. The background map represents the percentage of measurability of the horizontal movement. (Modified from Novellino et al.*, 2015).*

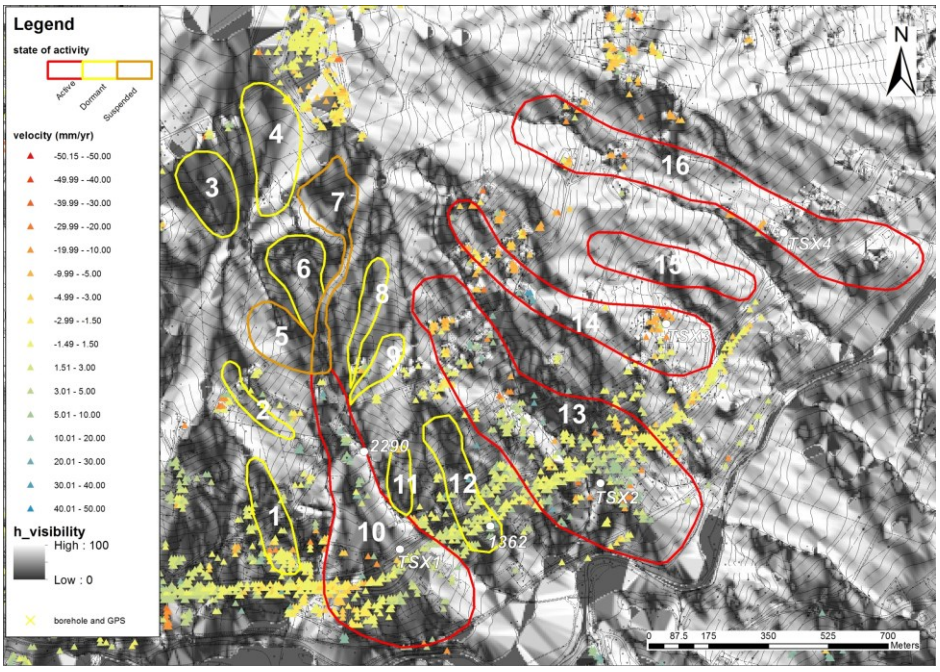

Figure 4.36 – TSX CPT results: positive values indicate displacements away from the sensor, negative values indicate displacements towards the sensor. The background map represents the percentage of measurability of the horizontal movement. (Modified from Novellino et al.*, 2015).*

CSK CPT-, TSX CPT- and TSX ISBAS-derived data are very similar and show a retrogressive evolution for landslides n.4 and n.7, more evident with the CSK data, which show movements involving also the water reservoir; the latter results to be stable in the ENVISAT and TSX data processing (fig. 4.34 and fig. 4.36).

On the other hand, the SS407 State Highway has an evident effect on the kinematics of landslides n.10 and n.13, generating an inflation effect above the road and a deflation effect beneath it.

This effect is more evident in the ISBAS-derived A-A' cross-sections where a jump of 6 mm/yr in the LOS velocities is recorded above and below the road, which results in a decreasing of the downward movements (fig. 4.37). The main difference in CSK and TSX data is represented by the water reservoir stability conditions: in the former elaboration the reservoir appears to be moving, with a rate $\geq$10mm/yr, while in the latter it appears to be stable as confirmed by field surveys and ISBAS results. The disagreement between CSK and TSX data can be interpreted as the beginning of a movement undetectable by the naked eye, which presumably started in April 2011, when the TSX data acquisition was no longer available.

ISBAS processing has been also considered, in order to fill gaps in radar coverage, highly evident for landslides n.3, n.4, n.5 and n.6 and the crown areas of n.15 and n.16; the parameters adopted for the processing, are listed in Table 4.8.

Spatial baseline threshold	300 m
Temporal baseline threshold	1 year
Multilooking factor (azimuth x range)	5 x 5
Coherence threshold	0.5
Number of interferograms	369
Interferograms threshold	80
SBAS points	782
ISBAS points	2751

Table 4.8 – Main data processing parameters for Costa della Gaveta ISBAS processing of TSX data.

The 550 ISBAS targets/Km^2 represent a satisfactory number of points in terms of radar coverage. Despite the ISBAS velocities upper-bound (+19.2 mm/yr) and lower-bound values are smaller (-21.5 mm/yr) than the CPT ones because of the different baselines adopted, the deformation rates look complexively similar. In fact, the most critical areas are represented by landslides n.10, n.13 and n.16.

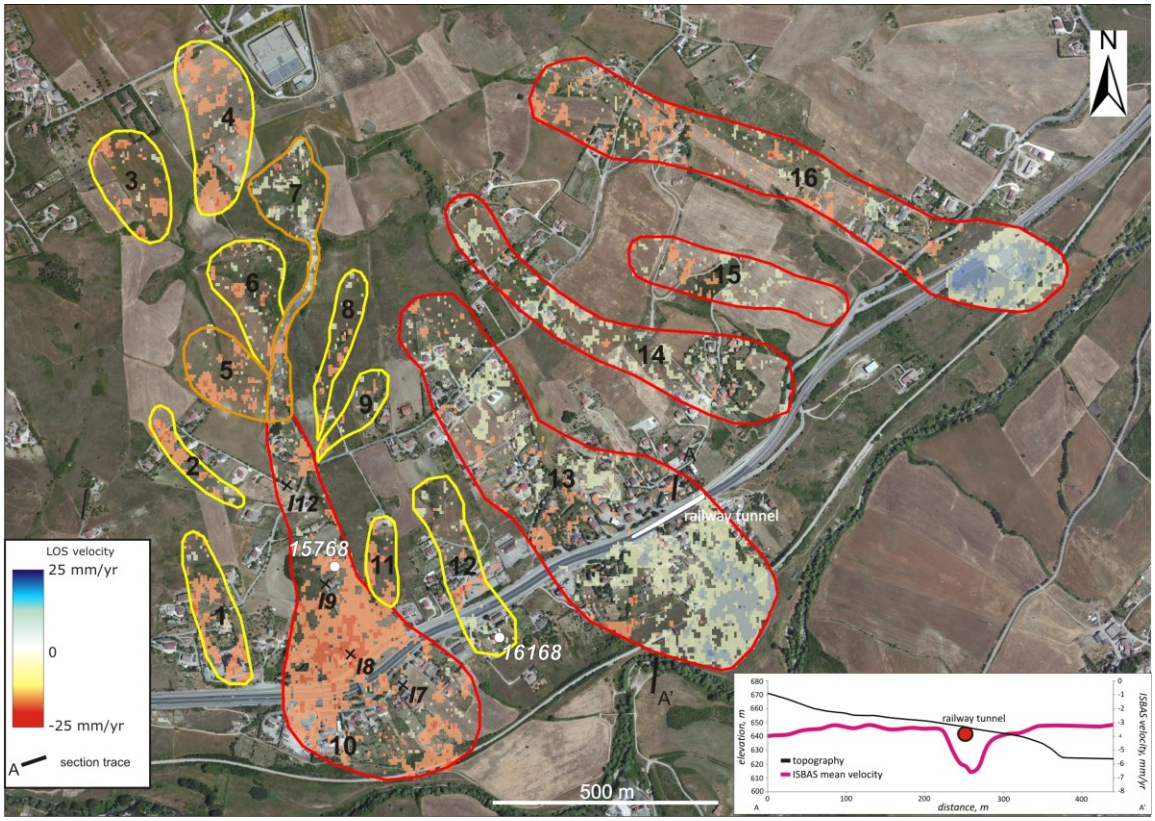

Figure 4.37 –TSX ISBAS results in raster format (10 m pixel resolution): positive values indicate displacements towards the sensor, negative values indicate displacements away from the sensor. In the inset, In the inset, profile of TSX ISBAS deformation rates along the A–A' cross section.

Figure 4.38 compares the results between the CSK CPT - TSX CPT time series (Novellino *et al*., 2015), the TSX ISBAS – TSX CPT time series and the TSX ISBAS - TSX CPT - inclinometers time series. These results have been calculated during the September 2010 - April 2011 time span only, because it is the time-slot covered by all the data.

The CSK CPT - TSX CPT time series indicate a good match for the four investigated points (fig. 4.39a). The TSX ISBAS - TSX CPT data also show a good match, with slight larger standard deviations typical of the ISBAS results (fig. 4.38b). As already observed with ENVISAT data, X-band

measurements display a small real displacement (fig. 4.38c), variable between 20% to 60% of the real displacements as showed from the percentage of measurability of the horizontal movement. These are persistently smaller than inclinometric velocities.

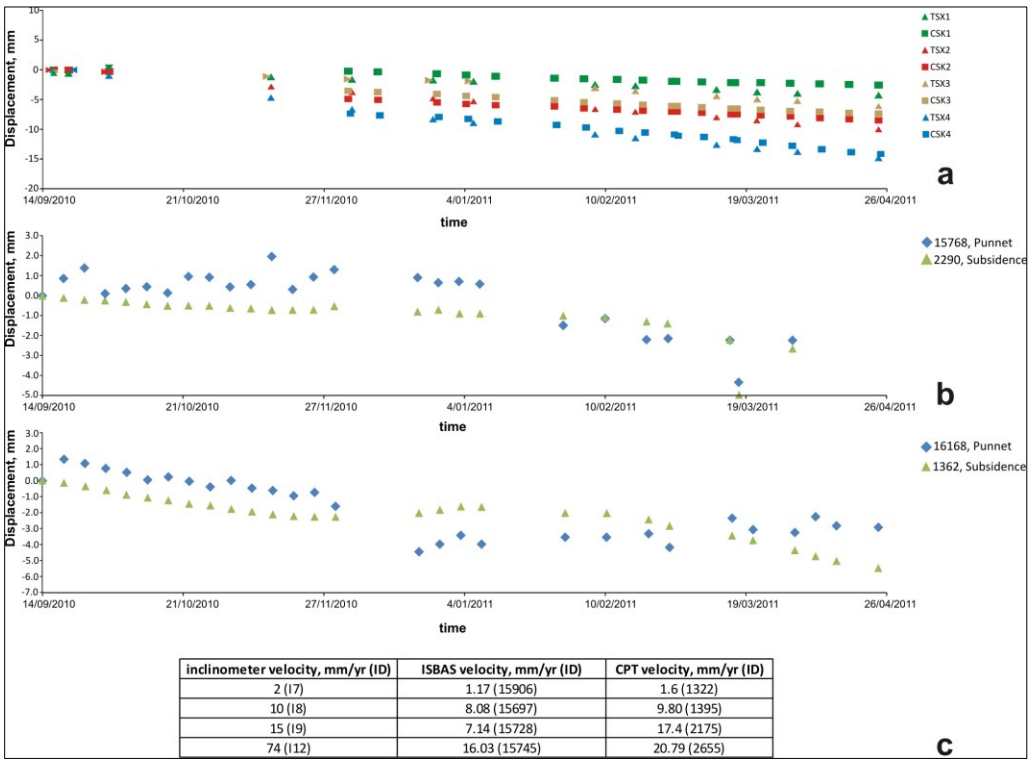

inclinometer velocity, mm/yr (ID)	ISBAS velocity, mm/yr (ID)	CPT velocity, mm/yr (ID)
2 (I7)	1.17 (15906)	1.6 (1322)
10 (I8)	8.08 (15697)	9.80 (1395)
15 (I9)	7.14 (15728)	17.4 (2175)
74 (I12)	16.03 (15745)	20.79 (2655)

Figure 4.38 – Comparison of the CSK CPT - TSX CPT time series (a). Comparison of the TSX ISBAS – TSX CPT time series (b). Comparison of the TSX ISBAS-TSX CPT-inclinometers time series (c). Inclinometric data from Di Maio et al.*, 2013. CPT signs have been inverted to simplify the comparison with ISBAS data. Point locations are indicated in Figures 4.35-4.36-4.37. Modified from Novellino* et al. *(2015).*

Bacause of the lower standard errors, the ENVISAT CPT and the TSX CPT time-series have been correlated with the potential triggering factors: earthquakes and rainfall.

The high seismicity of the area does not affect the Costa della Gaveta slope stability, despite thirty-eight earthquakes registered between 15/6/2003 and 26/4/2011 (fig. 4.39) within a radius of 19 Km from Costa della Gaveta (USGS, 2014). These seismic events were of too low magnitude, 2.6 M on average, to trigger new landslides or to reactivate dormant landslides (Keefer and Wilson, 1989) even if the peak ground deformations is estimated selecting the relationship proposed by Ausilio *et al*. (2007) for the Italian earthquakes.

According to the Potenza rain gauge station (659 m a.s.l.), whose coordinates are 40.3735 N and 15.4749 E, the ENVISAT time-series show a slight rainfall-displacement correlation, except for July 2006 and March 2009. In July 2006, the three points shown in Figure 4.40a result in displacements of almost 20mm for over 300 mm of rainfall occurred, when the average rainfall is lower than 50 mm. In March 2009, the same points result in displacements of almost 10mm for over 250 mm of rainfall occurred, when the average rainfall is lower than 80 mm (fig. 4.39).

TSX CPT data, because of the lower standard errors than the TSX ISBAS data, have been used to find a connection with precipitation data. The TSX CPT velocities are double the ENVISAT CPT velocities and the correlation with precipitation is particularly evident at the beginning of November 2010 when more than 250 mm of rainfall accumulated in less than fifteen days, compared to the 40 mm that generally characterizes the same period (Potenza rain gauge station). During this time span, the four points shown in Figure 4.40b have displacement never lower than 10 mm.

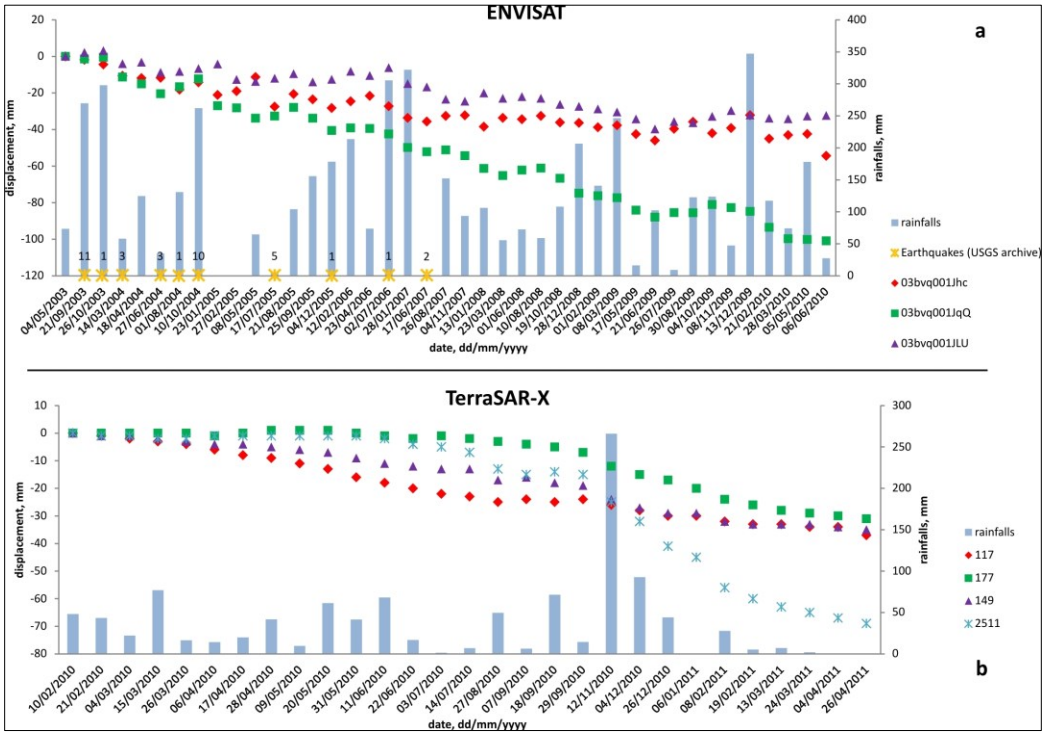

Figure 4.39 – The rainfall-displacement-earthquake correlation for ENVISAT CPT data (a) and TSX CPT data (b). In both cases rainfall precipitation have been aggregated equivalently to sensors' acquisition-time. The number of earthquakes is indicated above the corresponding star. Rainfall data derive from the Regional Environment Protection Agency of Basilicata.

A continuous GBSAR monitoring survey was conducted from December 2012 to March 2013, with a sampling rate (or revisiting time) of about five minutes over a 4 day period. The survey involved Ku-band IBIS-L SAR equipment installed in front of the Costa della Gaveta slope at a distance ranging from 700 m from the foot of the slope to 2000 m from the top of the slope (fig. 4.40a). Hundreds of SAR maps characterized by a range and cross-range resolution of approximately 0.5×0.5m were collected over the entire monitoring period. Despite the favourable positioning of the SAR system, the GBSAR measurements proved to be not reliable because the slope was affected by instability evidence during the monitoring period (fig. 4.40b).

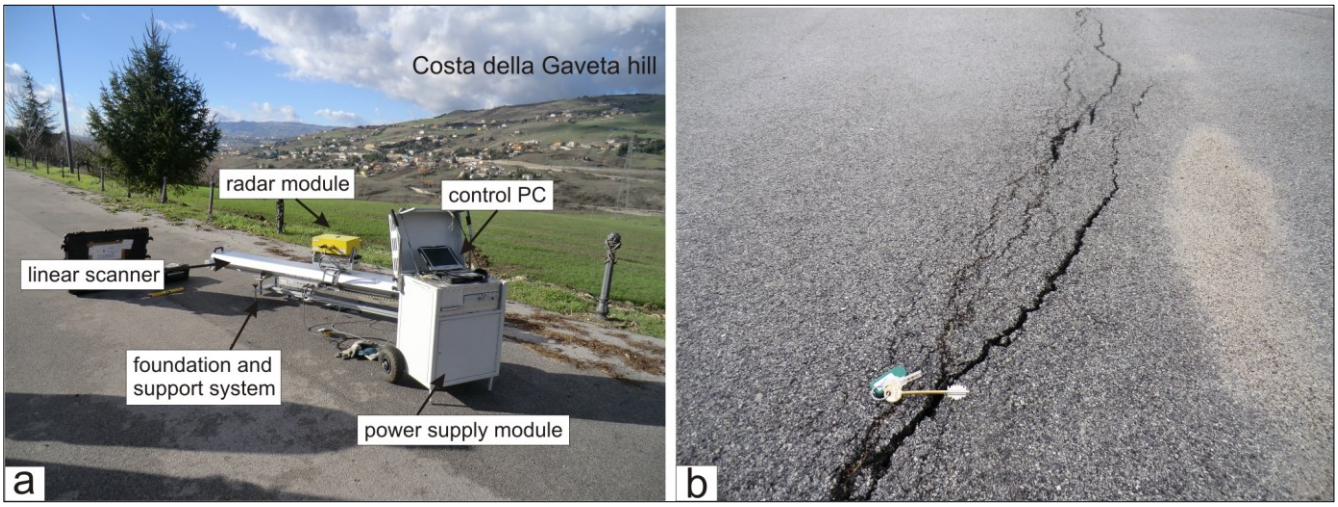

Figure 4.40 - Main components of the GBSAR system installed in front of the Costa della Gaveta slope (a); a fracture in the parking lot where the GBSAR was installed.

4.3.3 Landslide Susceptibility Map

Lithology, slope, aspect, land use, flow accumulation, road proximity, fault/fold distance and targets ISBAS velocity data have been used in the WoE analysis for the generation of the landslide susceptibility map (fig. 4.41). The geomorphology, such as slope and aspect, was calculated from a 5 x 5 m DEM. The geomorphic type was extracted from the soil database from CORINE land Cover map (EEA, 2007).

The WoE reveals how the slope aspect represent the most influential factors and, therefore, the highest susceptibility characterize all the southeastern sector of the Costa della Gaveta hill, especially where cohesionless and poorly sorted slope debris crops out (W_i^+=0.49 and W_i^-=-0.16). Only small and scattered portions of the SE-facing slope shows low- to moderate- landslide susceptibility linked with lower slope angle, while the overall susceptibility is drastically reduced on the southwest facing slopes. The northern sector is characterized by very-low level of landslide susceptibility, due to the outcropping of the Ariano Irpino Supersynthem (W_i^+=2.33 and W_i^-=-2.5). The overall susceptibility is

still high despite the physical countermeasures enacted to downgrade it during the last ten years (e.g., concrete walls).

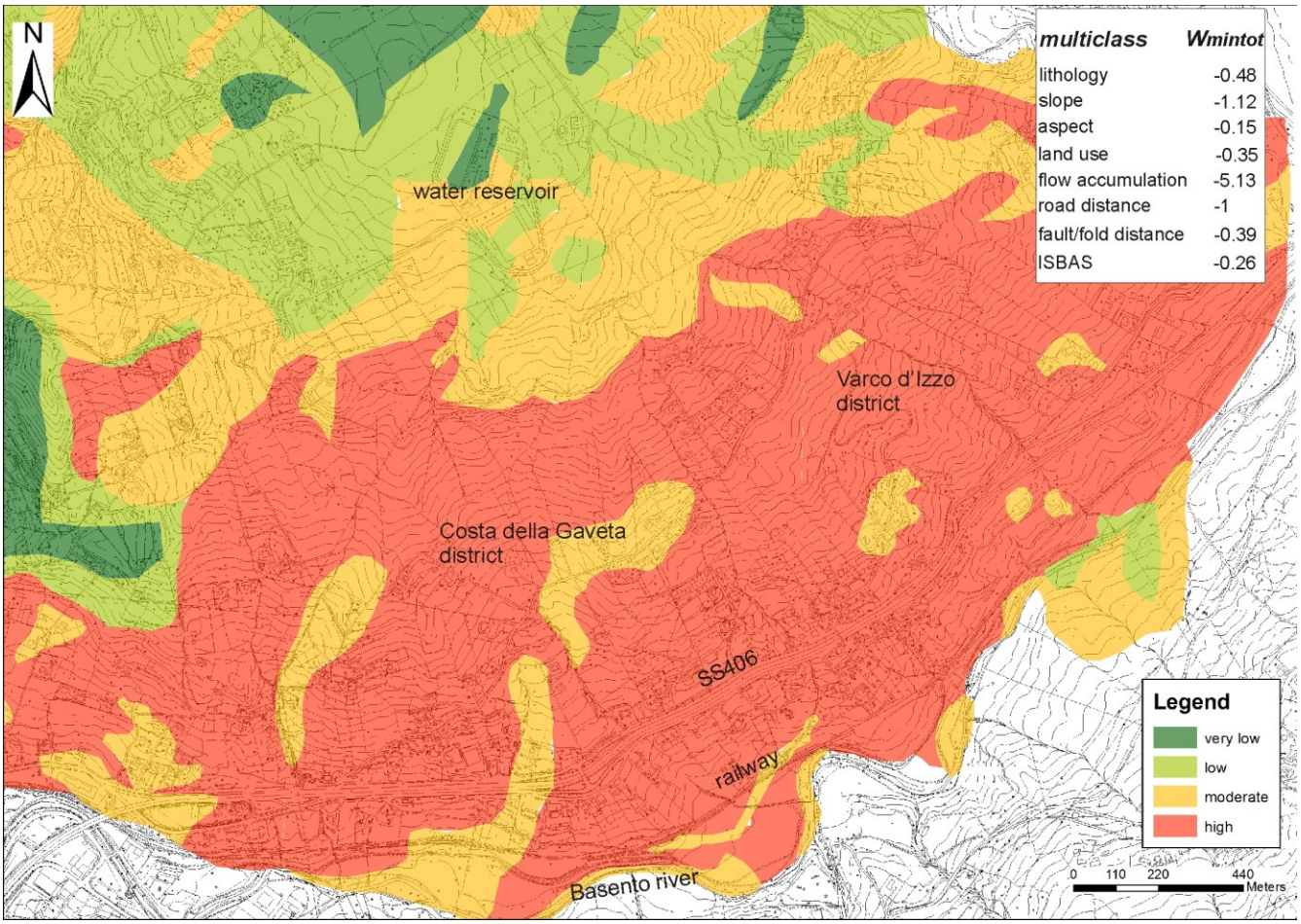

Figure 4.41 –WoE map for the Costa della Gaveta area.

A group of sixteen landslides affects the southern-facing slope of the Costa della Gaveta hill whose area amounts to 2.4 Km^2 (fig. 4.32). The group encompasses nine earth-flows, five rotational slides and two complex (rotational slides evolving into earth-flows) phenomena which, albeit slow, cause considerable damage to buildings and infrastructures, such as the State Highway n.407 (SS 407) and the Potenza-Metaponto railway line.

In particular:

- Landslides n.10, n.13, n.14 n.15 and n.16 are considered active, even if only some portions of this bodies are really moving. Particularly landslide n.10 shows higher displacement rates (>15

mm/year) in the upper portion while landslides n.13 and n.14 are faster in the foot areas. For landslide n.16, the highest displacement rates (>10 mm/year) are located near the crown accordingly to the main scarps and damage observed during the geomorphological field survey. Even if slope movements of some mm/yr have been recorded within the middle track of landslide n.10 and n.13, new houses have been built in the last years.

- Landslide n.1, n.2, n.3, n.4, n.6, n.8, n.9, n.11 and n.12 are inactive (dormant). In particular, n.3 and n.4 are shallow suspended slides with well-defined crowns and a retrogressive evolution. Landslide n.6 likely represents the crown area of the n.10 from which is separated by the material of landslide n.7.
- Landslide n.5 and n.7 are suspended.

Figure 4.40 shows that the Costa della Gaveta landslides are continuously moving and heavy rainfalls have accelerated this trend.

Even if the slope has proven to be troublesome for an adequate A-DInSAR analysis, due to the visibility condition, and unsuitable for GBSAR analysis, due to the lacking of a facing stable slope, the innovative monitoring data have deepened and extended the analysis of landslides already identified through conventional techniques and further Stripmap analysis are excluded at the moment.

On the other hand, due to the profusion of highly accurate ground truth data, is proposed the acquisition of new TSX Staring Spotlight images with a sub-metric spatial resolution (Mittermayer *et al*., 2012)

The Landslide Susceptibility Map reveals a widespread and unrecoverable high susceptibility for the Costa della Gaveta hill where, therefore, more than geotechnical operation, the most effective risk mitigation procedure is represented by legal restrictions to indirectly limit local land use or building construction practices.

4.4 Palermo province (Sicily region, Italy)

According to a study conducted by Environmental Agency System (ISPRA), in Sicily 69% of the municipalities are prone to hydraulic and/or geological risk, in accordance with the national average (68.9%) (ISPRA, 2007). In the Palermo province 716 instabilities (of the 3,657 inventoried in Sicily) have been recorded, for a total area of 68 Km^2 and a Landslide Index of 1.3%. Furthermore, the relatively high population density (255 inhabitants/Km^2) makes the Palermo province an area at high geological risk.

Differently from the three case-studies discussed previously, a large-scale landslide study has been carried out in the Palermo province, focusing on the following drainage basins: Belice, Eleuterio, Jato, Milicia, Nocella and Oreto river (fig. 4.42).

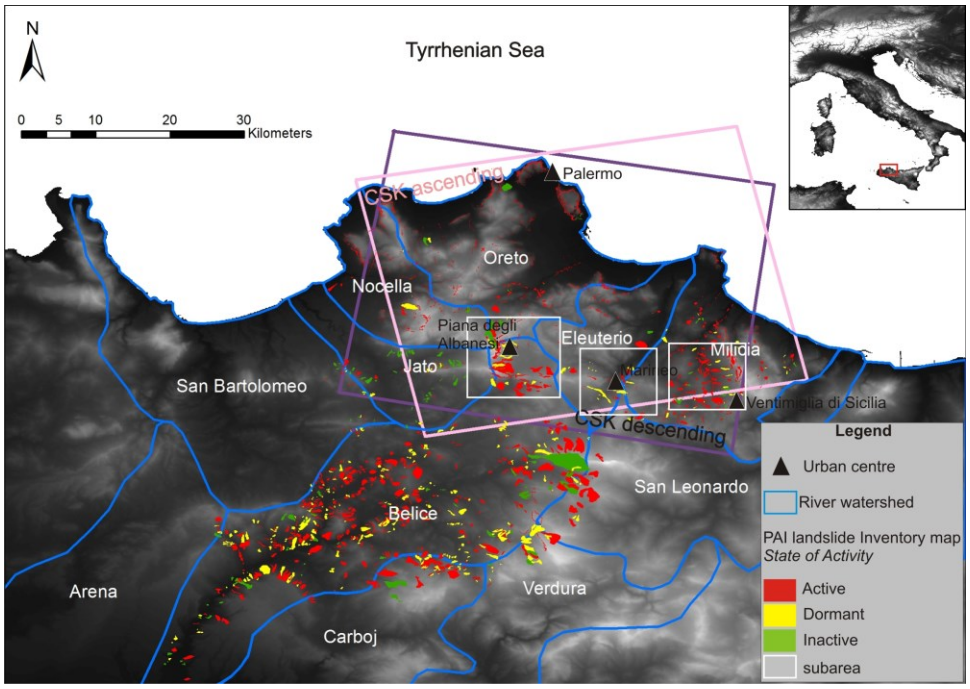

Figure 4.42 – Official Landslide Inventory Map (AdB Sicilia, 2006) and CSK footprints for northwestern Sicily.

Several ancillary data have been collected and used in supporting field surveys, these are:

- topographic maps at 1:25,000 scale, published in 1990–1994 and acquired from the Sicily Region

- Urban Atlas land cover map at 1:10,000 scale with 2.5 m spatial resolution, provided by the European Environmental Agency (EEA, 2006)
- Daily rainfall data acquired from Sicily Region and concerning Marineo, Piana degli Albanesi, Scanzano dam and San Giuseppe Jato rain gauge stations.
- Nine aerial photographs acquired from the Italian Military Geographic Institute and taken in year 2000 (Table 4.9). They have a flying height ranging from 4400 m to 5000 m and a scale of 1:29000 and 1:30000, respectively.

year	flying height, m	scale	frame
2000	5000	1:33000	3147
2000	5000	1:33000	3148
2000	5000	1:33000	3149
2000	5000	1:33000	3150
2000	4400	1:29000	768
2000	4400	1:29000	769
2000	4400	1:29000	773
2000	4400	1:29000	774
2000	4400	1:29000	775

Table 4.9 – Basic data of the aerial photographs employed in the stereoscopic interpretation.

- Hydro-geomorphological Setting Plan (HSP). The latter represents the official landslide inventory available for Sicily; the Hydro-geomorphological Setting Plan started in 2006 with additional modifications carried out until 2012. It was implemented by the Sicilian River Basin Authority (AdB Sicilia, 2006) and is essentially derived from air-photo interpretation.

The ancillary data have been used to select the most susceptible areas: Piana degli Albanesi, Marineo and Ventimiglia di Sicilia (fig. 4.42; Table 4.9), whose territory is almost completely represented by hilly or mountainous areas (with slope inclination >5°). In particular, the local morphology is controlled by the nature of the bedrock formations: carbonate reliefs related to the Panormide Unit and

Hyblean-Pelagian Domain and clayey hillslopes made of SCFs, the latter represented by the Sicilide Unit and the PSTB synorogenic deposits (fig. 2.8).

Carbonate reliefs show forms related to morphostructural evolution like scarps hundreds of meters high (>40^{o} in dipping) who represent fall-, topple- or DSGSD-prone areas.

In SCFs, the predominance of clayey dominant lithologies with poor mechanical properties due to the strong tectonic deformations experienced, from Early to Middle Miocene and from Late Miocene to Early Pliocene (Catalano R. *et al*., 2000), gives reason to the high LI and the predominance of creep, slides, flows and complex events as typical slope instabilities for the three selected subareas.

Here this kind of landslides amount to 172 of the 277 landslides detected in the HSP (Table 4.10).

area	**No. of landslides (No. of creep, slides, flows and complex events)**	**Surface extension**	**Landsliding area**	**Landslide Index (LI)**
Palermo province	716	4992 Km^2	68 Km^2	1.3 %
Piana degli Albanesi	120 (74)	90 Km^2	17.43 Km^2	20.03 %
Marineo	40 (26)	41 Km^2	2.88 Km^2	7.02 %
Ventimiglia di Sicilia	117 (72)	54 Km^2	13.45 Km^2	24.9 %

Table 4.10 – Main landsliding characteristics for each studied area (AdB Sicilia, 2006 and ISPRA, 2007).

Considering the low-seismicity of this portion of Sicily region during 2008-2011, the instabilities recorded in the three subareas have to be considered mainly triggered by seasonal precipitation, whose annual average height, referred to the 2008-2011 period, is of about 500 mm and is concentrated between October and February, with a minimum of about 5 mm during the dry season (June-September).

In conclusion, the predominance of slow-moving landslides makes the three subareas perfect targets for the A-DInSAR analysis. At the same time, fields surveys and aerial photos interpretation showed difficulties in distinguish shallow and slow forms of ground motion behavior while topographic

surveying techniques and geotechnical surveys would have been too expensive to perform on a regional scale.

4.4.1 Input SAR imagery and pre-processing

The radar data for the Palermo province consist of 74 COSMO-SkyMed Stripmap images (38 ascending and 36 descending) with 40x40 Km swath width and 3x3 m geometrical resolution. These cover the region of interest between November 2008 and October 2011, with ~40° look angle at the centre of the scene, and a nominal revisiting time of 16 days.

The ISBAS algorithm has been chosen for the A-DInSAR processing, because it increases the radar targets in non-urban areas (e.g., agricultural terrain, forests, vegetated terrain, water bodies or wetlands). Non-urban areas are extensively diffuse in the three selected sites where they represent, on average, over 60% of the surface. Consequently the absence or poor coverage of potential radar points does not allow for the use of conventional SBAS techniques. The low radar targets coverage is shown in the Target Suitability Map - TSM (fig. 4.43; Cigna *et al*., 2013).

TSM for X-band sensor shows highest predicted densities of radar targets (up to 8000 /km^2) over the urban areas of Piana degli Albanesi (fig. 4.43a), Bolognetta (fig. 4.43b) and Marineo (fig. 4.43c), while the lowest densities (< 5-20/km^2) correspond to water bodies (Piana degli Albanesi and Scanzano lakes).

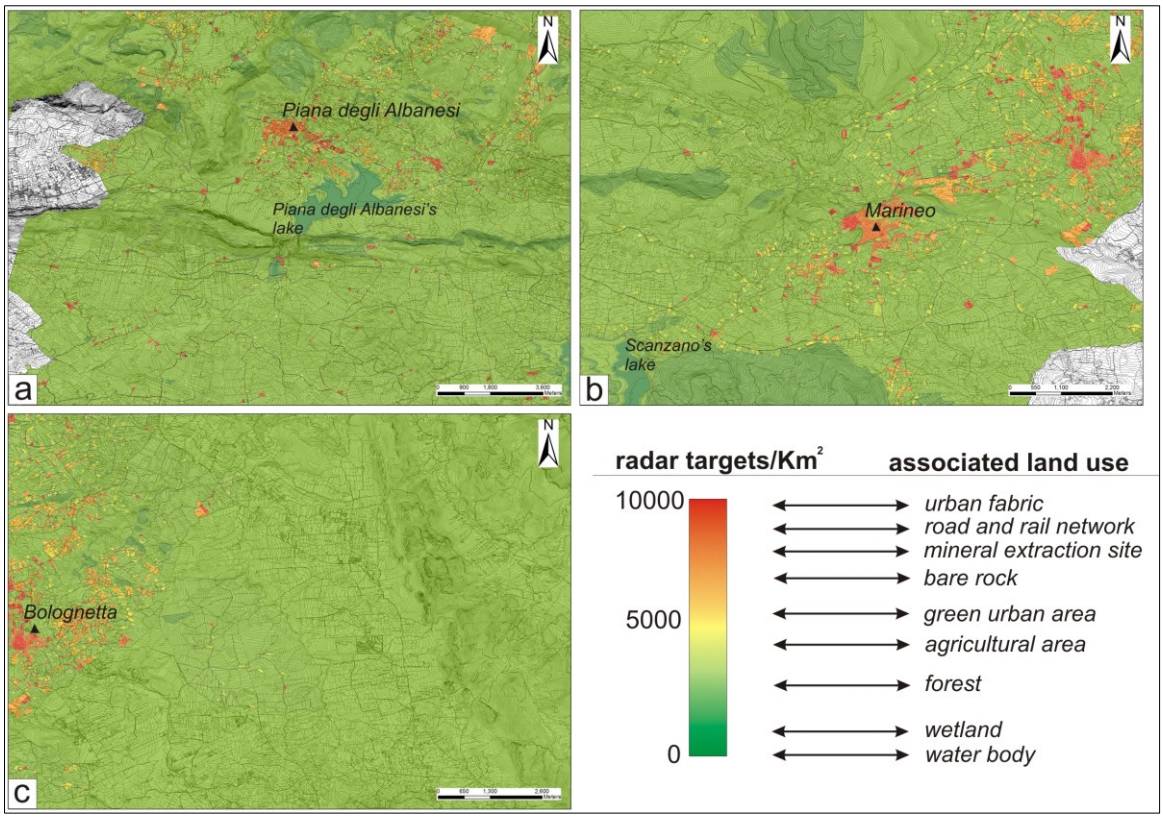

Figure 4.43 - Target Suitability Map of X-band data for the different land cover classes. Piana degli Albanesi (a), Marineo (b) and Ventimiglia di Sicilia areas (c).

In particular the Ventimiglia di Sicilia area is the most critical, because over 70% of the territory is characterized by a low-density of targets (fig. 4.43c). The ISBAS approach, differently from the standard A-DInSAR methodologies, overcomes the limitations due to land cover to guarantee an almost fully coverage in the regions of interest.

To obtain such a result a γ threshold of 0.4 was used to discriminate good from low coherence pixels and an interferogram threshold of 160 and 140 has been set for the 306 ascending and 298 descending interferograms, respectively (Table 4.11; Novellino *et al*., 2014b). Therefore, the radar targets takes into consideration intermittently coherence pixels that are added to the continuously coherent pixels (Cigna *et al*., 2014).

Spatial baseline threshold	500 m
Temporal baseline threshold	2 years
Multilooking factor (azimuth x range)	5 x 5
Coherence threshold	0.4
Number of interferograms	306asc – 298desc
Interferograms threshold	140/160

Table 4.11 – Main ISBAS data processing parameters of CSK data for Sicily.

The square root of the number of interferograms adopted for each pixel is mathematically given by the Standard Error (SE) and expressed in the 'cohcount' image.

The cohcount image shows how non-urban areas always account for fewer interferograms than urban areas (fig. 4.44) and this effect is particularly evident for higher γ values (fig. 4.45). With an average SE of ±1 mm/yr in the ISBAS target measurements, the class of stable points has been identified between ±2mm/yr.

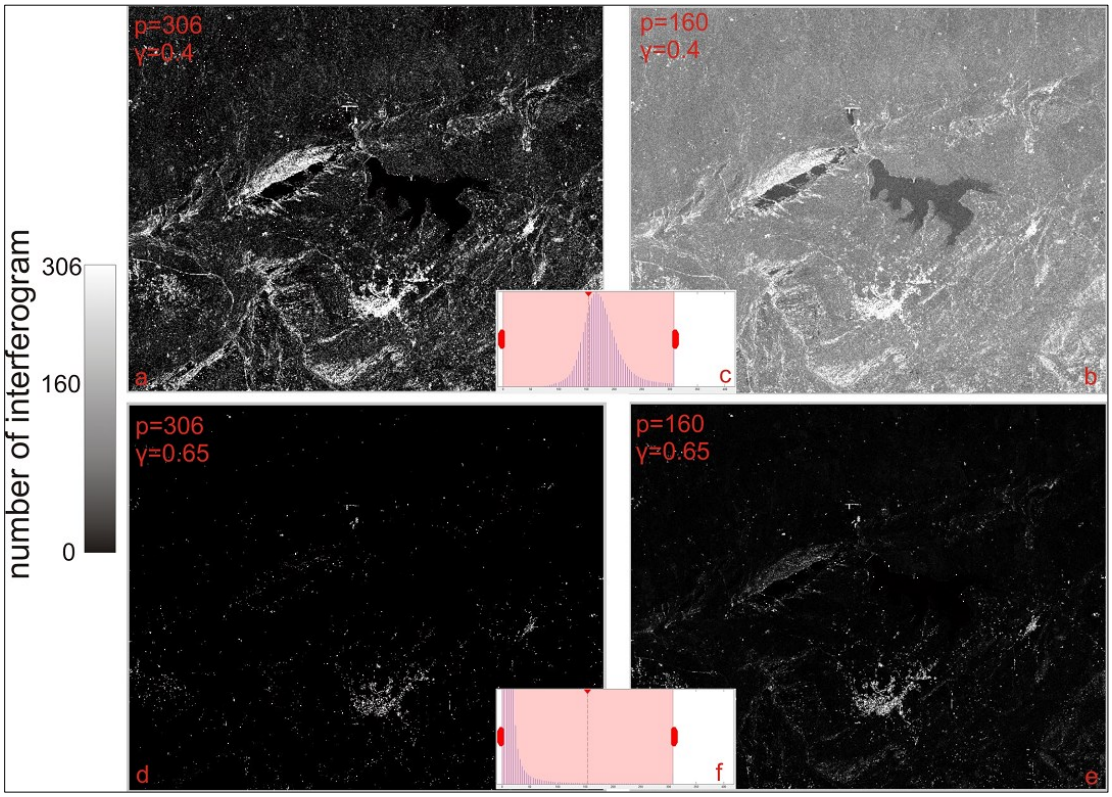

Figure 4.44 – Example of how γ and p affect the target coverage in the Piana degli Albanesi area: average coherence maps from all 306 interferograms and a γ threshold of 0.4 (a); average coherence maps from 160 interferograms and a γ threshold of 0.4 (b); frequency histogram of a and b (c); average coherence maps from all 306 interferograms and a γ threshold of 0.65 (d); average coherence maps from 160 interferograms and a γ threshold of 0.65 (e); frequency histogram of d and e (f).

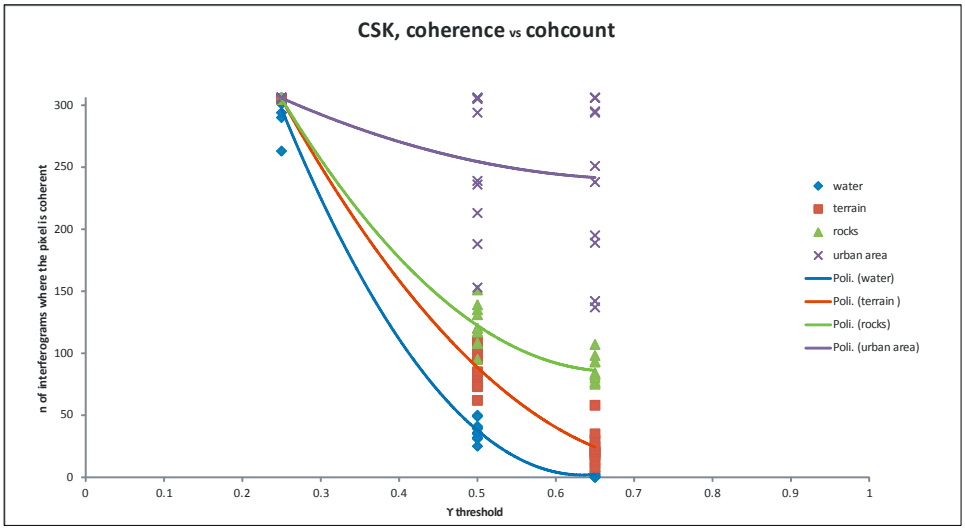

Figure 4.45 – Example of how the land cover affects the cohcount value in the CSK images: the higher the γ value threshold, the smaller the number of interferograms where the pixel is coherent. The non-urban areas are more affected by the γ value threshold as corroborated by the higher tilt angle of the fitting curve.

Three kinds of parameters have been taken into account to verify the possible exploitation and reliability of ISBAS data: (i) a threshold for the minimum numbers of radar targets inside a landslide,

(ii) the evaluation of the velocity along the slope dip direction and (iii) the comparison with conventional landslide mapping techniques, whose result will be illustrated in section 4.4.5.

As concern the minimum number of radar targets inside a landslide considered as sufficient for the inclusion in the updating landslide process, this value ranges from 5, for a landslide area <0.05 Km^2, to 20, for a landslide area >1 Km^2. Indeed, analyses established on considering single or few targets may not be indicative of a landslide process but more likely due to a single object (e.g. building settlement).

Through the 2,729,188 ISBAS points identified within the three study areas between ascending and descending geometries, 371,360 coincide with landsliding areas and <1% for the 368 phenomena surveyed do not have a sufficient number of radar targets.

In addition, the reliability of ISBAS results (both ascending and descending) is also geometrically implemented by considering the velocity along the slope dip direction; this parameter should always be positive implying that it follows the force of gravity. Therefore the LOS deformation data (V_{LOS}) has been converted, following the GIS-procedure of Cigna *et al*. (2012), to the steepest slope direction (V_{SLOPE}) for each landslide, using the equations [8 and 9]:

$$V_{SLOPE} = \rho * V_{LOS} \quad [8]$$

$$\rho = E_{LOS} * E_{SLOPE} + N_{LOS} * N_{SLOPE} + Z_{LOS} * Z_{SLOPE} \quad [9]$$

Where the ρ value represents the conversion factor related to the projection of the LOS to slope values, and E, N, and Z are the directional cosines of the LOS and the slope vectors in the east, north, and zenith directions, respectively.

The azimuth (α) and slope (β) angles of V_{SLOPE} were evaluated, as the average of the aspects and slopes of the 10 m DEM cells used to estimate the directional cosines of the slope through the equations [10, 11 and 12]:

$$E_{SLOPE} = \sin\alpha * \cos\beta \quad [10]$$

$$N_{SLOPE} = \cos\alpha * \cos\beta \quad [11]$$

$$Z_{SLOPE} = \sin\beta \quad [12]$$

An example of the V_{SLOPE} evaluation is given in Figure 4.46.

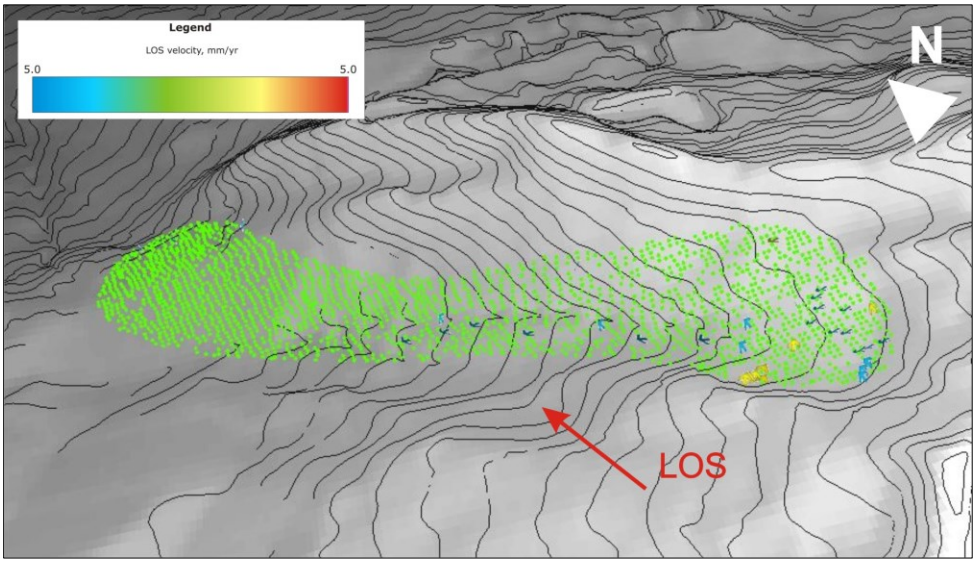

Figure 4.46 - 3D view of the updated landslide mapping in the Marineo village, captured from a ~45° SW angle. Heights of the DEM are amplified by a factor of 2. Velocity vectors of the landslide are shown with arrows; they refer to descending ISBAS data. Landslide location is labelled as Hotspot 1in Figure 4.56. A sudden collapse of a 50-m wide section of this flow occurred in the foot area on the 26th of February 2015.

4.4.2 Results from the Piana degli Albanesi area

The Piana degli Albanesi area surrounds the Piana degli Albanesi lake (610 m a.s.l.), developed from a gravity masonry dam built in 1923 to supply electricity to the local community (Papini *et al*. 2009).

Geologically, the area is characterized by the presence of the Hyblean-Pelagian and Imerese-Sicanian units, the Numidian Flysch (Johansson *et al*., 1998) and slope deposits (fig. 4.47).

The geomorphology is marked by a W-E striked carbonatic steep-slope ridge of the Hyblean-Pelagian and Imerese-Sicanian derivation (Kumeta and Maganoce massif), representing a physical barrier to the lake. The carbonatic relief is surrounded by a piedmont slope with an average inclination of 8^{o}, developed from the rock cover: the Numidian Flysch, the San Cipirello Marls Formation and the slope deposits. These materials form the hilly landscape of the Piana degli Albanesi area.

The lithological-geomorphological setting gives origin to two different kinds of landscape evolution: a carbonate highland landscape (La Pizzuta, Serra della Ginestra, Kumeta and Maganoce mounts) showing fall-, topple- or DSGSD-prone areas. The carbonates ridges delimit the 40 Km^2 extended valley of the Piana degli Albanesi lake both westwards and southwards. On the other hand, the hilly landscape consists of gentle slopes with sheet and gully erosion occurrence and a disarranged drainage system due to tens of active and dormant movements: mainly earth flows and complex landslides.

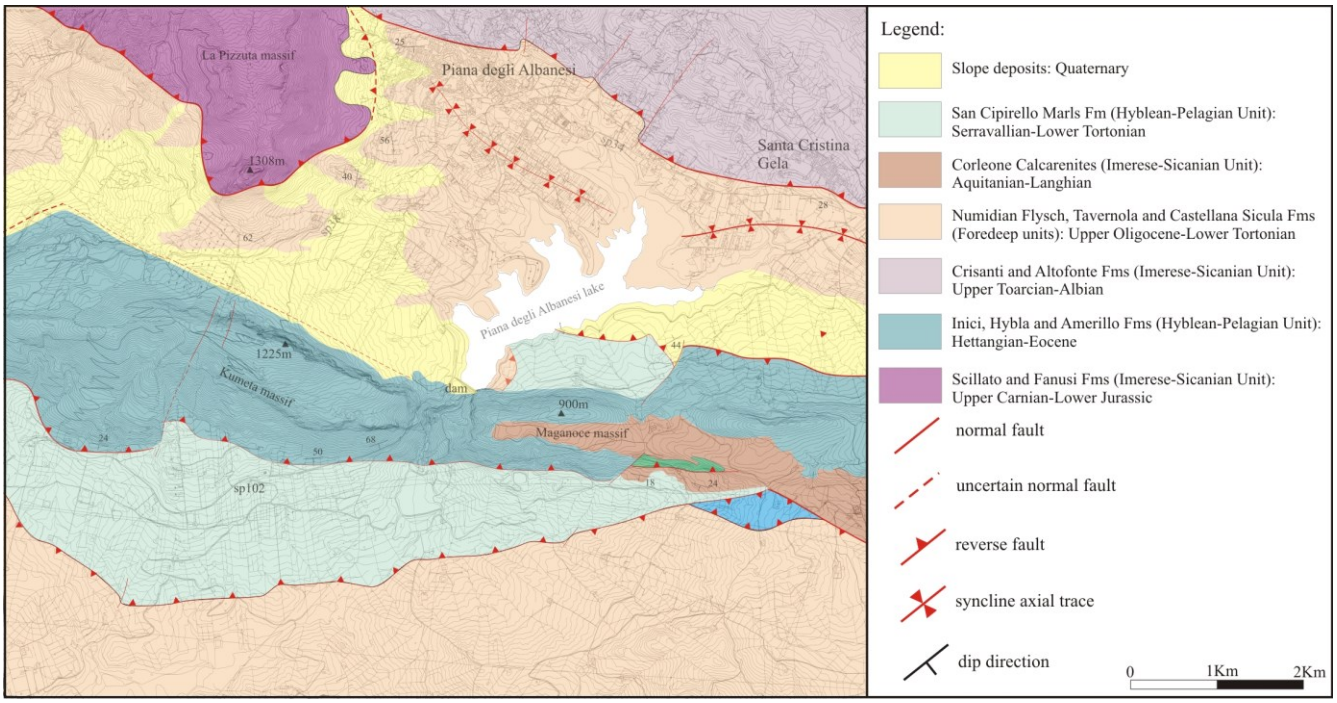

Figure 4.47 – Geological map of the Piana degli Albanesi area (after CARG, 2010b).

The ISBAS analysis has been conducted by choosing a portion along the main road (via Roma) in Santa Cristina Gela village as a stable point; the geographical coordinates of the stable point are 37.984953 N and 13.327830 E. The total number of points is 727,084 in the ascending geometry (point density of ≈8000/Km^2) and 894,496 (point density of ≈9000/Km^2) in the descending geometry over an area of about 90 Km^2 (fig. 4.48).

Layover and shadowing areas account for 3.2 Km^2 and 4.3 Km^2 in ascending and descending geometries, respectively. ISBAS velocity values range within -6.4 and +5.5 millimetres per year (fig. 4.48). According to the ISBAS results, the study has focused on areas particularly relevant for the landslide hazard and identified, following the work of Bianchini *et al*. (2012), as hotspots 1 and 2 in Figure 4.48.

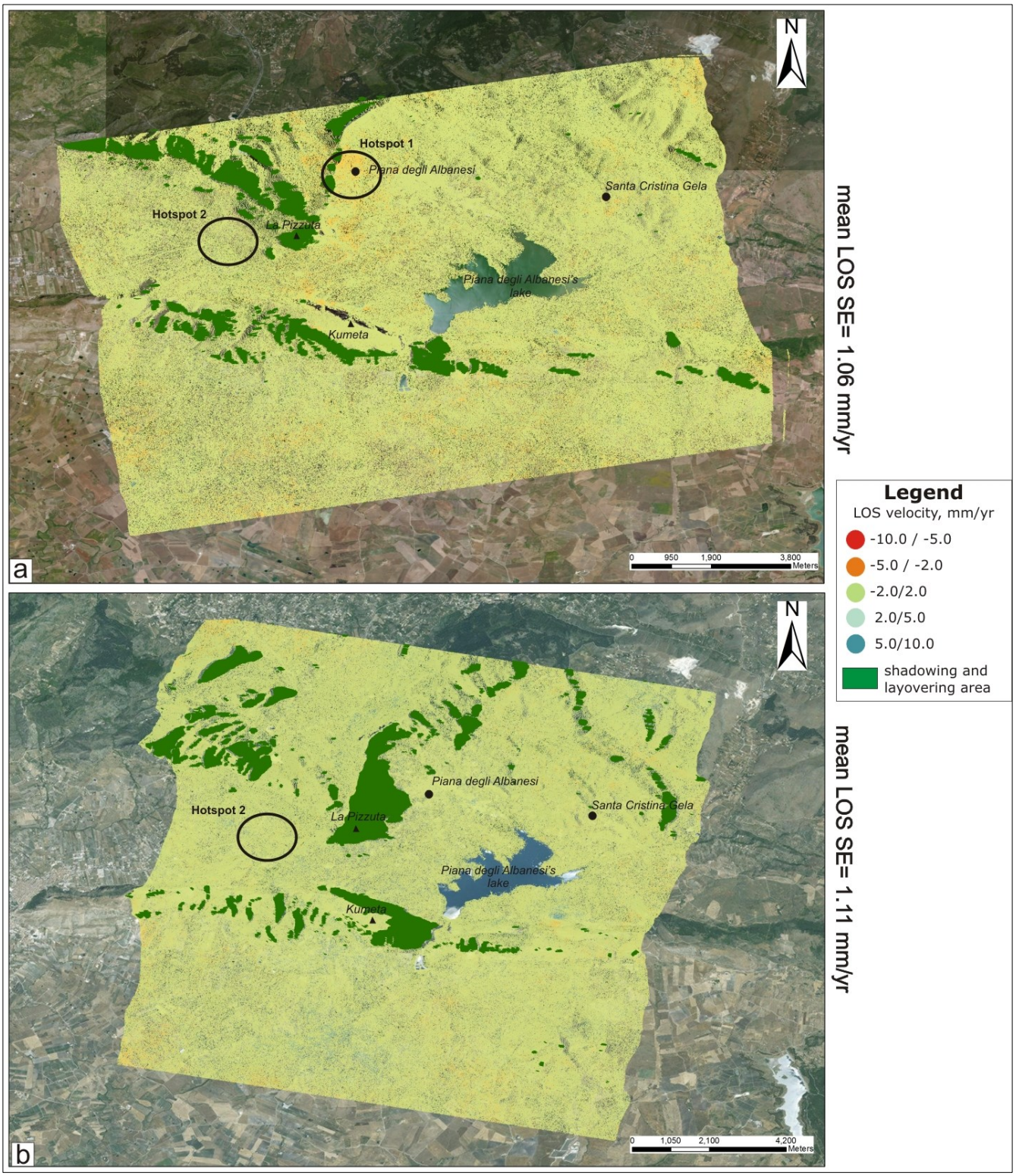

Figure 4.48 – The LOS velocities derived following ISBAS analysis for ascending (a) and descending data (b). Each point covers an area of approximately 15 m × 15 m on the ground.

Hotspot 1 corresponds to the Piana degli Albanesi village, where the instability creates light damage, corresponding to class 2 of the Chiocchio *et al*. scheme (see section 4.2.2.2), in the head area which shows the highest negative velocities, -4.5 mm/yr (fig. 4.49a).

The updating data has merged the two pre-existing phenomena of the HSP, one active and the other dormant, into a single dormant complex phenomenon extending 0.4 Km^2 (fig. 4.49).

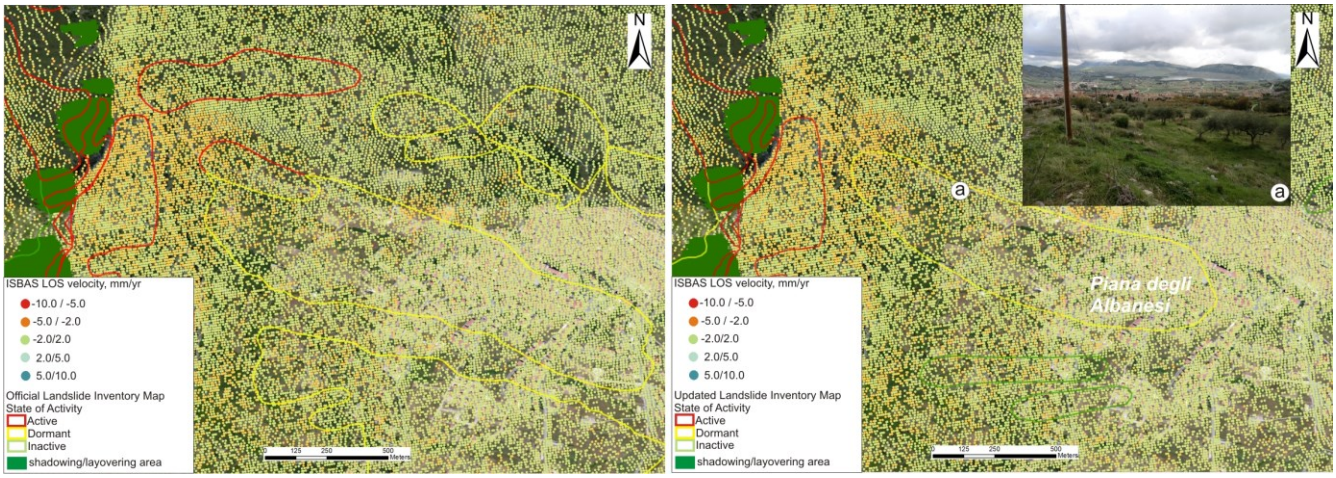

Figure 4.49 – Piana degli Albanesi - example of change in the landslide border between the official Landslide Inventory Map (on the left) and the updated Landslide Inventory Map (on the right) with the ascending ISBAS data. The corresponding damage is in the inset (a). The hotspot location is indicated in Figure 4.51 as No. 1.

Hotspot 2 reveals that the provincial road n.20 (SP20) has undergone considerable damage (fig. 4.50a) because of an active flow, extending over an area of 0.59 Km^2 and 2 Km in length. The landslide was reported from a field survey and then confirmed only from descending ISBAS data, that recorded a maximum velocity of 4mm/yr within the foot area. The event is not reported in the official HSP Landslide Inventory Maps of 2006 and 2012 (fig. 4.51). The ascending ISBAS data did not display evident movements because the landslide downward motion was NW, namely almost coincident with the azimuth of the CSK sensor.

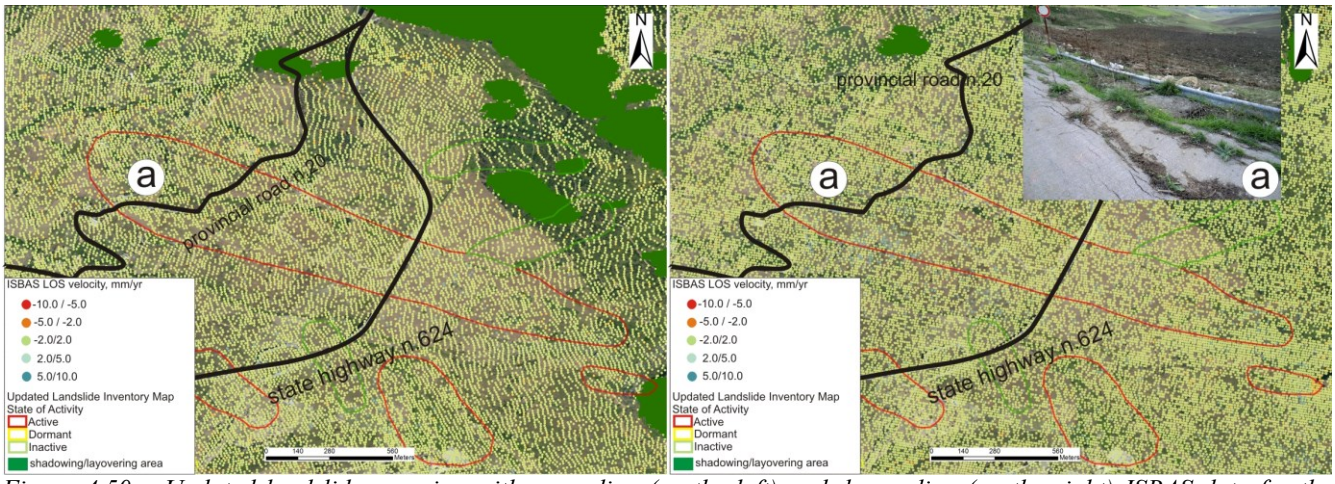

Figure 4.50 – Updated landslide mapping with ascending (on the left) and descending (on the right) ISBAS data for the landslide near State Highway n.624 with the corresponding damage in the inset (a). The hotspot location is indicated in Figure 4.51 with the No. 2.

Globally, the updated Landslide-Inventory Map of the Piana degli Albanesi area includes 179 phenomena, corresponding to an area of 19.7 km^2. The previous landslide-inventory reported 123 phenomena (and an area of 16.9 km^2), of which only 60, representing 33% of the total instabilities, were fully confirmed in the new chart, while 63 of the pre-existing landslides have been modified.

Creep and widespread are the most common phenomena in the updated Landslide Inventory Map. Falls and topples include 25 events, compared to the 18 events of the official HSP Landslide Inventory Map (fig. 4.51a).

Of the new 56 phenomena, 3 are active DSGSDs affecting the top of the carbonatic reliefs: La Pizzuta massif, Kumeta massif and Maganoce massif (fig. 4.51b). The most critical areas occur at the bottom of the eastern flank of the La Pizzuta massif and at the bottom of the northern side of the Kumeta massif where, collectively, 26 landslides are concentrated (fig. 4.51b).

The reason of such high landslide propensity is mainly due to the lithology: southwards of the Kumeta-Maganoce ridge, where San Cipirello Marls crop out, creep and flows prevail; slides, flows and creep assume a remarkable importance northwards because of the presence of the tectonized shale of the Numidian Flysch together with the slope deposits; instabilities are prompted by the dip-slope strata attitude at the bottom of the La Pizzuta massif, by the variation of water level in the Piana degli

Albanesi reservoir on the northern sector of Maganoce massif and by the high energy of the relief on the northern side of the Kumeta massif.

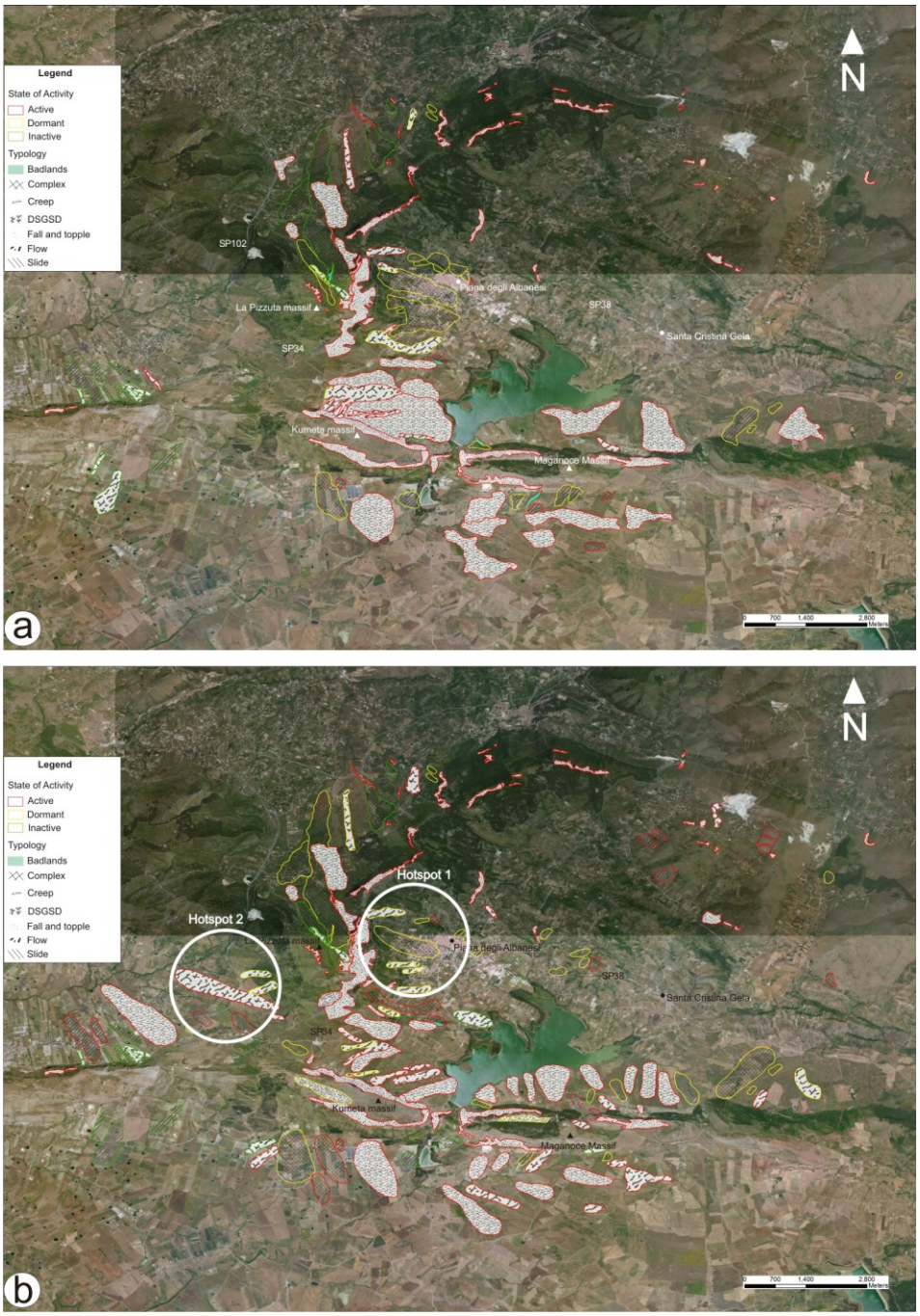

Figure 4.51 – Comparision between official HSP Landslide Inventory Map (a) and updated Landslide Inventory Map of Piana degli Albanesi area (b). Hotspot 1 is represented in Figure 4.49, hotspot 2 in Figure 4.50.

4.4.3 Results from the Marineo area

The Marineo area is included in the upper portion of the Eleuterio drainage basin (fig. 4.42). This area (fig. 4.52) is predominately affected by complex (rotational + flow) phenomena in the shale beds of the Numidian Flysch Formation and glauconitic biocalcarenites of the Corleone Calcarenites, cropping out at the footwall of thrusts where hangingwalls are represented by limestones of the Imerese-Sicanian Unit (Catalano and D'Argenio, 1978) and Hyblean-Pelagian Unit (Basilone, 2011).

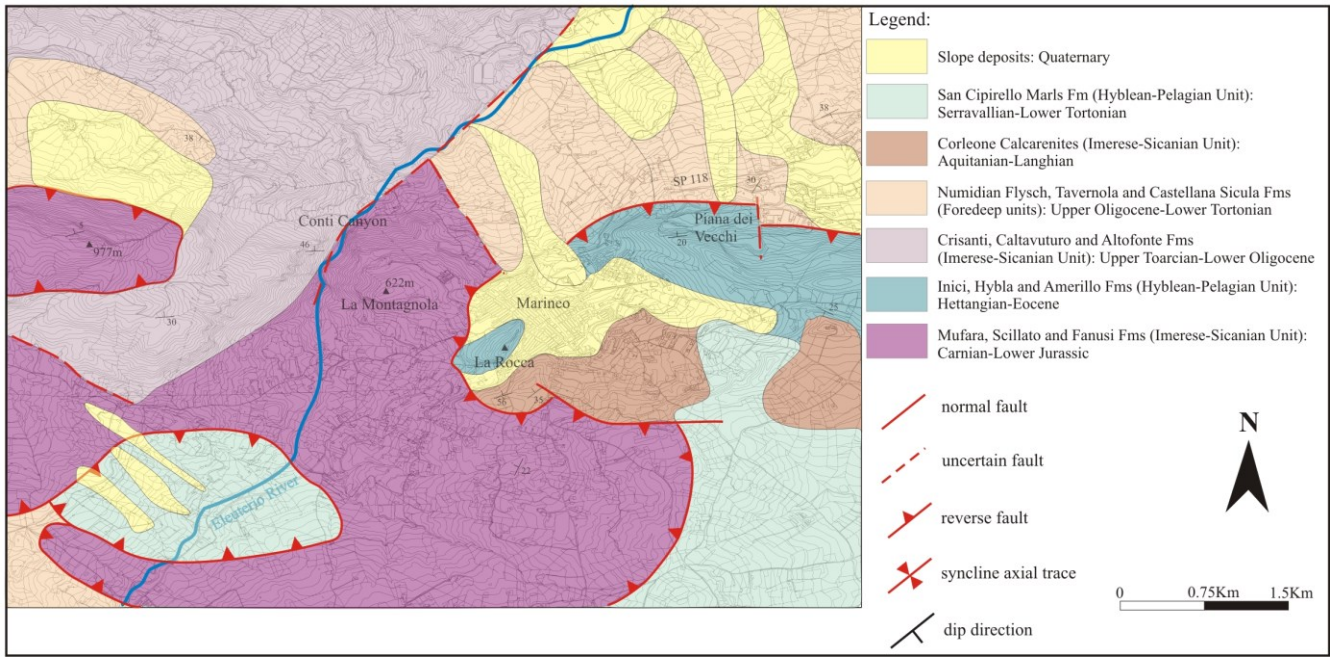

Figure 4.52 –Geological map of the Marineo area (after CARG, 2010c).

Over an area corresponding to 41 Km^2, ISBAS processing allowed the identification of 289,304 (point density of ≈7000/Km^2) and 183,096 (point density of ≈4500/Km^2) coherent and intermittently coherent pixels for the ascending and descending data stacks, respectively. The stable point has been chosen inside a football playground in the village of Marineo, whose geographical coordinates are 37.954727 N and 13.417973 E.

Layover and shadowing areas account for 0.6 Km^2 and 1.4 Km^2 in ascending and descending geometries, respectively, so they do not represent an obstacle to ISBAS coverage.

The LOS range is more restricted with respect to the Piana degli Albanesi area and included between -4.9 mm/yr and +4.5 mm/yr (fig. 4.53).

The study focused on areas particularly subject to landslide hazards: Hotspot 1, Hotspot 2, Hotspot 3 and Hotspot 4 of Figure 4.53.

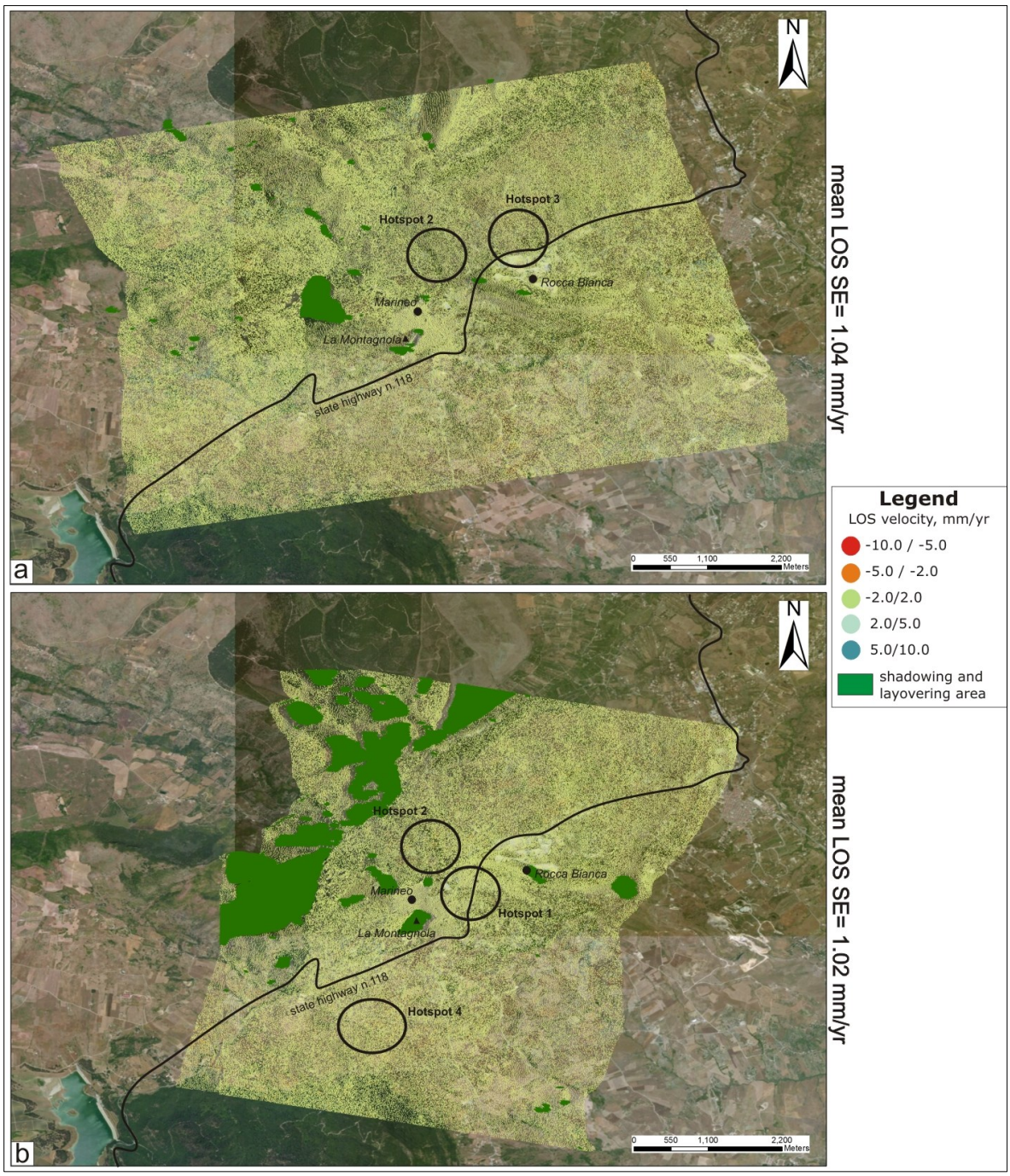

Figure 4.53 – LOS velocities derived following ISBAS analysis for ascending (a) and descending data (b). Each point covers an area of approximately 15 m × 15 m on the ground.

The village of Marineo is surrounded by three active slides occurring in the northern, eastern and southern sides of the settlement; the village is also affected by 2 falls on the western side involving limestones of the Imerese-Sicanian Unit forming the La Rocca massif (fig. 4.52). The easternmost and active slide is the largest one surrounding Marineo (0.33 Km^2) and, according to the historical records, caused the destruction of most of the village center during mutiple reactivations, starting from the 19^{th} century (Italian Royal Decree, 1920). This landslide corresponds to Hotspot 1 in Figure 4.53, showing a maximum velocity of 3.5 mm/yr from the descending dataset (fig. 4.46).

In the Hotspot 2 some remedial works have been realized, consisting in wood fences and stonework walls which are now partially disrupted (fig. 4.54a). Furthermore, within the foot area, ISBAS data localize 3 mm/yr velocities towards the sensor in the ascending geometry and similar but negative values in the descending geometry, because of the movement away from the sensor (fig. 4.54). With respect to the pre-existing perimeter, the active landsliding area has become smaller in the depletion area, due to the presence of ISBAS moving targets. The new landsliding area is 0.20 Km^2 while the previous one was 0.23 Km^2. Even such a small difference in landsliding area makes the difference in land management use and land planning, especially in urban areas where land use is very restricted.

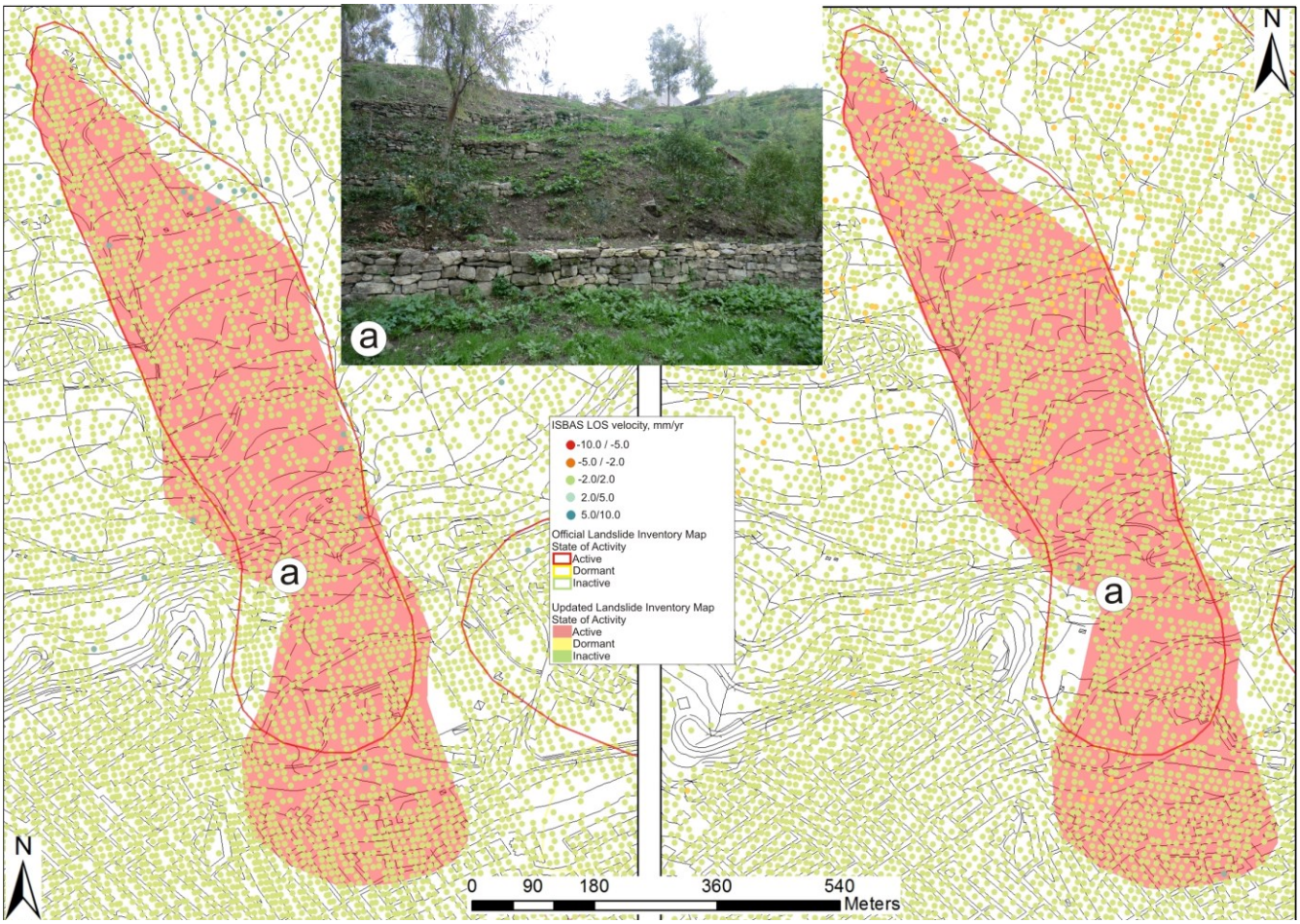

Figure 4.54 - Updated landslide mapping with ascending (on the left) and descending (on the right) ISBAS data for the northern landslide in the village of Marineo with the corresponding damage in the inset (a). Landslide location is indicated in Figure 4.56 as number 2.

Hotspot 3 refers to the Rocca Bianca mine, where the highest positive values were recorded. The targets delimit a shallow rotational slide involving a local road northernwards of the State Highway n.118 (fig. 4.55a). The damage mainly affected the perimeter walls of the villas.

Hotspot 4 represents an active flow occurring nearby State Highway n.118 and, where neither infrastructures nor outcrops are present, ISBAS data were useful to identify 1554 points in the ascending dataset and 2209 points in the descending dataset (fig. 4.55b). The highest values show velocities of -3.6 mm/yr. The original landsliding area, 0.1 Km^2, has been enlarged to 0.27 Km^2.

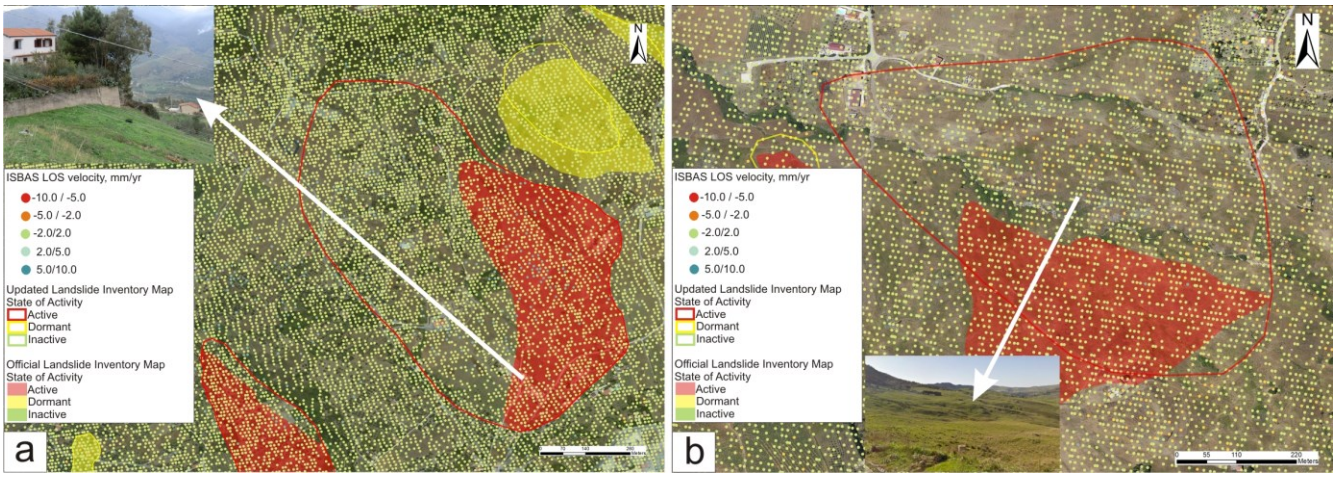

Figure 4.55 - Updated landslide mapping with ascending ISBAS data for the landslide in Rocca Bianca pit (a) and descending ISBAS data for the landslide on state highway n.118 (b). The location of hotspots are indicated in Figure 4.57 as No. 3 (a), and No. 4 (b).

In the Marineo area 51 landslides have been reported, with respect to the 40 of the HSP (2006): 11 new landslides have been added, 22 landslides have been confirmed and 18 have been modified. The new landsliding area accounts for 4.76 Km^2 while the HSP landsliding area corresponded to 2.85 Km^2.

Twenty-three of the updated landslides and badlands fall in the southern sector of the Conti Canyon, where the new instability scenario is the following (fig. 4.56):

- 6 landslides have been added.
- 6 landslides have been confirmed.
- For 2 landslides and 1 badlands area, their borders were changed.
- For 2 landslides, the typology was changed.
- For 5 landslides, typology, state of activity and boundary were changed.

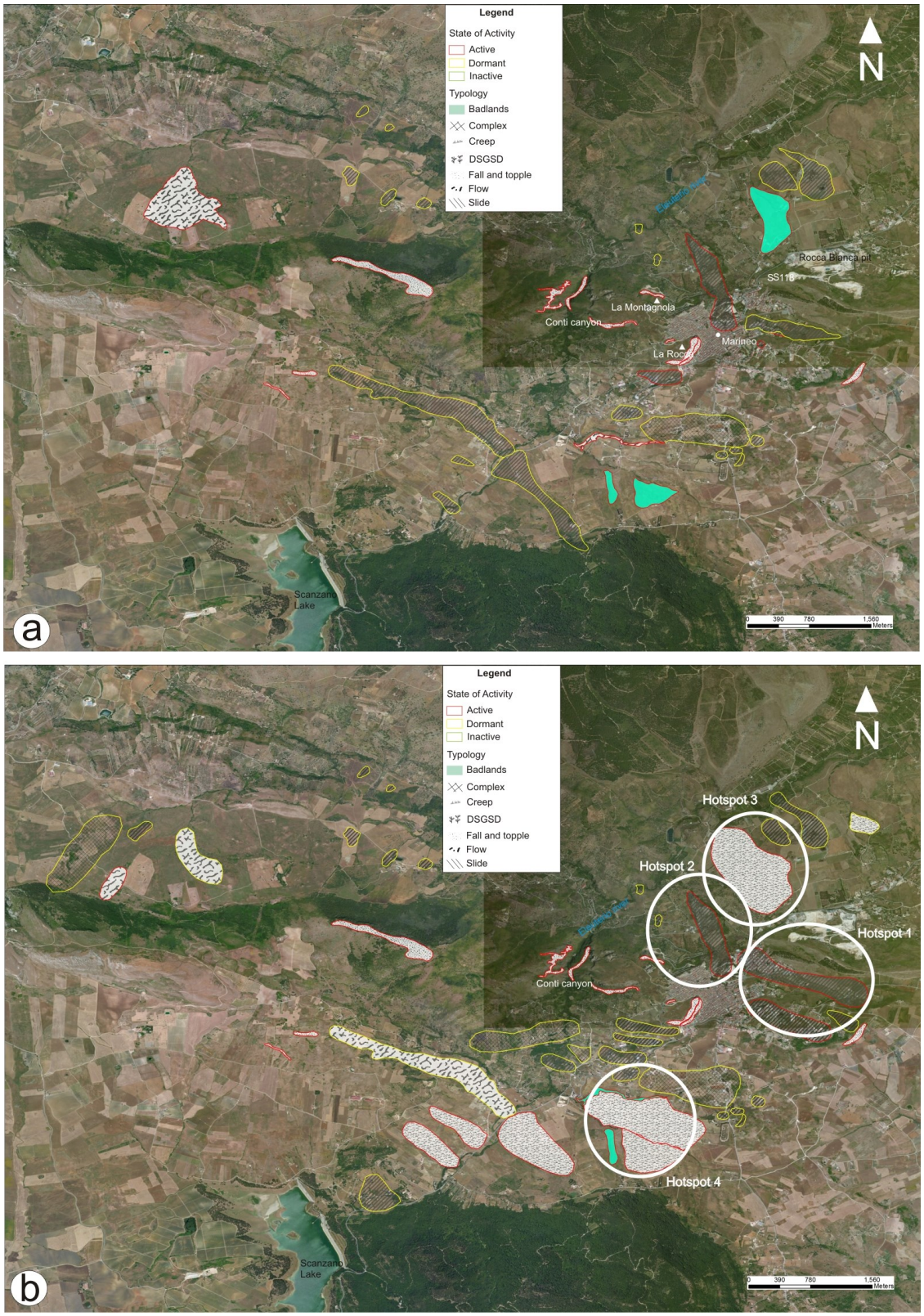

Figure 4.56 – Comparision between official HSP Landslide Inventory Map (a) and updated Landslide Inventory Map of Marineo area (b). Hotspot 1 is shown in Figure 4.46, hotspot 2 in Figure 4.54, hotspot 3 in Figure 4.55a and hotspot 4 in Figure 4.55b.

The predisposing factors of such landslides are related to the clayey dominant lithology of outcropping terrains crossed by watercourses with high erosion rates. The most important of them is the meandering Eleuterio river, whose path is continuously changing because of the landslide deposits accumulated on its watershed (fig. 4.52).

4.4.4 Results from the Ventimiglia di Sicilia area

The last area lies 5 km northwest of the Ventimiglia di Sicilia village, where most instabilities are located along a 3.5 km N-S elongated valley created by the Mennula river, a tributary of the Milicia river (fig. 4.42).

The eastern boundary of the watershed is represented by a NNW-SSE striked reverse fault scarp line with the marls and limestones of the Imerese-Sicanian Unit at the haningwall. The same fault creates a relief with an inclination of over 50^{o}, whose highest point is Pizzo della Trigna (1257 m a.s.l.) which favors a large number of falls in this area. The slope angle decreases ($<20^{o}$) moving towards the valley represented by the Numidian Flysch Formation, consisting also of scattered outcrops of clays belonging to the Sicilide Unit.

Along the Mennula valley, 31 extremely-slow flows and complex phenomena occur (fig. 4.62). The cause of such landslides is mostly related to the lithology of the outcropping terrains as well as to the local morphology of the area, characterized by high slope gradients and narrow watercourses forming the Cugno dell'Uovo, Finaita and Suvarita valleys (fig. 4.57).

Eight of those landslides are active and affect the State Highway n.16 (SS 16). No urban area is involved in such movements but only isolated buildings and infrastructures.

Due to the large extension of nearly inhabited slopes and valleys, the identification of landslides with standard A-DInSAR techniques has been difficult. Furthermore, aerial photographs at 1:33000 scale did not guarantee an adequate support for the analysis of small extended phenomena.

Nonetheless, the Ventimiglia di Sicilia area provides an unique opportunity to reveal the potential of the ISBAS technique, more than in Piana degli Albanesi and Marineo areas, because almost 70% of the surface is represented by agricultural, wetlands and forest areas (fig. 4.43c).

Over an area of 54 Km^2, ISBAS processing allowed the identification of 327,018 (point density of ≈6000/Km^2) and 308,190 (point density of ≈5700/Km^2) coherent and intermittently coherent pixels for the ascending and descending data stacks, respectively.

The stable point has been placed in a manor with the following geographical coordinates: 37.983015 N and 13.487724 E (fig. 4.58).

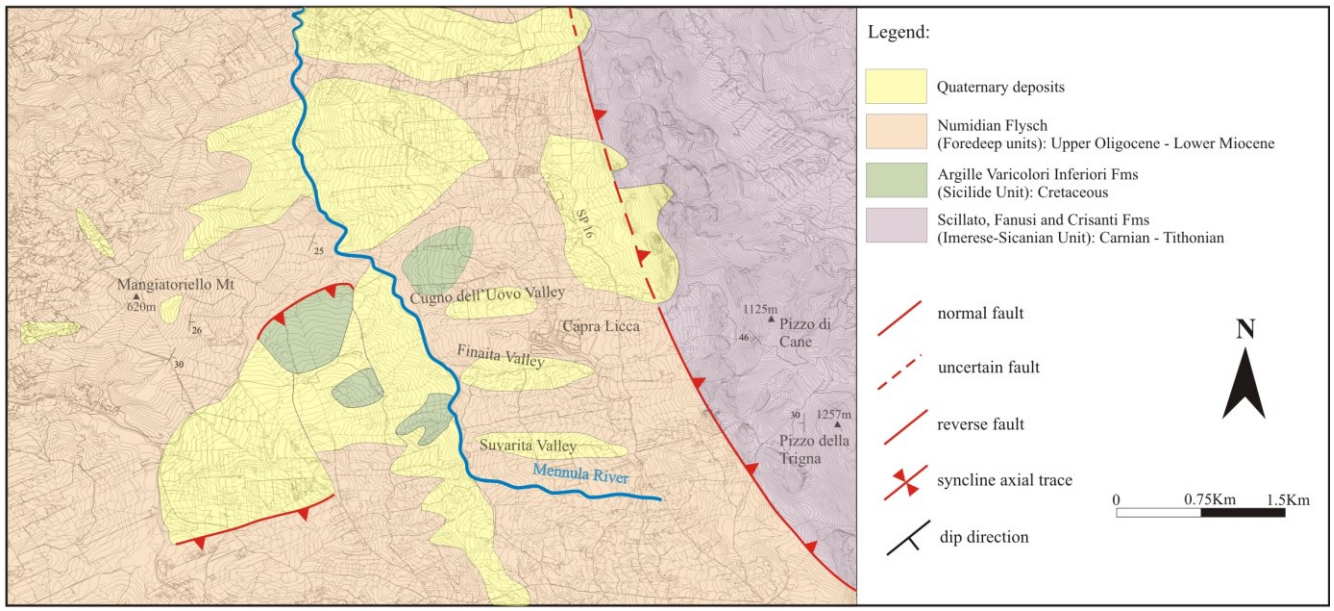

Figure 4.57 – Geological map of the Ventimiglia di Sicilia area (after CARG, 2010c).

Layover and shadowing areas account for 3.9 Km^2 and 0.5 Km^2 in ascending and descending geometries, respectively; the latter value is limited by the edge of the CSK descending frame.

The LOS ranges are between -6.3 mm/yr and +5.2 mm/yr. The occurrence of valleys dipping westwards and eastwards has supported the LOS radar measurements.

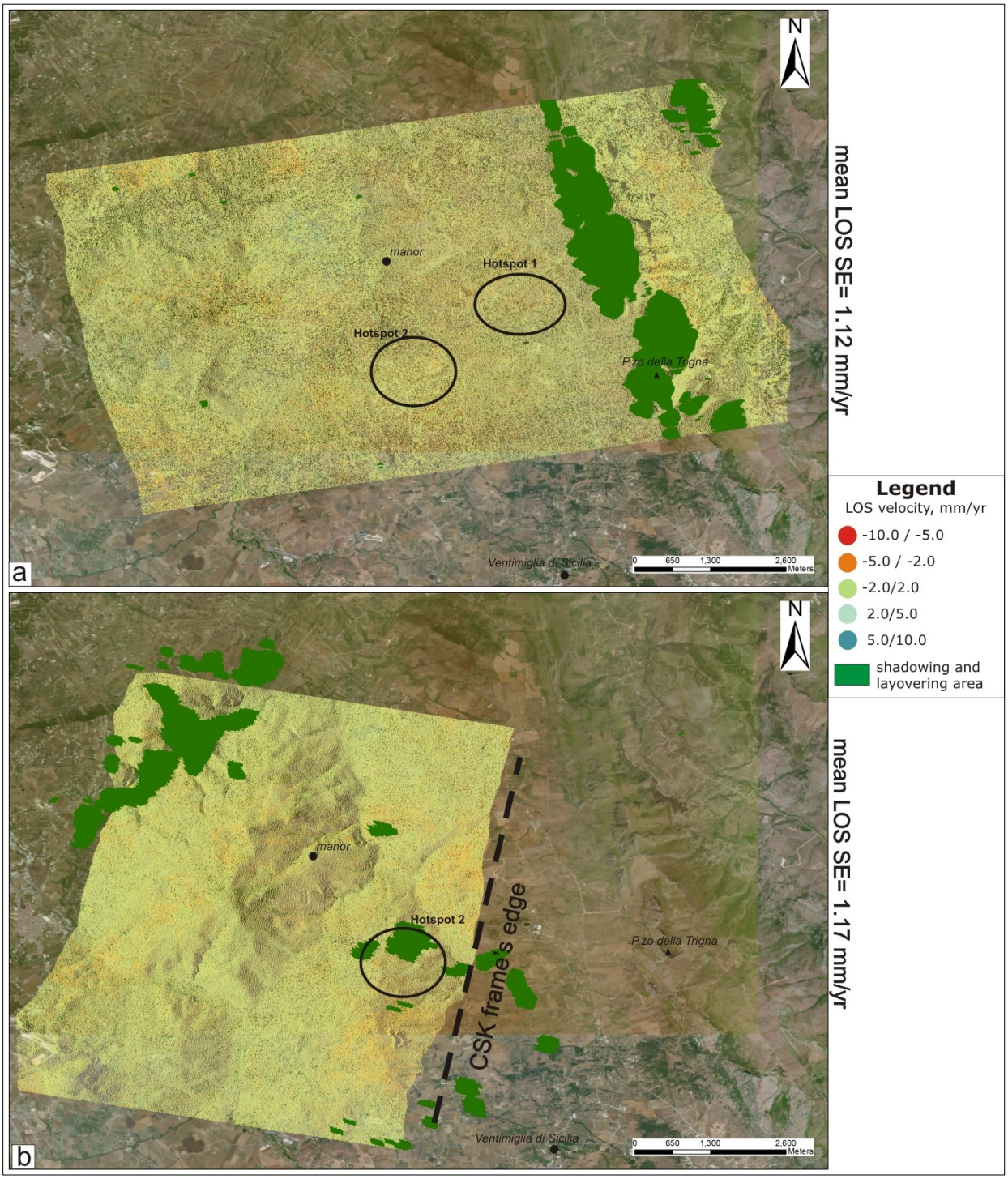

Figure 4.58 – LOS velocities derived from ISBAS analysis for ascending (a) and descending data (b). Each point covers an area of approximately 15 m × 15 m on the ground.

The area nearby Capra Licca agritourism is one of the most critical areas and is represented as number 1 in Figure 4.59. The hotspot is characterized by a flow, 0.66 Km^2 extended and 2.1 Km in length,

reaching 4.0 mm/yr in the head and -5.4 mm/yr in the foot area. The movement creates several anomalies on the road track of provincial road n.16 (SP16).

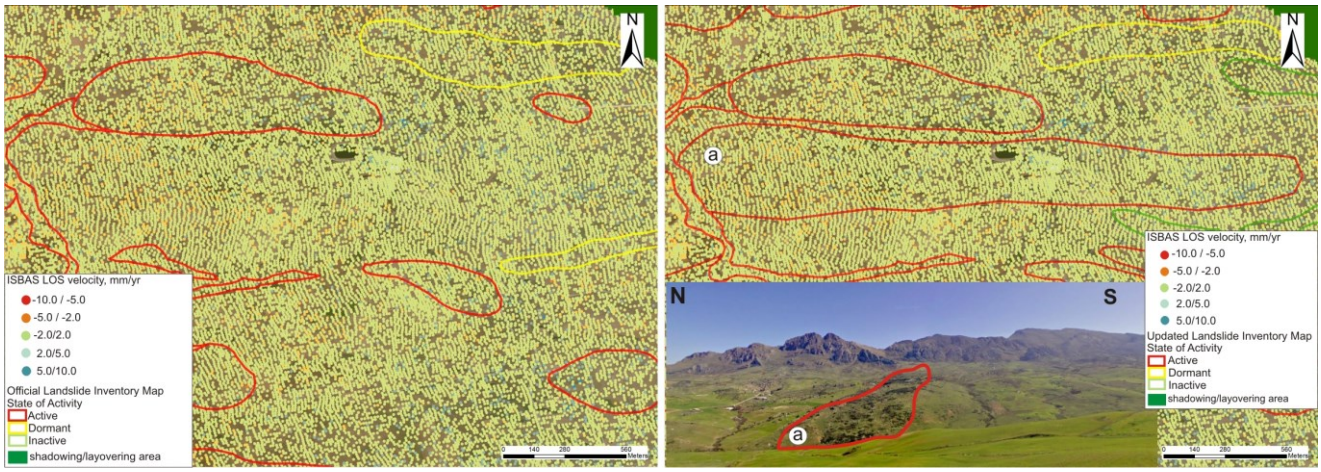

Figure 4.59 – Example of changes in the landslide boundary between the official Landslide Inventory Map (on the left) and the updated Landslide Inventory Map (on the right) with the ascending ISBAS data. The corresponding damage is shown in the inset (a). Hotspot location is indicated in Figure 4.62 with the No. 1.

Hotspot 2 is a complex and active landslide that has been widened from its original extension of 0.13 Km^2, as reported in the official Landslide Inventory Map, to 0.58 Km^2 in the updated Landslide Inventory Map, so as to involve the local road in the instability of the area (fig. 4.60).

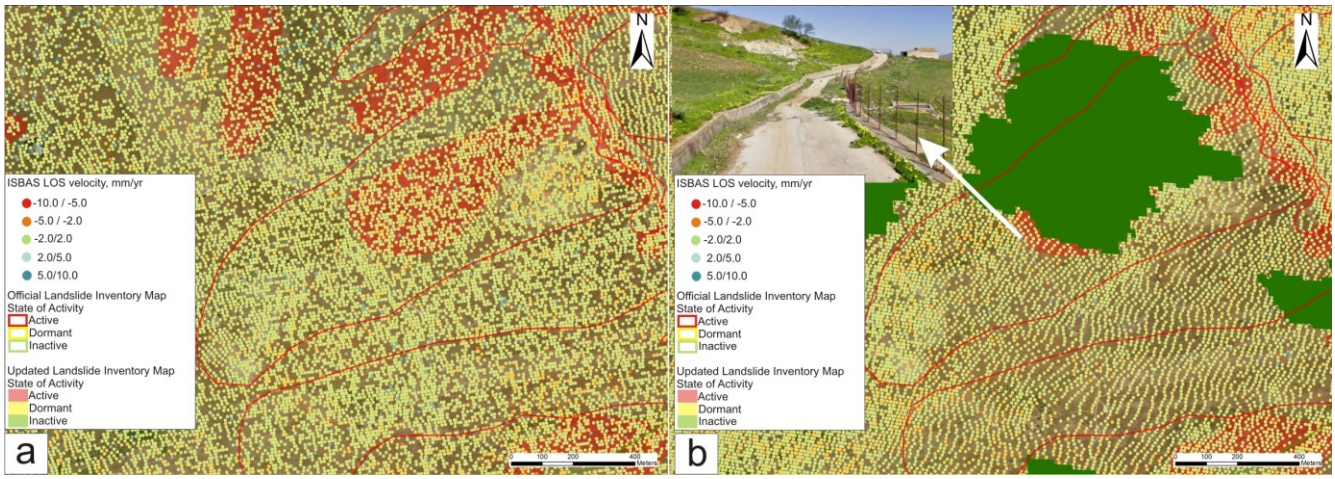

Figure 4.60 – Example of changes in the landslide boundary between the official Landslide Inventory Map and the updated Landslide Inventory Map with the ascending ISBAS data (a) and the descending ISBAS data (b). Hotspot location is indicated in fig. 4.62 with the No. 2.

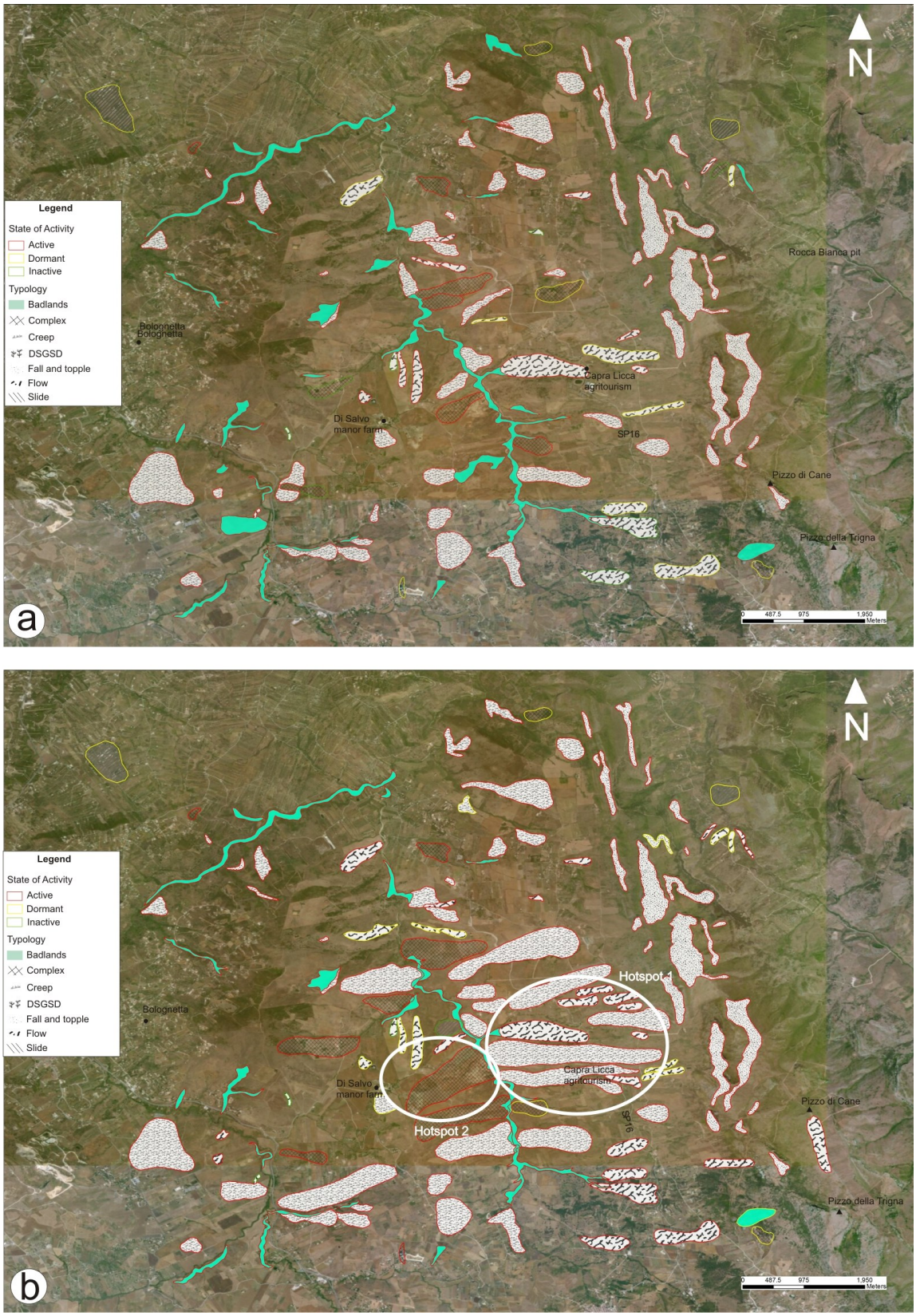

Figure 4.61 – Comparision between official HSP Landslide Inventory Map (a) and updated Landslide Inventory Map of Ventimiglia di Sicilia area (b). Hotspot 1 is shown in Figure 4.59, hotspot 2 in Figure 4.60.

The predisposing factors of such landslides are related to the clayey dominant lithology of the Numidian Flysch and Sicilide Unit and the high slope gradient associated to the tectonic scarps.

The updated inventory landslide map of the Ventimiglia di Sicilia area includes 117 landslides (and 19 badlands) for an area of 12.95 Km^2 with respect to the 98 landslides (and 28 badlands) and the corresponding 7.8 Km^2 of the official Landslide Inventory Map. Ten new landslides have been added in the updated Landslide Inventory Map, while 54% of the original instabilities have been confirmed. The decreasing in the number of badlands is linked with the reclassification of 9 of these as flows or complex landslides (fig. 4.61).

4.4.5 Palermo province: summary of the results and discussion

The ISBAS technique supported field surveys and photo-interpretation in northwestern Sicily, highlighting the efficiency of identification and mapping of unstable slopes at a large scale. The combined approach has contributed to updating the 2006 landslide inventory over an area of 182 Km^2, permitting to:

- Confirm phenomena where the typology, state of activity and boundary are unchanged ('Confirmed landslide' category of Table 4.12).
- Modify the state of activity of the pre-existing landslides ('State of Activity modified' category of Table 4.12).
- Modify the boundary of the pre-existing landslides ('Boundary modified' category of Table 4.12).
- Modify the typology of the pre-existing landslides ('Typology modified' category of Table 4.12).
- Modify more than one feature such as the state of activity, boundary and typology of the pre-existing landslides ('Activity, boundary, typology modified' category of Table 4.12).
- Identify new landslides ('New landslide' category of Table 4.12).

The results are summarized in Table 4.12.

	number	%
Confirmed landslide	156	42.6
State of Activity modified	31	8.5
Boundary modified	56	15.3
Typology modified	10	2.7
Activity, boundary, typology modified	36	9.8
New landslide	77	21

Table 4.12 – Report of the updating process of the official landslide inventory in northwestern Sicily.

The new Inventory Maps now include 345 landslides and 23 badlands corresponding to 39.4 km^2.

In particular (see Table 4.12):

- 156 landslides have been confirmed;
- 77 new events have been detected;

the remaining 133 previously mapped events (corresponding to 37% of the updated inventory) have been updated, modifying their typology, boundary and/or state of activity.

The main difference concerns flows: of the original 42, of which 18 are active; 77 flows were mapped during this research, 42 of which are active (fig. 4.62). On the other hand, A-DInSAR data have been less efficient to identify falls and topples which have increased from 78 to 86. The reason for reduced efficiency of A-DInSAR data is due to the high velocity, the geometrical distortions or the visibility constraints related to this kind of landslides.

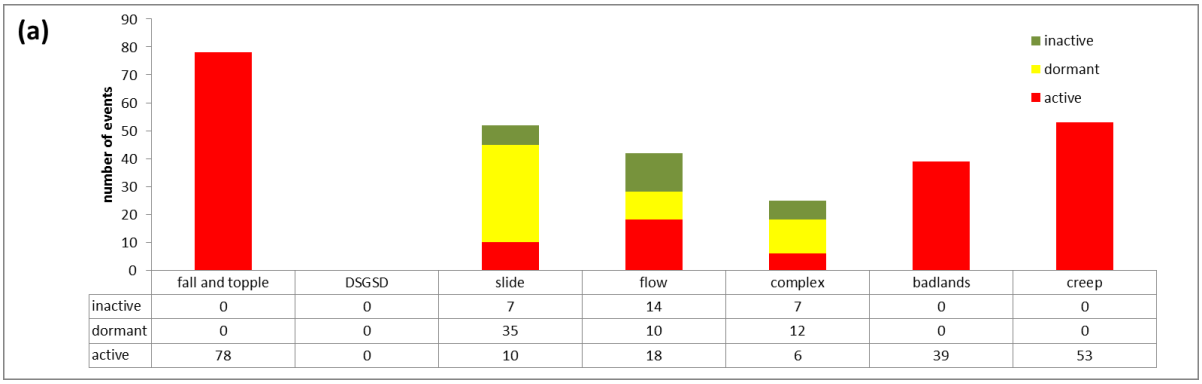

	fall and topple	DSGSD	slide	flow	complex	badlands	creep
inactive	0	0	7	14	7	0	0
dormant	0	0	35	10	12	0	0
active	78	0	10	18	6	39	53

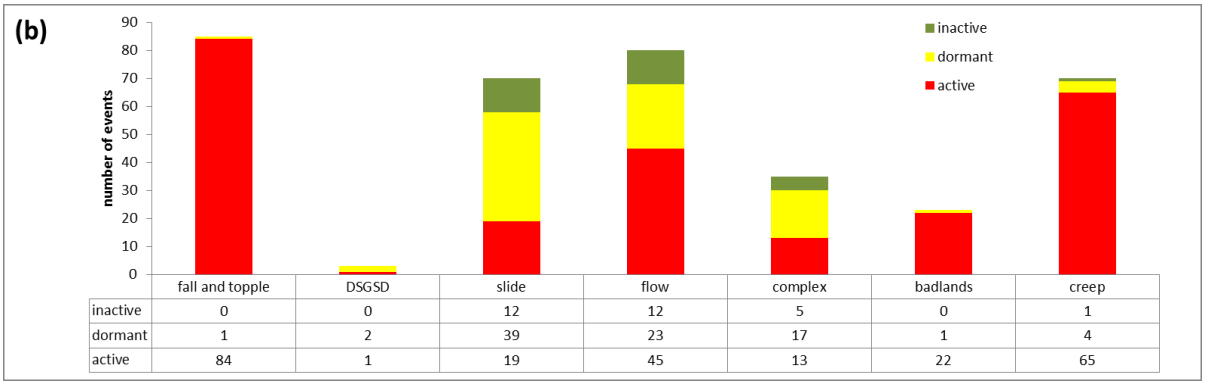

	fall and topple	DSGSD	slide	flow	complex	badlands	creep
inactive	0	0	12	12	5	0	1
dormant	1	2	39	23	17	1	4
active	84	1	19	45	13	22	65

Figure 4.62 - Bar graphs showing the official (a) and new (b) Inventory Maps events according to landslide typology and state of activity.

Summing up, the proposed updated landslide inventory accounts for 251 active, continuous or reactivated phenomena. Dormant and stabilized landslides are 87 and 30, respectively. In the official Landslide Inventory Map 204 were active, 57 dormant and 28 inactive.

Of the 133 modified landslides, field surveys mainly helped in defining landslide typology, while air-photos interpretation mainly helped in identifying landslide boundary; radar images mainly helped in identifying the landslide state of activity.

As already disclosed in section 4.4.1, the study of the Palermo province was aimed to update the official Landslide Inventory Maps and verifying, at the same time, the reliability of radar remote sensing for the landslides detection at a large-scale. Therefore, field surveys and aerial photograph instabilities have been compared with the instabilities deriving from the A-DInSAR analysis in the here called CARM (Conventional and A-DInSAR Results Matching) bar graph of Figure 4.63.

The comparison leads to four possible cases:

- **Perfect matching** (Class 1), total correspondence between events detected by satellite and conventional procedures. This only happens when the boundary and velocity information deriving from radar-mapped phenomena exactly correspond with the distribution and the state of activity of conventional-mapped phenomena.
- **Partial matching** (Class 2), partial correspondence between events detected by satellite and conventional procedures. This happens when the boundary and velocity information deriving from radar-mapped phenomena partially correspond with the distribution and the state of activity of conventional mapped phenomena.
- **No matching between conventional- and radar-mapped phenomena** (Class 3), phenomena that have not been radar-identified, but have only been identified by conventional techniques. This happens in areas affected by radar geometrical distortions, visibility constraints, N-S

movements and the lacking of ISBAS targets or, eventually, when the landslide velocity is out of the radar range (see A-DInSAR limitation in paragraph 3.2.1).

- **No matching between radar- and conventional-mapped phenomena** (Class 4), areas characterized by the presence of moving ISBAS targets, but not confirmed by conventional procedures.

Class 1 is directly proportional to the precision of the radar data: the higher the values, the more useful the radar information in terms of totally confirming conventionally detected phenomena. Class 2 considers areas where visibility restrictions, direction of motion, geometrical distortions and velocity limits do not permit the detection of the real movement along the slope and, therefore radar-derived landslides partially disagree with conventional-derived landslides. Class 3 encompasses phenomena identified by conventional procedures but not by satellite data because the obstacles quoted for Class 2 are strong to such an extent that satellite gives less information than conventional procedures. Finally, Class 4 collects movements where satellites give additional information because the displacements are imperceptible to the naked eye or are located in places inaccessible to the surveyor.

The CARM bar graph deriving from Sicilian case studies confirms the strong robustness of large-scale landslide mapping when field surveys are coupled with photo- and radar-interpretation because the advantages of one technique compensates for the weaknesses of the other one (fig. 4.63). Indeed 138 conventional-detected instabilities have been fully confirmed (corresponding to Class 1) from the A-DInSAR data. In addition, A-DInSAR data have allowed for the identification of 46 new phenomena (Class 4). Class 1 and 2 together amount for 59% of the 372 events. The 78 events of Class 2 includes landslides whose cartographic evidence (e.g. trend of contour lines, slope morphology, air-photo interpretation) do not perfectly match with the ISBAS data. The problem sometimes derives from the

temporal gap in the years of acquisition of the ancillary data and is intensified in areas with high rates of landscape evolution. Class 3 has an unexpected high value because almost one third of the events have not been recognized by A-DInSAR.

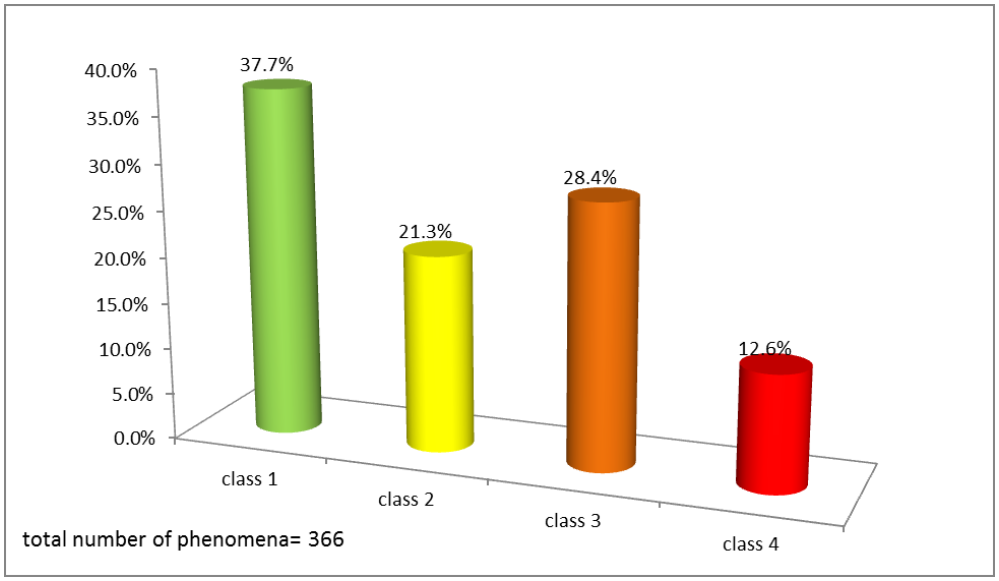

Figure 4.63 – CARM bar graph showing the comparison between conventional techniques and satellite capability in recognizing landslides. Percentages refer to: class 1 - perfect match, class 2 - partial match, class 3 and 4 - no matching between conventional- and radar-mapped phenomena (see text for explanation).

Figure 4.64 highlights how falls, topples and badlands influence the high values recorded for class 3 if the CARM classes are reclassified according to the landslide typology to indicate the number of events that belong to each class. This confirms the weakness of A-DInSAR data for the identification of these kind of events.

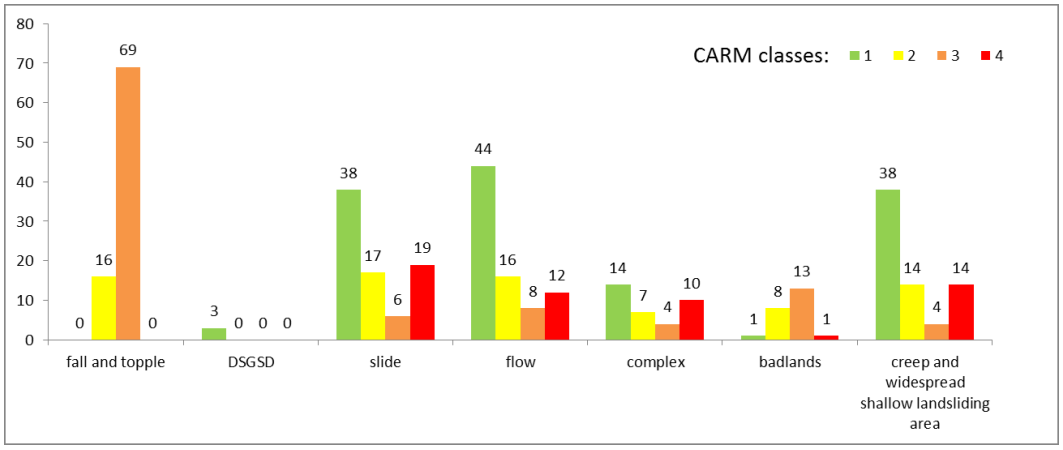

Figure 4.64 – CARM classes reclassification according to the instability typology.

On the other hand, Figure 4.64 also confirms that the best radar performances were achieved for the largest slides, i.e. flows and creep movements, where Class 1 reaches the highest values.

Chapter 5: Discussion

The four case studies demostrate how A-DInSAR techniques represent an efficient procedure for the analysis of slow-moving landslides as complementary tools compared to conventional techniques, particularly suitable for DSGSD, flows and slides.

They supported the geohazard assessment during the landslide mapping stage, the montoring stage and the susceptibility evaluation which also considered, for the first time, the LOS velocity as input layer in the WoE calculation.

The areas have been selected due to:

- their similar geological and geomorphological context, characterized by the presence of SCFs that give origin to slow-moving landslides;

- the unchecked urbanization and land management that have led many buildings and infrastructures to be erected on unstable slopes.

There the A-DInSAR data have been processed, validated, combined and interpreted, stressing the different use from municipal to regional scales. They showed good results that can be still improved and updated thanks to the innovations quoted in chapter 6.

- The investigation revealed that a complex landslide still affects the Termini-Nerano valley (Naples province) where none monitoring network has been established before; it shows the lowest landslide susceptibility compared to the other single-case studies because of the effectively small moving portion of the landslide and the extremely-slow velocity (<5 mm/yr) involved. Despite the ISBAS data allow here for a good radar target coverage, improvements are still possible thanks to the availability of descending data, for limiting the geometrical distorsions, and spaceborne data (from TSX or CSK) with a shorter revisiting time, for increasing the average coherence.

- This study deeply characterizes the DSGSD affecting the entire historical centre of Bisaccia (Avellino province) and just presumed in the previous geotechnical literature. The phenomenon has maximum velocity rates in the order of 30 mm/yr, but the erosional rate of the adjacent valleys represent even higher susceptibility sectors. Either the access to shorter revisiting time images or the use of PO techniques can implement the geomophological analysis to the Corvi and Ferrelli valleys where a total of 76 flows and 20 slides has been already identified.
- Costa della Gaveta (Potenza province) slope represents the most critical area analyzed by far, because 45% of the south-facing hill is subjected to instability due to 16 landslides with mean velocities higher than 10 mm/yr. The multidiscipinary approach supplies a clear and overall description of the phenomena overcoming the discordant inventories produced in the last years with conventional methods. Due to the huge amount of ground truth data, it is anyway expected the possibility of accessing to all of these data for a more consistent comparision with the adopted spaceborne data which represents, apart from Staring Spotlight acquisitions, the best achievable SAR measurements at the present moment.
- The lacking of updated information, in some places for the past 9 years, on the slope evolution represented the challenge pushing for the Sicilian case studies. The unprecedented contribution of the ISBAS alghoritm in the radar coverage of rural areas too has allowed the detection of 345 landslides with a significant contribution for flows, slides and creep movements. Of the three areas, Ventimiglia di Sicilia and, secondarily, Piana degli Albanesi show the highest landslide index, 24% and 22%, respectively, compared to Marineo, 12%. In Sicily the work demonstrates a time and cost efficient way to update the official landslides inventory maps with interferometric procedures, accounting for detailed surveys only for the most critical cases.

Further geological and geomorphological investigation can be still conducted in such a detail to upgrade the WoE evaluation starting from more detailed conditioning layers.

Globally, from point-wise to wide area analyses, this work showed how the integration of innovative techniques and conventional methods is the best way to obtain excellent and unambiguous results for landslide mapping and monitoring in terms of cost-benefit analysis, especially when the innovative methods can account for specific site surveys.

Indeed, whenever and wherever the A-DInSAR drawbacks (point density, geometrical distorsion, visibility and velocity limits) have prevented an adequate slope analysis, conventional monitoring, and in particular ground-truth data, came in support. Furthermore, ground-truth data cannot be completely substituted by A-DInSAR data because the former are always reliable and, at the same time, represent the only way to validate the latter.

Together they have supplied forewarning information about ongoing slope or engineering structure instabilities for small-scale studies while for large-scale analyses they have revealed a huge benefit in updating inventory maps of areas characterized by a slope evolution with predominance of slow-moving processes.

Chapter 6: Conclusion and future work

It is believed that this work sets a good example for enhance future studies of slow landsliding processes using A-DInSAR data and the recent ISBAS technique, through the contributions to knowledge of the research conducted.

Two are the future perspectives identified in this PhD thesis: one concerns the broader distribution of SAR data (1), the other the improvements of the A-DInSAR analysis (2).

1) The updated inventory maps and susceptibility maps produced through this study represent a contribution for the local and regional authorities, in order to give them the possibility to: mitigate landslide susceptibility, carry out further investigations to prevent slope instabilities, to mitigate the resulting damage or to arrange a near-real-time monitoring system (e.g., ADVICE of Allasia *et al*., 2013). These maps demonstrate the convenience of SAR data in land management, so it is expected to get SAR data more easily as an ordinary tool for local public institutions. The latter until now are not aware of the SAR data benefits in spite of the numerous national and international research projects carried out during recent years and confirming the appealing aspects of radar images in prevision, prevention and mitigation of landslides.

Of these project, the most important were: LEWIS (Landslide Early Warning Integrated System, 2002), italian ministry of environment's ESPRE (2002), SLAM (2003), Terrafirma (2003), TELLUS (2006), MORFEO (2008), DORIS (2010) and EC-FP7 PanGeo (2011).

The continous demanding of SAR data legitimizes the launch of the ESA Sentinel-1 mission in 2014 aimed at ensuring data continuity for global land surface monitoring with a free availability to all users via a simple pre-registration at https://scihub.esa.int/.

2) The A-DInSAR techniques, despite their wide application, still now represent a relatively new scientific field for Earth sciences applications and in particular for landslide investigations. Therefore it

is worth placing particular attention, in the near future, to ongoing improvements ensured by new sensors (2a), algorithms (2b) and interpretation procedures (2c). They will be aimed to guarantee better and reliable results, setting up long archives but also to involve slope phenomena leaved aside by A-DInSAR analysis until now: the fast moving landslides (falls, topples and debris flows) even in highly vegetated areas.

2a) The wider diffusion and newest acquisition from TerraSAR-X Staring Spotlight, KOMPSAT-5, Sentinel 1-A TOPSAR (De Zan and Guarnieri, 2006), ALOS-2 and PAZ sensors, will permit to obtain wider coverage from SAR images along with more detailed and updated information, sometimes immediately after the event, as a consequence of the reduced revisit time and/or the improved spatial resolution.

Increasing the acquisition of SAR images means more opportunities to obtain radar data with the suitable viewing angle in terms of incident angle and azimuth direction for a specific morphology, the only action able to overcome or limit the geometrical distorsion effects.

In fact the terrain distorsion related to the side-looking mode of SAR acquisitions proved to be a significant obstacle nowadays, especially in mountainous areas, with evident constraints on the feasibility of radar analysis. The solution comes from the Circular-scanning airborne SAR system where both sides of the flight path can be illuminated synchronously by steering the radar antenna to rotate continuously around with the vertical axis pointing to the Earth surface. This operating scenario provides observation of targets over a complete azimuthal coverage of 360 degrees, achieving highly sharp resolved images when compared to linear SAR acquisitions. Additionally, the resolution in vertical direction and hence the height information of the scene can be obtained by the help of a single pass of the radar only (Li and Zhu, 2010).

2b) The development of processing algorithms will be important to, firstly, obtain as much information as possible from SAR images and, secondly, improve the accuracy at sub-millimeter precision. Recently to obtain additional information from radar images, new algorithms (e.g., ISBAS SqueeSAR™) are able to evaluate distributed scatterers corresponding to low-reflectivity homogeneous areas or intemittently coherence pixels in the phase component. Other times, as occurred in the Temporal Sublook Coherence of Iglesias *et al*. (2015), the methods estimate the pixels' phase quality by exploiting the spectral properties of pointlike scatterers through the coherence evaluation of different sublooks of the image spectrum along a multitemporal set of SAR images. Contrary to standard PS techniques, the TSC is able to work even if the number of images available is small, typically less than 20.

In the case of rapid moving phenomena instead, the analysis of the amplitude component of the microwave signal, through the PO techiques, has been exploited. Despite the worse accuracies than InSAR (between 1/10 and 1/30 pixel size), PO has the advantages of an additional measurement in the azimuth direction (nearly parallel to the N–S), better resistance to the phase decorrelation and no need for phase unwrapping,which are all essential for the investigation of earthquake, volcanic eruption and glacier movements (Manconi and Casu, 2012).

Further improvement of accuracy can be obtained trough the regular use of high precision DEMs (pixel size of 1 m) of LiDAR and TanDEM-X derivation. The latter, launched in 2014 by the German Aerospace Center (DLR), is the TerraSAR-X's twin satellite and together fly in a closely controlled formation with typical distances between 250 and 500 m.

Finally new correction methods are now under developing to correct errors in the satellite orbits (Fattahi and Amelung, 2014) and tropospheric (Bekaert *et al*., 2015) that still generate evident uncertainties in the LOS estimation.

In recent years, great efforts have been made to resolve complete three-dimensional displacements from SAR measurements (Hu *et al*., 2014). The the amplitude-based PO and phase-based MAI techniques allow to measure the surface displacement in the azimuth direction together with the range and LOS displacement, respectively.

2c) The improving of a A-DInSAR interpretation procedures for landslide investigation is, by far, the most important contribution derivable from Earth scientists, especially for large scale studies.

From this point of view, it will be important to consider, in addition to SAR images, other remote sensing techniques (Scaioni *et al*., 2014): Unmanned Aerial Vehicles (UAV; Torrero *et al*., 2015), optical sensors (Lacroix *et al*., 2013) and Terrestrial Laser Scanner (Jaboyedoff *et al*., 2012). They have not been constantly exploited up, nor have been considered in this work but can guarantee new and unique data for landslide investigations anyway. These data could be adopted for landslide recognition, monitoring and susceptibility assessment (Scaioni, 2013).

The use of UAV aircrafts have been proposed for low-cost mapping application (Neitzel and Klonowski, 2011) and to generate orthophotos of areas affected by landslide phenomena.

Optical sensors allows for the recognition of different land covers and soil moisture content through the spectral information associated to each pixel (Santurri *et al*., 2010) and, finally, TLS helps in local scale investigation deriving high-resolution DEMs.

In conclusion remote sensing techniques, including A-DInSAR, are very promising but still require further development, which will be only possible thanks to their continuos application to different fields, among which the assessment of landslide hazard stands for a top-rank position.

References

Accaino F., Catalano R., Di Marzo L., Giustiniani M., Tinivella U., Nicolich R., Sulli A., Valenti V., Manetti P., 2011. *A crustal seismic profile across Sicily*. Tectonophysics, v.**508**: 52–61.

AdB Destra Sele, 2011. PAI, Piano Stralcio di Bacino per l'Assetto Idrogeologico. (in Italian)

AdB Sicilia, 2006 [online]. PAI, Piano Stralcio di Bacino per l'Assetto Idrogeologico. http://www.sitr.regione.sicilia.it/pai/ [Accessed 19 June 2014]. (in Italian)

Agliardi F., Crosta G., Zanchi A., 2001. *Structural constraints on deep-seated slope deformation kinematics*. Engineering Geology, v.**59**: 83-102.

Ahrens C. D., 2007. Meteorology Today: *An Introduction to Weather, Climate, and the Environment, 8th edition*. Thomson Brooks/Cole, Belmont, CA.

Aldiss D.T., Burke H.F., Chacksfield B., Bingley R., Teferle N., Williams S., Blackman D., Burren R., Press N., 2014. *Geological interpretation of current subsidence and uplift in the London area, UK, as shown by high precision satellite-based surveying*. Proceedings of the Geologists' Association, v.**125**: 1–13.

Alexander D., 1992. *On the Causes of Landslides: Human Activities, Perception, and Natural Processes*. Environmental Geology and Water Sciences, v.**20**: 165-179.

Allasia P., Manconi A., Giordan D., Baldo M., Lollino G., 2013. ADVICE: *A New Approach for Near-Real-Time Monitoring of Surface Displacements in Landslide Hazard Scenarios*. Sensors, v.**13**(7): 8285-8302. doi:10.3390/s130708285

Amadesi E., Vianello G., Bonfatti G., Pignone R., Preti D., 1977. *Guida alla realizzazione di una carta della stabilitā dei versanti. Regione Emilia Romagna*. Pitagora (ed), Bologna, 72pp. (in Italian)

Amato A., Cocco M., Pantosti D., Valensise G., 1989. *Investigating a complex earthquake with a multidisciplinary approach: the 1980, Irpinia, normal faulting event (M_s 6.9)*. EOS Transaction, American Geophysical Union, v.**70**: 1226.

Antonini G., Ardizzone F., Cardinali M., Galli M., Guzzetti F., Reichenbach P., 2002. *Surface deposits and landslide inventory map of the area affected by the 1997 Umbria-Marche earthquakes*. Bollettino della Societa Geologica Italiana, v.**121** (2): 843–853.

Atzori, 2013. *Understanding earthquakes: The key role of radar images*. Nuclear Instruments and Methods in Physics Research, v.**720**: 178–181.

Ausilio E., Silvestri F., Troncone A. Tropeano G., 2007. *Seismic displacement analysis of homogeneous slopes: a review of existing simplified methods with reference to Italian seismicity*. Proceedings of the "International Conference on Earthquake Geotechnical Engineering", Thessaloniki.

Bardi F., Frodella W., Ciampalini A., Bianchini S., Del Ventisette C., Gigli G., Fanti R., Moretti S., Basile G., Casagli N., 2014. *Integration between ground based and satellite SAR data in landslide mapping: The San Fratello case study*. Geomorphology, v.**223**: 45–60.

Barreca G., Maesano F.M., Carbone S., 2010. *The Tyrrhenian stage geodinamic evolution of Apenninic-Maghrebian orogen (Southern Apennines and Sicily)*. Italian Journal of Geosciences, v.**129**: 429-440.

Basilone L., 2011. *Geological Map of the Rocca Busambra-Corleone region (western Sicily, Italy): explanatory notes*. Bollettino della Società Geologica Italiana, v.**130**: 42-60.

Basso C., Ciampo G., Ciarcia S., Di Nocera S., Matano F., Torre M., 2002. *Geologia del settore irpino-dauno dell'Appennino meridionale: implicazioni sui domini paleo-geografici delle unità bacinali meso-cenozoiche e nuovi vincoli stratigrafici nell'evoluzione tettonica mio-pliocenica del settore esterno della catena*. Studi Geologici Camerti, v.**2**: 7-27. (in Italian)

Basso C., Di Nocera S., Esposito P., Matano F., Russo B., Torre M., 2001. *Stratigrafia delle successioni sedimentarie evaporitiche e post-evaporitiche del Messiniano superiore in Irpinia settentrionnale (Appennino meridionale)*. Bollettino della Società Geologica Italiana, v.**120**: 3-14. (in Italian)

Bateson L., Cigna F., Boon D., Sowter A., 2015. *The application of the Intermittent SBAS (ISBAS) InSAR methodto the South Wales Coalfield, UK*. International Journal of Applied Earth Observation and Geoinformation, v.**34**: 249–257.

Bechor N., Zebker H., 2006. Measuring two-dimensional movements using a single insar pair. Geophysical Research Letters, v.**33**: L16311.

Bekaert D.P.S., A. Hooper, T. J. Wright, 2015. *A spatially variable power law tropospheric correction technique for InSAR data*. J. Geophys. Res. Solid Earth, v.**120**: 1345–1356. DOI:10.1002/2014JB011558.

Berardino P., Fornaro G., Lanari R., Sansosti E., 2002. *A new Algorithm for Surface Deformation Monitoring based on Small Baseline Differential SAR Interferograms*. IEEE Transactions on Geoscience and Remote Sensing, v.**40**(11): 2375-2383.

Bernoulli D., Jenkins H.C., 1974. Alpine, Mediterranean and Central Atlantic Mesozoic facies in relation to the early evolution of the Tethys. In 'Modern and Ancient Geosynclinal Sedimentation', Dott R., Shaver R. (eds), Soc. Econ. Paleontol. Mineral, Spec. Publ., v.**19**:129-160.

Bianchini S., Cigna F., Righini G., Proietti C., Casagli N., 2012. *Landslide HotSpot Mapping by means of Persistent Scatterer Interferometry*. Environ. Earth Sci., v.**67**:1155–1172

Bianconi P., 1940. *Storia naturale dei terreni ardenti, dei vulcani fangosi, delle sorgenti infiammabali, dei pozzi idroppirici e di altri fenomeni geologici oprati dal gas idrogeno e dell'origine di esso gas*. Marsigli, Bologna: 164pp. (in Italian)

Bilotta E., Pellegrino A., Picarelli L., 1985. *Geotechnical properties and slope stability in structurally complex clay soils*. In Geotechnical Engineering in Italy. An overview. Golden Jubilee Volume, A.G.I..

Blanco-Sanchez P., Mallorquí J. J., Duque S., Monells D., 2008. *The Coherent Pixels Technique (CPT): An advanced DInSAR technique for nonlinear deformation monitoring*. Pure and Applied Geophysics, v. **165**: 1167-1194.

Bonardi D., Amore F.O. Ciampo G., De Capoa P., Miconnet P., Perrone V., 1988. *Il Complesso Liguride Auct.: stato delle conoscenze e problemi aperti sull'evoluzione pre-appenninica ed i suoi rapporti con l'Arco Calabro*. Memorie della Società Geologica Italiana, v.**41**: 17-35. (in Italian)

Bonardi G., Ciarcia S., Di Nocera S., Matano F., Sgrosso I., Torre M. 2009. *Carta delle principali unità Cinematiche dell'Appennino meridionale*. Bollettino della Società Geologica Italiana, v.**128**: 47-60. (in Italian)

Bonham-Carter G.F., Agterberg F.P., Wright D.F., 1989. *Weights of evidence modeling: a new approach to mapping mineral potential*. In 'Statistical Applications in the Earth Sciences', Agterberg F.P., Bonham-Carter G.F. (eds), Geological Survey Canada Paper, v.**89**(9): 171-183.

Borgatti L., Corsini A., Barbieri M., Sartini G., Truffelli G., Caputo G., Puglisi C., 2006. *Large reactivated landslides in weak rock masses: a case study from the Northern Apennines (Italy)*. Landslides, v.**3**: 115–124.

Brancaccio L., 1968. *Genesi e caratteri delle forme costiere nella Penisola sorrentina*. Bollettino Società dei Naturalisti in Napoli, v.**77**: 247-274. (in Italian)

Brunsden, D., 1985. *Landslide types, mechanisms, recognition, identification*. In: Morgan, C.S. (ed), Landslides in the South Wales Coalfield, Proceedings Symposium. The Polytechnic of Wales: 19-28.

Brunsden, D., 1993. *Mass movements; the research frontier and beyond: a geomorphological approach*. Geomorphology, v.**7**: 85–128.

Butler W.H.R., Grasso M., La Manna F., 1992. *Origin and deformation of the Neogene-Recent Maghrebian foredeep at Gela Nappe, SE Sicily*. Journal of the Geological Society of London, v.**149**: 547-556.

Butler W.H.R., Grasso M., 1993. *Tectonic controls on base-level variation and depositional sequences within thrust-top and foredeep basins: examples from the Neogene thrust belt of central Sicily*. Basin Research, v.**5**: 137-151.

Calcaterra S., Cesi C., Di Maio C., Gambino P., Merli K., Vallario M., Vassallo R., 2012. *Surface displacements of two landslides evaluated by GPS and inclinometer systems: a case study in Southern Apennines, Italy*. Natural Hazards, v.**61**: 257–266.

Calcaterra D., Di Martire D., Ramondini M., Calò F., Parise M., 2008. *Geotechnical analysis of a complex slope movement in sedimentary successions of the southern Apennines (Molise, Italy)*. In: Landslides and Engineered Slopes. Chen et al. eds., Taylor & Francis Group, London: 299-305.

Calcaterra D., Parise M., Palma B., 2003. *Combining historical and geological data for the assessment of the landslide hazard: a case study from Campania, Italy*. Natural Hazards and Earth System Sciences, v.**3**: 3–16.

Calcaterra D., Riso R., Di Martire D., 2004. *Assessing shallow debris slide hazard in the Agnano Plain (Naples, Italy) using SINMAP, a physically based slope-stability model*. In 'Landslides: evaluation and stabilization, Lacerda W., Ehrlich M., Fontoura S.A.B., Sayao A.S.F. (eds), Taylor & Francis Group, Rio de Janeiro: 177–183.

Capparelli G., Versace P., 2014. *Analysis of landslide triggering conditions in the Sarno area using a physically based model*. Hydrology and Earth System Sciences, v.**18**: 3225–3237.

Carbone S., Catalano S., Lazzari S., Lentini F., Monaco C., 1991. *Presentazione della carta geologica del Bacino del Fiume Agri (Basilicata)*. Memorie della Società Geologica Italiana, v.**47**: 129-143. (in Italian)

CARG, 2010a. *Note illustrative della Carta Geologica d'Italia: foglio 484 – Isola di Capri*. ISPRA. (in Italian)

CARG, 2010b. *Note illustrative della Carta Geologica d'Italia: foglio 607 - Corleone*. ISPRA. (in Italian)

CARG, 2010c. *Note illustrative della Carta Geologica d'Italia: foglio 608 - Caccamo*. ISPRA. (in Italian)

CARG, 2011. *Note illustrative della Carta Geologica d'Italia: foglio 484 - Capri*. ISPRA. (in Italian)

Casciello E., Cesarano Mas., 2000. Geological cross sections through the upper Ofanto Valley – relationship between tectonics and deposition in a piggy-back basin. Memorie della Società Geologica Italiana, v.55: 157–163.

Cascini L., Fornaro G., Peduto D., Ferlisi S., Di Nocera S., 2009. *A new approach to the use of dinsar data to study slow-moving landslides over large areas*. Proceedings of the 'Fringe 2009 Workshop', Frascati, Italy, 30 November - 4 December 2009.

Casero P., Roure F., Endignoux L., Moretti I., Muller C., Sage L., Vially R., 1988. *Neogene geodynamic evolution of the Southern Apennines*. Memorie della Società Geologica Italiana, v.**41**: 109-120.

Castelluccio R., 2010. *La franosità dell'abitato di Bisaccia e tipologie di interventi di sistemazione*. Master's degree Thesis, University of Naples. (in Italian)

Catalano R., D'Argenio B., 1978. *An essay of palinspastic restoration across the western Sicily*. Geologica Romana, v.**17**: 145-159

Catalano R., Franchino A., Merlini S., Sulli A., 2000. *Central western Sicily structural setting interpreted from seismic reflection profiles*. Mem. Soc. Geol. It., v.**55**: 5-16.

Catalano R., Merlini S., Sulli A., 2002. *The structure of western Sicily, central Mediterranean*. Petroleum Geoscience, v.**8**: 7-18.

Catalano R., Avellone G., Basilone L., Sulli A., 2010. *Note illustrative della Carta Geologica d'Italia alla scala 1:50000, foglio 607 "Corleone". Regione Siciliana*. ISPRA, SystemCart, 190pp. (in Italian)

Catalano S., Monaco C., Tortorici L., Paltrinieri W., Steel N., 2004. *Neogene-Quaternary tectonic evolution of the southern Apennines*. Tectonics, v.**23**, TC2003, doi:10.1029/2003TC001512.

Catani F, Farina P, Moretti S, Nico G, Strozzi T., 2005. *On the application of SAR interferometry to geomorphological studies: estimation of landform attributes and mass movements*. Geomorphology, v.**66**: 119-131.

Cello G., Mazzoli S., 1999. *Apennine tectonics in southern Italy: a review*. Geodynamics, v.**27**: 191-211.

Cesarano Mar., 2014. *Mineralogical and geotechnical characterization of Structurally Complex Formations involved in the slow moving landlides affecting the Southern Apennine*. PHD thesis, Federico II University of Naples, Department of Earth, Environment and Resources Sciences, Naples, Italy.

Cesarano Mar., Bish D.L., Cappelletti P., Belviso C., Cavalcante F., Fiore S., De Vita P., Langella A., de Gennaro M., 2013. *Understanding slope instability mechanisms through mineralogical characterization: the case history of the slow-moving Termini Nerano (Southern Italy) Landslide*. Proceedings of the XV International Clay Conference, Rio de Janeiro, July 7-11.

Chaussard E., Wdowinski S., Cabral-Cano E., Amelung F., 2014. *Land subsidence in central Mexico detected by ALOS InSAR time-series*. Remote Sensing of Environment, v.**140**: 94–106.

Cheng K.S., Wei C., Chang S.C., 2004. *Locating landslides using multi-temporal satellite image*s. Adv. Space Res. 2004, v.**33**: 96–301.

Chiocchio C., Iovine G., Parise M., 1997. *A proposal for surveying and classifying landslide damage to buildings in urban areas*. Proceedings of 'International Symposium Engineering Geology and the Environment', Athens, 23-27, 553-558.

Ciampalini A., Bardi F., Bianchini S., Frodella W., Del Ventisette C., Moretti, S., Casagli, N., 2014. *Analysis of building deformation in landslide area usingmultisensor PSInSAR™ technique*. Int. J. Appl. Earth Obs. Geoinform., v.**33**: 166–180.

Ciaranfi N., Dazzaro L., Pieri P., Rapisardi L., Sardella A., 1973. *Geologia della zona compresa fra Bisaccia (Av) ed il T. Olivento, presso Lavello (PZ)*. Memorie della Società Geologica Italiana, v.**12**: 279-315. (in Italian)

Ciarcia S., Mazzoli S., Vitale S., Zattin M., 2012. *On the tectonic evolution of the Ligurian accretionary complex in southern Italy*. Geological Society of America Bulletin, v.**124**: 463–483.

Ciarcia S., Tramparulo F.A., Vitale S., 2012. *Structural analysis and stratigraphy of Internal units (Calabria-Lucania boundary, Southern Italy)*. Rendiconti Online della Società Geologica Italiana, v. **21**: 77-79.

Cigna F., Bateson L., Jordan C., Dashwood C., 2013. *Nationwide monitoring of geohazards in Great Britain with InSAR: feasibility mapping based on ers-1/2 and Envisat imagery*. IEEE International Geoscience Remote Sensing Symposium, (IGARSS): 672-675.

Cigna F., Bianchini S., Casagli N., 2012. *How to assess landslide activity and intensity with Persistent Scatterer Interferometry (PSI): the PSI-based matrix approach*. Landslides, v.**10**(3): 267-283.

Cigna F., Del Ventisette C., Liguori V., Casagli N., 2011. *Advanced radar-interpretation of InSAR time series for mapping and characterization of geological processes*. Nat. Hazards Earth Syst. Sci., v.11: 865-881.

Cigna F., Novellino A., Jordan C.J., Sowter A., Ramondini M., Calcaterra D., 2014. *Intermittent SBAS (ISBAS) InSAR with COSMO-SkyMed X-band high resolution SAR data for landslide inventory mapping in Piana degli Albanesi (Italy)*. Proceedings of the "SPIE SAR Image Analysis, Modeling, and Techniques XIV" conference, v. **9243**.

Cocco E., Pescatore T., 1967. *L'evoluzione della sedimentazione miocenica nella penisola sorrentina*. Boll. Soc. Natur. in Napoli, v.**76**: 597-638. (in Italian)

Colangelo G., Lapenna V., Perrone A., Piscitelli S., Telesca L., 2006. *2D Self-Potential tomographies for studying groundwater flows in the Varco d'Izzo landslide (Basilicata, southern Italy)*. Engineering Geology, v.**88**: 274-286.

Colesanti C., Wasowski J., 2006. *Investigating landslides with space-borne Synthetic Aperture Radar (SAR) interferometry*. Engineering Geology, v.**88**: 173–199.

Cooper R.G., 2008. *Mass Movements in Great Britain*. Geological Conservation Review Series, Joint Nature Conservation Committee, Peterborough, v.**33**.: 348pp.

Confuorto P., Di Martire D., Ramondini M., Calcaterra D., 2014. *Differential SAR interferometry for slow-moving landslide monitoring in Crotone Province (Italy)*. Proceedings of 'the Analysis and Management of Changing Risks for Natural Hazards conference', Padua, 18-19 November.

Corominas J., van Westen C., Frattini P. Cascini L., Malet J.P., Fotopoulou S., Catani F., Van Den Eeckhaut M., Mavrouli O., Agliardi F., Pitilakis K., Winter M.G., Pastor M., Ferlisi S., Tofani V., Herva´s J., Smith J.T., 2014. *Recommendations for the quantitative analysis of landslide risk*. Bull Eng Geol Environ, v.**3**: 209–263.

Cosentino D., Cipollari P., Marsili P., Scrocca D., 2010. *Geology of the central Apennines: a regional review*. In 'The geology of Italy: tectonics and life along plate margins', Beltrando M., Peccerillo A., Mattei M., Conticelli S., Doglioni C. (eds), Journal of the Virtual Explorer, v.**36**. http://dx.doi.org/10.3809/jvirtex.2010.00223 (paper 12).

Cosentino D., Cipollari P., Pipponzi G., 2003. *Il sistema orogenico dell'Appennino centrale: vincoli stratigrafici e cronologia della migrazione*. In 'Evoluzione cinematica del sistema orogenico dell'Appennino centro-meridionale: caratterizzazione stratigrafico-strutturale dei bacini sintettonici', Cipollari P., Cosentino D. (eds), Studi Geologici Camerti, Numero Speciale 2003: 85–99. (in Italian)

Cosenza F., 2013. *Analisi geologico-tecnica della frana di Termini-Nerano*. Master's degree Thesis, University of Naples. (in Italian)

Costantini, M., Iodice A., Magnapane L., Pietranera L., 2000. *Monitoring terrain movements by means of sparse SAR differential interferometric measurements*. Proceedings of the IGARSS 2000, Honolulu, USA: 3225–3227.

Costantini M., Falco S., Malvarosa F., Minati F., 2008. *A new method for identification and analysis of persistent scatterers in series of SAR images*. Proceedings of the IGARSS, Boston, 6-11 July, v.**2**: 449–452.

Cotecchia V., Melidoro G., 1966. *Geologia e frana di Termini-Nerano (Penisola Sorrentina)*. Geologia Applicata e Idrogologia, v.**1**: 93-122.

Cotecchia F., Polemio M. Santaloia F., 2001. *Mechanics of a tectonized soil slope: influence of boundary conditions and rainfall*. Quarterly Journal of Engineering Geology and Hydrogeology, v.**34**: 165-185.

Crosetto M., Biescas E., Duro J., Closa J., Arnaud, A., 2008. *Generation of Advanced ERS and Envisat Interferometric SAR Products Using the Stable Point Network Technique*. Photogrammetric Engineering and Remote Sensing, v.**74**(4): 443–451.

Crosetto M., Monserrat O., Iglesias R., Crippa B., 2010. *Persistent scatterer interferometry: potential, limits and initial C- and X-band comparison*. Photogrammetric Engineering and Remote Sensing, v.**76** (9): 1061–1069.

Crozier M.J., 1989. *Landslides: causes, consequences and environment*. Taylor & Francis, Routledge.

Cruden D. M., 1991. *A simple definition of a landslide*. Bulletin International Association for Engineering Geology, v.**43**: 27–29.

Cruden D.M., Varnes D.J., 1996. *Landslides Types and Processes*. In Landslides: Investigation and Mitigation. Transportation Research Board Special Report, v.**247**,: 36–75.

Czuchlewski K.R., Weissel, J.K., Kim, Y., 2003. *Polarimetric synthetic aperture radar study of the Tsaoling landslide generated by the 1999 Chi-Chi earthquake, Taiwan*. Journal of Geophysical Research, v.**108**: doi: 10.1029/2003JF000037.

D'Elia B., 1991. *Deformation problems in the Italian structurally complex clay soils*. Proceedings of the "10th European Conference On Soil Mechanic and Foundation Engineering", Florence, v.**4**: 1159-1170.

Dai F.C., Lee C.F., 2002. *Landslide characteristics and slope instability modeling using GIS, Lantau Island, Hong Kong*. Geomorphology, v.**42**: 213– 228.

De Blasio I., Lima A., Perrone V., Russo M., 1981. *Nuove vedute sui depositi miocenici della Penisola Sorrentina*. Bollettino della Società Geologica Italiana, v.**100**: 57-70.

De Luca D.L., 2014. *Analysis and modelling of rainfall fields at different resolutions in southern Italy*. Hydrological Sciences Journal, v.**56**(8): 1536-1558. DOI: 10.1080/02626667.2014.926013

De Zan F., Guarnieri A.M., 2006. *TOPSAR: Terrain observation by progressive scans*. IEEE Trans. Geosci. Remote Sens., v.**44**: 2352–2360.

Debella-Gilo M., Kääb A., 2012. *Measurement of surface displacement and deformation of mass movements using Least Squares Matching of repeat high resolution satellite and aerial images*. Remote Sens., v.**4**: 43-67.

Del Gaudio V., Wasowski J., Pierri R, Mascia U,. Calcagnile G., 2000. *Gravimetrie study of a retrogressive landslide in southern Italy*. Surveys in Geophysics, v.**21**(4): 391-406.

Del Prete M., Giaccari E., Trisorio-Liuzzi G., 1992. *Rischio da frane intermittenti a cinematica lenta nelle aree montuose e collinari urbanizzate della Basilicata*. Gruppo Nazionale per la Difesa dalle Catastrofi Idrogeologiche, v.**841**: 84 pp. (in Italian)

Di Maio, C., Vassallo, R., Vallario, M., Pascale, S., Sdao, F., 2010. *Structure and kinematics of a landslide in a complex clayey formation of the Italian Southern Apennines*. Engineering Geology, v.**116**: 311–322.

Di Maio C., Vallario M., Vassallo R., 2013. *Plastic and viscous shear displacements of a deep and very slow landslide in stiff clay formation*. Engineering Geology, v.**162**: 53–66.

Di Maio C., Vallario M., Vassallo R., Bianca M., 2012. *Displacements of a large landslide in structurally complex clays*. In: Landslides and Engineered Slopes. CRC Press, v.**2**: 1189-1194.

Di Martire D., De Rosa M., Pesce V., Santangelo M.A., Calcaterra D., 2012. *Landslide hazard and land management in high-density urban areas of Campania region, Italy*. Natural Hazards Earth System Science, v.**12**: 905–926.

Di Martire D., Iglesias R., Monells D., Centolanza G., Sica S., Pagano L., Mallorquì J.J., Calcaterra D., 2014. *Comparison between Differential SAR interferometry and ground measurements data in the displacement monitoring of the earth-dam of Conza della Campania (Italy)*. Remote Sensing of Environment, v.**148**: 58-69.

Di Martire D., Ramondini M., 2012. *Integrazione di tecniche di monitoraggio da terra e da satellite per lo studio di due frane a cinematica lenta*. Incontro Annuale dei Ricercatori di Geotecnica - IARG 2012 Padua, 2-4 July. (in Italian)

Di Martire D., Ramondini M., Calcaterra D., Nirchio F., 2013. *Risultati preliminari del monitoraggio interferometrico di una frana a cinematica lenta mediante differenti sensori SAR in banda X*. Incontro Annuale dei Ricercatori di Geotecnica - IARG 2013 Perugia, 16-18 September. (in Italian)

Di Nocera, S., Fenelli G. B., Iaccarino G., Pellegrino A., Picarelli L., Urciuoli, G., 1995. *An example of the geotechnical implications of geological history*. In: Proceedings of the 11th European Conference on Soil Mechanics and Foundation Engineering, "The interplay between Geotechnical Engineering and Engineering Geology", Copenhagen, v.**8**: 39–48.

Di Nocera S., Matano F., Pinto F., 2011. *Caratteri geologici e stratigrafici del settore esterno dell'Appennino sannitico-irpino (Campania, Italia)*. Rendiconti online della Società Geologica Italiana, v.**17**: 95-98. (in Italian)

Dikau R., Brundsen D., Schrott L., Ibsen M.L., 1996. *Landslide Recognition: Identification, Movement and Causes*. Wiley, Chichester, 251pp.

Doglioni C., Harabaglia P., Martinelli G., Mongelli F., Zito G., 1996. *A geodynamic model of the southern Apennines accretionary prism*. Terra Nova, v.**8**: 540 – 547.

Donnelly L.J., Culshaw M.G., Hobbs P.R.N., Flint R.C., Jackson P.D., 2005. *Engineering geological and geophysical investigations of a slope failure at Edinburgh Castle, Scotland*. Bulletin of engineering geology and the environment, v.**64**(2):119-137.

DORIS, 2010 [online]. Ground Deformations Risk Scenarios: an Advanced Assessment Service. Global Monitoring for Environment and Security program. http://www.doris-project.eu/ [accessed on 13 November, 2014]

Dunnicliff, J., 1988. *Geotechnical Instrumentation for monitoring field performance*. Wiley (ed), New York, 608 p.

EC-FP7 PanGeo [online]. http://www.pangeoproject.eu/ [accessed on 13 November, 2014]

EEA, 2006 [online]. Urban Atlas. http://www.eea.europa.eu/data-and-maps/data/urban-atlas [accessed on 9 September, 2013]

EEA, 2007 [online]. *CLC2006 Technical Guidelines*. European Environment Agency (EEA)Technical report No. 17/2007., pp. 70. http://www.eea.europa.eu/publications/technical_report_2007_17 [accessed on 9 September, 2013]

EPRSE, 2002 [online]. Ministry of Environment and Territory of the Sea. http://www.pcn.minambiente.it/GN/progetto_pst.php?lan=en [accessed on 13 November, 2014]

ESA, 2007. *InSAR Principles: Guidelines for SAR Interferometry Processing and Interpretation, v.A-B*. Karen Fletcher, Noordwijk.

Esu F., 1977. *Behaviour of slopes in structurally complex formations*. Proceedings of the "International Symposium on the geotechnics of Structurally Complex Formations", Capri: 292–304.

Faccenna C., Funiciello F., Giardini D., Lucente P., 2001a. *Episodic back-arc extension during restricted mantle convection in the central Mediterranean*. Earth and Planetary Science Letters, v.**187**(1-2): 105 – 116.

Faccenna C., Becker T. W., Lucente F. P., Jolivet L., Rossetti F., 2001b. *History of subduction and back-arc extension in the central Mediterranean*. Geophysical Journal International, v.**145**: 809 – 820.

Fattahi H., Amelung F., 2014. *InSAR uncertainty due to orbital errors*. Geophys. J. Int., v.**199**: 549–560.

Fedele L., Scarpati C., Lanphere M., Melluso L., Morra V., Perrotta A., Ricci G., 2008. *The Breccia Museo formation, Campi Flegrei, southern Italy: geochronology, chemostratigraphy and relationship with the Campanian Ignimbrite eruption*. Bull Volcanol, v.**70**: 1189–1219.

Fell R., Corominas J., Bonnard C., Cascini L., Leroi E., Savage W., 2008. *Guidelines for landslide susceptibility, hazard and risk zoning for land use planning*. Engineering Geology, v.**102**: 85–98.

Fenelli G.B., 1986. *Alcuni peculiari aspetti relativi alla stabilità del colle di Bisaccia*. Atti 16° Convegno Nazionale di Geotecnica, Bologna, v.**3**: 191-196. (in Italian)

Fenelli G.B., Picarelli L., 1990. *The pore pressure field built up in a rapidly eroded soil mass*. Canadian Geotechnical Journal, v.**XXVII**: 387-392.

Fenelli G.B., Picarelli L., Silvestri F., 1992. *Deformation process of a hill shaken by the Irpinia earthquake in 1980*. Proceedings of the "Colloquio Italo-Francese su Stabilità dei Pendii in Zona Sismica", Bordighera: 47-62.

Ferretti A., Fumagalli A., Novali F., Prati C., Rocca F., Rucci A., 2011. *A new algorithm for processing interferometric data-stacks: SqueeSAR*. IEEE Transactions on Geoscience and Remote Sensing. http://dx.doi.org/10.1109/TGRS.2011.2124465.

Ferretti A., Prati C., Rocca F., 2001. *Permanent Scatterers in SAR Interferometry*. IEEE Transactions on Geoscience and Remote Sensing, v. **39** (I): 8-20.

Fiorillo F., Parise M., Wasowski J., 1996. *Slope instability in the Bisaccia area (Southern Apennines, Italy)*. Proc. 7th Int. Symp. on Landslides, v.**2**: 965–970.

Fornaro, G., Pauciullo, A., Serafino, F., 2007. *Multipass SAR Processing for urbanized areas imaging and deformation monitoring at small and large scales*. Urban Remote Sensing Joint Event URS 2007, Paris, 11-13 April.

Franklin A.J.,1984. *Slope instrumentation and monitoring*. In 'Slope Instability', Brunsden D. Prior D. B., John Wiley and Sons (eds), 1-25.

Frizon de Lamotte D., Raulin C., Mouchot N., Wrobel-Daveau J.-C., Blanpied C., Ringenbach J.C., 2011. *The southernmost margin of the Tethys realm during the Mesozoic and Cenozoic: initial geometry and timing of the inversion processes*. Tectonics, v.**30**, TC3002. http://dx.doi.org/10.1029/2010TC002691.

Gallicchio S., Marcucci M., Pieri P., Premolisilva I., Sabato L., Salvini G., 1996. *Stratigraphical data from a Cretaceous claystones sequence of the 'Argille Varicolori' in the Southern Apennines (Basilicata, Italy)*. Palaeopelagos, v.**6**: 261–272.

Giordan D., Allasia P., Manconi A., Baldo M., Santangelo M., Cardinali M., Corazza A., Albanese V., Lollino G., Guzzetti F., 2013. *Morphological and kinematic evolution of a large earthflow: The Montaguto landslide, southern Italy*. Geomorphology, v.**187**: 61–79.

Glade T, Stark P., Dikau R., 2005. *Determination of potential landslide shear plane depth using seismic refraction - a case study in Rheinhessen, Germany*. Bulletin of Engineering Geology and the Environment, v.**64**(2): 151-158.

Goldstein R. M., 1995. *Atmospheric limitations to repeat-track radar interferometry*. Geophysical Research Letters, v.22: 2517–2520.

Guerrera F., Martín-Martín M., Perrone V., Tramontana M., 2005. *Tectono-sedimentary evolution of the southern branch of the Western Tethys (Maghrebian Flysch Basin and Lucanian Ocean): consequences for Western Mediterranean geodynamics*. Terra Nova, v.**17**: 358–367.

Guha-Sapir D., Hoyois P., Below R., 2013. *Annual Disaster Statistical Review 2012: The Numbers and Trends*. Centre for Research on the Epidemiology of Disasters.

Guida D., Iaccarino G., Lanzara R., Peduto F., 1995. *Proposal of a landslide taxonomic classification*. Proceedings of the "5th annual scientific conference of the Earth Sciences Department, Federico II University of Naples". (in Italian)

Guzzetti F., Carrara A., Cardinali M., Reichenbach P., 1999. *Landslide hazard evaluation: an aid to a sustainable development*. Geomorphology, v.**31**: 181-216.

Guzzetti F., Reichenbach P., Cardinali M., Galli M., Ardizzone F., 2005. *Probabilistic landslide hazard assessment at the basin scale*. Geomorphology, v.**72**: 272–299.

Guzzetti F., Peruccacci S., Rossi M., Stark C.P., 2007. *Rainfall thresholds for the initiation of landslides in central and southern Europe*. Meteorology and Atmospheric Physics, v.**98**: 239-267.

Guzzetti F., Mondini A.C.,b, Cardinali M., Fiorucci F., Santangelo M., Chang K.T., 2012. *Landslide inventory maps: New tools for an old problem*. Earth-Science Reviews, v.**112**: 42–66.

Hanssen R.F., 2001. *Radar Interferometry: Data Interpretation and Error Analysis*. Kluwer Academic Publishers, Dordrecht.

Hanssen R.S., 2005. *Satellite radar interferometry for deformationmonitoring: a priori assessment of feasibility and accuracy*. International Journal of Applied Earth Observation, v.**6**: 253–260.

Hargrove W.W., Hoffman F.M., Hessburg P.F., 2006. *Mapcurves: a quantitative method for comparing categorical maps*. J Geograph Syst, v.**8**: 187–208. DOI 10.1007/s10109-006-0025-x

Herrera G., Notti D., García-Davalillo J.C., Mora O., Cooksley G., Sánchez M., Arnaud A., Crosetto M., 2011. *Analysis with C- and X-band satellite SAR data of the Portalet landslide area*. Landslides, v.**8**: 195–206.

Hetland E. A., Musé P., Simons M., Lin Y. N., Agram P. S., DiCaprio C. J., 2012. *Multiscale InSAR Time Series (MInTS) analysis of surface deformation*. Journal of Geophysical Research, v.**117**, B02404. doi:10.1029/2011JB008731.

Highland L.M., Bobrowsky P., 2008. *The landslide handbook - A guide to understanding landslides*. U.S. Geological Survey Circular 1325: 129 pp.

Hilley G.E., Bürgmann R., Ferretti, A., Novali F., Rocca F., 2004. *Dynamics of slow-moving landslides from permanent scatterer analysis*. Science, v.**304**: 1952–1955.

Hooper A., 2008. *A multi-temporal InSAR method incorporating both persistent scatterer and small baseline approaches*. Geophysical Research Letters, v.**35**, L16302, doi:10.1029/2008GL034654.

Hu J., Li Z.W., Ding X.L., Zhu J.J., Zhang L., Sun Q., 2014. *Resolving three-dimensional surface displacements from InSAR measurements: A review*. Earth-Science Reviews, v.**133**: 1–17.

Hutchinson J.N., 1988. *General report: morphological and geotechnical parameters of landslides in relation to geology and hydrology*. 5th International Symposium on Landslides, Lausanne, v.**1**: 3–35.

Iannace A., Capuano M., Galluccio L., 2011. *"Dolomites and dolomites" in Mesozoic platform carbonates ofthe Southern Apennines: geometric distribution, petrography and geochemistry*. Palaeogeography, Palaeoclimatology, Palaeoecology, v.**310**: 324–339. http://dx.doi.org/10.1016/j.palaeo.2011.07.025

Iglesias R., Mallorqui J.J., Monells, D., López-Martíne, C., Fabregas, X., Aguasca, A., Gili, J.A., Corominas, J., 2015. *PSI Deformation Map Retrieval by Means of Temporal Sublook Coherence on Reduced Sets of SAR Images*. Remote Sens., v.**7**: 530-563.

ISPRA, 2007. *Inventory of Landslide Phenomena in Italy - IFFI project*. www.isprambiente.gov.it/it/progetti/iffi-inventario-dei-fenomeni-franosi-in-italia [accessed on 12 September, 2014].

Italian Royal Decree, 1920. *Regio decreto-legge 5 Febbraio 1920 n.201*. Gazzetta Ufficiale del Regno d'Italia. (in Italian)

IUGS, 1997. *Quantitative risk assessment for slopes and landslides - the state of the art*. In: Cruden D., Fell R. (eds), Proceedings of the "International Workshop on Landslide Risk Assessment", Honolulu, USA, February 19–21: 3–12.

Jaboyedoff M., Oppikofer T., Abellán A., Derron M.H., Loye A., Metzger R., Pedrazzini A., 2012. *Use of LIDAR in landslide investigations: A review*. Nat. Hazard., v.**61**: 1–24.

Jenks G.F., 1967. *The Data Model Concept in Statistical Mapping*. International Yearbook of Cartography, v.**7**: 186-190.

Johansson M., Braakenburg N.E., Stow D.A.V., Faugères J.C., 1998. *Deep-water massive sands: facies, processes ad channel geometry in the Numidian Flysch, Sicily*. Sedimentary Geology, v.**115**: 233-265.

Jongmans D., Bièvre G., Schwartz S., Renalier F., Beaurez N., Orengo Y., 2009. *Geophysical investigation of a large landslide in glaciolacustrine clays in the Trièves area (French Alps)*. Engineering Geology, v.**109**: 45–56. doi:10.1016/j.enggeo.2008.10.005.

Kampes B.M., Adam N., 2005 [online]. *The STUN algorithm for persistent scatterer interferometry*. Proceedings of "Fringe 2005 Workshop", Frascati. Available at http://earth.esa.int/fringe2005/proceedings/papers/58_kampes.pdf [accessed on 29 April, 2014].

Keefer D.K., 1984. *Landslides caused by earthquakes*. Geological Society of America Bulletin, v.**95**: 406-421.

Keefer D.K., Wilson R. C., 1989. *Predicting earthquake-induced landslides, with emphasis on arid and semi-arid environments*. In Sadler P. M., and Morton D. M. (eds), 'Landslides in a semi-arid environment with emphasis on the Inland Valleys of Southern California: Riverside, California', Inland Geological Society of Southern California Publications, v.**2**(1): 118-149.

Klose M., Highland L., Damm B., Terhorst B., 2014. *Estimation of direct landslide costs in industrialized countries: Challenges, concepts, and case study*. In Landslide Science for a Safer Geoenvironment; Sassa, K., Canuti, P., Yin, Y., (eds); Springer: Berlin, Germany, 2014; v.**2**: 661-667.

Lacroix P., Zavala, B., Berthier E., Audin L., 2013. *Supervised method of landslide inventory using panchromatic SPOT5 images and application to the earthquake-triggered landslides of Pisco (Peru, 2007, Mw8.0)*. Remote Sens., v.**5**: 2590–2616.

Lagios E., Sakkas V., Novali F., Bellotti F., Ferretti A., Vlachou K., Dietrich V., 2013. *SqueeSAR™ and GPS ground deformation monitoring of Santorini Volcano (1992–2012): Tectonic implications*. Tectonophysics, v.**594**: 38–59.

Lapenna V, Lorenzo R, Perrone A., Piscitelli S., Rizzo E., Sdao F., 2005. *2D electrical resistivity imaging of some complex landslides in the Lucanian Apennine chain, southern Italy*. Geophysics, v.**70**(3): B11-B18.

Lentini F., Carbone S., Di Stefano A., Guarnieri P., 2002. *Stratigraphical and structural constraints in the Lucanian Apennines (southern Italy): tools for reconstructing the geological evolution*. Journal of Geodynamics, v.**34**: 141–158.

LEWIS, 2002 [online]. http://cordis.europa.eu/result/rcn/83810_en.html [accessed on 13 November, 2014]

Li Y., Zhu D., 2010. The Geometric-Distortion Correction Algorithm for Circular-Scanning SAR Imaging. IEEE Geoscience and Remote Sensing Letters, v.**7**(2): 376-380.

Longhitano S.G., 2008. *Sedimentary facies and sequence stratigraphy of coarse-grained Gilbert-type deltas within the Pliocene thrust-top Potenza Basin (Southern Apennines, Italy)*. Sedimentary Geology, v.**210**: 87-110.

Luzi G., 2010. *Ground based SAR interferometry: a novel tool for Geoscience*. In: Geoscience and Remote Sensing New Achievements, Imperatore P., Riccio D. (eds). DOI: 10.5772/9090

Maggiò F., Pellegrino A., 2002. *Sperimentazione in sito sul miglioramento della resistenza di un'argilla attiva con modifica della composizione chimica del liquido interstiziale*. Proc. Incontro Annuale dei Ricercatori di Geotecnica 2002 - IARG 2002, Naples, Italy. (in Italian)

Magliulo P., Di Lisio A., Russo F., 2009. *Comparison of GIS-based methodologies for the landslide susceptibility assessment*. Geoinformatica, v.**13**(3): 253-265.

Manzo M., Ricciardi G. P., Casu F., Ventura G., Zeni G., Borgstrom S., Berardino P., Del Gaudio C., Lanari R., 2006. *Surface deformation analysis in the Ischia Island (Italy) based on spaceborne radar interferometry*. J. Volcanol. Geotherm. Res., v.**151**(4): 399–416. doi:10.1016/j. jvolgeores.2005.09.010.

Marghany M., Hashim M., Cracknell A.P., 2011. *Simulation of shoreline change using AIRSAR and POLSAR C-band data,*. Environmental Earth Sciences, v.**64**: 1177–1189.

Massonnet D., Feigl K.L., 1998. *Radar interferometry and its application to changes in the Earth's surface*. Reviews of Geophysics, v.**36**(4): 441-500.

Massonnet D., Rabaute T., 1993. *Radar interferometry: Limits and potential*. IEEE Trans. Geosci. Remote Sensing, v.**31**: 455 464.

Matano F., Barbieri M., Di Nocera S., Torre M., 2005. *Stratigraphy and strontium geochemistry of Messinian evaporite-bearing successions of the southern Apennines foredeep, Italy: implications for the Mediterranean "salinity crisis" and regional palaeogeography*. Palaeogeography, Palaeoclimatology, Palaeoecology v.**217**: 87–114.

Mattioni L., Shiner P., Tondi E., Vitale S., Cello G., 2006. *The Argille Varicolori Unit of Lucania (Italy): a record of tectonic offscraping andgravity sliding in the Mesozoic-Tertiary Lagonegro Basin, southern Apennines*. Geological Society, London, Special Publications, v.**262**, 277-288.

Mazzoli S., Helman M., 1994. *Neogene patterns of relative plate motion for Africa–Europe: some implications for recent central Mediterranean tectonics*. Geologische Rundschau, v.**83**: 464–468.

McKean J., Roering J., 2004. *Objective landslide detection and surface morphology mapping using high-resolution airborne laser altimetry*. Geomorphology, v.**57**: 331- 351.

Menardi Noguera A., Rea G., 2000. *Deep structure of the Campanian-Lucanian Arc (southern Apennine, Italy)*. Tectonophysics, v.**324**(4): 239-265.

Mihalinec Z., Ortolan Z., 2008. *Landslide ''Granice'' in Zagreb (Croatia)*. In 'Landslides and engineered slopes: From the past to the future', Chen Z., Zhang J.M., Ho K.,Wu F.Q., Li Z.K. (eds). Proceedings of the tenth international symposium on landslides and engineered slopes. Taylor & Francis, Xi'an: 1587-1593.

Mikkelsen P. E., 1996. *Field instrumentation*. In: Turner, A.K. & R.L. Schuster (eds), Landslides. Investigation and mitigation. Transp. Res. Board Spec. Rep. 247, Nat. Res. Council, Washington, D.C., pp. 279-316.

Mittermayer J., Wollstadt S., Prats P., Scheiber R., Koppe W., 2012. *STARING SPOTLIGHT IMAGING WITH TERRASAR-X*. Geoscience and Remote Sensing Symposium (IGARSS) 2012, Munich, Germany, 22-27 July 2012: 1606 – 1609.

Monaco C., Tortorici L. 1995. *Tectonic role of ophiolite-bearing terranes in the development of the Southern Apennines orogenic belt*. Terra Nova, v.**7**: 153–160.

Monaco C., Tortorici L., Paltrinieri W., 1998. *Structural evolution of the Lucanian Apennines*. Journal of Structural Geology, v.**20**: 617–638.

Montgomery D.R., Dietrich W.E., 1994. *A physically based model for the topographic control on shallow landsliding*. Water Resources Research, v.**30**(4): 1153-1171.

Mora O., Mallorquí J.J., Broquetas A., 2003. *Linear and nonlinear terrain deformation maps from a reduced set of interferometric SAR images*. IEEE Transactions on Geoscience and Remote Sensing, v. **41**: 2243-2253.

MORFEO, 2008 [online]. http://www.morfeoproject.it/index.php?option=com_frontpage&Itemid=1 [accessed on 13 November, 2014]

Mostardini F., Merlini S., 1986. *Appennino centro-meridionale. Sezioni geologiche e proposta di modello strutturale*. Memorie della Societa` Geologica Italiana, v.**35**: 177–202. (in Italian)

Neitzel, F., Klonowski, J., 2011. *Mobile 3D mapping with a low-cost UAV system*. Int. Arch. Photogramm. Remote Sens. Spat. Inf. Sci, v.**38**: 1-6.

Nemcok A., 1972. *Gravitational slope deformation in high mountains*. Proceedings of the 24th International Geology Congress, Montreal, v.**13**: 132-141.

Nigro F., Renda P., 1999. *The North-Central Sicily Belt: structural setting and geological evolution*. Annales Societatis Geologorum Poloniae, v.**69**: 49-61.

Notti D., Garcia-Davallilo J.C., Herrera G. Mora O., 2010. *Assessment of the performance of X-band satellite radar data for landslide mapping and monitoring: Upper Tena valley case study*. Natural Hazards and Earth System Sciences, v.**10**: 1865-1875.

Notti D., Herrera G., Bianchini S., Meisina C., García-Davalillo J.C., Zucca F., 2014. *A methodology for improving landslide PSI data analysis*. International Journal of Remote Sensing, v.**35**, (6): 2186–2214.

Novellino A., Athab A.D., bin Che Amat M.A., Syafiudin M.F., Sowter A., Marsh S., Cigna F., Bateson L., 2014a. *Intermittent SBAS Ground Motion Analysis in Low Seismicity Areas: Case Studies in the Lancashire and Staffordshire coal-fields, UK*. Proceedings of the "Seismology from Space: Geodetic Observations and Early Warning of Earthquakes", Burlington House, London, UK. 9 May 2014.

Novellino A., Cigna F., Jordan C., Sowter A., Calcaterra D., 2014b. *Monitoring large-scale landslides and their induced hazard with COSMO-SkyMed Intermittent SBAS (ISBAS): a case study in north-western Sicily, Italy*. EGU General Assembly 2014. Geophysical Research Abstract, v.**16**, EGU2014-9621-1.

Novellino A., De Agostini A., Di Martire D., Ramondini M., Floris M., Calcaterra D., 2015. *Using Data from Multiple SAR Sensors in Landslide Characterization: Case Studies from Different Geomorphological Contexts in Italy*. Engineering Geology for Society and Territory, v.**2**: 395-398.

Oddone E., 1931. *Il terremoto dell'Irpinia del 23 luglio 1930*. Bollettino del Comitato Nazionale italiano per la Geodesia e la Geofisica I, **2**: 17-20. (in Italian)

Ogniben L., 1969. *Schema introduttivo alla geologia del confine Calabro–Lucano*. Memorie della Societa` Geologica Italiana, v.**8**: 453–763. (in Italian)

Papini F., Lo Valvo F., Brullo S., Cantoni A., Bardi A., Papini F., 2009. *Lago di Piana degli Albanesi*. Piano di Gestione "Invasi artificiali (Piana degli Albanesi)" – Regione Siciliana. (in Italian)

Parise M., Wasowski J., 1999. *Landslide activity maps for landslide hazard evaluation: three case studies from Southern Italy*. Natural Hazards, v.**20**: 159–183.

Pasuto A., Soldati M., 2013. *Lateral spreading*. In: Treatise on Geomorphology. Academic Press, SanDiego, v.**7**: 239–248.

Patacca E., Scandon, P., 2007. *Geology of the Southern Apennines*. In 'Results of the CROP Project Sub-project CROP-04 Southern Apennines (Italy)', Mazzotti A., Patacca E., Scandone P. (eds). Bollettino della Società Geologica Italiana (Italian Journal of Geoscience) special issue, v.**7**: 75-119.

Perrone A., Iannuzzi A., Lapenna V., Lorenzo P., Piscitelli S., Rizzo E., Sdao F., 2004. *High-resolution electrical imaging of the Varco d'Izzo earthflow (southern Italy)*. Journal of Applied Geophysics, v.**56**: 17-29.

Pescatore T., Renda P., Schiattarella M., Tramutoli M., 1999. *Stratigraphic and structural relationships between Meso-Cenozoic Lagonegro basin and coeval carbonate platforms in southern Apennines, Italy*. Tectonophysics, v.**315**: 269-286.

Pescatore, T., Renda, P., Tramutoli, M., 1988. *Rapporti tra le unità lagonegresi e le unità sicilidi nella media valle del Basento, Lucania (Appennino Meridionale)*. Memorie della Società Geologica Italiana, v.**41**: 353–361. (in Italian)

Petley D.J., 1984. *Ground investigation, sampling and testing for studies of slope instability*. In 'Slope instability', Brunsden D., Prior D. B., Wiley (eds), Chichester, 67-101.

Picarelli L., 2009. *Conoscere per prevedere (dall'equilibrio limite alla meccanica dei pendii)*. Proceedings of the "Ottava conferenza A. Croce", Rivista Italiana di Geotecnica, v.**4**: 51-68. [in Italian]

Picarelli L., Urciuoli G., Mandolini A., Ramondini M., 2006. *Softening and instability of natural slopes in highly fissured plastic clay shales*. Natural Hazards and Earth System Sciences, v.**6**: 529–539.

Picarelli L., Urciuoli, G., Ramondini M., Comegna L., 2005. *Main features of mudslides in tectonised highly fissured clay shales*. Landslides v.**2**: 15–30.

Plank, S., Singer, J., Minet, C., Thuro, K., 2012. *Pre-survey suitability evaluation of the differential synthetic aperture radar interferometry method for landslide monitoring*. International Journal of Remote Sensing, v.**33**(20): 6623–6637.

Pourghasemi H.R., Mohammady M., Pradhan B., 2012. *Landslide susceptibility mapping using index of entropy and conditional probability models in GIS: Safarood Basin, Iran*. Catena, v.**97**: 71–84.

Pradhan B., 2010. *Remote sensing and GIS-based landslide hazard analysis and cross-validation using multivariate logistic regression model on three test areas in Malaysia*. Advances in Space Research, v.**45**: 1244-1256.

Prati C., Ferretti A., Perissin D., 2010. *Recent advances on surface ground deformation measurement by means of repeated space-borne SAR observations*. Journal of Geodynamics, v.**49**: 161–170. doi:10.1016/j.jog.2009.10.011.

Prothero D.R., F. Schwab, 2003. *Sedimentary Geology*, 2nd edition. W.H. Freeman (ed), New York: 557 pp.

Racoules D., Bourgine B., de Michele M., Cozannet G. L., Luc C., Bremmer C., Veldkamp H., Tragheim D., Bateson L., Crosetto M., Agudo M., Engdahl M., 2006. *PSIC4: Persistent Scatterer Interferometry: independent validation and intercomparison of results*. Techical report, BRGM, BRGM/RP-55640-FR

Ramsay J.G., 1967. *Folding and fracturing of rocks*. McGraw-Hill, New York: 568 pp.

Reeves J.A., Knight R., Zebker A.H., Kitanidis K.P., Schreuder A.W., 2014. *Estimating temporal changes in hydraulic head using InSAR data in the San Luis Valley, Colorado*. Water Resources Research, v.**50**(5): 4459. DOI: 10.1002/2013WR014938

Reichenbach P., Guzzetti F., Cardinali M., 1998. M*ap of sites historically affected by landslides and floods in Italy, 2nd edition*. CNR, Gruppo Nazionale per la Difesa dalle Catastrofi Idrogeologiche, publication n. 1786, scale 1:1,200,000.

Rib H. T., Liang T., 1978. *Recognition and identification*. In 'Landslide Analysis and Control', Schuster R. L., Krizek R. J. (eds), National Academy of Sciences, Transportation Research Board Special Report 176, Washington, 34-80.

Rocca A., Mazzanti P., Perissin D., Bozzano F., 2014. *Detection of past slope activity in a desert area using Multi-Temporal DInSAR with ALOS PALSAR data*. Italian Journal of Engineering Geology and Environment, v.**1**: 35-49.

Roch K., H., Chwatal W., Brückl E., 2005. *Potentials of monitoring rock fall hazards by GPR: considering as example the results of Salzburg*. Landslides, v.**3**: 87-94.

Romeiser R., Breit H., Eineder M., Runge H., Flament P., de Jong K., Vogelzang J. , 2003. *On the suitability of TerraSAR-X split antenna mode for current measurements by along-track interferometry*. In Proceedings of the IGARSS conference, Toulouse, France.

Romeiser R., Breit H., Eineder M., Runge H., Flament P., de Jong K., Vogelzang J., 2005. *Current Measurements by SAR Along-Track Interferometry From a Space Shuttle*. IEEE Transactions on Geoscience and Remote Sensing, v.**43**: 2315-2324.

Romeiser R., Thompson D. R., 2000. *Numerical study on the along-track interferometric radar imaging mechanism of oceanic surface currents*. IEEE Trans. Geosci. Remote Sens., v.**38**(1): 446-458.

Rosen P.A., Hensley S., Joughin I.R., Li F.K., Madsen S.N., Rodríguez E., Goldstein R.M., 2000. *Synthetic Aperture Radar Interferometry*. Proceedings of the IEEE, v.**88**: 333-382.

Roure F., Casero P., Addoum B., 2012. *Alpine inversion of the North African margin and delamination of its continental lithosphere*. Tectonics, v.**31**, TC3006. http:// dx.doi.org/10.1029/2011TC00298.

Sabins F. F. Jr., 1978. *Remote sensing principles and interpretation*. Freeman, San Francisco: 426 pp..

Sabins F.F., 1996. *Remote Sensing: Principles and Interpretation*. W.H. Freeman, Company eds., New York: 494pp.

Salvati P., Guzzetti F., Reichenbach P., Cardinali M. Stark C.P., 2003. *Map of landslides and floods with human consequences in Italy*. CNR, Gruppo Nazionale per la Difesa dalle Catastrofi Idrogeologiche, publication n. 2822, scale 1:1,200,000.

Samsonov S., d'Oreye N., 2012. *Multidimensional time-series analysis of ground deformation from multiple InSAR data sets applied to Virunga Volcanic Province*. Geophysical Journal International, v. **191**: 1095-1108.

Santurri L., Carlà R., Fiorucci F., Aiazzi B., Baronti S., Cardinali M., Mondini A., 2010. *Assessment of very high resolution satellite data fusion techniques for landslide recognition*. Int. Arch. Photogramm. Remote Sens. Spat. Inf. Sci. 2010, v.**38**/B7: 492–496.

Sarmap, 2009. SAR guidebook [online]. http://www.sarmap.ch/pdf/SAR-Guidebook.pdf [accessed on 13 September 2013].

Sartori R., 1990. *The main results of ODP Leg 107 in the frame of Neogene to recent geology of the Perityrrhenian areas*. In: Kastens, K., Mascle, J. et al. (eds) Proceedings of the Ocean Drilling Program, Scientific Results, 107. Ocean Drilling Program, College Station, TX, 715–730.

Scaioni M., 2013. *Remote sensing for landslide investigations: From research into practice*. Remote Sens., v.**5**: 5488–5492.

Scaioni M., Longoni L., Melillo V., Papini M., 2014. Remote Sensing for Landslide Investigations: An Overview of Recent Achievements and Perspectives. Remote Sens., v.**6**. doi:10.3390/rs60x000x

Scandone P., Sgrosso I., 1965. *Sulla paleogeografia della Penisola Sorrentina dal Cretacico superiore al Miocene*. Boll. Soc. Natur. Napoli, v.**74**, 159-177.

Schmutz M., Albouy Y, Guerin R., Maquaire O., Vassal J., Schott, J. J., Descloitres M., 2000. *Joint electrical and time domain eleclromagnetism (TDEM) data inversion applied to the super sauze earthfiow (France)*. Surveys in geophysics, v.**21**(4): 371-390.

Scrocca D., 2010. *Southern Apennines: structural setting and tectonic evolution*. In 'The geology of Italy: tectonics and life along plate margins', Beltrando M., Peccerillo A., Mattei M., Conticelli S., Doglioni C. (eds), Journal of the Virtual Explorer, v.**36**, (13).

Shahabi H., Khezri S., Bin Ahmad B., Hashim M., 2014. *Landslide susceptibility mapping at central Zab basin, Iran: A comparison between analytical hierarchy process, frequency ratio and logistic regression models*. Catena, v.**115**: 55–70.

Shiner P. R., Mazzoli S., Cello G., 2004. *Interactions between thin and thick-skinned thrusting in the Val d'Agri area of the S. Apennines*. Proceedings of the '32nd International Geological Congress - International Union of Geological Sciences', Florence, Italy, 20 – 28 August.

Simons M., Rosen P. A., 2007. *Interferometric Synthetic Aperture Radar Geodesy*. Treatise on Geophysics, v.**3**: 391-446

Singhroy V., 2005. Remote sensing of landslides. In 'Landslide risk assessment'Glade, T., Anderson M. G., Crozier, M. J., John Wiley (eds), 469-492, 2005

SLAM, 2003 [online]. *Service for LAndslide Monitoring* [online]. http://due.esrin.esa.int/prjs/prjs52.php [accessed on 13 November, 2014]

Soeters R., van Westen C.J., 1996. *Slope instability recognition, analysis, and zonation*. In: Turner, A.K. & R.L. Schuster (eds), Landslides: Investigation and mitigation. Transportation Research Board Report 247, Nat. Res. Council, Washington, D.C.: 12-35.

Sowter A., Bateson L., Strange P., Ambrose K., Syafiudin M.F., 2013. *DInSAR estimation of land motion using intermittent coherence with application to the South Derbyshire and Leicestershire coalfields*. Remote Sensing Letters, v.**4**: 979-987.

Speight J.G., 1977. *Landform pattern description from aerial photographs*. Photogrammetry, v.**32**: 161-182.

Stampfli, G.M. and Borel, G.D. 2002. *A plate tectonic model for the Paleozoic and Mesozoic constrained by dynamic plate boundaries and restored synthetic oceanic isochrones*. Earth and Planetary Science Letters, v.**196**: 17-33.

Storti F., McClay K., 1995. *Influence of syntectonic sedimentation on thrust wedges in analogue models*. Geology, v.**23**: 999–1002.

Strozzi T.; Ambrosi C.; Raetzo H., 2013. *Interpretation of aerial photographs and satellite SAR interferometry for the inventory of landslides*. Remote Sensing, v.**5**: 2554–2570.

Strozzi T., Kouraev A., Wiesmann A., Wegmuller U., Sharov A., Werner C., 2008. *Estimation of Arctic glacier motion with satellite L-band SAR data*. Remote Sensing of Environment, v.**112**: 636-645.

Strozzi T., Luckman A., Murray T., Wegmuller U., Werner C. L., 2002. *Glacier motion estimation using SAR offset-tracking procedures*. IEEE T. Geosci. Remote, v.**40**(11), 2384–2391. DOI:10.1109/TGRS.2002.805079.

Syafiudin M.F., Sowter A., Aplin P., Vu T.T., Marsh S., Abidin H.Z., Novellino A., Athab A.D., bin Che Amat M.A., 2014. *Space geodesy observations for ground instability detection in the tectonically dynamic areas of Bandung basin and Lembang fault, Indonesia*. Proceedings of the "Seismology from Space: Geodetic Observations and Early Warning of Earthquakes", Burlington House, London, UK. 9 May 2014.

Tapete D., Fanti R., Cecchi R., Petrangeli P., Casagli N., 2012. Satellite radar interferometry for monitoring and early-stage warning of structural instability in archaeological sites. Journal of Geophysics and Engineering, v.**9**: S10-S25.

Teatini P., Tosi L., Strozzi T., 2011. *Quantitative evidence that compaction of Holocene sediments drives the present land subsidence of the Po Delta, Italy*. Journal of Geophysical Research, v.**116**(B8), http://dx.doi.org/10.1029/2010JB008122.

TELLUS, 2006 [online]. http://www.difesa.suolo.regione.campania.it/content/category/4/64/92/ [accessed on 13 November, 2014]

Terrafirma, 2003 [online]. http://www.terrafirma.eu.com/ [accessed on 13 November 2014].

Tofani V., Raspini F., Catani F., Casagli N., 2013. *Persistent Scatterer Interferometry (PSI) Technique for Landslide Characterization and Monitoring*. Remote Sensing, v.**5**: 1045-1065.

Torrero L., Seoli, L., Molino, A., Giordan, D., Manconi, A., Allasia, P., Baldo M., 2015. *The Use of Micro-UAV to Monitor Active Landslide Scenarios*. Lollino G. et al. (eds.), Engineering Geology for Society and Territory, Springer International Publishing, v.**5**: 701-704.

TRE, 2013. *Satellite data coverage* [online]. Available from: http://treuropa.com/wp-content/uploads/satellite-data-coverage.jpg [viewed 11 June 2014].

Turner A. K., Schuster R. L., 1996. *Landslides: Investigation and Mitigation*. Washington, D.C., National Research Council, Transportation Research Board Special Report 247, 673 pp..

Urciuoli G., 1992. *Rigonfiamento di un'argilla di alta plasticità e modellazione de fenomeni erosivi del colle di Bisaccia*. PHD thesis, Federico II University of Naples. (in Italian)

USGS, 2014 [online]. http://earthquake.usgs.gov/earthquakes/search/ [accessed on 30 September 2014].

Van Asch T.W.J., Buma J., van Beek L.P.H., 1999. *A view on some hydrological triggering systems in landslides*. Geomorphology, v.**30**: 25–32, doi:10.1016/S0169-555X(99)00042-2.

Varnes D. J., IAEG, 1984. *Landslide Hazard Zonation - a review of principles and practice*. Commission on Landslides. Paris, UNESCO, 60 pp..

Vassallo R., Di Maio C., 2006. *La frana di Costa della Gaveta a Potenza: analisi preliminare*. Incontro Annuale dei Ricercatori di Geotecnica - IARG 2006 Pisa, 26-28 June. (in Italian)

Vassallo R., Pagliuca R., Di Maio C., 2013. *Monitoring of the movements of a deep, slow, clayey landslide and 3D interpretation*. Italian J Eng Geol Environ Book Ser, v.**6**:359–367

Van Den Eeckhaut M., Vanwalleghem T., Poesen J., Govers G., Verstraeten G., Vandekerckhove L., 2006. *Prediction of landslide susceptibility using rare events logistic regression: a case-study in the Flemish Ardennes, Belgium*. Geomorphology, v.**76**: 392-410. doi:10.1016/j.geomorph.2005.12.003.

Van Westen C. J., 1992. *Medium Scale Landslide Hazard Analysis Using a PC Based GIS: A Case Study from Chinchina, Colombia*. In J.B. Alzate (ed), proceedings of the "Simposio Internacional sobre Sensores Remotes y Sistemas de Informacion Geografica (SIG) para el Estudio de Riesgos Naturales", Bogotà. Instituto Geografico Agustin Codazzi, Bogotà, v.**2**: 20pp.

Van Westen C.J., 1993. *Application of Geographic Information Systems to Landslide Hazard Zonation*. PHD thesis, Technical University Delft: 245 pp..

Van Westen C.J., Rengers N., Soeters R., 2003. *Use of Geomorphological Information in Indirect Landslide Susceptibility Assessment*. Natural Hazards, v.**30**: 399–419.

Van Zuidam, R.A., 1985. *Aerial photo-interpretation in terrain analysis and geomorphologic mapping*. International Institute for Aerospace Survey and Earth Sciences. Smits Publishers, The Hague. 442 pp.

Vannucchi P., Maltmanb A., Bettellia G., Clennellc B., 2003. *On the nature of scaly fabric and scaly clay*. Journal of Structural Geology, v.**25**: 673–688.

Varnes D.J., 1978. *Landslides, analysis and control*. Transportation Research Board Special Report, v.**176**: 11-33.

Varnes D. J., IAEG, 1984. *Landslide Hazard Zonation: a Review of Principles and Practice*. UNESCO Press, Paris, 63 pp..

Vassallo R., Di Maio C., 2006. *La frana di Costa della Gaveta a Potenza: analisi preliminare*. Incontro Annuale dei Ricercatori di Geotecnica - IARG 2006 Pisa, 26-28 Giugno. (in Italian)

Vitale S., Ciarcia S., 2013. *Tectono-stratigraphic and kinematic evolution of the southernApennines/Calabria–Peloritani Terrane system (Italy)*. Tectonophysics, v.**583**: 164–182.

Walter T.R., Shirzaei M., Manconi A., Solaro G., Pepe A., Manzo M., Sansosti E., 2014. *Possible coupling of Campi Flegrei and Vesuvius as revealed by InSAR time series, correlation analysis and time dependent modeling*. Journal of Volcanology and Geothermal Research, v.**280**: 104–110.

Wegmüller, U., Werner, C., Strozzi, T., Wiesmann, A., 2005 [online]. *ERS-ASAR integration in the interferometric point target analysis*. Proceedings of the "Fringe 2005 Workshop", Frascati, Italy, 28 November-2 December. http://earth.esa.int/workshops/fringe05/proceedings/papers/196_wegmuller.pdf [accessed on 17 July, 2014].

Wieczorek G.F., 1996. *Landslide triggering mechanisms*. In: Landslides: Investigations and Mitigation. Transportation Research Board Special Report, v.**247**: 76–90.

Wieczorek G.F., Snyder J.B., 2009. *Monitoring slope movements*. In 'Geological Monitoring. Geological Society of America', Boulder: 245–271.

WP/WLI, 1993a. *Multilingual Landslide Glossary*. UNESCO, Working Party on World Landslide Inventory, Bitech Publishers, Richmond.

WP/WLI, 1993b. *A suggested method for describing the activity of a landslide*. UNESCO, Working Party on World Landslide Inventory. Bulletin of IAEG, v.**47**: 53–57.

Yalcin A., Reis S., Aydinoglu A.C., Yomralioglu T., 2011. *A GIS-based comparative study of frequency ratio, analytical hierarchy process, bivariate statistics and logistics regression methods for landslide susceptibility mapping in Trabzon, NE Turkey*. Catena, v.85: 274–287.

Yilmaz I., 2009. *Landslide susceptibility mapping using frequency ratio, logistic regression, artificial neural networks and their comparison: a case study from Kat landslides (Tokat-Turkey)*. Computers & Geosciences, v.**35**: 1125–113.

Yin J.H., Zhu H.H., Jin W., 2008. *Monitoring of soil nailed slopes and dams using innovative technologies*. In 'Landslides and engineered slopes: from the past to the future', Chen Z, Zhang J-M, Ho K, Wu F-Q, Li Z-K (eds). Proceedings of the tenth international symposium on landslides and engineered slopes. Taylor & Francis, Xi'an: 1361–1366

Zischinsky U., 1966. *On the deformation of high slopes*. Proceedings of the First Congress of the Int. Soc. of Rock Mechanics, Lisboa, v.**6**/**11**: 179-185.

Zischinsky U., 1969. *Über Sackungen*. Rock Mechanics, v.**1**: 30-52. (in German)

Appendix

Rend. Online Soc. Geol. It., Vol. 24 (2013), pp. 95-97, 1 fig.

Application of DInSAR techniques to engineering geology studies in southern Italy

DIEGO DI MARTIRE (*), ALESSANDRO NOVELLINO (°), SERENA TESSITORE (°), MASSIMO RAMONDINI (*), DOMENICO CALCATERRA (°)

RIASSUNTO

Applicazione di tecniche DInSAR a problematiche geologico-tecniche dell'Italia meridionale.

In questa nota si presentano i primi risultati ottenuti dall'applicazione della tecnica dell'interferometria differenziale (DInSAR) ai fini del monitoraggio di frane, subsidenze e grandi infrastrutture, con riferimento ad alcuni casi-studio ubicati nelle regioni dell'Italia meridionale.

KEY WORDS: *Dams, DInSAR, landslides, Italy, subsidence.*

INTRODUCTION

In recent years Differential SAR Interferometry (DInSAR - GABRIEL *et alii*, 1989) has been increasingly used in engineering geology applications, such as ground deformations monitoring. DInSAR allows both "point-wise" and "wide area" investigations, preserving a high accuracy of the final results.

The results here described are part of a wider multi-disciplinary research program started in 2007 at the University of Naples "Federico II". The research is aimed at assessing the suitability of the DInSAR techniques applied to slow-moving natural phenomena, such as landslides and subsidence, or to the performance of large man-made structures (e.g. dams). To this scope several collaborations with Italian and foreign institutions (University of Pavia; University of Padua; University of Calabria; University of Basilicata; RSLab-UPC, Barcelona; IGME, Madrid) were established, which allowed to develop specific competences in SAR images processing, through the "Permanent Scatterers" (PS) and "Small BASeline" (SBAS) approaches, and in post-processing data interpretation.

GEOLOGICAL SETTINGS

The study areas (Fig. 1) fall within the Apennine-Maghrebian chain, which is a fold and thrust belt resulting from Upper Cretaceous to Quaternary convergence among the Corsica-Sardinia-Calabria blocks of European origin and the Apulian block (or Adriatic; MAZZOLI & HELMAN, 1994 and references therein), of African origin. These sectors encompass several superposed tectonic domains characterized by Mesozoic–Tertiary shallow water to slope-facies carbonates (e.g.: Apennine and Hyblean-Pelagian carbonate platforms) and pelagic basin successions (e.g.: Lagonegro-Molise basins) originated from the Apulian continental palaeomargin deformation, with the subsequent interposition of several Miocene–Pliocene thrust-top and foreland basin deposits, often filled by thick deltaic successions or by pyroclastic deposits.

In such a context, structurally complex formations are widespread: they are characterized by very poor mechanical properties, representing, one of the main factors predisposing to ground instabilities.

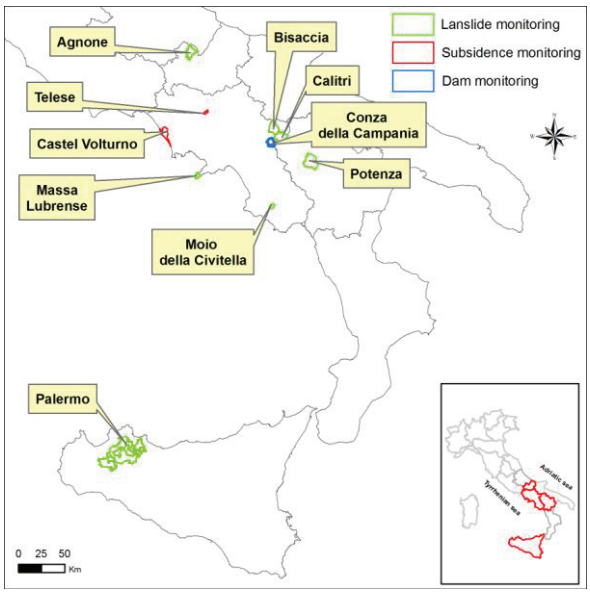

Fig. 1 – Location of the study areas.

LANDSLIDE MONITORING RESULTS

BISACCIA

Bisaccia, historically affected by a lateral spread, was built on a conglomeratic plateau developed in a braided deltaic environment during Pliocene (Ariano Irpino supersynthem). This formation unconformably lies on the Vallone del Toro unit, mainly formed by varicoloured shale and marly deposits, deriving from a Mesozoic pelagic basin. The interferometric datasets utilized are represented by the PS (ERS images - period

(*) Department of Civil, Building and Environmental Engineering, University of Naples Federico II.
(°) Department of Earth Sciences, Environment and Resources, University of Naples Federico II.

1992-2000), processed by TeleRilevamento Europa in ascending and descending acquisition, and by the 2003-2010 ENVISAT images, elaborated through a SBAS processing technique. The preliminary interpretation of interferometric analysis shows that in the Bisaccia historical center, due to the clayey bedrock deformation and its consequent lateral spread, the succession's upper portion is undergoing a collapse, progressively increasing from south (4.2 mm/yr) to north (15.5 mm/yr).

CALITRI

The choice of Calitri was suggested by the presence of a huge complex landslide, reactivated after the main shock of the M = 6.9 November 23, 1980 earthquake (BUDETTA *et alii*, 1990), where some inclinometer installations were found, deriving from old in-situ investigation campaigns, and measured again from 2008. The interferometric analysis has been carried out by processing the 2002-2010 ENVISAT images. The mean displacement rates detected vary between 0.10 and 0.34 cm/yr, which allow the landslide's velocity to be classified as extremely slow. Furthermore, SAR displacements have been projected on the LOS (Line Of Sight) direction in order to compare them with the corresponding inclinometer data, measured from March 2008 to June 2010. The results showed a good agreement between the two kinds of measurements, in terms of both direction and rate of movement.

COSTA DELLA GAVETA (POTENZA)

A further interferometric analysis involved the complex mass movements occurred on the northern slope of the Basento River valley, at Costa della Gaveta locality, east of Potenza (CALCATERRA S. *et alii*, 2012). ENVISAT ascending images have been processed in this case too, even though the time span considered was November 2007 – July 2010, due to the corresponding availability of GPS data. The results show that the velocities of the surveyed landslides vary between 1.5 cm/yr to 10 cm/yr, in accordance with the displacements obtained from GPS network. Such a comparison was performed after calculating the percentage of a potential movement that can be detected through the interferometric analyses (PLANK *et alii*, 2012), which are influenced by the characteristics of both the SAR geometry acquisition and of the slope.

MOIO DELLA CIVITELLA

The aim of this study was to assess the landslides' activity in two urban centres, Moio and Pellare (CALCATERRA *et alii*, 2008; DI MARTIRE *et alii,* 2011a, CALÒ *et alii*, 2012), where slide-flows and roto-translational slides are the most frequent types of slope instability; they involved a Quaternary cover consisting of heterogeneous debris in a silty-clayey matrix. ENVISAT images (53 ascending and 33 descending) accessible for the 2002-2010 period have been elaborated. The availability of images acquired from different orbits allowed the combination of results in order to obtain the E-W and vertical velocity components. The decomposition of the velocity vector showed that the horizontal component is predominant, confirming the kinematics of the surveyed landslides. Moreover, possible relationships between rainfall and rates of displacement are being studied, by comparing the time series of displacements and the corresponding cumulative rainfall.

MASSA LUBRENSE

The villages of Nerano and Termini, which belong to the Massa Lubrense municipality, since the beginning of 20th century have been affected by several reactivations of an earth flow that involves reworked varicoloured clay olistostromes and limestone olistoliths; the landslide, despite many engineering works, gave evidence of activity also in recent years. A PS analysis detected by ERS and ENVISAT images processing for the period 1992-2008 has been carried out. Satellite imagery analysis put in evidence a negligible movement in the detachment zone (<1 mm/yr), which becomes extremely slow in the accumulation zone (3 mm/yr). However, further information on the landslide will soon be available, thanks to new inclinometers installed in the summer of 2012.

AGNONE

In the catchment of the Vallone S. Nicola, a complex slope movement, to be considered as a reactivation of a pre-existing landslide, took place as a consequence of an intense rainfall event occurred on January 2003. Here a research project has been developed under the auspices of the Italian Spatial Agency (ASI) in order to test the applicability of the interferometric techniques based on SAR Very High Resolution (VHR) COSMO-SkyMed images; it required a dedicated algorithm, which was developed by our research team to process eleven images in descending orbits for the time span February 2011 - January 2012. In order to evaluate the results, eight thriedral corner reflectors, coupled with GPS antennas, were installed within the landslide body. Due to the small number of available images, only a preliminary processing was carried out, consisting of the elaboration of a coherence map. The latter has been compared with the map processed by Low Resolution images (ENVISAT), obtaining consistent improvements in terms of mean coherence values (from 0.15 for LR images to 0.70 for VHR images) in the corners' position.

PALERMO PROVINCE

Seven municipalities, located in the Palermo province (Sicily) are presently under study, where a variety of active and dormant landslides are present. They all develop onto the Late Cretaceous-Miocene portion of the Hyblean-Pelagian pelagic platform domain (NIGRO & RENDA, 1999) (such as the Hybla and Amerillo formations), and the related foreland basin deposits (Corleone and San Cipirello formations) and the related foreland basin deposits. The Palermo district was a test area for the new generation of COSMO-SkyMed satellites.

Here, the very high PS density (more than 1000 PS/km^2) allowed a definitely better spatial and spectral resolution than previous constellations (DI MARTIRE *et alii*, 2011b).

After the moving targets detection, a specific field survey was performed, aimed at validating the satellite information regarding landslide type and state of activity. Such a survey evidenced a high reliability of the new satellite constellation in recognizing very slow moving events, even on low angle slopes, where the conventional "ground-truth" is not easily achieved.

SUBSIDENCE MONITORING RESULTS

The urban area of Telese Terme is affected by subsidence and sinkhole phenomena (CALCATERRA *et alii*, 2010). Forty-seven images (corresponding to 65 interferograms), acquired over ascending orbits of the ENVISAT satellite system (track 358 – frame 819) and covering the 2003 – 2010 time interval, have been processed through a SBAS-based technique. The analysis dealt with an area where in 2002 and 2006 two sinkholes, classified as "cover subsidence sinkholes", occurred, and where an underground cave was found. The mean velocities map obtained shows that the subsidence area is localized in the western part of the city (resting on fluvial-marsh deposits) and in the area above the underground cave. DInSAR results will be compared to a micro-gravimetric survey to be carried out in the area and to structural analysis of the buildings affected by severe damage.

DAM MONITORING RESULTS

An application of a DInSAR technique to monitor the deformations of the Conza della Campania dam (Italy) has been carried out. The time span analyzed was May 2004 – July 2010, corresponding to 36 ENVISAT images in ascending orbit. For the same time interval, data regarding vertical displacements measured by extensometers installed inside the dam during the construction were considered. A preliminary statistical study was carried out, in order to compare the measurements obtained from the two different monitoring techniques. The results highlighted a good correlation (varying between 0.770 – 0.915) between the ground measurements and the vertical component of the LOS displacement.

CONCLUSIONS

In all the study areas the use of interferometric techniques displayed results which proved to be consistent with field surveys and traditional monitoring approaches (inclinometers, extensometers and GPS measurements). In the near future, the second stage of the Italian Extraordinary Plan for Environmental Remote Sensing and the availability of VHR last generation images, acquired by TerraSAR-X, COSMO-SkyMed and SENTINEL constellations, will hopefully allow us to obtain better results in terms of ground resolution and revisiting time.

ACKNOWLEDGMENTS

SAR images (ENVISAT) and PS data (ERS, ENVISAT and COSMO-SkyMed) were provided by the Italian Ministry of Environment, Territory and Sea. Prof. J.J. Mallorqui (Department of Signal Theory and Communications, UPC, Barcelona) is gratefully acknowledged for his helpful collaboration in the data processing.

REFERENCES

BUDETTA P., CALCATERRA D., DE RISO R., SANTO A. (1990) - *Geologia e fenomeni franosi dell'alta valle del Fiume Ofanto (Appennino meridionale)*. Mem. Soc. Geol. It., **45**, 309-324.

CALCATERRA D., ESPOSITO A., FUSCHINI V., GALLUCCIO F., GIULIVO I., NARDÒ S., RUSSO F., TERRANOVA C. (2010) - *L'utilizzo della tecnica PSINSAR™ per l'individuazione ed il monitoraggio di sinkholes in aree urbanizzate della Campania: i casi di Telese Terme (BN) e Sarno (SA)*. Atti 2° Workshop Intern. "I sinkholes. Gli sprofondamenti catastrofici nell'ambiente naturale ed in quello antropizzato", 3-4 dicembre 2009, Roma, 931-948,

CALCATERRA D., RAMONDINI M., CALÒ F., LONGOBARDI V., PARISE M., GALZERANO C. (2008) - *DInSAR techniques for monitoring slow-moving landslides*. In: Chen et al. (Eds.) - Landslides and Engineered Slopes, vol. 2, 1095-1101, Taylor & Francis Group, London.

CALCATERRA S., CESI C., DI MAIO C., GAMBINO P., MERLI K., VALLARIO M. & VASSALLO R. (2012) - *Surface displacements of two landslides evaluated by GPS and inclinometer systems: a case study in Southern Apennines, Italy*. Natural Hazards, **61**, 257–266.

CALÒ F., CALCATERRA D., IODICE A., PARISE M. & RAMONDINI M. (2012) - *Assessing the activity of a large landslide in southern Italy by ground-monitoring and SAR interferometric techniques.* Int. J. of Remote Sensing, **33**(11), 3512-3530.

DI MARTIRE D., IODICE A., RAMONDINI M., RUELLO G. & CALCATERRA D. (2011a) - *Combined observations of surface displacements using Differential Interferometry SAR (DInSAR) and traditional monitoring techniques.* Proc. 8th Intern. Symp. on Field Measurements in GeoMechanics, Berlin, Germany, 12-16 September 2011, 13 pp.

DI MARTIRE D., DE LUCA G., RAMONDINI M. & CALCATERRA D. (2011b) - *Landslide-related PS data interpretation by means of different techniques.* Proc. of the 2nd World Landslides Forum, 3-7 October 2011, Rome, **6**, 360- 366.

GABRIEL A.K., GOLDSTEIN R.M. & ZEBKER H.A. (1989) - *Mapping small elevation changes over large areas: Differential interferometry*. J. Geophys. Res., **94**, 9183-9191.

MAZZOLI S. & HELMAN M. (1994) - *Neogene patterns of relative plate motion for Africa–Europe: some implications for recent central Mediterranean tectonics*. Geologische Rundschau, **83**, 464–468.

NIGRO F. & RENDA P. (1999) - *The North-Central Sicily belt: structural setting and geological evolution*. Annales Societatis Geologorum Poloniae, **69**, 49-61.

PLANK S., SINGER J., MINET C. & THURO K. (2012) - *Pre-survey suitability evaluation of the differential synthetic aperture radar interferometry method for landslide monitoring*, Int. J. of Remote Sensing, **33**(20), 6623-6637.

Intermittent SBAS (ISBAS) InSAR with COSMO-SkyMed X-band high resolution SAR data for landslide inventory mapping in Piana degli Albanesi (Italy)

Francesca Cigna*[a], Alessandro Novellino[b], Colm J. Jordan[a], Andrew Sowter[c], Massimo Ramondini[d], Domenico Calcaterra[b]
[a]British Geological Survey, Natural Environment Research Council, Keyworth, UK; [b]Dept. of Earth Sciences, Environment and Resources, Federico II University of Naples, Naples, Italy; [c]Nottingham Geospatial Institute, University of Nottingham, Nottingham, UK; [d] Dept. of Civil Architectural and Environmental Engineering, Federico II University of Naples, Naples, Italy

ABSTRACT

In the context of recent advances in InSAR processing techniques to retrieve higher persistent scatterer and coherent target densities over unfavourable land cover classes, this study tests the Intermittent Small Baseline Subset (ISBAS) approach to update the landslide inventory around the town of Piana degli Albanesi (Italy), an area where only 2% of the land appears suitable to generate radar scatterers based on a pre-survey feasibility assessment. ISBAS processing of 38 ascending mode and 36 descending mode COSMO-SkyMed StripMap HIMAGE SAR scenes at 3m resolution allows identification of ~726,000 and ~893,000 coherent and intermittently coherent pixels for the ascending and descending data stacks respectively. Observed improvements in the number of ISBAS solutions for the ascending mode are greater than 40 times compared to the conventional SBAS approach, not only for urban and rocky terrains, but also rural and vegetated land covers. Line of sight ground motion rates range between -6.4 and +5.5 mm/yr in 2008-2011, although the majority of the processed area shows general stability, with average rates of -0.6 mm/yr in the ascending and -0.1 mm/yr in the descending mode results. Interpretation of the ISBAS deformation rates, integrated with targeted field surveys and aerial photo-interpretation, provides a new and more complete picture of landslide distribution, state of activity and intensity in the test area, and allows depiction of very slow and extremely slow landslide processes even in areas difficult to access, with unprecedented coverage of results.

Keywords: InSAR, SBAS, ISBAS, ground motion, intermittent coherence, COSMO-SkyMed, landslide inventory

1. INTRODUCTION

A number of Interferometric Synthetic Aperture Radar (InSAR) processing approaches to estimate ground motion have been developed since the 1990s[1-7], and many successful applications carried out over recent years to prove the worth of these techniques to support landslide identification, delineation, assessment of state of activity and monitoring[8-16]. Obtaining InSAR results is, however, particularly challenging across non-urban land covers, such as vegetated terrain, rural regions, hilly and mountainous areas, where landslides generally occur but only a few persistent radar reflectors or coherent pixels can be identified[17-19]. Recent developments in InSAR processing techniques have been aimed at improving the coverage of results, in both urban and non-urban land covers. The SqueeSAR™ approach[20] and the Intermittent Small Baseline Subset (ISBAS) technique[21] are examples of such efforts of the InSAR community, and they are proving capable of greatly increasing the coverage of InSAR results by including distributed scatterers and intermittently coherent pixels, respectively, in their processing solutions. These new techniques have been successfully applied to the study of land motions in areas of natural and anthropogenic geohazards[22-24].

In this context of InSAR recent advances, this study is focused on a test area in north-western Sicily (Italy), which is affected by landsliding. The area includes the town of Piana degli Albanesi and namesake artificial lake, and the hydroelectric station and minor basin of Guadalami; the latter water bodies both along the Belice River (Figure 1a). According to the Italian Landslide Inventory produced by the Institute for Environmental Protection and Research in

* fcigna@bgs.ac.uk; phone +44 115 936 3551; fax +44 115 936 3446

SAR Image Analysis, Modeling, and Techniques XIV, edited by Claudia Notarnicola, Simonetta Paloscia, Nazzareno Pierdicca, Proc. of SPIE Vol. 9243, 92431B · © 2014 SPIE
CCC code: 0277-786X/14/$18 · doi: 10.1117/12.2067424

2007, a large portion of this area is affected by mass movement processes and the landslide index (i.e. ratio between landslide affected areas and total area, based on 1km by 1km cells) reaches values over 20% in some of its sectors to the west and east of the lake, though these statistics are renown to largely underestimate the actual hazard scenario[25].

Only ~2% of this region shows good potential for persistent scatterer InSAR applications, mainly in built-up areas and where man-made structures are present. This picture is based on a pre-survey feasibility study and analysis of land covers and their suitability to provide radar scatterers, carried out using the feasibility methodology discussed in [17].

Landslide-affected slopes in this area are mainly concentrated across rural and semi-vegetated terrain, hence unfavourable land covers, where C- and X-band multi-interferogram InSAR is less likely to succeed. In order to overcome land cover constraints for InSAR applications in non-urban terrain, ground motions in Piana degli Albanesi were therefore analysed by exploiting the ISBAS technique. Intermittently coherent pixels are considered during the analysis, and the coverage of InSAR results is thereby extended to rural, woodland, grassland and agricultural terrains. ISBAS outputs are combined with analysis of ancillary data, including geological, geomorphological and pre-existing landslide inventory maps, and on site surveys for an independent validation of landslide ground motion directions, state of activity and typology.

1.1 Pre-processing of COSMO-SkyMed imagery

Input data for this study consist of two stacks of X-band high resolution SAR images acquired by the Dual-Use (Civilian and Defence) end-to-end Earth Observation System named as COnstellation of small Satellites for Mediterranean basin Observation (COSMO-SkyMed) of the Italian Space Agency and the Ministry of Defence. 38 ascending and 36 descending mode StripMap HIMAGE 3m resolution SAR images were used. These cover the region of interest between November 2008 and October 2011, with ~40° look angle at the centre of the scene, and nominal revisiting time of 16 days.

After precise co-registration to single masters, subsets of the full scenes were selected for both ascending and descending modes, centered at 13.27° E and 37.97° N, to the west of Piana degli Albanesi Lake. The scenes were then multi-looked using a factor of 5 in both azimuth and range to reduce phase noise, thus obtaining 15m resolution pixels. To minimize temporal and spatial decorrelation, differential interferograms were generated for small baseline SAR pairs only, these identified by maximum normal baselines of 500m and maximum temporal separation of 2 years, which resulted in 306 interferograms for the ascending and 298 for the descending mode. The subtraction of initial topographic components was performed using a 5m DEM derived using topographic maps at 1:5,000 scale, published in 1990–1994 and distributed by the Regional Cartographic Center.

1.2 Intermittent SBAS (ISBAS) analysis

The ascending and descending mode stacks of interferograms were analysed to select intermittently coherent pixels, following the processing approach described in [21], which in turn builds upon the low-pass SBAS method described by [3]. Coherent pixels were identified by using a coherence threshold of 0.4 to discriminate high from low coherence pixels. A minimum number of 160 and 140 coherent interferograms per pixel was also employed as further threshold to limit the subsequent unwrapping only to pixels for which the best 160 ascending mode interferograms (or 140 for the descending mode) showed an average coherence greater than 0.4. These thresholds allowed, for each mode, coverage of around 90% of the region of interest with ground motion results, in terms of either coherent or intermittently coherent pixels.

Further steps of the processing followed the conventional low-pass SBAS approach[3], with the exception that both coherent and intermittently coherent pixels were processed. This means that in each interferogram, the sparse network of pixels considered coherent or intermittently coherent was unwrapped, by masking out any pixel resulting either rejected throughout the full stack of interferograms, or only in a subset of the latter, due to its intermittent nature.

The location used as reference and to which all ISBAS solutions were referred, was set within the urban fabric of Santa Cristina Gela, to the east of the lake (see Figure 1a). Linear velocities and their standard errors, improved heights and respective errors, as well as average temporal coherence and minimum number of coherent interferograms, and time series of ground motion were generated for both interferogram stacks, in ascending and descending mode.

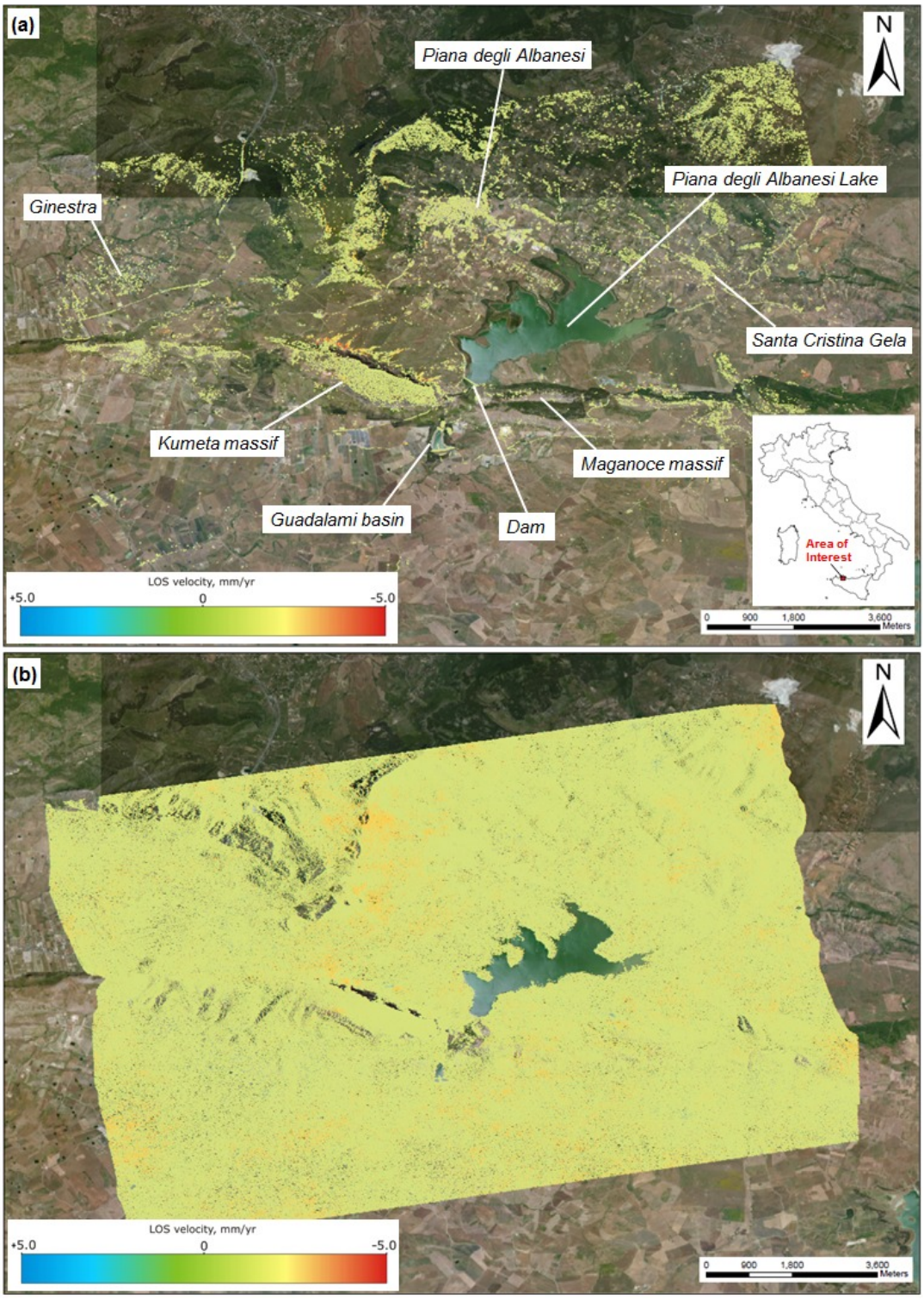

Figure 1: Annual ground motion rates for the area of Piana degli Albanesi (Italy), obtained from the (a) SBAS and (b) ISBAS processing of COSMO-SkyMed StripMap HIMAGE ascending mode data acquired between 2008 and 2011. Motion velocities are saturated to ±5.0 mm/yr. SBAS and ISBAS results are overlapped onto World Imagery [Source: Esri, DigitalGlobe, GeoEye, i-cubed, Earthstar Geographics, CNES/Airbus DS, USDA, USGS, AEX, Getmapping, Aerogrid, IGN, IGP, swisstopo, and the GIS User Community].

2. ISBAS RESULTS AND DISCUSSION

2.1 Coverage and estimated ground motion velocity

Over 726,000 coherent and intermittently coherent pixels were identified based on the processing of the ascending data, of which ~710,000 are intermittently coherent, thus representing an increase of more than 40 times the conventional SBAS solution, which encompasses ~16,000 coherent pixels. The average density of ISBAS results in ascending mode across the processed subset reaches 6,000 pixels/km^2 compared to ~140 pixels/km^2 for the SBAS solution (Figure 1a-b). A similar scenario was revealed by the processing results for the descending dataset, which allowed identification of over 893,000 coherent and intermittently coherent pixels, for an average density greater than 5,200 pixels/km^2.

SBAS solutions are mainly concentrated in areas dominated by stable scatterers, where urban settlements and linear structures (both road infrastructure and the dam) are present, as well as across areas of debris and rocky terrain, for instance onto the Kumeta massif (Figure 1a). Processing of intermittently coherent areas extends the coverage of results to almost the entire region of interest (Figure 1b), with the exception of radar layover and shadow areas in the north-western and central portions of the processed subset, and in the steep valley between Kumeta and Maganoce massifs, and water bodies of the Piana degli Albanesi Lake and the Guadalami basin.

Minimum and maximum observed annual velocities along the satellite Line Of Sight (LOS) range between -5.8 and +4.3 mm/yr in the ISBAS ascending mode results, and between -6.4 and +5.5 mm/yr in the descending mode results. Nonetheless, in both cases the majority of the processed area shows general stability, with average rates of -0.6 mm/yr in the ascending and -0.1 mm/yr in the descending mode results, and most ISBAS pixels move at rates within the range ±1.5 mm/yr, the latter usually considered as the stability threshold.

2.2 Landslide mapping with ISBAS and field-surveying

Multi-temporal COSMO-SkyMed ISBAS results were combined with ancillary data, including geological, geomorphological and pre-existing landslide inventory maps. On site surveys were also used for independent validation of landslide ground motion directions, state of activity and typology (Figure 2). A summary of the findings of this analysis are reported below, although the detailed discussion of these is beyond the scope of this paper.

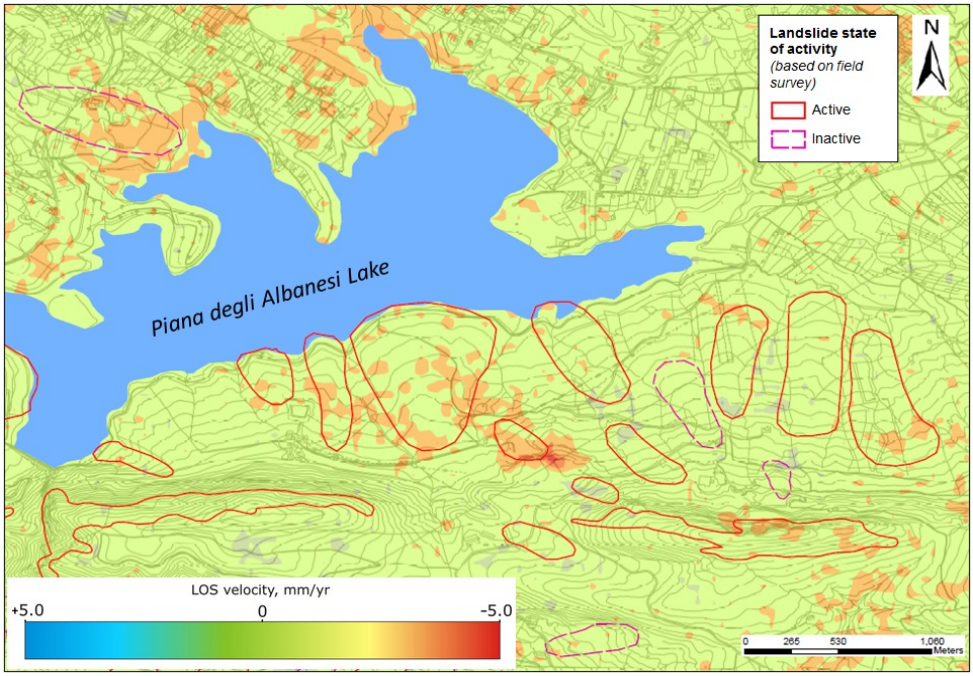

Figure 2: Interpolated ISBAS annual rates of ground motion in 2008-2011 for the area south of Piana degli Albanesi Lake, with indication of the boundaries of active and inactive landslides identified based on the field survey, overlapped onto 1:5,000 scale topographic maps distributed by the Regional Cartographic Center.

COSMO-SkyMed ISBAS results reveal that during 2008-2011 slopes surrounding Piana degli Albanesi artificial lake to the south and east moved at LOS rates between -1.5 and -5 mm/year (Figure 2), likely related to presence of structurally complex formations in the area of the Kumeta and Maganoce thrust fault.

Detailed information about very slow and extremely slow (according to the classification by [26]) landslide ground motion occurring in the investigated area confirms evidence and data gathered during field investigations, interpretation of aerial photographs carried out by the authors, and the pre-existing landslide inventory, and also complements the latter data sources by allowing improvement of landslide boundary delineation, even in some areas difficult to access. Predominance of complex and flow type landslides together with deep-seated gravitational slope deformations is found, the former linked to outcrops of marly and clayey lithologies and, the latter to the superposition of brittle carbonate over ductile rocks. Landslide mapping from field surveying is largely improved, by both redefining landslide boundaries, and identifying states of activity based on COSMO-SkyMed LOS rates for the years 2008-2011 and background information from the Italian Landslide inventory, the latter referenced to 2007, hence before the temporal coverage of the processed satellite data.

3. CONCLUSIONS

The outcomes of this work can be mainly discussed with regard to: (i) the performance of newly developed InSAR techniques across a region where only 2% of the land appeared suitable to generate radar scatterers based on pre-survey feasibility assessment; and (ii) the added value of both the processing technique and the high resolution data stack to the scope of updating the landslide inventory over Piana degli Albanesi in southern Italy.

The ISBAS test shows the improvement in the coverage of processing solutions that new InSAR techniques can provide for a variety of land covers, including non-urban and vegetated regions, where the likelihood of conventional approaches to identifying stable radar targets is very low. For the test area of Piana degli Albanesi, the low-pass ISBAS approach was employed to process two stacks of COSMO-SkyMed StripMap HIMAGE scenes, and allowed unprecedented coverage of ground motion monitoring results to be achieved, with an increase in this case of up to 40 times the conventional SBAS solutions. The combination of deformation estimates with field investigations, aerial photo-interpretation and information from the pre-existing landslide inventory, resulted in an updated picture of landsliding processes affecting the region, including improved landslide delineation, assessment of state of activity and intensity. This study and its output will support the forthcoming generation of landslide susceptibility and risk maps at new levels of spatial detail and temporal updating that were not previously achievable in Italy and elsewhere.

ACKNOWLEDGEMENTS

This research was carried out in the framework of the cooperation between the University of Naples Federico II, the British Geological Survey (BGS) and the University of Nottingham (UoN), during the research visit of A. Novellino at BGS and UoN under the supervision of F. Cigna and A. Sowter. COSMO-SkyMed StripMap HIMAGE data stacks were made available to the University of Naples Federico II by the Italian Ministry for the Environment, Land and Sea. 1:5,000 scale topographic maps distributed by the Regional Cartographic Center. World Imagery available at: http://goto.arcgisonline.com/maps/World_Imagery. F. Cigna and C. Jordan publish with the permission of the Executive Director of the BGS, Natural Environment Research Council.

REFERENCES

[1] Rosen, P. A., Hensley, S., Joughin, I. R., Fuk, K. L., Madsen, S. N., Rodriguez, E. and Goldstein, R. M., "Synthetic aperture radar interferometry," Proceedings of the IEEE, 88(3), 333-382 (2000).

[2] Crosetto, M., Monserrat, O., Iglesias, R. and Crippa, B., "Persistent Scatterer Interferometry: Potential, Limits and Initial C- and X-band Comparison," Photogrammetric Engineering and Remote Sensing, 76(9), 1061-1069 (2010).

[3] Berardino, P., Fornaro, G., Lanari, R. and Sansosti, E., "A new algorithm for surface deformation monitoring based on small baseline differential SAR interferograms," Geoscience and Remote Sensing, IEEE Transactions on, 40(11), 2375-2383 (2002).
[4] Ferretti, A., Prati, C. and Rocca, F., "Permanent scatterers in SAR interferometry," Geoscience and Remote Sensing, IEEE Transactions on, 39(1), 8-20 (2001).
[5] Werner, C., Wegmuller, U., Strozzi, T. and Wiesmann, A., "Interferometric point target analysis for deformation mapping." 2003 IEEE International Geoscience and Remote Sensing Symposium, IGARSS 2003 21-25 July 2003, 7, 4362-4364 (2003).
[6] Blanco, P., Mallorqui, J. J., Duque, S. and Navarrete, D., "Advances on DInSAR with ERS and ENVISAT Data using the Coherent Pixels Technique (CPT)." 2006 IEEE International Geoscience and Remote Sensing Symposium, IGARSS 2006, 31 July 2006 - 4 Aug. 2006, 1898-1901 (2006).
[7] Lanari, R., Mora, O., Manunta, M., Mallorqui, J. J., Berardino, P. and Sansosti, E., "A small-baseline approach for investigating deformations on full-resolution differential SAR interferograms," Geoscience and Remote Sensing, IEEE Transactions on, 42(7), 1377-1386 (2004).
[8] Bianchini, S., Cigna, F., Righini, G., Proietti, C. and Casagli, N., "Landslide HotSpot Mapping by means of Persistent Scatterer Interferometry," Environmental Earth Sciences, 67(4), 1155-1172 (2012).
[9] Bovenga, F., Wasowski, J., Nitti, D. O., Nutricato, R. and Chiaradia, M. T., "Using COSMO/SkyMed X-band and ENVISAT C-band SAR interferometry for landslides analysis," Remote Sensing of Environment, 119, 272-285 (2012).
[10] Cigna, F., Bianchini, S. and Casagli, N., "How to assess landslide activity and intensity with Persistent Scatterer Interferometry (PSI): The PSI-based matrix approach," Landslides, 10(3), 267-283 (2013).
[11] Colesanti, C. and Wasowski, J., "Investigating landslides with space-borne Synthetic Aperture Radar (SAR) interferometry," Engineering Geology, 88(3–4), 173-199 (2006).
[12] Herrera, G., Gutiérrez, F., García-Davalillo, J. C., Guerrero, J., Notti, D., Galve, J. P., Fernández-Merodo, J. A. and Cooksley, G., "Multi-sensor advanced DInSAR monitoring of very slow landslides: The Tena Valley case study (Central Spanish Pyrenees)," Remote Sensing of Environment, 128, 31-43 (2013).
[13] Strozzi, T., Ambrosi, C. and Raetzo, H., "Interpretation of Aerial Photographs and Satellite SAR Interferometry for the Inventory of Landslides," Remote Sensing, 5(5), 2554-2570 (2013).
[14] Meisina, C., Zucca, F., Notti, D., Colombo, A., Cucchi, A., Savio, G., Giannico, C. and Bianchi, M., "Geological Interpretation of PSInSAR Data at Regional Scale," Sensors, 8(11), 7469-7492 (2008).
[15] Wasowski, J. and Bovenga, F., "Investigating landslides and unstable slopes with satellite Multi Temporal Interferometry: Current issues and future perspectives," Engineering Geology, 174, 103-138 (2014).
[16] Calò, F., Calcaterra, D., Iodice, A., Parise, M. and Ramondini, M., "Assessing the activity of a large landslide in southern Italy by ground-monitoring and SAR interferometric techniques," International Journal of Remote Sensing, 33(11), 3512-3530 (2012).
[17] Cigna, F., Bateson, L. B., Jordan, C. J. and Dashwood, C., "Simulating SAR geometric distortions and predicting Persistent Scatterer densities for ERS-1/2 and ENVISAT C-band SAR and InSAR applications: Nationwide feasibility assessment to monitor the landmass of Great Britain with SAR imagery," Remote Sensing of Environment, 152, 441-466 (2014).
[18] Plank, S., Singer, J. and Thuro, K., "Assessment of number and distribution of persistent scatterers prior to radar acquisition using open access land cover and topographical data," ISPRS Journal of Photogrammetry and Remote Sensing, 85, 132-147 (2013).
[19] Tapete, D. and Cigna, F., "Rapid mapping and deformation analysis over cultural heritage and rural sites based on Persistent Scatterer Interferometry," International Journal of Geophysics, 2012, ID 618609, 1-19 (2012).
[20] Ferretti, A., Fumagalli, A., Novali, F., Prati, C., Rocca, F. and Rucci, A., "A New Algorithm for Processing Interferometric Data-Stacks: SqueeSAR," Geoscience and Remote Sensing, IEEE Transactions on, 49(9), 3460-3470 (2011).
[21] Sowter, A., Bateson, L., Strange, P., Ambrose, K. and Syafiudin, M., "DInSAR estimation of land motion using intermittent coherence with application to the South Derbyshire and Leicestershire coalfield," Remote Sensing Letters, 4(10), 979-987 (2013).
[22] Tapete, D., Fanti, R., Cecchi, R., Petrangeli, P. and Casagli, N., "Satellite radar interferometry for monitoring and early-stage warning of structural instability in archaeological sites," Journal of Geophysics and Engineering, 9(4), S10 (2012).

[23] Bateson, L., Cigna, F., Boon, D. and Sowter, A., "The application of the Intermittent SBAS (ISBAS) InSAR method to the South Wales Coalfield, UK," International Journal of Applied Earth Observation and Geoinformation, (2014).
[24] Meisina, C., Notti, D., Zucca, F., Ceriani, M., Colombo, A., Poggi, F., Roccati, A. and Zaccone, A., [The Use of PSInSAR™ and SqueeSAR™ Techniques for Updating Landslide Inventories], In Margottini, C., Canuti, P. and Sassa, K.: "Landslide Science and Practice," Springer Berlin Heidelberg, 1, pp. 81-87 (2013).
[25] ISPRA, [IFFI, Inventario dei Fenomeni Franosi in Italia], (2007).
[26] Cruden, D. M. and Varnes, D. J., [Landslide types and processes], In Turner, A. K. and Shuster, R. L.: "Landslides: Investigation and Mitigation," Transportation Research Board, Special Report 247, pp. 36-75 (1996).

Using Data from Multiple SAR Sensors in Landslide Characterization: Case Studies from Different Geomorphological Contexts in Italy

62

Alessandro Novellino, Anna De Agostini, Diego Di Martire, Massimo Ramondini, Mario Floris, and Domenico Calcaterra

Abstract

An application of Differential Interferometry SAR (DInSAR) technique based upon C- and X-band SAR imagery is here presented. The aim of this study was to assess SAR technology's applicability and reliability for landslide detection and monitoring. To this purpose, two test sites have been selected, both located in Italy, which are affected by slow-moving landslides: Rovegliana, falling within the North-Eastern sector of Italian Alps, and Varco d'Izzo, which belongs to the Southern Apennines. Results from C-band (ERS and EnviSat) and X-band (COSMO-SkyMed and TerraSAR-X) imagery data allowed to identify several unstable areas previously undetected for the Rovegliana site, while the state of activity of Varco d'Izzo landslides was confirmed.

Keywords

Landslides • A-DInSAR • X and C sensors

62.1 Introduction

The study of landslides with satellite sensors now relies on some decades of solid applications thanks to many works that have demonstrated a huge potential for geohazards monitoring (Sansosti et al. 2014 and reference therein) by using a wide range of spatial scales (regional to local), temporal samplings (yearly to days) and significantly high precisions (up to a few millimeters). This work aims at: (a) displaying the potential of advanced interferometric techniques for detection and monitoring of landslide-related ground deformations at local scale, (b) identifying their boundaries and (c) defining their annual displacement rates. Geological and geomorphological surveys were also conducted in order to improve the knowledge of the areas and to confirm radar results. Rovegliana (Fig. 62.1a) is the first study area and is located on the left side of the Agno Valley (Province of Vicenza, Eastern Italian Alps).

The second area (Fig. 62.1b) is located along the left bank of the Basento river valley, in a zone called Varco d'Izzo, some km east of Potenza (Basilicata region).

A. Novellino (✉) · D. Calcaterra
Department of Earth Sciences, Environment and Resources, Federico II University of Naples, Largo San Marcellino 10, 80138 Naples, Italy
e-mail: Alessandro9188@hotmail.com

D. Calcaterra
e-mail: domenico.calcaterra@unina.it

A. De Agostini · M. Floris
Department of Geosciences, University of Padua, Via Gradenigo 6, 35131 Padua, Italy
e-mail: anna.deago@libero.it

M. Floris
e-mail: mario.floris@unipd.it

D. Di Martire · M. Ramondini
Department of Civil, Architectural and Environmental Engineering, Federico II University of Naples, via Claudio 21, 80125 Naples, Italy
e-mail: diego.dimartire@unina.it

M. Ramondini
e-mail: massimo.ramondini@unina.it

G. Lollino et al. (eds.), *Engineering Geology for Society and Territory – Volume 2*,
DOI: 10.1007/978-3-319-09057-3_62,

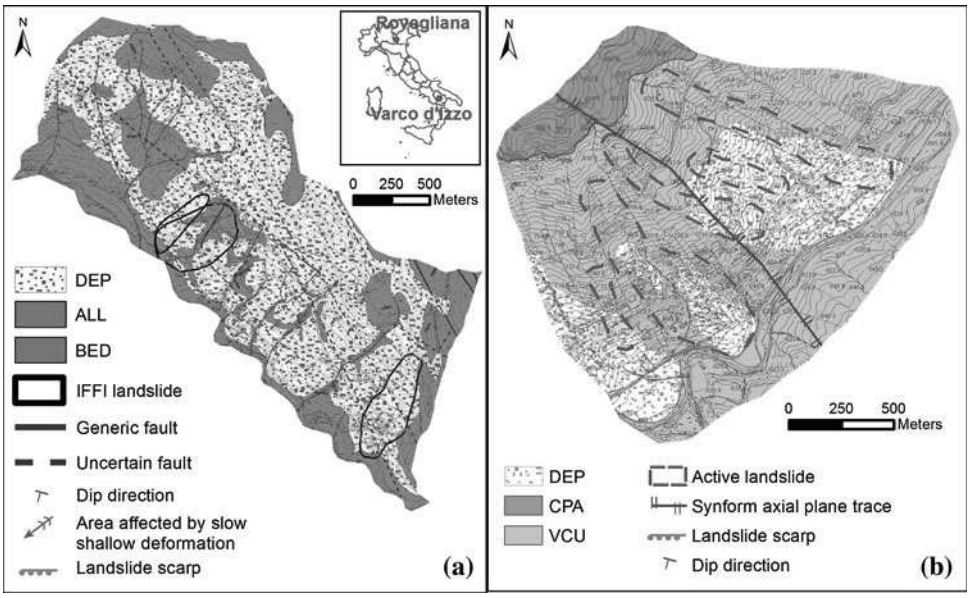

Fig. 62.1 **a** Geological and geomorphologic map of the Rovegliana slope (modified from Barbieri et al. 1980) and location of IFFI landslides. Slope deposits (*DEP*), alluvial deposits (*ALL*), bedrock formations (*BED*). **b** Geologic and geomorphologic map of Varco d'Izzo slope. Slope deposits (*DEP*), Corleto Perticara formation (*CPA*), varicoloured clays unit (*VCU*)

62.2 Geological, Structural and Geomorphological Setting

The landslide in the Rovegliana area (Fig. 62.1a) develops on a slope with an average dip angle of 20° and a SW aspect, and mainly involves Quaternary colluvial/eluvial and landslide deposits. The former are lithologically homogeneous with a good sortening, whereas the latter are heterogeneous and their block size ranges from metric to centimetric with a prevalent clayey matrix (Barbieri et al. 1980).

Sliding surfaces are probably located at the contact between the Quaternary deposits and the bedrock, which is composed of phyllites of the Southern Alps Crystalline Basement and Permo–Triassic calcareous and silicoclastic sedimentary succession. Geological and geostructural setting of the Rovegliana slope is controlled by the presence of a regional strike-slip fault (Schio-Vicenza Fault). Its activity (from Mesozoic extensions to Paleogenic Alpine shortening) caused the dislocations of the sedimentary succession, worsening the geomechanical properties of the bedrock masses which, in turn, represents, along with the presence of several clayey/silty horizons, the main landslide predisposing factor. In the Varco d'Izzo area (Fig. 62.1b), five earth flows have been inventoried, which show a very slow to extremely slow velocity (Cruden and Varnes 1996) with rupture surfaces located at a depth never exceeding 40 m below the ground level (Di Maio et al. 2010).

Landslides affect the upper portion of the Varicoloured Clays Unit (VCU), a clayey succession including also marly-clayey levels and turbiditic calcareous marls, calcilutites and calcarenites intervals, with an overall thickness of 300 m. VCU is characterized by a pervasive extensional jointing which created a preferential hydrographical pattern along a NW–SE direction and is also a relevant landslide predisposing factor.

The five inventoried landslides start at an elevation between 820 m and 760 m a.s.l. along a SE-facing hill, whose slope angle is 8° and vary from 500 m to 1,100 m in length; they reach the valley bottom causing severe damage to a highway and a railway track.

62.3 Processing Algorithms and Data Set

The study involved the use of Differential Interferometry Synthetic Aperture Radar (DInSAR) technique. Very high resolution (VHR) in X-band and medium resolution (MR) C-band images have been processed.

In the Rovegliana area, 65 ERS-1 and ERS-2 descending images (from May 1995 to December 2000) and 29 descending EnviSat images (from January 2003 to August 2010) were used. These data sets have been analysed by means of the PSInSAR technique (Ferretti et al. 2001), which investigates the SAR images at full resolution in those points with higher and stable values of backscattering (reflectivity) along time (the so-called Permanent Scatterers, PS).

At Varco d'Izzo, a stack of 43 ascending images from the COSMO-SkyMed archive (CSK—from September 2010 to November 2011) and of 29 ascending images from Terra-SAR-X archive (TSX—from February 2010 to April 2011) were used. Both data sets have been processed by means of the Coherent Pixels Technique (CPT-Mora et al. 2003) algorithm, which belongs to the SBAS techniques family. The latter, selecting points through the coherence value (cross-correlation coefficient between two SAR images),

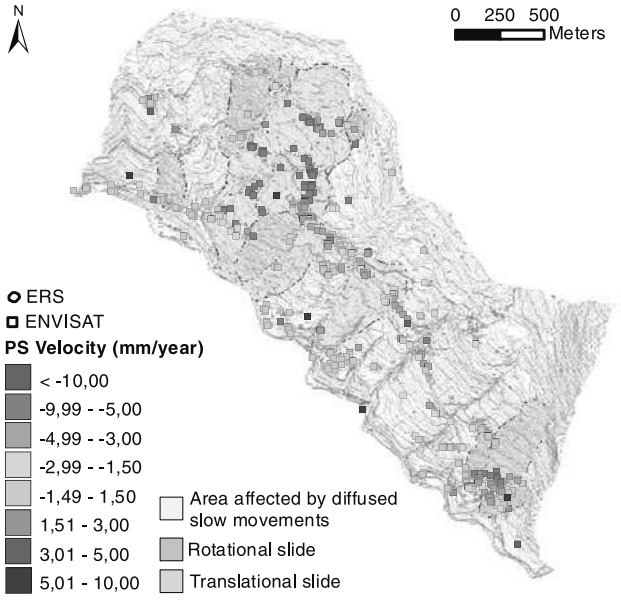

Fig. 62.2 PS deformation rates for the Rovegliana slope. Values are measured along the descending LOS

performs well in non-urban or scarcely vegetated areas. Processing results are represented by the displacement rate map and the time-series of deformations along the Line of Sight—LOS.

62.4 Results of Interferometric Analysis

For the Rovegliana site PS data, mainly corresponding to the existing houses, allowed to identify eleven unstable areas, previously undetected, and to define their rate of movement (Fig. 62.2). The highest displacement LOS velocity values are between 6 and 9 mm/year and affect the middle-left zone of the study area. The previously inventoried landslides, which affect the village in the lower-right part of the slope, were identified by PS data as well. They revealed an annual displacement rate between 5 and 7 mm/year, similar to that measured with the total station monitoring conducted between 2006 and 2009, when an annual displacement rate of 10 to 13 mm/year was recorded. The difference between PSI and in situ monitoring velocity values is probably due to the projection of real movement (WSW–ESE direction) along LOS direction (NE–SW).

It is worth pointing out that both ERS and EnviSat satellite constellations identified the unstable areas and the displacement rate was very similar for the two analysed periods.

For the Varco d'Izzo landslides, the highest displacement rates (>10 mm/year) are located near the landslides' crowns, where the main scarps have been observed during the geomorphological field survey. It is worth pointing out that the positive (sensor to target direction) or negative (target to sensor direction) values depend on the geometry (right look-side in ascending orbit) of acquisition (Di Martire et al. 2013). The latter, in terms of incident and heading angle, also causes the difference between displacement rate values recorded by the TSX and CSK sensors (Plank et al. 2012). Finally, the time-series of deformations, along the slope direction, are shown in Fig. 62.3. Such results have only been calculated in the points with significant DInSAR deformations during the September 2010–April 2011 time span, which is the time slot common to both sensors. As shown in the graphs (Fig. 62.3), the comparison between the sensors' measurements demonstrates a very consistent agreement in all the investigated points, thus confirming the reliability of this DInSAR technique.

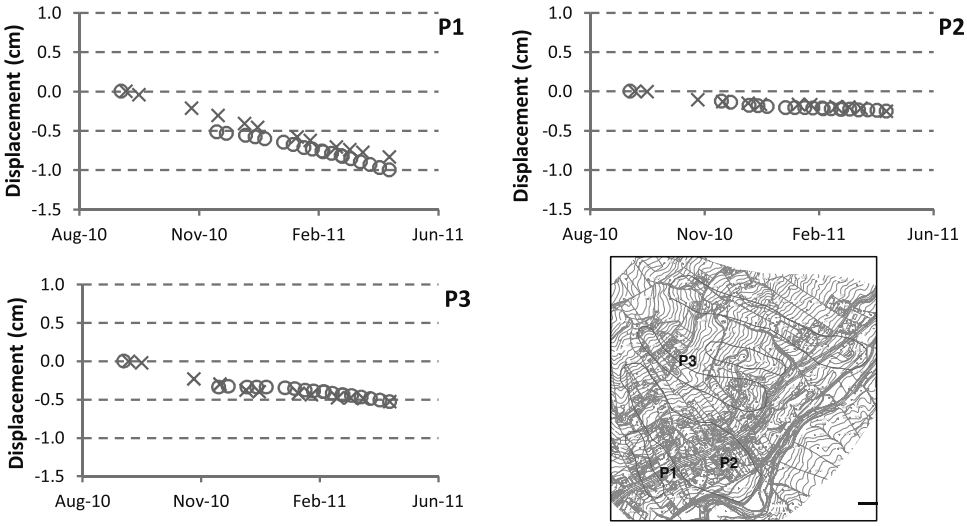

Fig. 62.3 COSMO-SkyMed (*red*) and TerraSAR-X (*blue*) time-series of deformations processing for the Varco d 'Izzo landslides

62.5 Concluding Remarks

PS and CPT data obtained from interferometric processing were very helpful in analyzing slope instabilities of the case studies here discussed. Once again, remote sensing techniques allowed to overcome the usual drawbacks of conventional field detection and monitoring methods (e.g. GPS, laser scanning, optical photos, LIDAR), which, especially when used over wide areas, are quite expensive and time-consuming. PS and CPT results contributed to perform a reliable detection of landslide areas with respect to traditional monitoring techniques. Furthermore, a relevant improvement in results has been reached by the use of VHR images (CSK and TSX) instead of EnviSat ones (Di Martire et al. 2012). Indeed, such images are able, on one hand, to detect a larger number of points thanks to a finer resolution cell (3 m × 3 m), and, on the other one, to better assess the evolution in time of the phenomena, having a shorter revisiting-time (8 and 11 days respectively).

Acknowledgments ERS and EnviSat images were provided by the Italian Ministry of Environment, Territory and Sea, represented by dr. S. Costabile; CSK data by the Italian Space Agency Geodesy Space Centre, represented by Dr. F. Nirchio; TSX data by the German Aerospace Center through the GEO1589 project (P.I. Davide Notti—University of Pavia, Italy).

References

Barbieri G, De Zanche V, Di Lallo E, Mietto PE, Sedea R (1980) Profiles and explanatory notes of the geological map of Recoaro area. Memorie di Scienze Geologiche 34:23–52

Cruden DM, Varnes DJ (1996) Landslide types and processes. In: Turner AK, Schuster RL (eds) Landslides: investigation and mitigation. Transportation Research Board, Washington D.C., pp 36–75

Di Maio C, Vassallo R, Vallario M, Sdao F (2010) Structure and kinematics of a landslide in a complex clayey formation of the Italian Southern Apennines. Eng Geol 116:311–322

Di Martire D, De Luca G, Ramondini M, Calcaterra D (2013) Landslide-related PS data interpretation by means of different techniques. In: Margottini C, Canuti P, Sassa K (eds) Landslide science and practice, vol 2. Springer, Heidelberg, pp 347–355

Di Martire D, Ramondini M, Vassallo R, Di Maio C (2012) Integration of ground-and satellite monitoring techniques for the study of two slow-moving landslides. In: Incontro Annuale dei Ricercatori di Geotecnica, Padova, 2–4 July 2012

Ferretti A, Prati C, Rocca F (2001) Permanent Scatterers in SAR interferometry. IEEE Trans Geosci Remote Sens 39:8–20

Mora O, Mallorqui JJ, Broquetas A (2003) Linear and nonlinear terrain deformation maps from a reduced set of interferometric SAR images. IEEE Transa Geosci Remote Sens 41:2243–2253

Plank S, Singer J, Minet C, Thuro K (2012) Pre-survey suitability evaluation of the differential synthetic aperture radar interferometry method for landslide monitoring. Int J Remote Sens 33:6623–6637 (2012)

Sansosti E, Berardino P, Bonano M, Calo F, Castaldo R, Casu F, Manunta M, Manzo M, Pepe A, Pepe S, Solaro G, Tizzani P, Zeni G, Lanari L (2014) How second generation SAR systems are impacting the analysis of ground deformation. Int J Appl Earth Obs Geoinf 28:1–11